

---

# Impact of High-Latitude Atmosphere-Ionosphere Coupling on the Space Weather

Florian Ludwig Günzkofer

---



München 2024



---

# Impact of High-Latitude Atmosphere-Ionosphere Coupling on the Space Weather

Florian Ludwig Günzkofer

---

Dissertation  
der Fakultät für Physik  
der Ludwig-Maximilians-Universität  
München

vorgelegt von  
Florian Ludwig Günzkofer  
aus Bogen

München, den 16. April 2024

Erstgutachter: Prof. Dr. Markus Rapp

Zweitgutachter: PD Dr. Gunter Stober

Tag der mündlichen Prüfung: 06. Juni 2024

# Zusammenfassung

Der Schutz von satelliten- und bodengebundener Infrastruktur vor den Auswirkungen des sogenannten *Weltraumwetters* macht die Entwicklung von verlässlichen Weltraumwettervorhersagen notwendig. Das Weltraumwetter wird von vielen Vorgängen ausgehend von der Sonnenoberfläche bis hin zur Erdatmosphäre und -ionosphäre beeinflusst. Die Variabilität der Ionosphäre wird überwiegend von der Sonne und dem Sonnenwind bestimmt. Allerdings tragen auch dynamische Atmosphärenprozesse, die sich bis in den Höhenbereich der Ionosphäre ausbreiten, signifikant zum Weltraumwetter bei. Aufgrund der Wechselwirkung von neutraler Atmosphäre und Ionosphäre durch Teilchenkollisionen entsteht die ionosphärische Dynamoschicht, auch als Übergangsregion bezeichnet, in ungefähr 80 – 120 km Höhe. In hohen geographischen Breiten fließen in dieser Region starke elektrische Ströme, die geomagnetische Störungen verursachen und das ionosphärische Plasma aufheizen. Da viele Atmosphären- und Weltraumwetterprozesse auf sehr kleinen Zeit- und Größenskalen stattfinden, müssen sie in Ionosphärenmodellen parametrisiert werden. Daher wird für verlässliche Weltraumwettervorhersagen ein verbessertes Verständnis der Wechselwirkung zwischen dem Neutralgas der Atmosphäre und dem Plasma der Ionosphäre benötigt. Diese Dissertation untersucht den Einfluss der Atmosphären-Ionosphärenkopplung in hohen Breitengraden auf das Weltraumwetter und den Beitrag von dynamischen Atmosphärenprozessen zur Variabilität der Übergangsregion.

Atmosphärische Gezeiten können sich nach oben ausbreiten und interagieren mit gezeitenähnlichen Winden die durch die polare Plasmakonvektion induziert werden. Es wird gezeigt, dass gezeiten-artige Atmosphärenwellen oberhalb der Übergangsregion lokal induziert werden und nicht mit Gezeitenwellen aus niedrigeren Atmosphärenschichten in Verbindung stehen. Dreidimensionale Beobachtungen von atmosphärischen Schwerewellen und propagierenden ionosphärischen Störungen werden durch die Kombination eines Meteor Radar Clusters und eines Inkohärenten Streuradars erzielt. Die Wellenparameter der ionosphärischen Störungen können mit der Dispersionsrelation von Schwerewellen beschrieben werden, was auf Weltraumwettervorhersagen übertragen werden kann. Es wird demonstriert wie Thermosphärenwinde aus solchen Wellenbeobachtungen abgeleitet werden können. Der Übergang von einer kollisionsdominierten zu einer kollisionsfreien Ionosphäre führt zu einem Maximum der elektrischen Leitfähigkeit in der ionosphärischen Dynamoschicht. Das Aufheizen der Ionosphäre durch elektrische Ströme wird in physikalischen Modelle empirisch skaliert, um das Fehlen von Prozessen zu kompensieren, die unterhalb der Modelauflösung stattfinden. In dieser Arbeit wird der benötigte Skalierungsfaktor untersucht

und Nachschlagetabellen für eine verbesserte Skalierung werden zur Verfügung gestellt. Abschließend wird die Kollisionsfrequenz von Ionen und Neutralteilchen, die den Schlüsselparameter der Atmosphären-Ionosphärenkopplung darstellt, untersucht. Eine neue Methode zur Messung der Kollisionsfrequenz wird vorgestellt. Es wird beobachtet, dass das vertikale Profil der Kollisionsfrequenz signifikant von der Klimatologie abweichen kann. Diese Abweichungen müssen verstanden und in Weltraumwettervorhersagen miteinbezogen werden.

# Abstract

To protect ground- and satellite-based infrastructure from harm due to the so-called *space weather*, it is necessary to develop reliable space weather forecasts. Space weather involves a large number of processes from the surface of the Sun to the Earth's atmosphere-ionosphere system. The variability of the ionosphere is largely determined by the Sun and the solar wind. However, atmospheric dynamic processes propagating to ionospheric altitudes contribute significantly to space weather. Additionally, the collisional coupling of the neutral atmosphere and the ionosphere leads to the formation of the ionospheric dynamo/transition region at about 80 – 120 km altitude. At high latitudes, strong electric currents at these altitudes cause geomagnetic disturbances and heat the ionospheric plasma. Since many space weather processes take place on small temporal or spatial scales, they have to be empirically described for ionospheric modeling. Therefore, reliable space weather forecasts require an improved understanding of atmosphere-ionosphere coupling. This thesis investigates the impact of high-latitude atmosphere-ionosphere coupling on space weather and the contribution of atmospheric waves to the variability of the transition region.

Atmospheric tides can propagate upward and interact with tidal winds forced by the polar plasma convection. It is shown that tidal winds above the transition region are forced locally and not associated with tidal waves from lower atmospheric regions. Three-dimensional observations of atmospheric gravity waves and traveling ionospheric disturbances are obtained by combining a meteor radar cluster and an incoherent scatter radar. The wave characteristics of the ionospheric disturbances can be described with the gravity wave dispersion relation which can be applied for space weather forecasts. It is demonstrated how thermosphere neutral winds can be inferred from such wave observations.

The transition from a collisional to a collision-less ionosphere causes a maximum of electric conductivity in the ionospheric dynamo region. The heating of the ionosphere by electric currents is empirically scaled in physics-based models to compensate for missing processes that take place on scales below the model resolution. This thesis investigates the required scaling factor and look-up tables for improved scaling are provided. Finally, the ion-neutral collision frequency, which is the key parameter of atmosphere-ionosphere coupling, is investigated. A new method for direct ion-neutral collision frequency measurements is presented. It is observed that the collision frequency profile can deviate quite significantly from the climatology. These deviations need to be understood and included in space weather forecasts.



# Contents

<b>Zusammenfassung</b>	<b>iii</b>
<b>Abstract</b>	<b>v</b>
<b>1 Introduction</b>	<b>1</b>
1.1 The ionosphere, space weather, and atmosphere-ionosphere coupling . . . .	1
1.2 The ionospheric dynamo/transition region . . . . .	6
1.2.1 The role of plasma-neutral collisions . . . . .	6
1.2.2 Ionospheric conductivities . . . . .	8
1.3 Atmospheric processes in the transition region . . . . .	11
1.3.1 Tidal oscillations . . . . .	12
1.3.2 Atmospheric gravity waves and traveling ionospheric disturbances .	13
1.4 The scientific objective of this thesis and the state of the art . . . . .	14
<b>2 Methods - measurements and modeling</b>	<b>19</b>
2.1 Incoherent Scatter Radars . . . . .	20
2.1.1 Level 1 and 2 - the two-peak incoherent scatter spectrum and ISR plasma parameters . . . . .	20
2.1.2 Level 3 - 3D dynamics and neutral atmosphere parameters . . . . .	22
2.2 EISCAT and EISCAT_3D . . . . .	26
2.3 Meteor Radars . . . . .	27
2.4 Atmosphere-Ionosphere models . . . . .	28
2.4.1 Empirical atmosphere, ionosphere, and convection models . . . . .	29
2.4.2 General Circulation Models . . . . .	30
<b>3 Results</b>	<b>31</b>
3.1 <i>In situ</i> forcing of semidiurnal tidal oscillations in the transition region . . .	31
3.2 Inferring neutral wind velocities from AGW-TID observations . . . . .	33
3.3 Optimizing the empirical scaling factor for model Joule heating rates . . .	35
3.4 Direct measurement of ion-neutral collision frequency profiles . . . . .	37
<b>4 Summary and Outlook</b>	<b>39</b>
<b>A Published Articles</b>	<b>41</b>

---

<b>B Climatology of <math>\nu_{in}/\omega_i \approx 0</math> condition</b>	<b>113</b>
<b>Bibliography</b>	<b>115</b>
<b>Danksagung</b>	<b>125</b>

# List of Figures

1.1	Atmosphere-Ionosphere layers and composition . . . . .	2
1.2	Schematic of the polar plasma convection . . . . .	4
1.3	Atmosphere-Ionosphere coupling schema . . . . .	5
1.4	The ionospheric dynamo region . . . . .	7
1.5	Ionospheric conductivities and currents . . . . .	10
1.6	Time-scales and dynamics of atmospheric waves . . . . .	11
1.7	TIE-GCM neutral atmosphere zonal wind and temperature . . . . .	13
1.8	Gravity waves in the lower atmosphere and the MLT region . . . . .	14
2.1	The two-peak incoherent scatter spectrum . . . . .	21
2.2	Schematic of mono- and tristatic EISCAT experiments . . . . .	22
2.3	ISR measurements of ion-neutral collision frequency . . . . .	25
2.4	Photographs of EISCAT and EISCAT_3D sites . . . . .	26
2.5	Meteor radar principle and the Nordic Meteor Radar Cluster . . . . .	28
3.1	Ratio of 12 h to 24 h oscillation amplitude in the transition region . . . . .	32
3.2	AGW-TID observations and inferred wind profile . . . . .	34
3.3	Vertical profiles of EISCAT and TIE-GCM Joule heating rates . . . . .	36
3.4	EISCAT ISR spectra and inferred collision frequency profile . . . . .	38
B.1	Collision to gyro-frequency ratio climatology . . . . .	113



# Chapter 1

## Introduction

### 1.1 The ionosphere, space weather, and atmosphere-ionosphere coupling

Though most commonly known for its already outdated application in television flat screens, the *plasma* state of matter is highly important for both science and technology. Nuclear fusion reactors fueled with a Deuterium-Tritium plasma might play a crucial role in emission-free power generation in the future. But plasma is also a part of already commonly applied technologies, e.g. plasma-welding and -cutting or the disinfection of medical tools. In nature, plasma is actually the by far most abundant state of matter in the visible universe and makes up for the majority of star and interstellar medium. On Earth, however, the only widely known natural plasma phenomenon is lightning. The largest, though far less commonly known, abundance of plasma in the Earth system is the so-called *ionosphere*.

The ionosphere is a plasma embedded in the Earth's atmosphere. Electromagnetic radiation and precipitating solar, magnetospheric, and galactic particles in combination with a complex set of chemical reactions lead to the partial ionization of the neutral atmosphere and formation of the ionosphere. Figure 1.1 a) shows the vertical layering of the neutral atmosphere (determined by the neutral temperature profile) and the ionosphere (determined by the plasma density profile). The density profiles of the most important ion and neutral particle species are shown in Figure 1.1 b).

Ionosphere research became of importance following the first trans-Atlantic radio transmissions in the early 20th century to explain the reflection of radio signals (Marchant, 1916). It was proposed that these transmissions were possible due to an electrically conducting layer of the atmosphere at around 100 km altitude which was therefore called *E region*. After the existence of the E region was confirmed by Appleton and Barnett (1925), further electrically conducting layers in the upper atmosphere were discussed (Appleton, 1927). Two other main layers with a local abundance of plasma were identified and consequently called *D region* and *F region* (see Figure 1.1 a). In these regions, the ionization is dominated by the absorption of extreme ultraviolet (EUV) radiation (F region, wavelengths

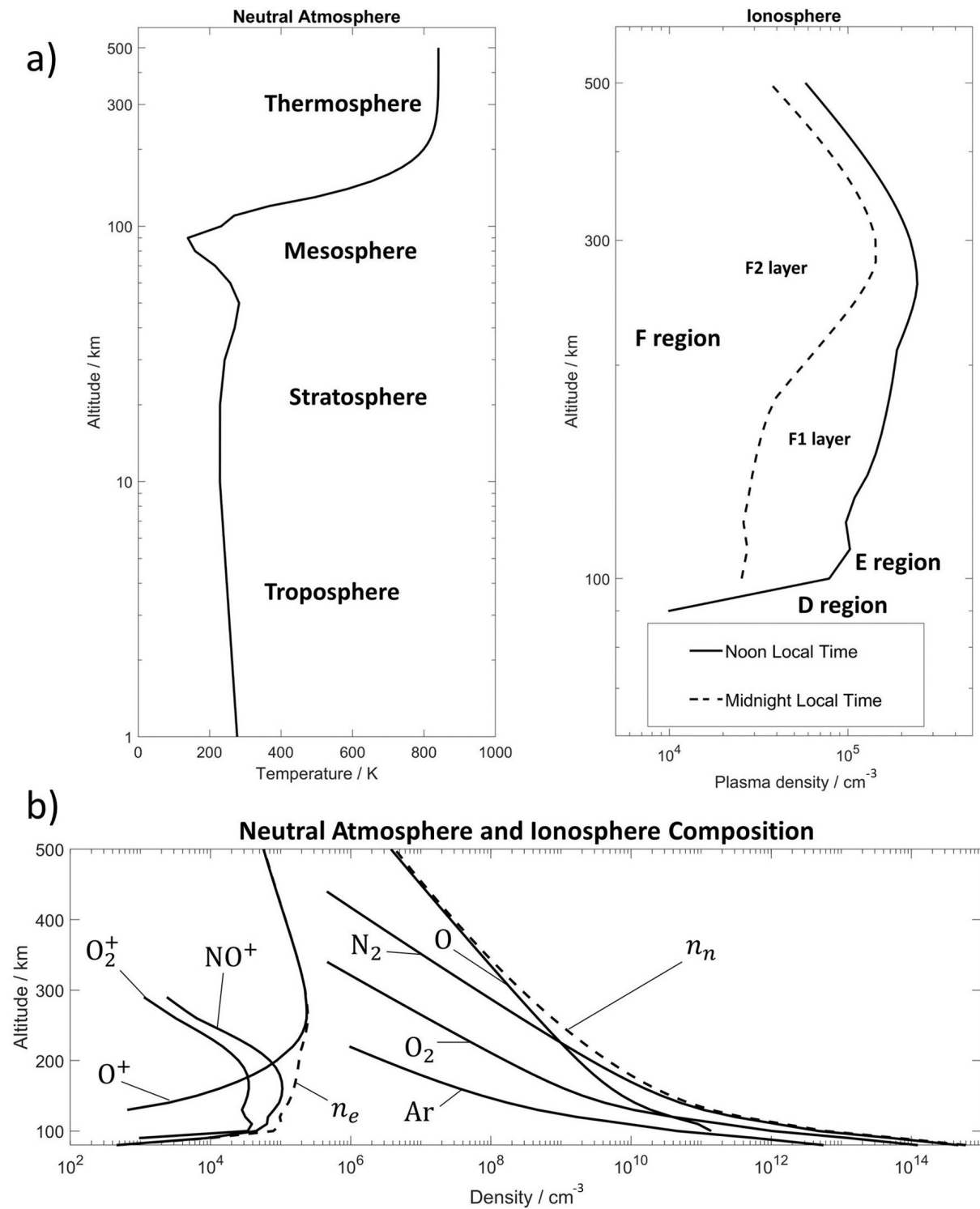


Figure 1.1: a) Vertical profiles of neutral gas temperature (left) and plasma density (right). These two quantities are used to distinguish the different layers of the neutral atmosphere and the ionosphere. b) Density profiles of ion and neutral particle species at ionosphere altitudes. All profiles in this figure were obtained from empirical climatologies of the neutral atmosphere (NRLMSIS, Picone et al., 2002) and the ionosphere (IRI, Bilitza et al., 2022).

$\lambda \sim 10 - 120$  nm), soft X-rays (E region,  $\lambda \sim 0.1 - 10$  nm) and Lyman  $\alpha$  radiation (D region,  $\lambda = 121.6$  nm, resonant absorption by Nitric Oxide) (Kelley, 2009; Schunk and Nagy, 2009). At high latitudes, precipitating protons and electrons contribute significantly to the ionization of the atmosphere (Baumjohann and Treumann, 1996).

The layering of the ionosphere and its day-night variation shown in Figure 1.1 a) are determined by an equilibrium of ionization and recombination processes as described in (Rishbeth and Garriott, 1969, Chapter 3.6). The dominant plasma loss process of the ionosphere is the dissociative recombination of molecular ions. In the D and E regions where molecular ions are predominant, the recombination rate increases with the square of the plasma density, i.e.  $r_1 = \alpha n_e^2$ , with the constant recombination parameter  $\alpha$ . In the F region, however, atomic oxygen ions  $O^+$  are a significant constituent of the ionosphere.  $O^+$  ions are lost due to the so-called *two-stage loss process* proposed by Bates and Massey (1947). The first stage is the collisional charge transfer from atomic to molecular ions. The charge transfer rate is linearly correlated with the plasma density, i.e.  $r_2 = \beta n_e$ . The charge transfer takes place via collisions of atomic ions and neutral molecules and therefore the transfer parameter is correlated to the neutral density, i.e.  $\beta \propto n_n$ . The second stage of the *two-stage loss process* is the dissociative recombination of the molecular ions with rate  $r_1$ . Due to the exponential decrease of the neutral atmosphere density, there is a transition from  $\alpha \ll \beta$  to  $\alpha \gg \beta$  within the F region.

The total plasma loss rate is determined by the slower of the two processes. Therefore, the recombination of the lower F region occurs at the dissociative recombination rate  $r_1$  (equivalent to the D and E regions) which is referred to as  *$\alpha$ -recombination*. In the upper F region, the recombination occurs at the charge transfer rate  $r_2$  which is referred to as  *$\beta$ -recombination*. Important ionospheric characteristics caused by this transition are

- the splitting of the F region in an F1 and an F2 layer (Figure 1.1 a).
- the strong decrease and sometimes even vanishing of the D, E, and F1 regions at nighttime (Figure 1.1 a).
- the transition from predominantly molecular ions in the D and E regions to atomic ions in the F2 region (Figure 1.1 b).

It should be noted that the ionosphere plasma consists mostly of single-charged positive ions and electrons. Therefore, the plasma density  $n_i$  is equivalent to the electron density  $n_e$ . At about 1000 km altitude, atomic hydrogen ions become the predominant plasma species which marks the transition from the ionosphere to the *protonosphere*.

Historically, the existence of the ionosphere was discussed even before the possibility of trans-Atlantic radio communication. It has been known for some time that the needle of a magnetic compass regularly deviates from magnetic north which was attributed to electric currents in the high-altitude atmosphere (Gauss, 1838; Glassmeier and Tsurutani, 2014). This was the first example of the impact of the so-called *space weather* on human technology. Space weather describes the chaotic variability of the near-Earth space environment (including the thermosphere-ionosphere system) and is mostly determined by the

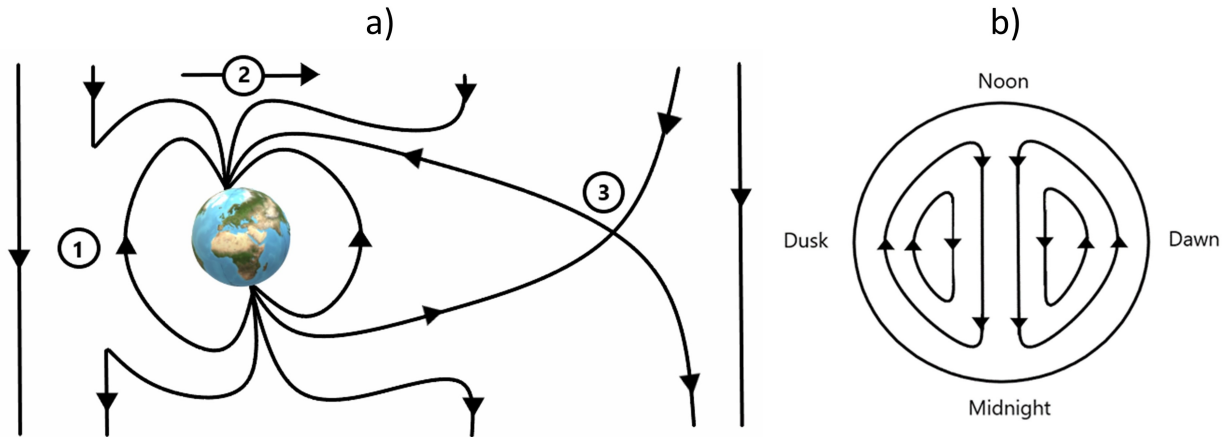


Figure 1.2: a) Side-view (Sun towards the left) of the cycle of the Earth’s magnetic field lines merging with the interplanetary magnetic field (1), being dragged over the poles (2), and reconnecting at the night-side (3). Afterwards, the magnetic field lines relapse at auroral latitudes back to the day side and the cycle begins anew. b) Top-view of the convection pattern of the Earth’s magnetic field lines, and consequently the ionosphere plasma, over the northern polar and auroral region.

activity of the Sun and the solar wind. This includes regular variations (e.g. the 28-day solar rotation or the approximately 11-year solar activity cycle) as well as intermittent eruptions (e.g. solar flares or mass ejections) known as *solar storms*. The variability of the thermosphere-ionosphere system additionally undergoes daily and yearly variations due to the Earth’s rotation and revolution around the Sun. The advanced technological standard of human infrastructure and especially the intrusion of mankind into space increased the risk of space weather threats. Notable space weather impacts are geomagnetically induced currents (GICs) in power grids (Pulkkinen et al., 2017) and disturbances of radio signals required for (satellite) communication and navigation (Ishii et al., 2024). Very recently, the *Starlink event* has received broad media attention. Atmospheric heating following a moderate geomagnetic storm increased the air friction along the orbit of 49 Starlink satellites, which led to the loss of most of them (Dang et al., 2022).

Due to the geometry of the Earth’s magnetic field, the polar regions are of major importance for space weather research. The high-latitude ionosphere is strongly forced by the *polar plasma convection* caused by the interaction of the Earth’s magnetic field with the solar wind and the interplanetary magnetic field (IMF).

As illustrated in Figure 1.2 a), the IMF, which is frozen-in in the solar wind plasma, merges with the Earth’s magnetic field at the day side of the Earth. The merged field lines are dragged over the poles by the solar wind and stretched out at the night side of the Earth. The Earth’s magnetic field lines reconnect eventually and relapse back at auroral latitudes on the dawn- and dusk sides. This results in a two-cell convection pattern of the field lines which is shown in Figure 1.2 b). The ionospheric plasma is coupled to the magnetic field lines which results in the large-scale plasma convection at high latitudes.

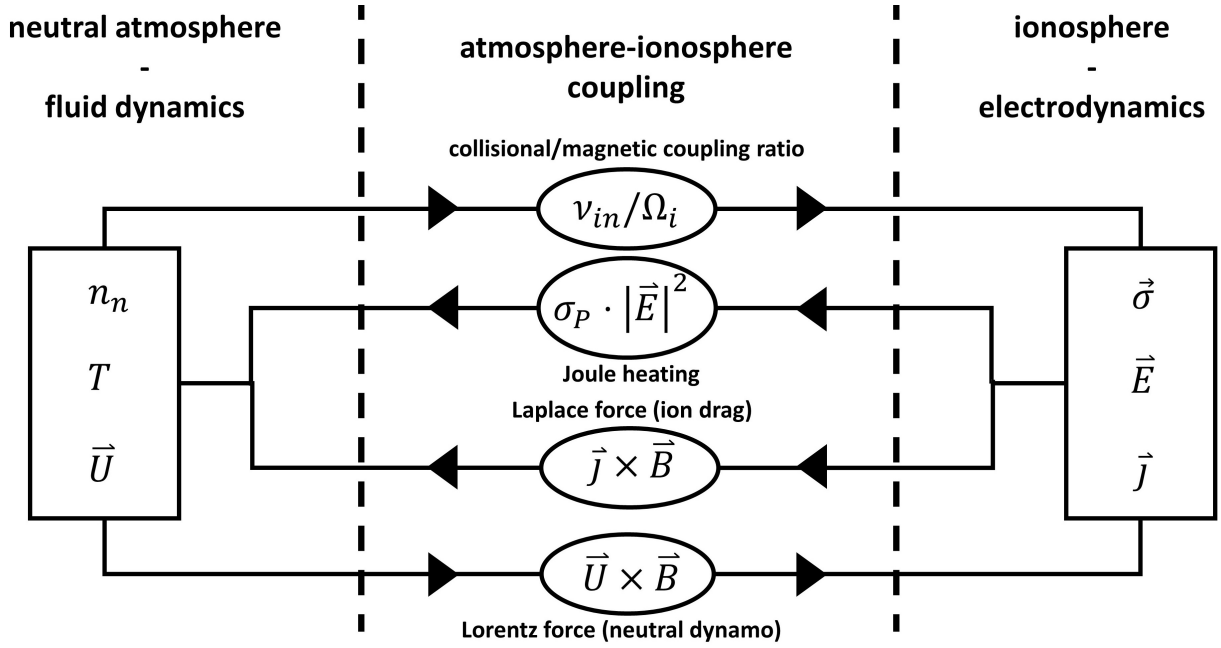


Figure 1.3: Illustration of atmosphere-ionosphere coupling and the involved processes.

The magnetic field convection cycle was first described in Dungey (1961) and is therefore often referred to as *Dungey cycle*.

In addition to the external forcing by the Sun and the solar wind, atmospheric processes and atmosphere-ionosphere coupling contribute significantly to the variability of the ionosphere and space weather. It can be seen in Figure 1.1 b) that the ionospheric plasma density is several orders of magnitude lower than the neutral particle density in the thermosphere. The collisional coupling of the neutral atmosphere and the ionosphere is therefore strongly impacted by the neutral atmosphere dynamics. Figure 1.3 shows schematically how the neutral atmosphere and the ionosphere are coupled.

The neutral atmosphere is described by the state variables neutral particle density  $n_n$ , temperature  $T$ , and neutral wind velocity  $\vec{U}$ . The state variables of the ionosphere are the electric field  $\vec{E}$ , the current density  $\vec{j}$ , and the conductivity tensor  $\vec{\sigma}$  (see Section 1.2.2). These quantities are interlinked by several coupling processes, e.g

1. The collision frequencies of plasma and neutral particles, i.e. electron-neutral and ion-neutral collision frequencies  $\nu_{en}$  and  $\nu_{in}$ , are the key parameters of the collisional atmosphere-ionosphere coupling.  $\nu_{en}$  and  $\nu_{in}$  are directly correlated to the neutral particle density  $n_n$ . The ratios of  $\nu_{en/in}$  to the electron/ion gyro-frequency  $\Omega_{e/i}$  has a major influence on the ionospheric conductivity tensor  $\vec{\sigma}$ . It can be shown that the exponential decrease of  $n_n$  and  $\nu_{en/in}$  with altitude leads to maxima of the *Pedersen* and *Hall* components of the conductivity tensor at about 80 – 120 km altitude.
2. The *Pedersen* component  $\sigma_P$  of the conductivity tensor and the ionospheric electric

field  $\mathbf{E}$  determine the rate of *Joule heating* due to the dissipation of ionospheric currents. Joule heating is one of the major heating mechanisms of the upper atmosphere.

3. Due to the friction between the ionosphere and the neutral atmosphere, ion and neutral particle dynamics impact each other. The force on the ions due to ionospheric currents (referred to as *Laplace force*) is imposed on the neutral atmosphere via ion drag. In turn, the neutral dynamics  $\mathbf{U}$  exert a drag force on the ions which are then impacted by the Lorentz force. This is often referred to as the *neutral dynamo* effect.

The maximum of ionospheric conductivities caused by the collisional coupling of the neutral atmosphere and the ionosphere is essential for space weather research. It can be shown that the ionospheric currents responsible for multiple space weather threats can only flow at a very narrow altitude range, the so-called *ionospheric dynamo region*. The formation of this region and the ionospheric conductivity tensor  $\vec{\sigma}$  will be introduced in Section 1.2. Atmosphere dynamics in this region have a strong impact on the ionospheric variability due to the neutral dynamo effect. Therefore, Section 1.3 will give an overview of atmospheric dynamics in the ionospheric dynamo region.

## 1.2 The ionospheric dynamo/transition region

Ionospheric conductivities and currents maximize in the ionospheric dynamo region at approximately 80 – 120 km altitude. This is caused by a transition of the collisional atmosphere-ionosphere coupling due to the exponentially decreasing neutral atmosphere density. Below the dynamo region, the ionosphere is fully collisional with the neutral atmosphere. At higher altitudes, the atmosphere-ionosphere coupling is of minor importance for the dynamics of the plasma particles which are coupled to the Earth's magnetic field lines. Therefore, the ionospheric dynamo region is also commonly referred to as the *ionospheric transition region*, and both terms will be used synonymously in this thesis.

### 1.2.1 The role of plasma-neutral collisions

The competition between collisional atmosphere-ionosphere coupling and magnetic coupling can be expressed with the ratio of plasma-neutral collision frequencies  $\nu_{in/en}$  to ion/electron gyro-frequencies  $\Omega_{i/e}$ . The strength of the Earth's magnetic field is approximately constant over the altitude range of the ionospheric dynamo region. Therefore, the electron gyro-frequency  $\Omega_e$  can be assumed constant. The ion gyro-frequency  $\Omega_i$  only varies slowly with the mean ion mass. The ratio of collision to gyro-frequencies is consequently determined by the vertical collision frequency profiles. Assuming rigid-sphere collisions, Chapman (1956) derived the ion-neutral collision frequency formula

$$\nu_{in} = 2.6 \cdot 10^{-9} \cdot (n_n + n_i) \cdot A^{-0.5}, \quad (1.1)$$

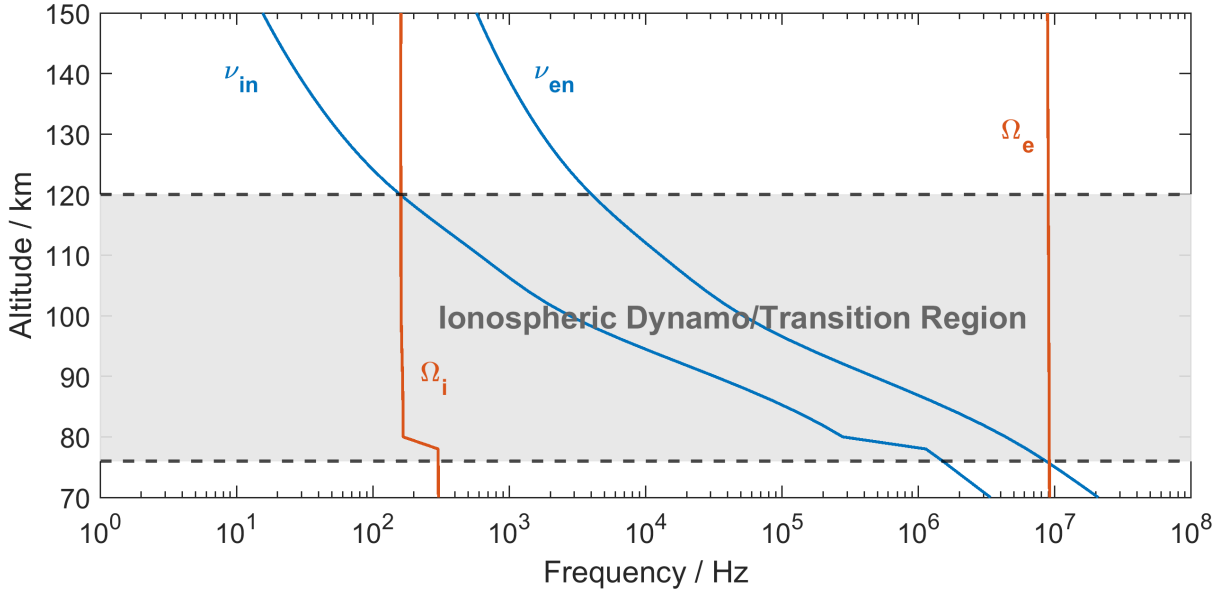


Figure 1.4: Vertical profiles of ion/electron collision frequencies  $\nu_{in}$  and  $\nu_{en}$  and ion/electron gyro-frequencies  $\Omega_i$  and  $\Omega_e$ . The boundaries of the ionospheric transition region are determined by  $\nu_{in} = \Omega_i$  at the top and  $\nu_{en} = \Omega_e$  at the bottom. The frequency profiles have been calculated from empirical climatologies of the neutral atmosphere (NRLMSIS, Picone et al., 2002), the ionosphere (IRI, Bilitza et al., 2022), and the Earth’s magnetic field (IGRF, Alken et al., 2021).

where particle densities are given in units  $[\text{cm}^{-3}]$  and  $A$  is the mean nuclear particle mass in atomic mass units. Also assuming rigid-sphere collisions, Nicolet (1953) showed that the electron-neutral collision frequency is

$$\nu_{en} = 5.4 \cdot 10^{-10} \cdot n_n \cdot T_e^{0.5} \quad (1.2)$$

with the electron temperature  $T_e$ . Equations 1.1 and 1.2 show that the ionospheric collision frequencies are directly correlated to the neutral particle density since  $n_n \gg n_i$ . Example profiles of collision and gyro-frequencies illustrating the dynamo region are shown in Figure 1.4.

It can be seen that both  $\nu_{in}$  and  $\nu_{en}$  decrease nearly exponentially with altitude. The exponential decay of collision frequencies leads to a transition from a *highly collisional plasma*  $\nu_{in/en} \gg \Omega_{i/e}$  to a *magnetized collision-less plasma*  $\nu_{in/en} \ll \Omega_{i/e}$ . During this transition, an altitude range with  $\nu_{in} \gg \Omega_i$  and  $\nu_{en} \ll \Omega_e$  exists which is the ionospheric transition region. It should be noted that the profiles in Figure 1.4 are calculated from empirical models. The exact boundaries of the transition region (here 76 km and 120 km) vary with respect to local time, geographic location, and other parameters. It has even been suggested that heating processes in the dynamo region cause a significant uplift of neutral particles above 120 km altitude and thereby strongly increase  $\nu_{in}$  (Oyama et al., 2012). This would lead to an extension of the ionospheric dynamo region to higher altitudes

which would significantly impact the ionosphere in general.

## 1.2.2 Ionospheric conductivities

In the ionospheric transition region, the ions are collisionally coupled to the neutral atmosphere while the electrons are coupled to the magnetic field as shown in Figure 1.4. This situation allows for charge separation and thereby the flow of electric currents which corresponds to a maximum in conductivity. The derivation of the ionospheric conductivity tensor  $\vec{\sigma}$  is summarized in this Section and can also be found in several textbooks (e.g. Baumjohann and Treumann, 1996; Schunk and Nagy, 2009; Kelley, 2009).

In the transition region, the ionosphere is a *magnetized*, *collisional*, and *partly-ionized* plasma. The first two of these attributes describe the equations of motion for electrons and ions which, assuming steady-state conditions, are

$$\pm e (\mathbf{E} + \mathbf{v}_{i/e} \times \mathbf{B}) = m_{i/e} \nu_{i/e} \mathbf{v}_{i/e}. \quad (1.3)$$

The ion/electron velocity  $\mathbf{v}_{i/e}$  is determined by an equilibrium of the Lorentz force and friction. *Partly-ionized* refers to a non-negligible neutral particle density which, in fact, exceeds the plasma density by far (see Figure 1.1 b). Therefore, neutral particles are the main collision partner for both ions and electrons and the ion/electron collision frequencies  $\nu_{i/e}$  become the ion/electron-neutral collision frequencies  $\nu_{in}$  and  $\nu_{en}$  respectively. The electric current carried by ions and electrons can be expressed as

$$\mathbf{j}_{i/e} = \pm e n_e \mathbf{v}_{i/e} \quad (1.4)$$

where it is already assumed that ion and electron densities are equal, i.e.  $n_i = n_e$ . Equations 1.3 and 1.4 can be rewritten in the general form of *Ohm's law*

$$\mathbf{j}_{i/e} = \vec{\sigma}_{i/e} \cdot \mathbf{E}. \quad (1.5)$$

Since the total current is simply  $\mathbf{j} = \mathbf{j}_e + \mathbf{j}_i$ , the three dimensional conductivity tensor can be expressed as  $\vec{\sigma} = \vec{\sigma}_e + \vec{\sigma}_i$ . Using a reference frame in which the magnetic field points along the z-axis  $\mathbf{B} = B \mathbf{e}_z$ ,  $\vec{\sigma}$  reduces to

$$\vec{\sigma} = \begin{pmatrix} \sigma_P & -\sigma_H & 0 \\ \sigma_H & \sigma_P & 0 \\ 0 & 0 & \sigma_{\parallel} \end{pmatrix}. \quad (1.6)$$

Hereby, the *Pedersen* conductivity  $\sigma_P$ , *Hall* conductivity  $\sigma_H$ , and field-parallel conductivity  $\sigma_{\parallel}$  are introduced. Straightforward calculation shows that the ionospheric conductivities are

$$\begin{aligned}
\sigma_P &= \left( \frac{\nu_{en}}{\nu_{en}^2 + \Omega_e^2} + \frac{m_e}{m_i} \frac{\nu_{in}}{\nu_{in}^2 + \Omega_i^2} \right) \frac{n_e e^2}{m_e}, \\
\sigma_H &= - \left( \frac{\Omega_e}{\nu_{en}^2 + \Omega_e^2} + \frac{m_e}{m_i} \frac{\Omega_i}{\nu_{in}^2 + \Omega_i^2} \right) \frac{n_e e^2}{m_e}, \\
\sigma_{\parallel} &= \left( \frac{1}{\nu_{en}} + \frac{m_e}{m_i} \frac{1}{\nu_{in}} \right) \frac{n_e e^2}{m_e}.
\end{aligned} \tag{1.7}$$

It should be explicitly noted that the electron gyro-frequency  $\Omega_e$  carries the sign of the electron charge, i.e.  $\Omega_e < 0$ . The electric field can be split into a component  $\mathbf{E}_{\perp}$  perpendicular to the magnetic field and a component  $\mathbf{E}_{\parallel}$  parallel to it. In the here applied reference frame, these components become  $\mathbf{E}_{\perp} = E_x \mathbf{e}_x + E_y \mathbf{e}_y$  and  $\mathbf{E}_{\parallel} = E_z \mathbf{e}_z$ . *Ohm's law* in Equation 1.5 for the total current  $\mathbf{j} = \mathbf{j}_e + \mathbf{j}_i$  can then be written as

$$\mathbf{j} = \sigma_{\parallel} \mathbf{E}_{\parallel} + \sigma_P \mathbf{E}_{\perp} - \sigma_H (\mathbf{E}_{\perp} \times \mathbf{B}) / B. \tag{1.8}$$

It can be seen that this results in three types of currents, one *field-aligned* current  $\mathbf{j}_{\parallel}$  parallel to the magnetic field lines and two *field-transverse* currents perpendicular to the magnetic field lines. The two field-transverse currents are different in their orientation towards  $\mathbf{E}_{\perp}$ , i.e. the *Pedersen* current  $\mathbf{j}_P \parallel \mathbf{E}_{\perp}$  and the *Hall* current  $\mathbf{j}_H \perp \mathbf{E}_{\perp}$ . From Equation 1.7, vertical profiles of the three ionospheric conductivities can be calculated. Vertical profiles of the three components of the conductivity tensor are shown in Figure 1.5. Since  $\sigma_{\parallel}$  is several orders of magnitude larger than the field-transverse conductivities, the latter are scaled by a factor of  $10^6$  to be shown in the same diagram.

Figure 1.5 a) shows the vertical profiles of  $\sigma_P$ ,  $\sigma_H$ , and  $\sigma_{\parallel}$  at 70 – 200 km altitude. The field-aligned conductivity increases continuously with altitude since the collision frequencies decrease exponentially and the magnetic field lines are nearly perfect conductors. Currents along the magnetic field lines, induced by the interaction of Earth's magnetic field and the solar wind, can therefore flow freely and become very strong. The *Pedersen* and *Hall* conductivities, on the other hand, show distinct maxima at approximately 110 km ( $\sigma_H$ ) and 120 km ( $\sigma_P$ ) altitude. It can be seen from Equation 1.7 that these distinct maxima are the result of the special conditions for  $\nu_{in}/\Omega_i$  and  $\nu_{en}/\Omega_e$  that define the ionospheric transition region. The flow of electric currents perpendicular to the magnetic field lines is therefore restricted to a very narrow altitude range. At high latitudes, where the magnetic field lines are nearly vertical, this results in a current system as depicted in Figure 1.5 b).

The solar wind particles, mostly electrons and protons, flow through the Earth's magnetic field (downward oriented at northern high latitudes) and thereby induce an electric field  $\mathbf{E}_{SW} = -\mathbf{v}_{SW} \times \mathbf{B}$ . Since magnetic field lines are nearly infinitely good conductors, this difference in electric potential results in upward and downward field-aligned currents.

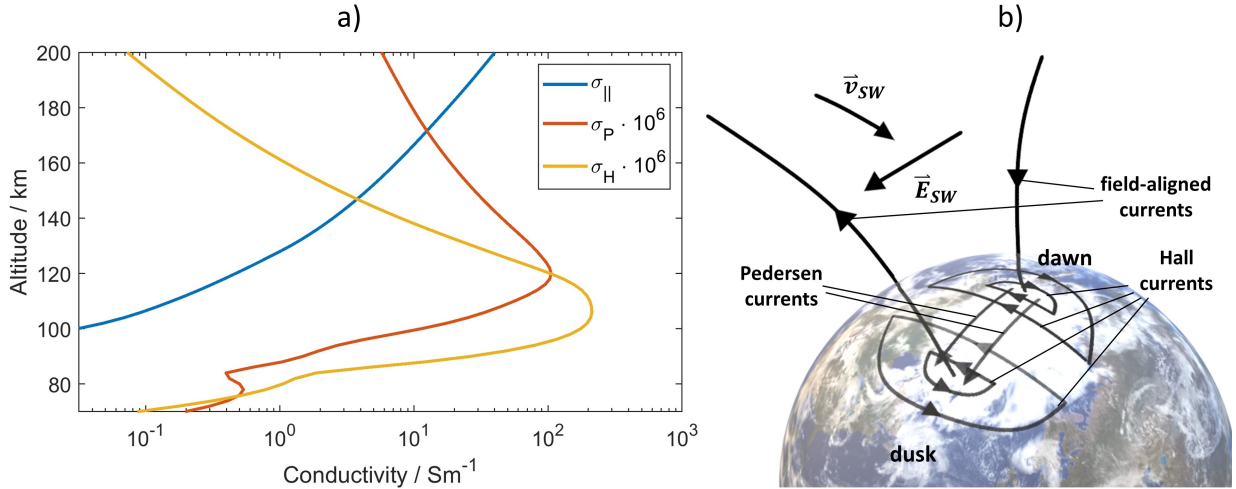


Figure 1.5: a) Vertical profiles of ionospheric conductivities. The *Pedersen* and *Hall* conductivity profiles show distinct maxima within the ionospheric dynamo region. The profiles were calculated from empirical climatologies of the neutral atmosphere (NRLMSIS, Picone et al., 2002), the ionosphere (IRI, Bilitza et al., 2022), and the Earth’s magnetic field (IGRF, Alken et al., 2021). b) Illustration of the ionospheric current system at high latitudes. The interaction of the solar wind with the Earth’s magnetic field induces currents along the magnetic field lines. The strong field-aligned currents are closed by the field-perpendicular *Pedersen* and *Hall* currents.

Thereby, the induced electric field propagates to lower altitudes nearly undisturbed. In the ionospheric dynamo region where the field-transverse conductivities maximize, this results in the flow of *Pedersen* and *Hall* currents as shown in Figure 1.5 b). Since it is parallel to the induced electric field, the *Pedersen* current closes the ionospheric current system. This results in the so-called *Joule heating* of the ionosphere plasma with the local heating rate  $q_J = \mathbf{j}_P \cdot \mathbf{E} = \sigma_P \mathbf{E}^2$ . Due to their rotational geometry, the *Hall* current loops cause disturbances to the Earth’s magnetic field which can induce secondary currents in power grids, the previously mentioned GICs. These disturbances can be measured with magnetometers and are often used to characterize the space weather activity, e.g. with the *Kp* (*planetare Kennziffer*) index (Bartels et al., 1939; Matzka et al., 2021). It can be seen that several important space weather impacts are caused by the electric currents in the ionospheric dynamo region. Consequently, a reliable space weather forecast requires a thorough understanding of the collisional atmosphere-ionosphere coupling and the underlying vertical collision frequency profiles.

The variability of the ionospheric current system at high latitudes is dominated by the geomagnetic forcing from the solar wind. However, processes from the lower atmosphere can impact the ionosphere via the neutral dynamo  $\mathbf{U} \times \mathbf{B}$  and contribute to the ionospheric variability. It is estimated that approximately 20% – 30% of the ionospheric variability is forced by atmospheric processes on various time scales (Thayer, 2000; Forbes et al., 2000; Rishbeth, 2006; Baloukidis et al., 2023).

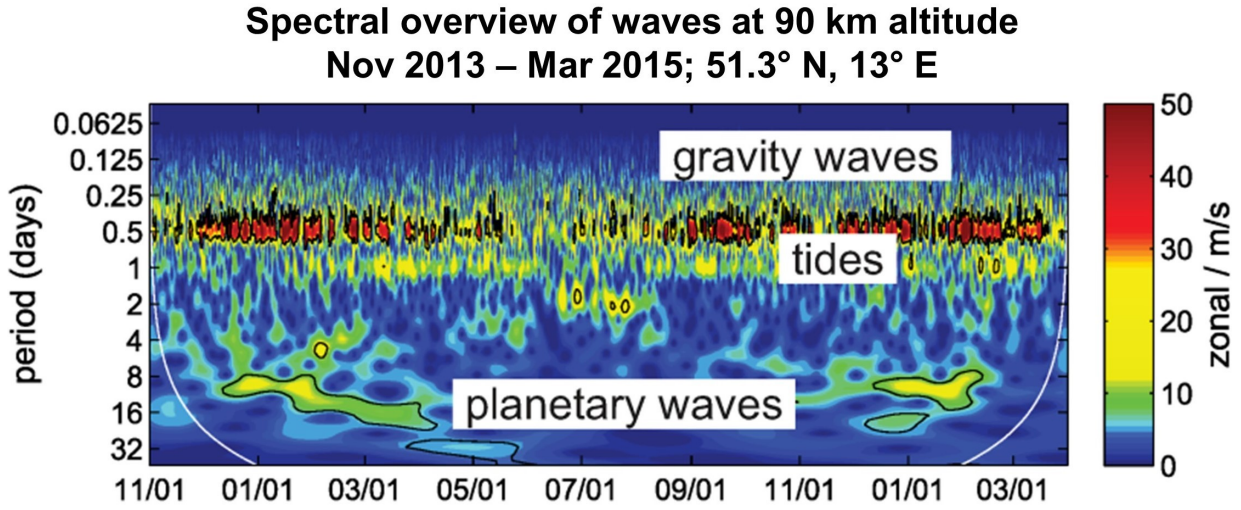


Figure 1.6: Meteor radar measurements of neutral atmosphere dynamics in the zonal wind at 90 km altitude. Shown are the spectral amplitudes of oscillations between 90 minutes and 32 days for a period of 17 months. Figure credit: Stober (2019).

### 1.3 Atmospheric processes in the transition region

As shown in Figure 1.1, the ionosphere is embedded in the background neutral atmosphere. The ionospheric transition region overlaps with the mesosphere and lower-thermosphere (MLT) region. Figure 1.3 introduced the neutral atmosphere's impact on the ionosphere due to the neutral dynamo effect. The neutral dynamo electric field  $\mathbf{E}_{dyn} = \mathbf{U} \times \mathbf{B}$  significantly impacts the ionospheric current system (Vickrey et al., 1982; Baloukidis et al., 2023). Atmospheric dynamics imposed on the ionosphere plasma also impact the radio communication with satellites (Ishii et al., 2024).

Neutral atmosphere dynamics in the MLT region can be forced *in situ* by absorption of solar EUV radiation or by ionospheric processes, e.g. Joule heating. However, a large part of the atmospheric dynamics in the MLT region is caused by processes forced in lower atmospheric regions which propagate upwards to ionospheric altitudes. Figure 1.6 shows an overview of the wave dynamics measured in the zonal neutral wind at 90 km altitude by the Collm (51.3°N, 13°E) meteor radar (see Section 2.3).

The strongest amplitudes are found for atmospheric tides with a period of 12 h, also called semidiurnal tides, which are found almost continuously throughout the year. Diurnal tides with a 24 h period are also present at most times though with a considerably lower amplitude. Atmospheric gravity waves (AGWs) are generally present at all times as well, though their activity can vary strongly. AGW oscillation periods range from approximately 10 min to several hours. Longer-scale oscillations, e.g. planetary waves, are only present at certain times of the year. This thesis will focus on the impact of atmospheric tides and gravity waves on the ionosphere and space weather. Therefore, Section 1.3.1 will introduce atmospheric tides in general and give an overview of which tidal modes are expected to

impact the ionospheric dynamo region. Atmospheric gravity waves and their ionospheric imprint, traveling ionospheric disturbances (TIDs), will be introduced in Section 1.3.2.

### 1.3.1 Tidal oscillations

Atmospheric tides, other than the more commonly known ocean tides, are predominantly thermally forced by solar irradiation. Tidal oscillations of the atmosphere are generated mainly in the stratosphere due to UV absorption by ozone, but also due to IR absorption of water vapor in the troposphere or EUV absorption in the MLT region. Since solar irradiation has a diurnal, i.e. 24 h, variation, atmospheric tides are mainly forced with a 24 h period. However, since the solar irradiation does not follow a continuous 24 h oscillation but goes to zero on the night side, higher harmonic components, i.e. semidiurnal, terdiurnal, etc., are forced with lower amplitudes as well (Lindzen, 1979; Andrews et al., 1987). In the reference system of a local observer, tidal modes forced by solar irradiation migrate westward along with the Sun and are therefore called *migrating tides*. Their zonal wavenumber is equivalent to their temporal wavenumber, the two most common migrating tidal modes are therefore the DW1 (diurnal, westward-propagating tide with zonal wavenumber 1) and SW2 (semidiurnal, westward-propagating tide with zonal wavenumber 2). *Non-migrating tides* are forced, e.g. by local heat release in the troposphere due to special weather phenomena, and can have an impact on both the neutral atmosphere and the ionosphere (Immel et al., 2006; Oberheide et al., 2011). Especially the DE3 component has been found to have a significant impact on the equatorial thermosphere-ionosphere dynamics (Häusler and Lühr, 2009; Lühr and Manoj, 2013). However, the migrating components DW1 and SW2 are usually the strongest tidal modes at ionospheric altitudes (Lindzen, 1979; Andrews et al., 1987; Lühr and Manoj, 2013).

It has been noted in the 19th century that at middle latitudes, pressure fluctuations on the Earth's surface follow a semidiurnal, rather than a diurnal, pattern. This can be explained by the vertical propagation of tidal modes. While the SW2 tide can propagate in vertical directions at all latitudes, the DW1 mode can only do so at low latitudes, approximately from 30° S to 30° N (Andrews et al., 1987). Therefore, semidiurnal oscillations are dominant both on the ground as well as in the MLT region at middle and high latitudes. This can be seen in the zonal neutral wind and the temperature of the neutral atmosphere at 100 km altitude as given by the *Thermosphere Ionosphere Electrodynamics-General Circulation Model (TIE-GCM)* shown in Figure 1.7. TIE-GCM and other atmosphere-ionosphere models are introduced in Section 2.4.

The diurnal and semidiurnal variations of neutral wind and temperature can be seen in Figure 1.7. Around the equator, we find one maximum and one minimum in each plot, indicating a strong migrating diurnal tide. At higher latitudes, two maxima and minima can be identified in both the zonal wind and the neutral temperature, indicating that diurnal tidal modes are vertically trapped and therefore semidiurnal tides dominate at 100 km altitude.

Additionally to the vertically propagating tidal modes, tidal oscillations can also be forced in the MLT region directly. The aforementioned absorption of EUV radiation forces pre-

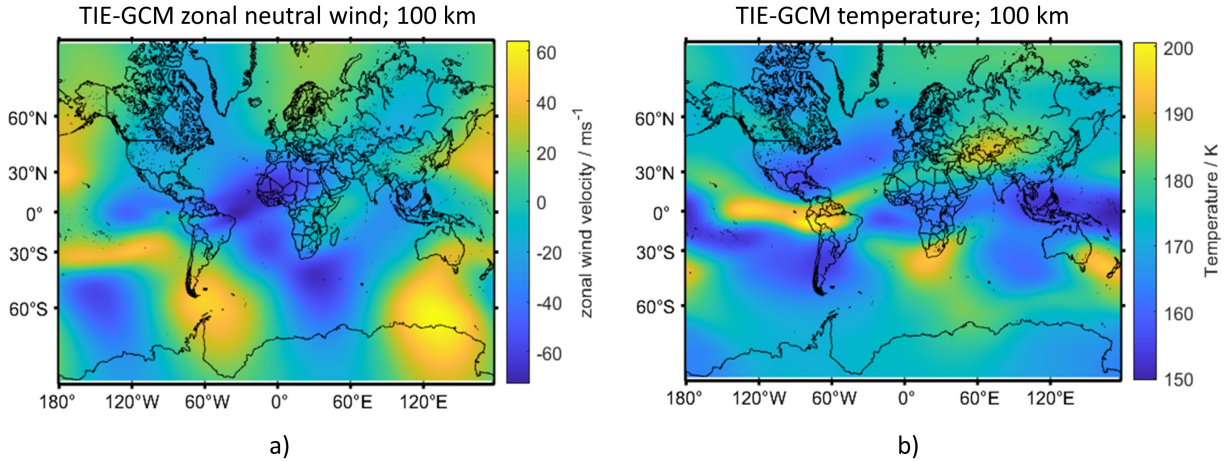


Figure 1.7: a) Zonal neutral wind and b) neutral temperature at 100 km altitude given by the TIE-GCM (Richmond et al., 1992), a physics-based thermosphere-ionosphere model, show tidal oscillations in the MLT region.

dominantly diurnal tidal oscillations at ionospheric altitudes (Straus et al., 1975). Another mechanism that can force tidal oscillations is the high-latitude plasma convection introduced in Section 1.1. The plasma convection pattern shown in Figure 1.2 b) is transferred to the neutral particles via friction. The convection pattern is Sun-fixed and therefore observed as a DW1 tide by a local observer. At high latitudes, it is assumed that upward-propagating SW2 tides are dominant up to about 110 – 120 km altitude and *in situ* forced diurnal tides dominate above (Lindzen, 1979; Andrews et al., 1987; Nozawa et al., 2010).

### 1.3.2 Atmospheric gravity waves and traveling ionospheric disturbances

The Earth's atmosphere is a stratified gas, i.e. its density continuously decreases with altitude. If an air parcel is lifted to higher altitudes, it is surrounded by less dense air and therefore pulled down by buoyancy-reduced gravity. This results in an internal density oscillation of the atmosphere, a so-called *Brunt-Väisälä oscillation*. Under the right conditions, such a buoyancy oscillation can propagate in both vertical and horizontal directions which is then referred to as *atmospheric gravity wave (AGW)* (Andrews, 2000). Sources of gravity waves in the lower atmosphere are weather fronts or mountain winds. So-called *orographic* gravity waves are the result of dense air being pushed up over a mountain-front and into the less dense atmosphere on the Lee side. As AGWs propagate upward into less dense gas, their amplitude increases, and the waves become unstable and break. The breaking of gravity waves transfers the momentum of the wave to the background atmosphere and can, in turn, induce so-called *secondary gravity waves* (Becker and Vadas, 2018; Vadas and Becker, 2018; Vadas et al., 2018). Therefore, atmospheric gravity waves transport momentum from the lower atmosphere into the MLT region and are of high

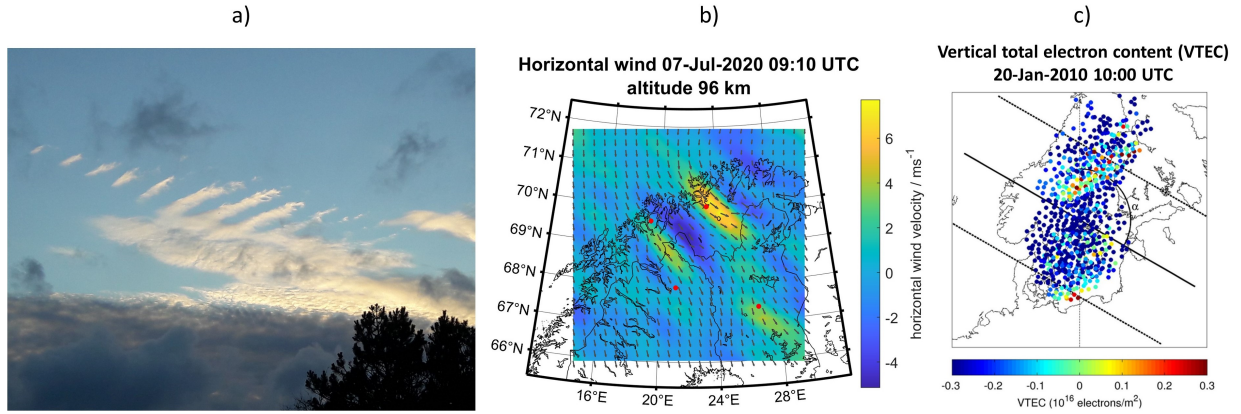


Figure 1.8: Gravity waves visible in a) the lower atmosphere as cloud ripples, b) in filtered meteor radar neutral wind measurements in the MLT region, and c) in the vertical total electron content (VTEC) of the ionosphere. Figure credit: a) Helen Schneider, b) Günzkofer et al. (2023a), and c) van de Kamp et al. (2014).

importance for the dynamics of the middle and upper atmosphere (Andrews et al., 1987; Fritts and Alexander, 2003).

In the ionosphere, AGWs cause an imprint, the so-called *traveling ionospheric disturbances (TIDs)*, which can be observed in the electron density and other ionosphere parameters (Hocke and Schlegel, 1996; Vlasov et al., 2011). However, TIDs can also be caused by electrodynamic or heating processes directly in the thermosphere-ionosphere (Brekke, 1979; Hocke and Schlegel, 1996; Tsugawa et al., 2007). Therefore, it is important to distinguish between *in situ* forced TIDs and those resulting from upward-propagating gravity waves. Figure 1.8 shows atmospheric gravity waves at different altitudes.

In the troposphere, gravity waves can be observed as cloud ripples (Figure 1.8 a) due to the vertical oscillation of air parcels and the consequent condensation and evaporation of water damp. It can be seen from neutral wind measurements with meteor radars (Section 2.3) that AGWs notably impact the winds in the MLT region (Figure 1.8 b). In the ionosphere, AGW-TIDs cause significant variations of the electron density. This can be seen in horizontal maps of the *vertical total electron content (VTEC)*, i.e. the height-integrated electron density, of the ionosphere (Figure 1.8 c). As mentioned before, this ionospheric variability due to AGW-TIDs is relevant for radio and satellite communication and an important aspect of space weather (Ishii et al., 2024).

## 1.4 The scientific objective of this thesis and the state of the art

It is apparent that space weather is the result of a highly complicated combination of external forcing and atmosphere-ionosphere coupling processes. The eventual goal of space and

heliospheric physics is the development of currently existing atmosphere-ionosphere models into reliable space weather forecasts. One of the main challenges is that many processes have to be empirically parameterized due to computational limits, e.g. the polar plasma convection and atmospheric gravity waves. However, an advanced empirical understanding of many processes is not possible due to the limited measurement capabilities, especially at the altitudes of the ionospheric transition region. Therefore, the main scientific objective of this thesis is to address the following research question:

**What is the impact of atmospheric waves and collisional atmosphere-ionosphere coupling on the ionospheric variability and the space weather?**

In Section 1.1, the high importance of the high-latitude ionospheric dynamo region for space weather has been demonstrated. Therefore, the investigations in this thesis will be specifically focused on the polar and auroral latitudes. Upward-propagating atmospheric tides and atmospheric gravity waves are known to significantly impact the upper atmosphere (see Section 1.3). However, both types of waves can also be forced *in situ* in the thermosphere due to ionospheric processes. Assessing the respective impact of propagating and *in situ* forced waves on the ionospheric variability is necessary to appropriately include them in future space weather forecasts.

In Section 1.2, it has been shown how the collisional atmosphere-ionosphere coupling and the transition from a collision-dominated to a collision-free ionosphere leads to the formation of the ionospheric dynamo region. As discussed in Section 1.1, the currents in the high-latitude ionospheric dynamo region are a significant element of the space weather. Within this thesis, the ionospheric currents and the underlying vertical collision frequency profiles will be investigated. The aim is to improve the quantitative understanding of collisional atmosphere-ionosphere coupling which will allow us to improve the empirical representation of certain processes in space weather predictions.

It can be seen, that a complete investigation of the atmospheric impact on space weather exceeds the scope of a single thesis. However, the posed research question can be answered by combining detailed investigations of multiple atmosphere-ionosphere coupling processes. To achieve the objective of the thesis, the following four research sub-questions will be addressed. An overview of the state of the art regarding each research sub-question is given here.

**Q1: What are the predominant tidal oscillation modes in the high-latitude ionospheric dynamo region and their forcing mechanisms?**

As introduced in Section 1.3.1, upward-propagating atmospheric tides are known to significantly impact the ionosphere (Immel et al., 2006; Oberheide et al., 2011). At high latitudes, however, the polar plasma convection forces tidal oscillations in the neutral atmosphere via ion drag. To properly assess the importance of atmospheric tides for the tidal variability of the ionosphere, we first need to measure and understand the respective impact of the different forcing mechanisms.

The standard textbook assumption for tidal oscillations at high latitudes is that upward-propagating semidiurnal tides are the dominant forcing mechanism up to  $\sim 110 - 120$  km altitude. At higher altitudes, diurnal tidal oscillations forced *in situ* by the plasma convection or EUV absorption are expected to be the strongest forcing mechanisms (Lindzen, 1979; Andrews et al., 1987; Nozawa et al., 2010). The main problem for measurements of high-latitude tidal oscillations is the *thermospheric gap* at about 120 – 400 km (Oberheide et al., 2011). At these altitudes, the measurement capabilities of neutral atmosphere dynamics are highly limited, since it is not possible to perform *in situ* satellite-based measurements. Optical instruments like lidars and Fabry-Pérot interferometers (FPIs) are mostly limited to nighttime measurements and are often restricted by weather conditions. Additionally, both lidars and FPIs cover the altitudes of the ionospheric transition region only sporadically. Campaign-based measurements with Incoherent Scatter Radars (ISRs) (see Section 2.1) have been applied to investigate tidal oscillations in the high-latitude ionosphere up to 120 km (Nozawa et al., 2010). More recently developed statistical methods allow to increase the altitude limit of neutral wind measurements by incoherent scatter radars (Nygrén et al., 2011). With these improved ISR measurement capabilities, the interaction of upward-propagating and *in situ* generated tidal oscillations in the ionospheric dynamo region will be investigated. Additionally, for the first time, a combined ISR and meteor radar measurement dataset will be used to investigate the vertical propagation of atmospheric tides with an adaptive spectral filter. Physics-based model runs allow to determine the respective impact of different forcing mechanisms by varying the parameterization of the plasma convection, EUV absorption, and upward-propagating tides.

**Q2: How are the wave properties of atmospheric gravity waves, and the medium-scale traveling ionospheric disturbances induced by them, impacted by the background neutral winds in the MLT region?**

Traveling ionospheric disturbances (TIDs) are a major contributor to ionospheric variability and their prediction is an important aspect of the development of space weather forecasts (Borries et al., 2023). However, TIDs occur on a wide range of spatial and temporal scales and so far, the main focus of TID predictions has been on large-scale disturbances which are mainly forced by ionospheric processes (Hocke and Schlegel, 1996). Medium-scale TIDs, however, can be forced by upward-propagating atmospheric gravity waves which are generally not resolved in atmosphere-ionosphere models. To include medium-scale TIDs in space weather forecasts, we need to understand how atmospheric gravity waves impose these disturbances on the ionosphere and how their characteristics are impacted by atmospheric dynamics.

To understand and model the characteristics of gravity wave-forced ionospheric disturbances, it is first necessary to measure them accurately in three dimensions. Since there is no single instrument that covers a large enough range in both vertical and horizontal directions with a sufficient resolution to resolve gravity waves, a combination of multiple instruments is required. Incoherent scatter radars have been successfully used to measure the temporal scales and vertical structure of medium-scale TIDs (Nicolls and Heinselman,

2007; Nicolls et al., 2010, 2013; van de Kamp et al., 2014). Measuring the horizontal structure has been attempted, amongst others, with vertical total electron content (VTEC) measurements from navigation satellite signals (van de Kamp et al., 2014). However, disturbances in the height-integrated VTEC cannot be conclusively linked to disturbances in vertically resolved ISR electron density measurements. Additionally, the disturbances observed in VTEC measurements mainly occur at the altitude of maximum electron density, i.e. at about 200 – 300 km. Upward-propagating gravity waves do not impact these altitudes as much as the ionospheric dynamo region. Horizontally distributed meteor radar clusters (see Section 2.3) will be applied to identify atmospheric gravity waves at 80 – 100 km altitude. By analyzing the wave characteristics, it will be shown that these gravity waves are the source of medium-scale traveling ionospheric disturbances observed in ISR measurements at about 110–170 km altitude. The combination of these instruments allows us to obtain three-dimensional measurements of the waves. It will be investigated whether the characteristics of the ionospheric disturbances can be described with the dispersion of atmospheric gravity waves (Vadas and Fritts, 2005). This might be important for the parameterization of AGW-TIDs in future space weather forecasts and would also allow to infer information about the background thermosphere dynamics.

**Q3: Does the required scaling of Joule heating rates in thermosphere-ionosphere models vary with geomagnetic conditions and the parameterization of the polar convection field?**

The interaction of the Earth’s magnetic field and the solar wind induces strong electric fields in the high-latitude ionosphere. Due to the maxima of *Pedersen* and *Hall* conductivity in the ionospheric dynamo region, strong electric currents can flow perpendicular to the magnetic field lines at these altitudes. Therefore, the Joule heating due to *Pedersen* currents in the high-latitude ionospheric dynamo region is a major heat source for the thermosphere-ionosphere system. For computational reasons, the temporal and spatial resolution of thermosphere-ionosphere models is limited. Processes on temporal and spatial scales below the model resolution can contribute significantly to the Joule heating (Codrescu et al., 1995; Brekke and Kamide, 1996). An empirical scaling of Joule heating rates in physics-based models of the thermosphere-ionosphere system is therefore required and might also be necessary for future space weather forecasts.

In this thesis, the empirical scaling of Joule heating rates in thermosphere-ionosphere models is evaluated on the example of the TIE-GCM (see Section 2.4). This model applies a constant scaling factor of 1.5 on the Joule heating rates (Codrescu et al., 1995). However, it has been shown previously that this factor is only valid on average and the actually required scaling might vary with local time, geographic location, and geomagnetic activity (Emery et al., 1999; Baloukidis et al., 2023). Additionally, there are multiple approaches to parameterize the high-latitude electric fields in thermosphere-ionosphere models which significantly affects the model Joule heating rates. The empirical scaling of Joule heating rates should take the electric field parameterization into account. One of the only instruments that allow for local Joule heating rate measurements in the ionospheric dynamo

region are incoherent scatter radars (Vickrey et al., 1982; Thayer, 2000; Kavanagh et al., 2022; Baloukidis et al., 2023). The model Joule heating rates will be compared to Joule heating rates calculated from ISR electric field measurements. The required scaling factor will be investigated with respect to geomagnetic and solar wind conditions as well as local time and the electric field parameterization.

**Q4: Do ion-neutral collision frequencies in the dynamo region deviate significantly from climatology profiles and how can they be measured without any previous assumptions?**

The role of ion-neutral collisions for the coupling of neutral atmosphere and ionosphere has been introduced in Section 1.2.1. Knowledge of the vertical profile of the ion-neutral collision frequency is essential when studying atmosphere-ionosphere coupling, e.g.

- For the calculation of E region neutral winds from ISR measurements, the assumption of climatology collision profiles is considered a major source of uncertainties (Williams and Viridi, 1989; Nozawa et al., 2010).
- The ion-neutral collision frequency profile impacts the altitude at which the *Pedersen* conductivity and the Joule heating rate maximize (Baloukidis et al., 2023).
- The ambipolar diffusion of meteor trails is affected by the ion-neutral collision frequency (Stober et al., 2023) which is therefore important for the measurement capabilities of meteor radars (see Section 2.3).

Reliable measurements of ion-neutral collision frequencies are therefore essential for investigating and understanding the coupling of neutral atmosphere and ionosphere.

The most common approach to determine the ion-neutral collision frequency is to assume climatology profiles that can be calculated from empirical neutral atmosphere models (see Section 2.4). It has been shown previously that the actual collision frequency profile can deviate notably from the climatology average (Nygrén, 1996; Oyama et al., 2012). *In situ* measurements with satellites (Palmroth et al., 2021) and sounding rockets (Rapp et al., 2001) are strongly limited in altitude and measurement time. Classical remote sensing measurement methods of the collision frequency are either limited concerning the geomagnetic conditions or require additional assumptions about the state of the ionosphere (Nygrén, 1996). Direct ion-neutral collision frequency measurements without further assumptions are possible with simultaneous observations of two incoherent scatter radars at different radar frequencies (Grassmann, 1993; Nicolls et al., 2014). The analysis of such dual-frequency ISR measurements with a method based on standard incoherent scatter analysis software is presented, presumably for the first time, in this thesis. Vertical profiles of the ion-neutral collision frequency are inferred from multiple measurement campaigns and compared to climatology profiles. Thereby, the uncertainties originating from the application of climatology collision profiles can be estimated.

# Chapter 2

## Methods - measurements and modeling

There is a large number of different measurement methods to study the lower ionosphere, e.g. *in situ* measurements with sounding rockets and low Earth orbit satellites, active and passive optical observations as well as various types of radar techniques (Palmroth et al., 2021). However, all of these methods are limited in either altitude, measurement time, or horizontal coverage. *Incoherent Scatter Radars (ISRs)* are one of the few instruments that cover the entire altitude range of the ionospheric dynamo region with a high vertical resolution. Though ISRs are extremely energy-consuming and expensive instruments, continuous measurements up to several weeks have been performed with a high time-resolution  $\sim 1$  min, which allows to study processes on a wide range of temporal scales. Another main advantage of ISRs is that they allow us to measure or infer a large number of ionosphere and neutral atmosphere parameters. However, ISRs have no or only very limited horizontal coverage and are therefore often used in combination with other measurement instruments.

Section 2.1 describes the concept of incoherent scatter radars and their capabilities. In the European sector of the auroral zone, the EISCAT Scientific Association operates several ISRs. The existing EISCAT radar systems are introduced in Section 2.2 as well as the new EISCAT\_3D system currently under construction. Section 2.3 describes the principle of *Meteor Radars* which are well-established measurement instruments for atmospheric dynamics at high altitudes. Meteor radar measurements will be leveraged for the extension and validation of ISR measurements in this thesis.

Due to the limitations of ionospheric measurements, atmosphere-ionosphere models are highly important. Both empirical and physics-based models are commonly applied to provide information about the ionosphere which are not available from measurements. In turn, the improvement of existing models and the eventual development of forecasts for the atmosphere-ionosphere system requires the validation of model outputs by comparison to measurements. Section 2.4 introduces several empirical and physics-based models of the atmosphere-ionosphere system that are applied in this thesis.

## 2.1 Incoherent Scatter Radars

As the name suggests, incoherent scatter radars do not require coherent scattering of the radio signal from a compact target. ISRs measure the fraction of the radio signal that is incoherently backscattered by the free electrons in the ionosphere. The elastic scattering of a radio signal by a free-electron, also called *Thomson scattering*, has an extremely low scatter cross-section  $\sigma_t \sim 10^{-29} \text{ m}^{-2}$ . Therefore, high transmission powers and large aperture antennas are required to obtain a sufficiently strong backscattered signal which is the reason for the high power consumption of ISRs.

Multiple levels of incoherent scatter radar measurements can be distinguished. The raw antenna voltages induced by the received radio signal are referred to as *level 0* measurements. Commonly, ISR facilities provide the data as auto-correlation function (ACF) of the signal which is referred to as *level 1* data. The Fourier transform of the ACF gives the power spectral density of the received radio signal. Knowledge about the underlying physics of the scatter process allows to infer multiple *level 2* plasma parameters from the power spectral density.

### 2.1.1 Level 1 and 2 - the two-peak incoherent scatter spectrum and ISR plasma parameters

The strength of the backscattered signal is directly correlated to the total scatter cross-section which allows us to infer the electron density  $n_e$  at the scatter altitude. However, the ionospheric electrons are not completely free but rather organized in micro-structures due to plasma waves and instabilities. The most important one is the *ion acoustic wave* which has the dispersion relation (Akbari et al., 2017)

$$\omega = \pm k \sqrt{\frac{k_B}{m_i} (T_e + \gamma_i T_i)}. \quad (2.1)$$

The dispersion relation relates the wave frequency  $\omega$  to the wave number  $k$  and depends on the Boltzmann constant  $k_B$ , the mean ion mass  $m_i$ , the ion and electron temperatures  $T_i$  and  $T_e$ , and the adiabatic coefficient of the ions  $\gamma_i$ . For  $k = 2\pi/\lambda_r$ , where  $\lambda_r$  is the radar wavelength, there is constructive interference of the scattered radio signal and the power spectrum of the measured signal shows two clear maxima at  $\pm\omega$ . The two maxima are not infinitely sharp peaks but broadened and shifted by thermal effects, Landau-damping, and Doppler shifting which results in the typical two-peak incoherent scatter spectrum shown in Figure 2.1.

The altitude-dependence of the spectral amplitude of the scattered radio signal can be seen in Figure 2.1 a). The spectral amplitude of the two-peak spectrum maximizes at approximately 200 – 300 km altitude. These are the altitudes of the F region (see Figure 1.1 a) with the highest electron densities of the ionosphere and, therefore, the radio signal shows a pronounced backscattering in this region. Below about 200 km altitude, the two peaks of the spectrum are shifted to lower absolute frequencies, and at about 100 km

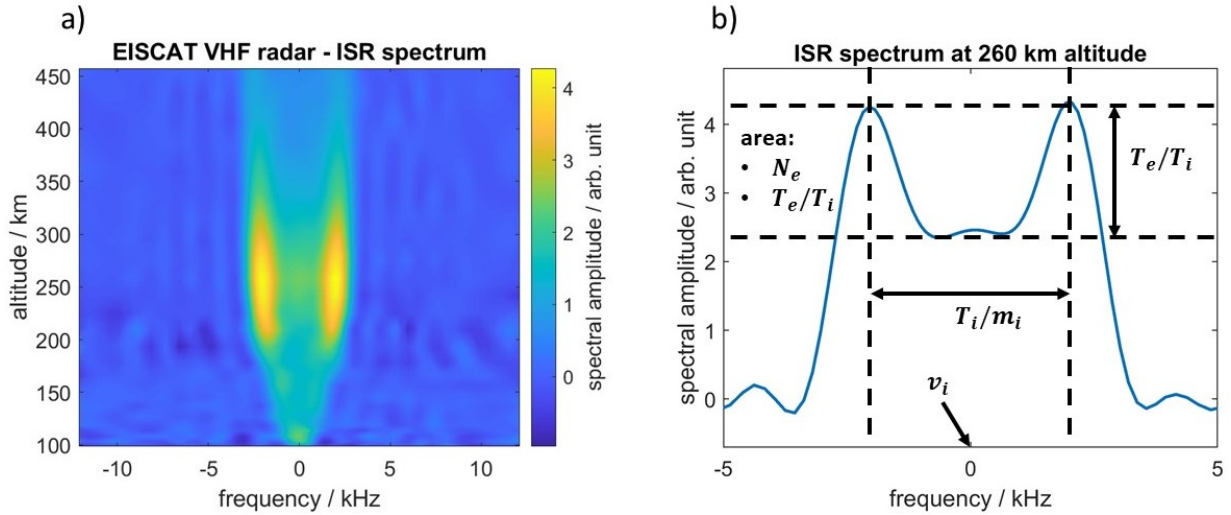


Figure 2.1: The typical two-peak incoherent scatter spectrum resulting from constructive interference of the scattered signal in the presence of the ion acoustic wave. a) Spectral amplitude of the measured signal 100 – 450 km altitude. b) Spectral amplitude at 260 km altitude and how the different plasma parameters affect the shape of the spectrum.

altitude, the two peaks can no longer be distinguished. Figure 2.1 a) illustrates that the strength of the incoherently scattered radio signal depends strongly on the electron density. For large ionization levels, the total altitude range of ISR measurements can extend even down to about 70 – 80 km altitude.

Figure 2.1 b) shows the two-peak spectral amplitude at 260 km altitude and indicates how the different quantities in Equation 2.1 affect the shape of the spectrum. As mentioned before, the total, i.e. frequency-integrated, signal power is determined by the electron density  $n_e$ . Thermal broadening of the two peaks leads to a local minimum of the spectrum in between the peaks. The difference in spectral amplitude between the peaks and the local minimum in between is impacted by the ratio of electron to ion temperature  $T_e/T_i$  through the process of *Landau damping* (Landau, 1946). This process also changes the integrated signal power, which must be accounted for when calculating the electron density. The ratio of ion temperature to mean ion mass  $T_i/m_i$  determines the distance of the two peaks in the frequency space. A general ion drift  $v_i$  along the line-of-sight of the radar beam causes a Doppler shift of the entire two-peak spectrum along the frequency axis.

One parameter from Equation 2.1 that has not been considered is the ion adiabatic coefficient  $\gamma_i$ . The term  $\gamma_i T_i$  is ambiguous and therefore either  $\gamma_i$  or  $T_i$  has to be assumed *a priori*. The adiabatic coefficient is the ratio of the gas heat capacities for constant pressure and constant volume. Essentially, it describes how the plasma particles store thermal energy and depends on the degrees of freedom of the plasma particles. Assuming only atomic ions, i.e. no rotational and vibrational degrees of freedom, a magnetized plasma that allows ion motion only along one dimension has an adiabatic coefficient  $\gamma_i = 3$ . At E and D region altitudes, neither the assumption of a fully magnetized plasma nor of only

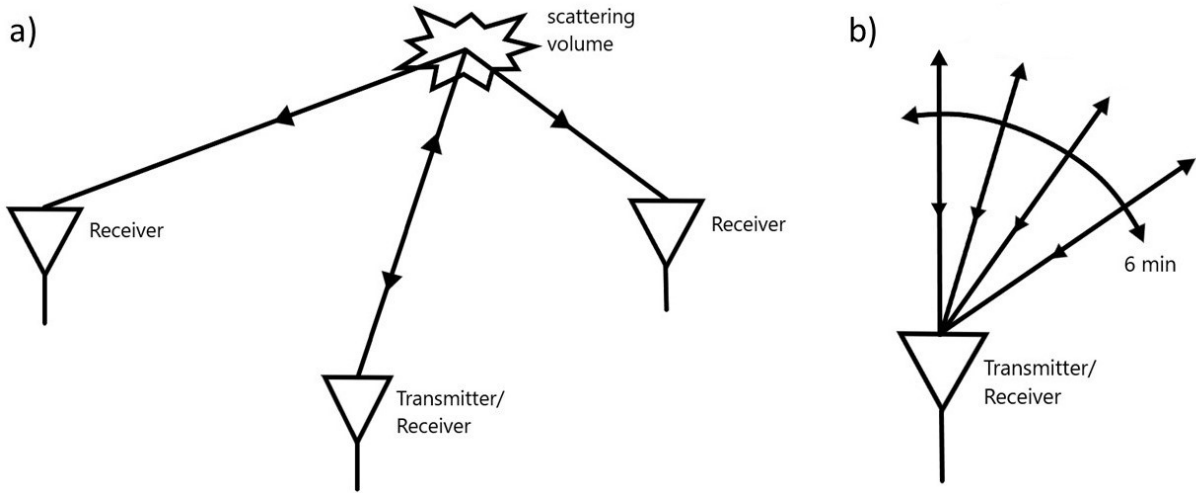


Figure 2.2: Schematic drawings of the geometry of a) *tristatic* and b) *monostatic* ISR experiments that allow to infer 3D ion velocities.

atomic ions holds. However, while the ion temperature is a highly variable parameter, the adiabatic coefficient can be well approximated from average plasma composition and collision profiles. Therefore,  $\gamma_i$  is usually assumed from empirical climatologies, and  $T_i$  is inferred from the incoherent scatter spectrum for most ISR experiments.

The parameters that can be directly inferred from the incoherent scatter spectrum are therefore the electron density  $n_e$ , the electron and ion temperatures  $T_e$  and  $T_i$ , the mean ion mass  $m_i$ , and the line-of-sight ion velocity  $v_i$ . To obtain these *level 2* measurements from the *level 1* ACFs, standard incoherent scatter analysis software can be applied, e.g. the Grand Unified Incoherent Scatter Design and Analysis Package (GUISDAP) (Lehtinen and Huuskonen, 1996).

### 2.1.2 Level 3 - 3D dynamics and neutral atmosphere parameters

By applying special radar set-ups or certain assumptions on the state of the ionosphere-thermosphere system, additional *level 3* plasma and also neutral atmosphere parameters can be inferred.

#### 3D ion velocity and electric field vector

Since the Doppler shift of the incoherent scatter spectrum allows us to infer the line-of-sight ion velocity, measurement set-ups can be designed to obtain 3D ion velocity vectors. Figure 2.2 shows schematics of two such measurement set-ups.

For the *tristatic* set-up shown in Figure 2.2 a), the main ISR transmitter/receiver dish is operated in combination with two remote receiver dishes. The remote receiver dishes are pointed to intersect the radar beam at a certain altitude. Each of the three receiver dishes measures the line-of-sight velocity in its respective pointing direction. A simple coordinate

transform allows to calculate the 3D ion velocity vector in a geographic reference frame, i.e. eastward, northward, and upward.

The *monostatic* set-up only requires the main ISR transmitter/receiver dish. The dish is steered between multiple pointing directions, obtaining the line-of-sight ion velocity from each direction. This measurement mode is therefore often referred to as *beam-swinging* mode. Figure 2.2 b) illustrates the *beam-swinging* mode of the EISCAT ultra-high frequency (UHF) ISR which will be introduced in Section 2.2. In this example, the radar dish is rotated through a cycle of four pointing directions with a cycle time of 6 minutes. Equivalent to *tristatic* experiments, the 3D ion velocity vector in a geographical reference frame can be obtained by a coordinate transform. However, more sophisticated statistical methods have been developed, most notably the application of *stochastic inversion* which allows to account for the uncertainty of each measurement (Nygrén et al., 2011).

It can be seen that the main disadvantage of *monostatic* measurements is the time resolution. For a single pointing direction, incoherent scatter measurements are typically integrated over  $\sim 1$  min intervals to obtain a sufficient data quality that allows to infer plasma parameters. It should be noted that shorter intervals are possible for F region measurements or generally high ionization. The EISCAT UHF *beam-swinging* mode applies a dwell time of 1 min per pointing direction and requires about 30 s to steer the dish between positions which leads to a time resolution of 6 min. *Tristatic* measurements do not require the mechanical motion of any radar dishes and therefore the same time resolution as for regular ISR measurements can be achieved. However, *tristatic* measurements are restricted to a single altitude level at which the pointing directions of the main radar and the two remote receiving sites intersect. *Monostatic* measurements allow to obtain the same altitude resolution as regular ISR experiments. It should be noted that the four pointing directions disperse with altitude and 3D ion velocity vectors can only be inferred if the plasma motion is horizontally uniform across the four measurement positions.

Since the F region ionosphere can be assumed as collision-less (see Appendix B), the ion velocity is determined by the  $E \times B$ -drift. Therefore, the ionospheric electric field vector  $\mathbf{E}$  can be calculated from the F region ion velocity  $\mathbf{v}^F$  as

$$\mathbf{E} = -\mathbf{v}^F \times \mathbf{B}. \quad (2.2)$$

The Earth's magnetic field  $\mathbf{B}$  changes very slowly and the International Geomagnetic Reference Field (IGRF) (Barraclough, 1988; Alken et al., 2021) can generally be assumed. Since magnetic field lines are very good conductors, the F region electric field can be assumed to propagate down to E region altitudes only slightly altered by the increasing magnetic field strength. The E region electric fields can be applied, e.g. to calculate Joule heating rates from dissipating ionospheric currents (Vickrey et al., 1982; Kavanagh et al., 2022; Baloukidis et al., 2023) or E region neutral winds (Nozawa et al., 2010).

### Neutral wind

From the altitude-dependent ion velocity vector  $\mathbf{v}_i(z)$  and the electric field vector  $\mathbf{E}$ , the E region neutral wind  $\mathbf{u}(z)$  can be calculated assuming the *steady-state ion mobility equation*

(Brekke et al., 1973)

$$\frac{\partial \mathbf{v}_i(z)}{\partial t} = \frac{\Omega_i}{B} (\mathbf{E} + \mathbf{v}_i(z) \times \mathbf{B}) + \nu_{in}(z) (\mathbf{u}(z) - \mathbf{v}_i(z)) = 0. \quad (2.3)$$

It can be seen that in the F region, where  $\nu_{in} \ll \Omega_i$  can be assumed, Equation 2.3 becomes Equation 2.2. Several statistical methods to solve Equation 2.3 for the neutral wind vector in the E region have been discussed (Heinselman and Nicolls, 2008; Nygrén et al., 2011). The most straightforward approach, however, is to directly solve Equation 2.3 for  $\mathbf{u}(z)$ , which is valid for a sufficient vertical resolution of the measurements (Bering and Mozer, 1975; Rino et al., 1977). The direct-solution approach has been applied in previous studies (Nozawa et al., 2010).

### Ion-neutral collision frequency

The importance of the ion-neutral collision frequency  $\nu_{in}$  has been discussed in Section 1.2.1. The vertical  $\nu_{in}$  profile is essential for the ionospheric dynamo region, the ionospheric currents, and the coupling of the neutral atmosphere and ionosphere. Additionally, it is required to infer neutral winds from ISR measurements (see Equation 2.3).

Ion-neutral frequencies can be obtained from *in situ* satellite measurements of the neutral density by applying Equation 1.1. The neutral density is derived from the atmospheric drag force acting on the satellites and a global data set of neutral density measurements at 200 - 500 km altitude has been obtained in the last 50 years (Palmroth et al., 2021). There have been plans about satellite missions on elliptical orbits, providing *in situ* measurements as low as 150 km altitude or even below by releasing sub-satellites (Sarris et al., 2020). *In situ* measurements of the neutral density in the ionospheric dynamo region are possible with sounding rockets (Rapp et al., 2001). However, both satellites and sounding rockets are strongly limited in altitude and measurement time.

The impact of the ion-neutral collision frequency on the ion adiabatic coefficient  $\gamma_i$  allows to infer  $\nu_{in}$  from ISR measurements under certain assumptions. One very common method is to assume equal ion and electron temperature  $T_i = T_e$  (e.g., Kofman and Lathuillere, 1985; Nygrén, 1996). This assumption, however, is only valid up to approximately 110 km altitude and only for low Joule heating rates (Nygrén, 1996). Another technique applies ISR measurements of the vertical ion velocity and 3D electric field vector. The ion-neutral collision frequency can then be calculated from the vertical component of the steady-state ion mobility equation in Equation 2.3 (Nygrén et al., 1987; Oyama et al., 2012). However, this method is restricted by three important assumptions: (1) Reliable measurements are only possible above  $\sim 106$  km where the ion velocities are controlled by ionospheric electrodynamics. (2) There is no vertical neutral wind, i.e.  $u_z = 0$ . (3) The electric field is strong enough that neutral dynamo effects can be neglected, i.e.  $E \gtrsim 20$  mVm<sup>-1</sup>. A detailed description of this method and a discussion of its restrictions can be found in Oyama et al. (2012).

Nygrén (1996) compared both methods for ISR measurements from a single day and the obtained ion-neutral collision frequencies are shown in Figure 2.3 a). These early measure-

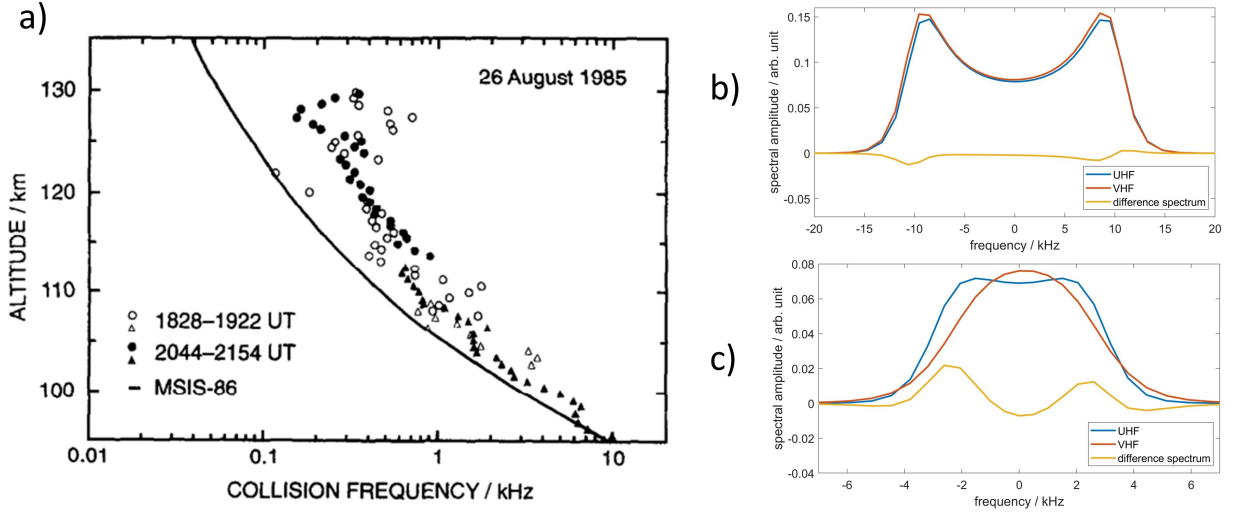


Figure 2.3: a) Measurements of the ion-neutral collision frequency applying the  $T_i = T_e$  method (triangles) and the steady-state vertical ion velocity method (dots). A climatology  $\nu_{in}$  profile is shown for comparison (solid line). The figure was taken from Nygrén (1996) with permission from Elsevier. The impact of  $\nu_{in}$  on the incoherent scatter spectrum depends on the radar frequency. This can be seen by comparing the spectra of two ISRs for b) low  $\nu_{in}$  in the F region and c) high  $\nu_{in}$  in the E region.

ments indicated that the actual  $\nu_{in}$  profile can deviate quite significantly from climatology profiles. The upper boundary of the ionospheric dynamo region shown in Figure 1.4 is therefore not fixed at a certain altitude but can vary strongly. However, both methods applied to obtain the measurements shown in Figure 2.3 a) are subject to quite significant assumptions and limitations.

Direct measurements of the ion-neutral collision frequency which require no further assumptions about the background conditions and are not restricted by altitude are more difficult. Simultaneous measurements of two ISRs with significantly different radar frequencies have been shown to allow for direct  $\nu_{in}$  measurements (Grassmann, 1993). Figure 2.3 b) and c) show the incoherent scatter spectra of a very-high frequency (VHF;  $f = 224$  MHz) and an ultra-high frequency (UHF;  $f = 929$  MHz) ISR at different collision frequencies. It should be noted that the VHF spectra are scaled to UHF frequencies for this comparison following the procedure described in Grassmann (1993). It can be seen that the two spectra are highly similar at low collision frequencies, i.e. in the F region. In the E region, where  $\nu_{in}$  is considerably higher, the two spectra show distinct differences in shape. Grassmann (1993) suggested multiple methods to infer the ion-neutral collision frequencies from dual-frequency ISR measurements. Nicolls et al. (2014) were the first to apply one of these methods, a simultaneous fit of the incoherent scatter spectra with a combined error function. The first application of the *difference spectrum* method was presented in Günzkofer et al. (2023b) and is part of this thesis. This method allows to analyze both ISR measurements separately and can therefore be based on standard ISR analysis software.

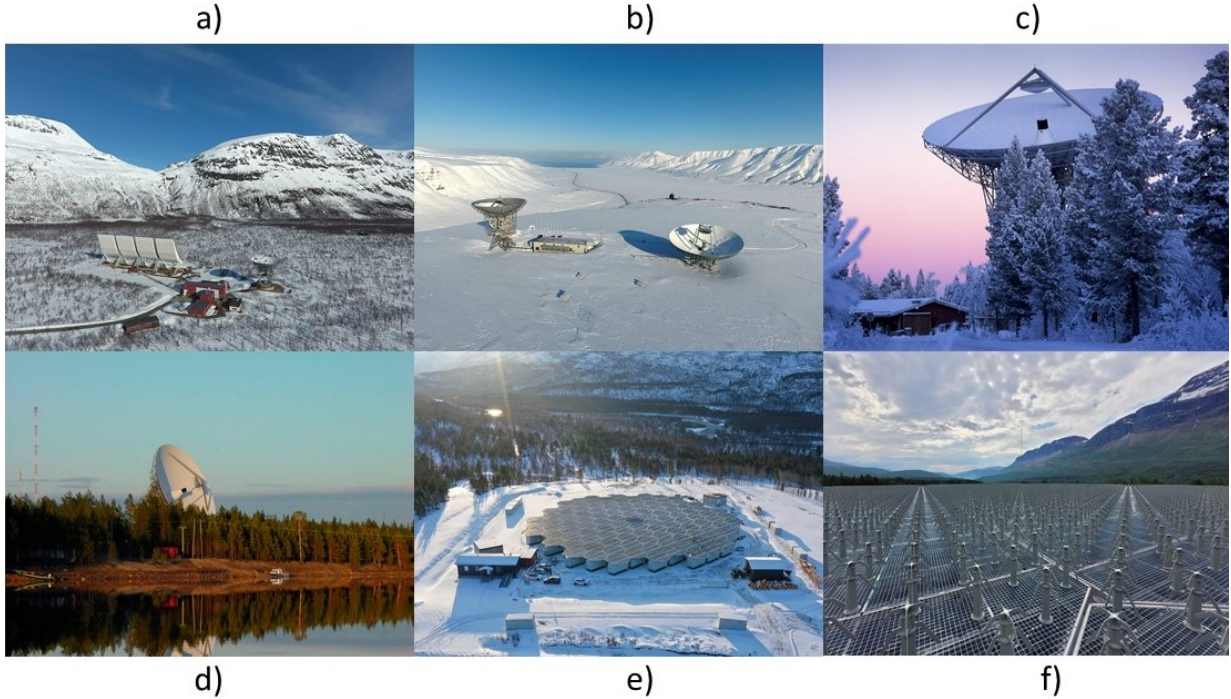


Figure 2.4: a) EISCAT site in Tromsø, Norway with the VHF (left) and UHF (right) radars. b) EISCAT site on Svalbard, Norway with the EISCAT ESR system. c) Remote VHF receiver dish in Kiruna, Sweden. d) Remote VHF receiver dish in Sodankylä, Finland. e) EISCAT\_3D site in Skibotn, Norway during the build-up of the new phased array radar. f) The antenna elements of the EISCAT\_3D radar in Skiboten. Figure credit: The EISCAT Scientific Association and the individual photographers Craig Heinselmann (a, b, and d), Lars-Göran Vanhainen (c), Johan Svensson (e), and Harri Hellgren (f).

## 2.2 EISCAT and EISCAT\_3D

At the moment, approximately ten incoherent scatter radars are operated worldwide. Several of them are located at high northern latitudes, either in the auroral zone or in the polar cap. The European Incoherent Scatter (EISCAT) Scientific Association operates multiple ISRs and support systems at several sites in northern Europe shown in Figure 2.4.

The current EISCAT systems include three ISRs: the ultra-high frequency (UHF, 929 MHz) ISR and very-high frequency (VHF, 224 MHz) ISR in Tromsø, Norway ( $69.6^\circ$  N,  $19.2^\circ$  E) and the EISCAT Svalbard Radar (ESR) on Svalbard, Norway ( $78.2^\circ$  N,  $16^\circ$  E). Additionally, the EISCAT Scientific Association operates two receive-only stations in Kiruna, Sweden ( $67.9^\circ$  N,  $20.4^\circ$  E) and Sodankylä, Finland ( $67.4^\circ$  N,  $26.6^\circ$  E). The systems currently operated by the EISCAT Scientific Association are shown in Figures 2.4 a) - d). Technical documentation of these systems (e.g., dish sizes/shapes, radar modes, and operation programmes) can be found in Tjulin (2022).

The EISCAT\_3D system (McCrea et al., 2015) is a new ISR that is currently in the

build-up and commissioning phase. EISCAT\_3D will be a so-called *active phased array* ISR which does not require large antenna dishes to focus the transmitter beam and the backscattered radio signal. Instead, a focused transmission beam is achieved by a positive overlap (coherent interference) of the same radio signal transmitted by multiple small antennas combined to an antenna array. This requires that the radio signal is transmitted by all antennas at a slightly different phase, hence the name phased array radar. Similarly, the very weak, backscattered radio signal is not focused by large receiver dishes but by adding up the phase-shifted signals measured by each single antenna. The phase shifts during signal transmission and reception determine the pointing direction of the radar which can therefore be steered electronically. The main advantage of phased array radars is therefore that multibeam measurements, e.g. the *beam-swing* mode in Figure 2.2 b), do not require long cycle times. Simultaneous measurements with up to 30 beams are planned to allow vertically and horizontally resolved ISR measurements which will be another major improvement of the EISCAT\_3D system.

The main site of the EISCAT\_3D system will be close to Skibotn, Norway (69.4° N, 20.3° E) and is shown in Figure 2.4 e). The radar consists of 109 hexagonal antenna arrays, each made up of 91 dipole antenna elements which are shown in Figure 2.4 f). The EISCAT\_3D ISR is also planned to allow for *tristatic* measurements, utilizing two remote receiving sites in Kaiseniemi, Sweden, and Karesuvanto, Finland. The long-term goal is to have a total of five measurement sites receiving the EISCAT\_3D radio signal.

## 2.3 Meteor Radars

Meteoroids entering the Earth's atmosphere are vaporized by friction and form an ionized meteor trail. The trail plasma is thermalized by the atmosphere, undergoes ambipolar diffusion, and drifts with the background neutral wind. Meteor radars can leverage the Doppler shift of the coherent scatter signal from the trail plasma to measure neutral wind velocities at an altitude of approximately 70 - 110 km (Hocking et al., 2001). Meteor radar measurements have been applied extensively to study the neutral atmosphere dynamics of the lower thermosphere (e.g., Pokhotelov et al., 2018; Stober et al., 2021b, and references there within). Meteor radar data is also shown in Figures 1.6 and 1.8 b). The working principle of MLT wind measurements with meteor radars is shown in Figure 2.5 a).

The radio signal is backscattered by the plasma column that is the meteor trail. The backscattering can be described as a mirror-like reflection from the specular point. An array of receiver antennas allows to determine the angle under which the meteor is detected (Stober, 2019) and the radial drift velocity can be inferred. Multiple meteor detections under different angles then allow to infer the 3D neutral wind velocity.

A very recent, major improvement is the application of meteor radar clusters that combine measurements of multiple meteor radars with overlapping fields of view. One such cluster is the Nordic Meteor Radar Cluster (Stober et al., 2021a, 2022) which includes radars in Tromsø (TRO, Norway), Alta (ALT, Norway), Kiruna (KIR, Sweden), and Sodankylä (SOD, Finland) as shown in Figure 2.5 b). The Nordic Meteor Radar Cluster allows

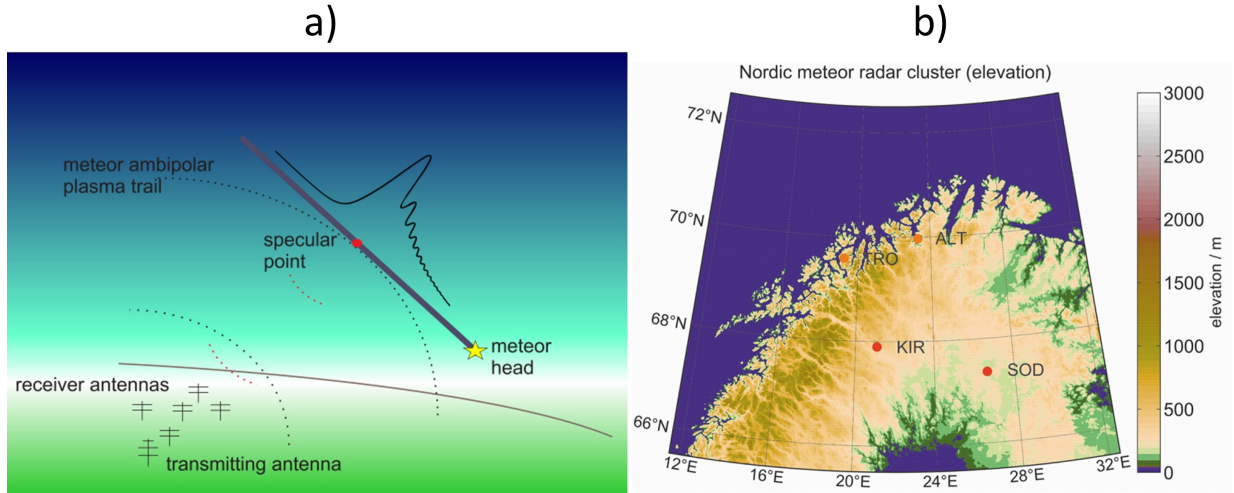


Figure 2.5: a) Illustration of the meteor radar working principle. b) Stations of the Nordic Meteor Radar Cluster. Figure credit: a) Stober (2019) and b) Stober et al. (2021a).

horizontally resolved neutral wind measurements over an area of  $660 \times 660$  km with a 30 km resolution. Therefore, both the vertical and the horizontal structure of atmospheric gravity waves (see Section 1.3.2) can be investigated. Additionally, the overlap of the fields of view leads to a significantly higher number of meteor trail detections, allowing for a higher time resolution.

## 2.4 Atmosphere-Ionosphere models

Though incoherent scatter radars and meteor radars are very powerful instruments for studying atmosphere-ionosphere coupling processes, they both have distinct limitations. Radars only provide local measurements at a single point of the Earth's surface and even multibeam phased-array ISRs and meteor radar clusters are strongly limited in horizontal coverage. Meteor radars are limited in altitude to about 70 – 110 km where meteor trails form. And even though it has been shown in Section 2.1 that multiple ionosphere and neutral atmosphere parameters can be inferred from ISR measurements, there are limitations to what information we can obtain. Atmosphere-ionosphere models can provide information that is not available from measurements though the capabilities of these models have to be assessed carefully.

First of all, one has to distinguish between empirical and physics-based models. Empirical models infer the state of a system from certain input parameters by statistical estimation from a large measurement dataset. Empirical models therefore give an average background state, in atmospheric physics called *climatology*, and cover predictable changes with e.g. local time, day of the year, or throughout a solar cycle, very well. They can be applied to provide information about the slow-changing background state of the atmosphere-ionosphere system but do not allow to study specific processes, e.g. atmospheric waves.

Physics-based models on the other hand apply physical laws to calculate the state of a system from initial conditions. Physics-based models can reproduce specific processes in the atmosphere-ionosphere system since they include the underlying physical laws. However, their spatial and temporal resolution is limited by computational resources, e.g. gravity waves are often not resolved in atmosphere-ionosphere models but empirically parameterized instead. Physics-based models require an initial state and, as far as possible, exact boundary conditions to give accurate results. Some physics-based atmosphere-ionosphere models are whole-atmosphere models and extend down to the surface of the Earth. They can be restrained (*nudged*) to meteorological measurements at low altitudes which are way more common than measurements at ionospheric altitudes. Since the Sun and the solar wind can not be included in atmosphere-ionosphere models, the external forcing by plasma convection and particle precipitation is mostly empirically parameterized as well.

With increasing computational power, improved understanding of the physical processes, and a larger number of measurements, physics-based models might eventually be developed into reliable forecasts of the atmosphere-ionosphere system and space weather. The validation of model results with observations is essential for this development. Therefore atmosphere-ionosphere models are both, an extension of our limited measurement capabilities and the motivation to conduct measurements. The empirical and physics-based atmosphere-ionosphere models applied for this thesis will be briefly introduced.

### 2.4.1 Empirical atmosphere, ionosphere, and convection models

The different versions of the *US Naval Research Laboratory Mass Spectrometer and Incoherent Scatter Radar (NRLMSIS)* model (in earlier versions only called *MSIS*) are commonly applied as empirical climatology of the Earth's neutral atmosphere (Hedin, 1991; Picone et al., 2002). The (NRL)MSIS model gives the densities of seven neutral particle species and the neutral atmosphere temperature from the ground to 1000 km altitude and includes local time-, seasonal-, and solar cycle-dependent variations.

The *International Reference Ionosphere (IRI)* is an empirical ionosphere model based on a large number of ground- and satellite-based observations (Rawer et al., 1978; Bilitza et al., 2022). The IRI model gives the densities of five ion species, the ion and electron temperatures, and the electron density (equivalent to the sum of the five ion densities). (NRL)MSIS and IRI are often combined to obtain a climatology of the atmosphere-ionosphere system and have been leveraged to create Figures 1.1, 1.4, and 1.5 a).

As mentioned previously, external forcing of the ionosphere e.g. from the solar wind has to be empirically parameterized in physics-based models. The polar plasma convection introduced in Figure 1.2 is one of the main external forcing mechanisms in the high latitude ionosphere. There are several empirical convection models, two of the most commonly applied ones are the *Heelis* (Heelis et al., 1982) and the *Weimer* (Weimer, 2005) models. The convection pattern can be expressed as an electric potential field  $\Phi$ , i.e. the ion convection velocity is given as  $\mathbf{v}_i = (\mathbf{E} \times \mathbf{B}) / B^2 = (-\nabla\Phi \times \mathbf{B}) / B^2$ . The *Heelis* model infers the polar electric potential field from the *Kp* index that is commonly applied to quantify the general level of geomagnetic activity (Bartels et al., 1939). The *Weimer* model applies

a set of spherical functions to infer the potential field from several solar wind parameters and the interplanetary magnetic field.

### 2.4.2 General Circulation Models

General Circulation Models (GCMs) are physics-based atmosphere models that solve the discretized, basic fluid dynamics equations and chemistry on a spherical grid. GCMs that cover ionospheric altitudes have to include the required electrodynamics and ion chemistry as well. Whole-atmosphere models require boundary conditions for the Earth's surface and can be coupled with other models describing e.g. the Earth's ocean and land surface. As mentioned before, whole-atmosphere models can be *nudged* to meteorological measurements at lower altitudes (below approximately 30 – 50 km).

The *Ground-to-topside model of Atmosphere and Ionosphere for Aeronomy (GAIA)* consists of separate atmosphere, ionosphere, and electrodynamics models which are coupled (Jin et al., 2008, 2012). It is a whole-atmosphere model, constrained to measurements up to about 30 km altitude, and provides amongst other parameters plasma and neutral particle densities, temperatures, and 3D neutral winds and ion velocities. At high latitudes, GAIA does apply a symmetric convection pattern with a fixed cross-polar potential difference of 40 kV. This corresponds to a constant, low geomagnetic activity. It should be noted that the different parts of GAIA employ different coordinate systems, i.e. the atmosphere model applies hydrostatic pressure levels while the ionospheric model is based on fixed altitude gates with a resolution of 10 km. The model parameters are therefore available on different grids.

The *Whole-Atmosphere Community Climate Model with thermosphere and ionosphere extension (WACCM-X)* is the atmospheric part of the *Community Earth System Model (CESM)* (Hurrell et al., 2013; Liu et al., 2018). Both the neutral atmosphere and the ionosphere equations are solved on a hydrostatic pressure level grid. Below approximately 50 km altitude, the model is *nudged* to meteorological measurements. The polar plasma convection is parameterized with the *Heelis* model described in the previous section. The WACCM-X is continuously updated, the most notable recent progress being the development of a high-resolution version that aims to resolve atmospheric gravity waves directly (Liu et al., 2023).

Other than the two GCMs described so far, the *Thermosphere Ionosphere Electrodynamics - General Circulation Model (TIE-GCM)* (Richmond et al., 1992) is not a whole-atmosphere model. As the name suggests, it only describes the neutral atmosphere and ionosphere at thermospheric altitudes above approximately 98 km. At the lower boundary, a climatology model is applied to include upward propagating tides from the lower and middle atmosphere. The TIE-GCM applies hydrostatic pressure levels and the polar plasma convection can be parametrized with the *Heelis* and the *Weimer* model. Since it does not cover the entire atmosphere, the TIE-GCM requires significantly less computational power and is therefore available to a wider range of researchers. Within the German Aerospace Center (DLR), TIE-GCM runs with personal specifications can be performed on the high-performance data analysis cluster *Kratos*. TIE-GCM data is shown in Figure 1.7.

# Chapter 3

## Results

The science questions presented in Section 1.4 have been investigated and the results have been published in the articles attached in Appendix A. Following, the main findings of each publication are presented.

### 3.1 *In situ* forcing of semidiurnal tidal oscillations in the transition region (Günzkofer et al., 2022)

We analyzed an EISCAT UHF ISR measurement campaign that took place over approximately 20 days during September 2005 (Nozawa et al., 2010). A stochastic inversion method (Nygrén et al., 2011) was applied to obtain 3D ion velocity vectors and the neutral winds were calculated with the steady-state ion mobility equation (see Equation 2.3). In combination with the Kiruna meteor radar, this allowed us to investigate tidal oscillations of the neutral wind at an altitude range of 80 – 142 km. An adaptive spectral filter (ASF) method (Stober et al., 2021b) was applied to determine the amplitudes and phases of tidal oscillations in the zonal and meridional neutral wind components. The amplitude ratio of semidiurnal and diurnal oscillations is shown in Figure 3.1.

It was found that the zonal neutral wind exhibits a transition from predominant semidiurnal oscillations to diurnal oscillations at about 110 – 120 km altitude. This is in agreement with the expected behavior for tidal oscillations in the high-latitude thermosphere-ionosphere described in Section 1.3.1 (Andrews et al., 1987; Nozawa et al., 2010). The meridional neutral wind, however, showed strong 12 h tidal oscillations at altitudes  $\lesssim 110$  km and  $\gtrsim 130$  km. The existence of an upper band of strong semidiurnal oscillation is in contradiction to the classical expectations. The phase of the semidiurnal oscillations obtained from the ASF analysis showed a steady phase progression up to about 120 km altitude. This indicates that upward-propagating atmospheric tides are the origin of these oscillations. At higher altitudes, a constant phase was observed which suggests that the upper band of semidiurnal oscillations in Figure 3.1 is forced *in situ* in the thermosphere. Multiple thermosphere-ionosphere model runs with GAIA, WACCM-X, and TIE-GCM were investigated for signs of semidiurnal oscillations at  $\gtrsim 130$  km altitude. From global

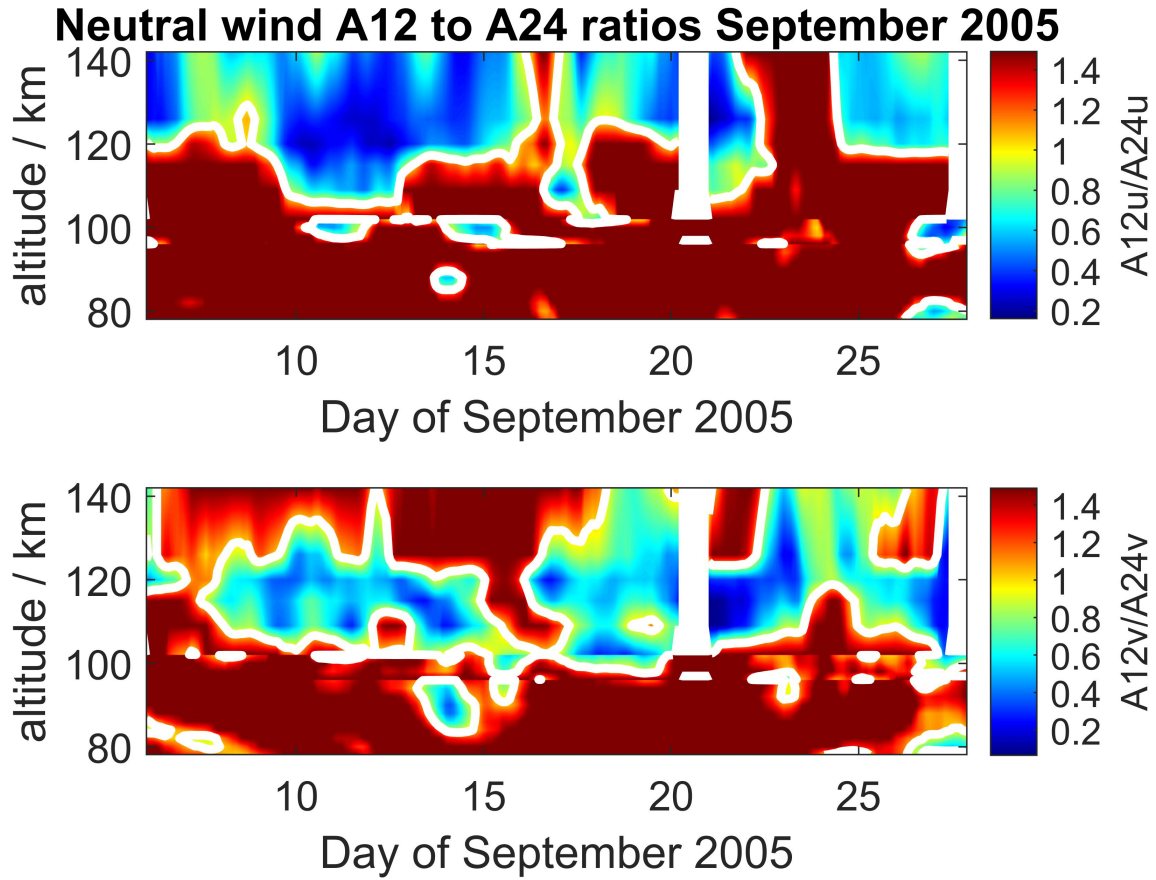


Figure 3.1: Ratio of semidiurnal to diurnal oscillation amplitude in the zonal (top) and meridional (bottom) neutral wind (Figure 3 in Günzkofer et al., 2022).

thermosphere-ionosphere model data, the zonal wavenumber of tidal oscillations can be determined in addition to the wave period. An extended ASF method was applied to determine the amplitudes and phases of diurnal and semidiurnal oscillations with zonal wavenumbers  $-3 \leq k \leq 3$  at the location of the EISCAT UHF ISR. It was found that the migrating modes DW1 and SW2 show the strongest amplitudes in the ionospheric transition region. Additionally, all models showed significant semidiurnal oscillations of the meridional neutral wind velocity above about 130 km altitude. The absence of such oscillations in the zonal wind component was also reproduced in all model runs. In total, five model runs with different representations of the most important forcing mechanisms of tidal oscillations in the transition region (upward-propagating atmospheric tides, polar plasma convection, and EUV absorption) were analyzed. It was found that in model runs with constant, weak polar plasma convection, the semidiurnal oscillation amplitude above 130 km altitude is significantly reduced in comparison to models with parameterized convection. For a constant, low EUV irradiation, the models showed a sporadically reduced

amplitude in the upper band of semidiurnal oscillations compared to parameterized EUV irradiation. The absence of upward-propagating tides from lower atmospheric regions, however, only affected the semidiurnal oscillations below about 120 km altitude.

Therefore, both measurement and model results suggest the existence of strong semidiurnal oscillations in the meridional neutral wind above  $\sim 130$  km altitude. No such oscillations are found in the zonal wind component. Measurements of the tidal phase and mechanistic model investigations of the most common forcing mechanisms suggested *in situ* forcing of these oscillations. In the strongly driven high-latitude ionosphere, upward-propagating atmospheric tides seem to be of minor importance above the transition region. This is a vast contrast from the equatorial latitudes where tidal waves from the lower atmosphere significantly impact the ionosphere (Immel et al., 2006; Häusler and Lühr, 2009; Lühr and Manoj, 2013). Both the polar plasma convection and the absorption of EUV radiation seem to contribute significantly to the *in situ* forcing of semidiurnal oscillations in the thermosphere. A day-night asymmetry of the polar plasma convection pattern would explain the presence of semidiurnal oscillations in the meridional but not the zonal wind component.

## 3.2 Inferring neutral wind velocities from AGW-TID observations (Günzkofer et al., 2023a)

Three-dimensional observations of atmospheric gravity wave-traveling ionospheric disturbances (AGW-TIDs) mostly require the combination of multiple instruments to obtain the required coverage and resolution (van de Kamp et al., 2014). We analyzed measurements with the EISCAT VHF ISR and the Nordic Meteor Radar Cluster for signs of AGW-TIDs. The EISCAT measurements were analyzed at 110 – 170 km altitude with a time resolution of 1 min. The meteor radar measurements cover a horizontal area of  $660 \text{ km} \times 660 \text{ km}$  over Fennoscandia (see Figure 2.5 b) at 80 – 100 km altitude with a time resolution of 10 min. The application of Fourier filters allowed the extraction of wave signatures in the ISR electron density and the meteor radar neutral wind measurements. Figure 3.2 a) and b) show the vertical and horizontal wave signatures found with the respective instruments.

Least-square fits of the wave patterns in the time-altitude and horizontal measurement cross-sections were applied. From the fitted wave patterns, the vertical phase lines (red and dotted lines in Figure 3.2 a) and the wave parameters, i.e. vertical and horizontal wavelengths  $\lambda_z$  and  $\lambda_H$ , wave period  $\tau$ , and propagation direction  $\alpha$ , were determined. Since the meteor radar measurements allow to investigate a limited altitude range, the wave period  $\tau$  and the vertical wavelength  $\lambda_z$  could be determined from both measurements to some extent. It was found that these two parameters agree reasonably well at the closest altitudes of both measurements. This suggests that the TID is the ionospheric signature of the observed AGW.

The dispersion relation of AGWs relates the wave parameters to the conditions and dynamics of the background neutral atmosphere. Assuming the neutral atmosphere given by the empirical NRLMSIS model, the neutral wind velocity along the direction of the horizontal

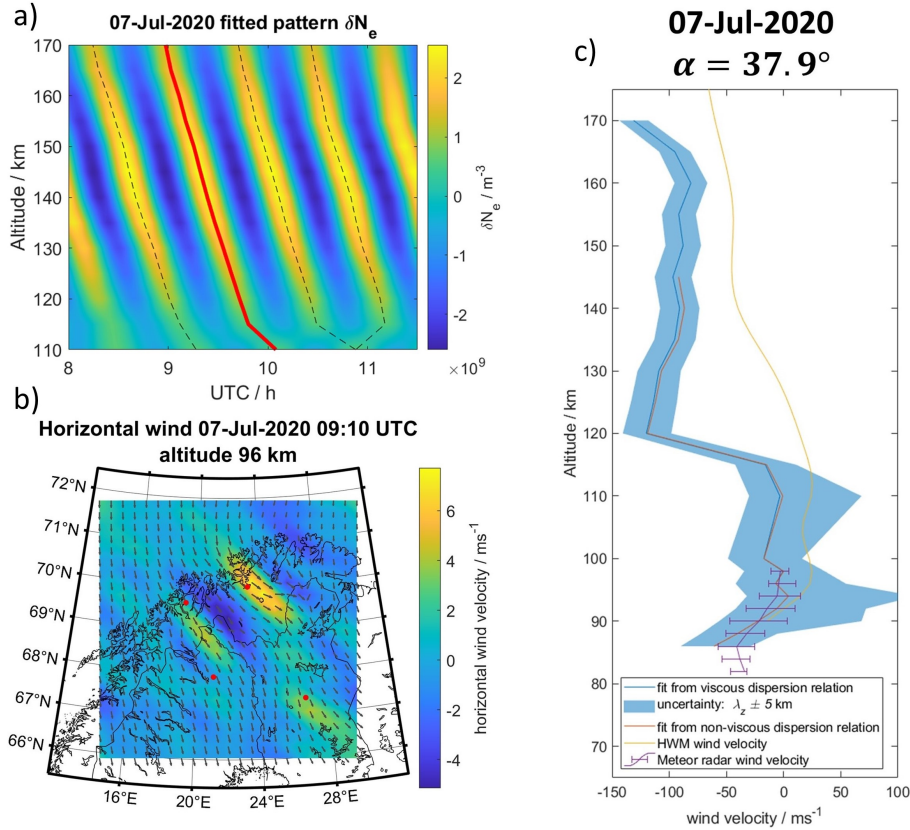


Figure 3.2: a) A TID is observed in filtered electron density measurements with the EISCAT ISR. The vertical and temporal wave characteristics are determined from the phase lines (dotted and red). b) Filtering the neutral wind velocity measured with the Nordic Meteor Radar Cluster allows to infer the horizontal wave parameters of an AGW. c) A vertical neutral wind profile can be inferred by applying the wave parameters and the gravity wave dispersion relation (Figures 4, 6, and 7 in Günzkofer et al., 2023a).

wave vector can be inferred using the obtained wave parameter measurements (Nicolls and Heinselman, 2007; Nicolls et al., 2013). A non-linear least-square fit was applied to determine the vertical neutral wind profile from the viscous and non-viscous formulations of the gravity wave dispersion relation (Vadas and Fritts, 2005). The obtained profiles were compared to the neutral wind measurements with the Nordic Meteor Radar Cluster and the profile given by the empirical Horizontal Wind Model (HWM14, Drob et al., 2015). The neutral wind profiles are shown in Figure 3.2 c).

It can be seen that the neutral wind profiles inferred from both dispersion relation formulations agree well up to about 145 km altitude. At higher altitudes, the fit of the non-viscous dispersion relation does not converge, presumably due to the increase of atmospheric viscosity with altitude. The inferred neutral wind profiles agree well with the meteor radar measurements at about 85 – 100 km altitude. The profiles also follow the general trend of

the climatology wind profile at higher altitudes.

In summary, it was shown that a combination of the EISCAR ISR and the Nordic Meteor Radar Cluster observations allows us to connect TID and AGW observations and perform 3D wave measurements. It can be seen that the thermospheric neutral wind impacts the TID wave parameters according to the gravity wave dispersion relation. This is important for ionosphere and space weather research in multiple ways. For one, this shows that an empirical parameterization of gravity wave-forced TIDs in thermosphere-ionosphere models can utilize the gravity wave dispersion relation. Including such parameterizations might significantly improve the representation of how atmospheric processes impact ionospheric variability. Additionally, AGW-TID observations might provide a new method for neutral wind measurements in the lower thermosphere, potentially helping to close or narrow the *thermospheric gap* (Oberheide et al., 2011) of wind measurements.

### 3.3 Optimizing the empirical scaling factor for model Joule heating rates (Günzkofer et al., 2024)

We studied how the known variation of Joule heating rates in the TIE-GCM atmosphere-ionosphere model with geomagnetic conditions, magnetic local time, and ion convection parameterization (Baloukidis et al., 2023) affects the necessary empirical scaling of model Joule heating rates. A database of more than 2000 hours of EISCAT ISR beam-swing measurements was assembled and analyzed with the GUISDAP software package. The obtained line-of-sight ion velocities were converted to 3D ion velocity vectors by applying a stochastic inversion method (Nygrén et al., 2011). For each measurement campaign included in the database, we conducted two TIE-GCM runs with *Heelis* and *Weimer* polar plasma convection parameterization. The F region electric field vector can be calculated from the measurement and model ion velocities using Equation 2.2 assuming a collision-less ionosphere at these altitudes (see Appendix B). Vertical profiles of the local Joule heating rate were calculated from the measurement and model results for electron density and ionospheric electric field (Vickrey et al., 1982). The neutral atmosphere density and wind velocities were taken from the TIE-GCM results. Figure 3.3 a) shows the three median Joule heating rate profiles at 90 – 185 km altitude for one measurement campaign included in the database. It is known that atmosphere-ionosphere models require empirical scaling of the Joule heating rate to compensate for dynamics that are not resolved in the model (Codrescu et al., 1995). Therefore, a non-linear least square fit of the vertical profile was conducted to determine the ideal scaling factor. Figure 3.3 b) shows the same profiles after the two model profiles have been scaled. The height-integrated Joule heating rates are given in the figure legend.

It was found that the standard scaling factor  $f = 1.5$  applied in the TIE-GCM is appropriate for average conditions and both *Heelis* and *Weimer* convection. In the next step, the Joule heating rate profiles were binned with respect to the  $Kp$  index, solar wind parameters, and the magnetic local time. Since the model output interval is larger than the

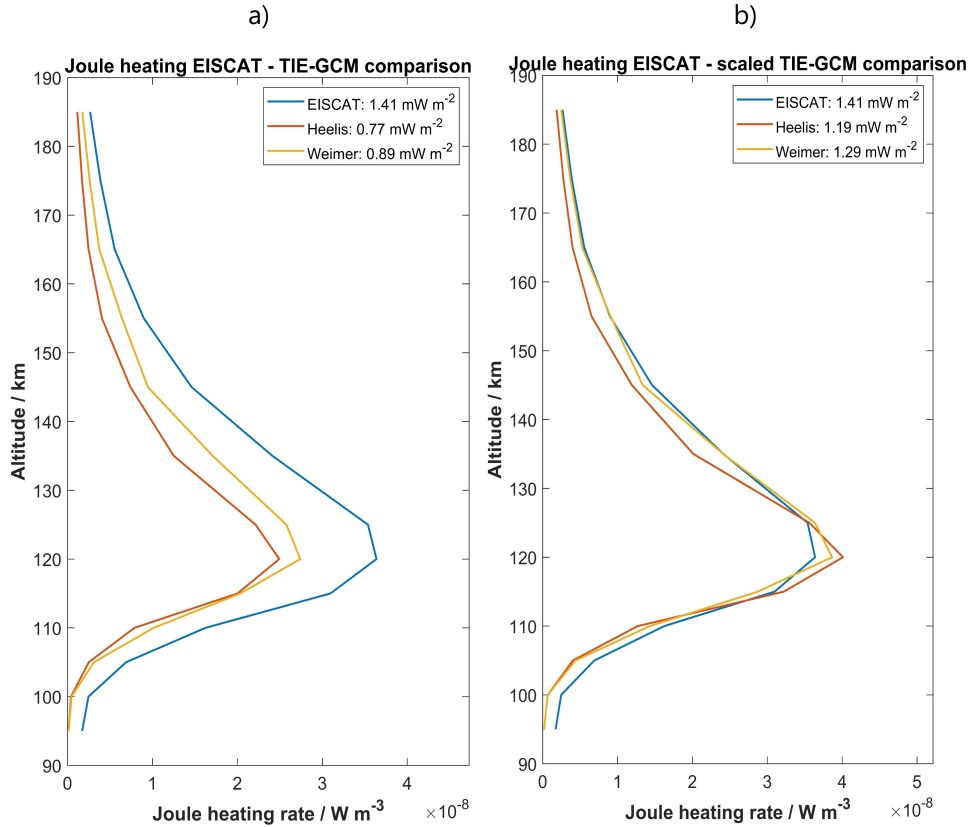


Figure 3.3: a) Vertical profiles of the local Joule heating rate calculated from EISCAT ISR measurements and TIE-GCM model runs with *Heelis* and *Weimer* convection parameterization. b) The two model profiles are linearly scaled to fit the Joule heating rates calculated from EISCAT measurements (Figure 3 in Günzkofer et al., 2024).

measurement resolution, a nearest-neighbor interpolation was applied to obtain the same number of Joule heating profiles calculated from measurement and model results. For each bin, the median profile was calculated and the required scaling factor was determined. We found that the required Joule heating rate scaling factor varies within a range of  $f \sim 0.5 - 20$ . Distinct correlations of the Joule heating rate and the required scaling factor with geomagnetic and solar wind conditions, magnetic local time, and the applied convection model were found. The strongest deviations from the standard  $f = 1.5$  factor were found for low  $Kp$  index and weak solar wind forcing. However, since the Joule heating rates are generally low under these conditions, the absolute uncertainty caused by the scaling factor is minor. At high geomagnetic and solar wind activity, however, small deviations of the required scaling factor were found to have a quite significant impact on the absolute Joule heating rate. The variation of the Joule heating rate with magnetic local time was found to be generally well represented by the model results. However, distinct deviations were found, e.g. *Weimer*-driven TIE-GCM runs tend to underestimate the Joule heating

rate during day- and overestimate them during nighttime.

It was shown that a constant Joule heating rate scaling factor leads to significant uncertainties in model Joule heating rates compared to heating rates calculated from measurements. Assuming that future space weather forecasts will not be able to resolve sufficiently small temporal and spatial scales, an accurate empirical scaling of Joule heating rates will be required. The main result of this work was the creation of several look-up tables for the required scaling factor under various conditions. This allows users of the TIE-GCM to adjust the Joule heating rates accordingly.

### 3.4 Direct measurement of ion-neutral collision frequency profiles (Günzkofer et al., 2023b)

Measuring the ion-neutral collision frequency is often limited by a large number of requirements to the ionospheric conditions (Nygrén, 1996; Oyama et al., 2012). Dual-frequency ISR measurements allow us to directly measure the ion-neutral collision frequency (Grassmann, 1993). We planned, scheduled, and analyzed multiple simultaneous EISCAT UHF and VHF campaigns. In these campaigns, different EISCAT ISR radar modes were applied to investigate different regions of the thermosphere-ionosphere. Figure 3.4 a) shows the measured incoherent scatter spectra obtained during the DLR EISCAT campaign on 27 September 2021. It can be seen how the signal amplitude varies with altitude and how the UHF and VHF spectra change their shape differently with varying collision frequencies.

Several analysis methods have been suggested to infer the ion-neutral collision frequency from dual-frequency ISR measurements (Grassmann, 1993). Simultaneous analysis of both spectra with a combined error function is presumably the most reliable method but requires implementing a highly specialized analysis software (Nicolls et al., 2014). We presented the (to our knowledge) first implementation of the so-called *difference spectrum* method (Grassmann, 1993). Hereby, the two spectra are analyzed separately with the standard GUISDAP ISR software and combined into the difference spectrum in a second step. This second step requires the scaling of the VHF spectrum to UHF frequencies. A correction parameter  $\beta$  is introduced during this scaling process to compensate for technical differences between the two radars. The  $\beta$  parameter is determined at F region altitudes where the ionosphere can be assumed as collision-less (see Appendix B). A distinct altitude dependence of the  $\beta$  parameter was observed for some campaigns. This is presumably caused by the different beam shapes of the EISCAT UHF and VHF radars and a consequent variation of the overlap volume with altitude. The difference spectrum method requires only minor changes to the GUISDAP software. Therefore, it can be applied by a wide range of researchers and it can be easily adapted for different radar modes.

A non-linear least-square fit of the difference spectrum was applied to infer the ion-neutral collision frequency profile shown in Figure 3.4 b). The inferred profile is compared to the climatology profile calculated from the neutral atmosphere density given by the empirical NRLMSIS model according to Equation 1.1. It can be seen that the inferred ion-neutral

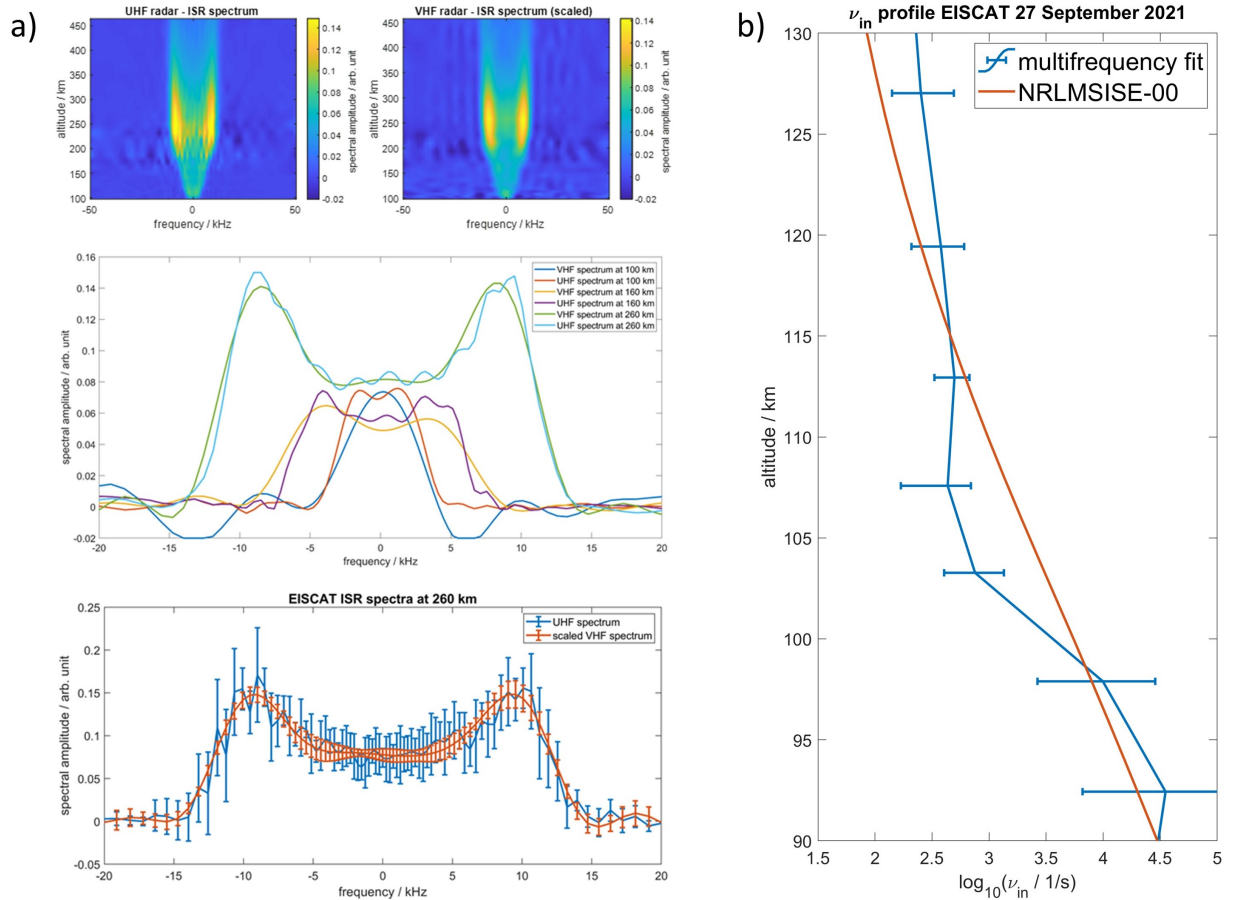


Figure 3.4: a) Incoherent scatter spectra obtained from simultaneous EISCAT UHF and VHF measurements. b) Ion-neutral collision frequency profile inferred with the difference spectrum method compared to a climatology profile (Figures 1 and 2 in Günzkofer et al., 2023b).

collision frequency profile deviates significantly from the climatology profile though the general trend and range of values agree well. Such notable deviations from climatology profiles have been reported previously (see Figure 2.3, Nygrén, 1996) and were interpreted as the result of neutral atmosphere up-welling due to ionospheric heating processes (Oyama et al., 2012). The profile shown in Figure 3.4 b) could therefore be caused by ionospheric heating at about 100 – 115 km altitude which results in a reduced neutral density in this region. Consequently, the atmospheric density is increased at higher altitudes.

Since climatology ion-neutral collision frequency profiles are very commonly assumed in atmosphere-ionosphere coupling studies (see e.g., Günzkofer et al., 2022, 2024), being able to directly and reliably measure these profiles is a major improvement. As shown in Section 1.2, the ion-neutral collision frequency profile is of major importance for the conductivity tensor in the ionospheric dynamo region. Knowledge about the dynamics of the ion-neutral collision frequency profile might therefore be essential for space weather forecasts.

# Chapter 4

## Summary and Outlook

The objective of this thesis was to quantitatively determine the impact of atmospheric waves and collisional atmosphere-ionosphere coupling on space weather. Due to its high importance for space weather, the focus of this thesis was the high-latitude ionospheric dynamo region. Two types of atmospheric waves (tides and gravity waves) have been studied, especially the respective impact of upward-propagating and *in situ* generated waves. The characteristics of atmospheric gravity waves and the ionospheric disturbances caused by them were investigated. Electric currents in the high-latitude dynamo region can cause potentially disastrous space weather impacts on human infrastructure. This thesis investigated the Joule heating of the upper atmosphere caused by *Pedersen* currents. The required empirical scaling of Joule heating rates in current atmosphere-ionosphere models (and presumably also future space weather forecasts) was studied. These currents are the result of the collisional coupling between the neutral atmosphere and the ionosphere, i.e. the vertical profile of the ion-neutral collision frequency. This thesis presented a new method for direct ion-neutral collision frequency measurements.

It was shown that the impact of upward-propagating atmospheric waves on the high-latitude ionosphere is different for tides and gravity waves. The influence of upward-propagating atmospheric tides was limited to  $\lesssim 120$  km altitude due to the strong tidal forcing of the polar plasma convection. Upward-propagating gravity waves were shown to cause variability of the ionosphere up to F region altitudes. Atmospheric waves therefore do contribute to space weather but their impact seems to be limited in the presence of strong external forcing. However, especially atmospheric gravity waves and the accompanying traveling ionospheric disturbances might be important for future space weather prediction capabilities. Additionally, the observation of ionospheric disturbances allows us to infer information about the neutral atmosphere at altitudes that are scarcely covered by atmospheric measurement instruments. The collisional coupling of the neutral atmosphere and the ionosphere was shown to impact the space weather significantly. The representation of the upper atmosphere Joule heating in atmosphere-ionosphere models was improved. Many space weather applications and models rely on climatology ion-neutral collision frequency profiles. This thesis presented direct measurements of the collision frequency and showed significant deviations from the climatology. Such measurements might be extended to im-

prove our understanding of the collisional atmosphere-ionosphere coupling and increase the accuracy of ionosphere and space weather models.

In summary, quantifying the impact of atmospheric waves and collisional atmosphere-ionosphere coupling on space weather requires a thorough understanding of a large number of processes. The presented work improved both measurement capabilities and quantitative understanding of several atmosphere-ionosphere coupling processes. This thesis, therefore, helps to empirically parameterize the impact of high-latitude atmosphere-ionosphere coupling for future space weather forecasts.

Future investigations of high-latitude space weather rely on the development and operation of new measurement instruments. The EISCAT\_3D radar will increase our measurement capabilities and provide an enormous step forward in high-latitude space weather research. Multibeam experiments, possible due to the phased array concept, will significantly increase the time resolution of 3D ion velocity and electric field measurements. Studies of the plasma convection pattern and the neutral wind velocity will be significantly improved. A low-power continuous operation mode would allow to measure the neutral wind continuously instead of on a campaign basis. The tidal dynamics in the upper atmosphere could be investigated more extensively and the interaction of atmospheric and *in situ* tides could be studied more closely. Similarly, the available measurements of ionospheric currents will strongly increase and allow the validation of atmosphere-ionosphere models with higher reliability. This could be applied to *Pedersen* currents and the consequent Joule heating as shown in this thesis as well as to *Hall* currents and the consequent geomagnetic disturbances. Another application of multibeam ISR experiments is to conduct horizontally resolved measurements. With a sufficient number of beams, it might be possible to obtain 3D measurements of TIDs from ISR observations. If it can be shown that these TIDs are induced by atmospheric gravity waves, neutral atmosphere parameters could be inferred from 3D TID observations.

An extension of the Nordic Meteor Radar Cluster by further radar stations would increase the time resolution and altitude range of wind measurements due to a larger number of total meteor detections. Thereby, highly resolved 3D AGW observations would be possible in the mesosphere and lower thermosphere. These could be applied to obtain a database of AGW characteristics and improve empirical AGW parameterizations for space weather predictions. Automated detection and characterization of AGWs could be obtained by replacing the Fourier filter methods applied in this thesis with a 3D S-transform technique. The dual-frequency ISR experiments presented in this thesis will not be possible with the upcoming EISCAT\_3D system since it will include only a single transmitter. During the first measurements of the EISCAT\_3D ISR, there is the possibility of triple-frequency ISR experiments in combination with the EISCAT UHF and VHF radars which will be decommissioned soon after. Such historically unique measurements would allow to validate the difference spectrum method presented in this thesis. Whether the EISCAT Scientific Association will aim for scientific triple-frequency experiments is currently under debate. In the long term, it should be aimed to add a second transmitter to the EISCAT\_3D system to continue and extend the ion-neutral collision frequency measurements.

# Appendix A

## Published Articles

### Determining the Origin of Tidal Oscillations in the Ionospheric Transition Region With EISCAT Radar and Global Simulation Data

#### Bibliographic information

Günzkofer F., Pokhotelov D., Stober G., Liu H., Liu H.-L., Mitchell N. J., Tjulin A., and Borries C. Determining the Origin of Tidal Oscillations in the Ionospheric Transition Region With EISCAT Radar and Global Simulation Data. *Journal of Geophysical Research: Space Physics*, **127**, e2022JA030861, 2022.

DOI: <https://doi.org/10.1029/2022JA030861>

©2022. The Authors.

#### Author's contribution

For this publication, I applied the steady-state ion mobility equation to compute neutral wind velocities from EISCAT measurements of the ion velocity, which were provided by A. Tjulin. I determined tidal phases and amplitudes in the neutral wind measurements by adjusting and applying an Adaptive Spectral Filter software originally written and provided by G. Stober. I performed the same analysis on measurements from the Kiruna meteor radar (provided by N.J. Mitchell) and data from the WACCM-X, GAIA, and TIE-GCM models. WACCM-X data was provided by H.-L. Liu, GAIA data was made available to me by H. Liu and I performed the TIE-GCM models runs using the High-Performance-Data-Analysis Cluster 'Kratos' from the DLR Institute for Data Science in Jena. My work was supervised by D. Pokhotelov, G. Stober, and C. Borries. As the first author, I wrote large parts of the manuscript, but all authors were involved in revising the text.

# JGR Space Physics



## RESEARCH ARTICLE

10.1029/2022JA030861

### Key Points:

- Twenty-day long EISCAT radar campaign shows a complex mixture of semidiurnal and diurnal tidal oscillations
- Three global circulation models show similar tidal structuring and allow to determine the influence of different forcing mechanisms
- Adaptive spectral filtering (ASF) technique allows robust fitting of tidal amplitudes and phases

### Correspondence to:

F. Günzkofer,  
florian.guenzkofer@dlr.de

### Citation:

Günzkofer, F., Pokhotelov, D., Stober, G., Liu, H., Liu, H.-L., Mitchell, N. J., et al. (2022). Determining the origin of tidal oscillations in the ionospheric transition region with EISCAT radar and global simulation data. *Journal of Geophysical Research: Space Physics*, 127, e2022JA030861. <https://doi.org/10.1029/2022JA030861>

Received 18 JUL 2022  
Accepted 15 SEP 2022

## Determining the Origin of Tidal Oscillations in the Ionospheric Transition Region With EISCAT Radar and Global Simulation Data

F. Günzkofer<sup>1</sup> , D. Pokhotelov<sup>1</sup> , G. Stober<sup>2</sup>, H. Liu<sup>3</sup> , H.-L. Liu<sup>4</sup> , N. J. Mitchell<sup>5,6</sup> , A. Tjulin<sup>7</sup> , and C. Borries<sup>1</sup> 

<sup>1</sup>Institute for Solar-Terrestrial Physics, German Aerospace Center (DLR), Neustrelitz, Germany, <sup>2</sup>Institute of Applied Physics & Oeschger Center for Climate Change Research, Microwave Physics, University of Bern, Bern, Switzerland, <sup>3</sup>Department of Earth and Planetary Science, Kyushu University, Fukuoka, Japan, <sup>4</sup>High Altitude Observatory, National Center for Atmospheric Research, Boulder, CO, USA, <sup>5</sup>British Antarctic Survey, Cambridge, UK, <sup>6</sup>Department of Electronic & Electrical Engineering, University of Bath, Bath, UK, <sup>7</sup>EISCAT Scientific Association, Kiruna, Sweden

**Abstract** At high-latitudes, diurnal and semidiurnal variations of temperature and neutral wind velocity can originate both in the lower atmosphere (UV or infrared absorption) and in the thermosphere-ionosphere (ion convection, EUV absorption). Determining the relative impact of different forcing mechanisms gives insight to the vertical coupling in the ionosphere. We analyze measurements from the incoherent scatter radar (ISR) facility operated by the EISCAT Scientific Association. They are complemented by meteor radar data and compared to global circulation models. The amplitudes and phases of tidal oscillations are determined by an adaptive spectral filter (ASF). Measurements indicate the existence of strong semidiurnal oscillations in a two-band structure at altitudes  $\lesssim 110$  and  $\gtrsim 130$  km, respectively. Analysis of several model runs with different input settings suggest the upper band to be forced in situ while the lower band corresponds to upward-propagating tides from the lower atmosphere. This indicates the existence of an unexpectedly strong, in situ forcing mechanism for semidiurnal oscillations in the high-latitude thermosphere. It is shown that the actual transition of tides in the altitude region between 90 and 150 km is more complex than described so far.

**Plain Language Summary** Solar and atmospheric variability influence the ionosphere, causing critical impacts on satellite and ground-based infrastructure. Determining the dominant forcing mechanisms for ionosphere variability is important for prediction and mitigation of these threats. However, this is a challenging task due to the complexity of solar-terrestrial coupling processes. Tidal oscillations (mostly 12 and 24-hr periods) allow for a rough estimations of whether forcing from “above” or “below” dominates. The classical understanding is that 12-hr oscillations propagate upwards from below while 24-hr oscillations are forced at high altitudes. We analyze data from two radar systems and three global ionosphere models and show that the altitude structure of tidal oscillations is in fact more complex than classically assumed.

### 1. Introduction

The ionospheric dynamo region marks the transition from a collision-dominated plasma below approximately 90 km to a nearly collisionless plasma above approximately 150 km. Across this transition region, ion/electron gyrofrequencies  $\Omega_{i/e}$  are of the same order as collision frequencies  $\nu_{in/en}$ . Therefore, Pedersen and Hall conductivities maximize at these altitudes. Pedersen and Hall currents perpendicular to the magnetic field close the global magnetospheric field-aligned current system. Dynamic processes in the transition region can be forced either from “above” (plasma convection, in situ absorption of solar irradiance, auroral precipitation, etc.) or from “below” (upward-propagating waves from the lower atmosphere). Determining the actual forcing of specific effects in the transition region will help understanding the complex solar-terrestrial coupling processes.

One parameter to quantify the respective impact of atmospheric and solar effects are tidal neutral wind oscillations. The largest amplitudes can be expected for diurnal (24 hr period) and semidiurnal (12 hr period) variations. Upward-propagating atmospheric tides of both periods are mostly forced due to UV absorption by stratospheric ozone and infrared absorption by tropospheric water vapor. The classical tidal theory (Andrews et al., 1987; Lindzen, 1979; Oberheide et al., 2011) suggests the semidiurnal atmospheric tides to dominate at latitudes above approximately 45°. However, predominantly diurnal wind oscillation forced by EUV absorption at high altitudes

©2022. The Authors.

This is an open access article under the terms of the [Creative Commons Attribution License](https://creativecommons.org/licenses/by/4.0/), which permits use, distribution and reproduction in any medium, provided the original work is properly cited.

are expected to increase at high-latitudes (Straus et al., 1975). In the same region, the reconnection between the Earth's magnetic field and the interplanetary magnetic field leads to a large-scale plasma convection pattern (see e.g., Kelly, 2009). From the frame of reference of a local observer, this is perceived as 24-hr oscillation of ion velocities. This motion is transferred to the neutral particles via ion drag and frictional heating. It is classically assumed that there is a transition from dominant 12 hr to dominant 24 hr oscillation regimes at approximately 110–120 km altitude (Andrews et al., 1987) which has also been observed (Nozawa et al., 2010). However, there has been evidence for nonnegligible semidiurnal oscillations as far up as approximately 250 km (Lee et al., 2018; Schunk & Nagy, 2009; Wu et al., 2017). Whether these 12 hr oscillations are forced by atmospheric tides propagating up into the F-region or in situ generated oscillations remained an open question. One problem here is a general lack of continuous measurements in the region from 120 to 250 km.

We employ two well-established observation techniques to measure neutral wind velocities across the mesosphere-lower-thermosphere region: meteor radars and incoherent scatter radar (ISR). While meteor radars are restricted in altitude coverage by meteor trail occurrence, ISR can in principle cover the whole range from the mesopause well into the thermosphere. The actual altitude coverage, however, depends on the experiment mode and can therefore be limited. In this paper, we leverage the co-located Nordic Meteor Radar Network to validate the EISCAT neutral wind measurements. Based on the combined neutral wind data set, we estimated 12 and 24 hr oscillations at altitudes between 80 and 142 km. It has to be considered that local measurements do not provide information on the zonal wave number to separate migrating (sun-synchronous) and nonmigrating modes. We analyze data from three global ionosphere models (GAIA, WACCM-X, and TIE-GCM) to overcome the limitations of measurements in latitude, longitude, and altitude. This allows to analyze global tidal modes and the variation of amplitudes with latitude. Additionally, it can be investigated how well the amplitude variation over the limited measurement range fits the general structure. Model runs with different geomagnetic, solar, and atmospheric input can be leveraged to compare the impact of the most important forcing mechanisms. Oscillation amplitudes are extracted by applying an adaptive spectral filter (ASF) technique (Stober et al., 2017).

The further structure of the paper is as follows. Section 2 presents the experimental setup and outlines the respective methods of neutral wind measurements and amplitude fitting. The ionosphere models and the specifics of the analyzed runs are briefly introduced in Section 3. Section 4 presents the results from the analysis of measurement data and highlights the most important findings. The analysis and findings from model data are shown in Section 5. Section 6 summarizes the results from both observation and model data analyses and the paper is concluded in Section 7.

## 2. Instruments and Methods

### 2.1. EISCAT Ultra High Frequency Incoherent Scatter Radar

The EISCAT ultra high frequency (UHF) radar at Tromsø (69.6°N, 19.2°E) (Folkestad et al., 1983) is a powerful ISR with about 1.5–2 MW peak power on transmission operating at a frequency of 930 MHz. The system employs a dish with 32 m in diameter resulting in a beam width of about 0.7° corresponding to an antenna directive gain of approximately 48.1 dBi.

In this paper, we analyze UHF EISCAT observations collected during a campaign over more than 20 days in September 2005. This data set presents one of the longest continuous ISR measurements ever performed worldwide. More details on the experiment, data gaps, and data quality throughout the campaign are presented in Nozawa et al. (2010). Here, we make use of the existing data base. The EISCAT UHF radar in Tromsø was operated in the beam swinging mode in which the radar rotates back and forth between four different pointing directions (south, south-east, field aligned, and vertical) (Collis, 1995). The dwell times at the four positions and the rotation times in between result in a total time resolution of approximately 6 min. From the line of sight ion velocities measured at each pointing direction, three dimensional ion velocity vectors can be derived by inverting the radial wind equation (Nygrén et al., 2011). The advantage of beam swinging measurements is that it does not require rotating the dishes of remote receiving sites to obtain vector velocities for several altitudes. However, beam swinging measurement are limited to E-region altitudes, where the four beams have not yet dispersed too far. Three-dimensional ion velocity vectors are calculated for seven altitude gates between 96 and 142 km. An additional gate was obtained with the remote receivers at Kiruna and Sodankylä which were pointed with a fixed elevation to intersect the vertical beam at approximately 300 km altitude. The ion velocity uncertainties originate from the incoherent scatter spectrum fit uncertainties propagated through the geometrical transformation.

## 2.2. Neutral Wind Calculation From ISR Measurements

The procedure of calculating E-region neutral wind velocities  $\mathbf{u}$  from incoherent scatter measurements was described in Brekke et al. (1973). It assumes a steady ion velocity  $\mathbf{v}_i$  due to an equilibrium of Lorentz and ion-neutral friction force. For sufficient altitude resolution, the direct solution of the steady state ion mobility equation can be applied (Rino et al., 1977)

$$\mathbf{u} = \mathbf{v}_i - \frac{\Omega_i}{B\nu_{in}} (\mathbf{E} + \mathbf{v}_i \times \mathbf{B}). \quad (1)$$

Equation 1 requires knowledge of the magnetic field  $\mathbf{B}$ , the ion gyrofrequency  $\Omega_i$ , the ion-neutral collision frequency  $\nu_{in}$ , and the electric field  $\mathbf{E}$ . As magnetic field, the international geomagnetic reference field (IGRF) (Barraclough, 1988) is employed. The ion gyrofrequency is calculated from the magnetic field strength and the mean ion mass  $m_i = 30.5$  amu. The electric field can be calculated at F-region altitudes and assumed to be the same (geometrical effects aside) in the E-region (Brekke et al., 1973; Nozawa & Brekke, 1999; Nozawa et al., 2010). Since ion-neutral collisions can be neglected at higher altitudes, the F-region ion velocity  $\mathbf{v}_{i,F}$  is determined by  $E \times B$ -drifts. The electric field is then calculated as  $\mathbf{E} = -(\mathbf{v}_{i,F} \times \mathbf{B})$  where  $\mathbf{v}_{i,F}$  is obtained from the highest altitude channel at approximately 300 km. The atmospheric forcing from below strongly depends on the altitude dependent ion-neutral collision frequency  $\nu_{in}$ . Commonly, collision frequencies are inferred from a model neutral atmosphere (e.g., MSIS Hedin, 1991) and a collision model which can be either empirical (Chapman, 1956) or analytical (Schunk & Walker, 1973). In this paper, we apply the NRLMSISE-00 model (Picone et al., 2002) and the empirical model for ion-neutral collision frequencies

$$\nu_{in} = 2.6 \cdot 10^{-9} \cdot n_n [\text{cm}^{-3}] \cdot A^{-1/2} [\text{s}^{-1}] \quad (2)$$

described in Chapman (1956); Kelly (2009), with neutral particle density  $n_n$  and  $A = m_i$  [amu]. However, the accuracy of any collision model at altitudes  $\geq 120$  km has to be considered carefully (Nozawa et al., 2010; Williams & Virdi, 1989). A direct measurement of the ion-neutral collision frequencies would be possible with the current EISCAT system due to its multifrequency capability with simultaneous operation of UHF and VHF radars (Grassmann, 1993; Nicolls et al., 2014). However, there were no multifrequency experiments scheduled during the investigated campaign. This could provide an option for further improvement in future investigations.

## 2.3. Meteor Radar

Since the derivation of neutral wind velocities from EISCAT measurements is not as well established, meteor radar measurements can be used as a reference at the lower boundary. In this paper, measurements from EISCAT and the Kiruna meteor radar will be merged to test the validity of the procedure described in the previous section. As an additional advantage, the total observed altitude range is extended significantly downwards.

Meteor radars have become a ubiquitous sensor capable of monitoring winds in the mesosphere and lower thermosphere. These instruments observe small meteoroids, which are formed when extraterrestrial particles with a sufficient kinetic energy enter the Earth's atmosphere. Small meteoroids can penetrate deep into the atmosphere until they encounter a sufficiently dense region. The impinging atmospheric molecules and atoms decelerate and heat the particles to such an extent that the meteoric material is vaporized and atoms are released from the meteoroid. Due to the collisions with the ambient neutral atmosphere the released atoms are thermalized and form an ambipolar diffusing plasma trail, often called a meteor trail. This trail provides a coherent scatter target and allows to measure wind velocities since it drifts with the neutral winds. Specular meteor radars detect most of these trails at altitudes between 70 and 110 km. For a large enough number of meteor trails, horizontal wind velocities can be measured with an "all-sky"-fit (Hocking et al., 2001). This is usually done with a time resolution of 1 hr and 2 km altitude bins.

In Kiruna (67.9°N, 21.1°E), a meteor radar has been continuously operated since 1999 and therefore provides measurement for the time of the EISCAT campaign described above. Meteor radars have been used for the investigation of various types of waves in the upper atmosphere, including atmospheric tides, and provide a well-tested measurement method (Pokhotelov et al., 2018; Stober et al., 2021).

## 2.4. Adaptive Spectral Filtering

The determination of tidal amplitudes and phases is done using the adaptive spectral filtering (ASF) technique (Stober et al., 2017). Thereby, the neutral wind data in zonal and meridional direction is separately fitted for a mean background wind and several periodic components. We apply two separate filters on measurement and model data. A local ASF is used to fit for 24, 12, and 8 hr oscillations in a combined neutral wind data set from ISR and meteor radar measurements. A global ASF is applied on model data which allows to obtain zonal wavenumbers additionally to oscillation periods. The nomenclature of global tidal modes gives information on period (D: diurnal, S: semidiurnal), propagation direction (W: westward, E: eastward) as seen from an observer at a fixed geographic location on Earth and the zonal wavenumber  $k$  (Smith, 2012). While in principle the latter can take any integer value, we will restrict our analysis to  $0 \leq k \leq 3$  since the by far largest amplitudes are expected for the two sun-synchronous, migrating tidal modes DW1 and SW2 (Smith, 2012). Unless otherwise stated, amplitudes in this paper have been averaged over a sliding window of 1 day length. The ASF has shown to be a robust frequency analysis method for unequally spaced data (spatially and temporal). The technique is also reliable for higher relative uncertainties of the fitted data since it takes these uncertainties into account. Due to the fitting of phases, the propagation of nonstationary processes (phase drifts over time) can be estimated similar to holographic analysis (Stober et al., 2020). The robustness of the fitting for short-time windows enables a good resolution of the day-to-day variability of amplitudes compared to other methods. The ASF has been successfully extended and applied to fit for global tidal modes (Baumgarten & Stober, 2019; Stober et al., 2020).

## 3. Models

### 3.1. Ground-To-Topside Model of Atmosphere and Ionosphere for Aeronomy

The Ground-to-Topside Model of Atmosphere and Ionosphere for Aeronomy (GAIA) is a global circulation model (GCM) giving neutral dynamics for all altitudes from the ground up to approximately 600 km (Jin et al., 2012). GAIA data has been compared and verified with experiment data from numerous different apparatuses for time spans up to several decades. The GAIA data set used for the analysis presented in Section 5 has been previously applied for long-term investigations in H. Liu et al. (2017) and Stober et al. (2021). We summarize the most important features and refer to these publications for more detailed information.

The atmosphere up to approximately 30 km altitude is constrained to the JRA-25/55 reanalysis (Kobayashi et al., 2015) using a nudging technique. The measurements used in the reanalysis are listed in Onogi et al. (2007). While the solar irradiance, and thereby EUV absorption, is parametrized with the F10.7 index, the geomagnetic activity is set to a constant value. Therefore, the cross polar potential is held at 30 kV for all model data, corresponding to a moderate level of geomagnetic activity. The neutral wind components are provided on a grid with a resolution of  $1^\circ$  in latitude and  $2.5^\circ$  in longitude. The altitude resolution is  $1/5$  of the respective scale height at each altitude. The analysis presented in this paper has been conducted with preprocessed files giving the data in 10 km altitude bins. The time resolution is 0.5 hr.

### 3.2. Whole Atmosphere Community Climate Model Extension (SD)

The Community Earth System Model is a combination of models covering different parts of the Earth system (Hurrell et al., 2013). The Whole Atmosphere Community Climate Model Extension WACCM-X (H.-L. Liu et al., 2018) is the part of the CESM describing the atmosphere from the ground up to  $\gtrsim 500$  km. The data presented in this paper was generated with a Special Dynamics run WACCM-X(SD) (Gasparini et al., 2020) and previously used in Stober et al. (2021). Again, we only give a brief overview and refer to the mentioned publications.

The lower atmosphere is constrained up to approximately 50 km to NASA's reanalysis MERRA (Gelaro et al., 2017; Rienecker et al., 2011). Other than the analyzed GAIA run, WACCM-X(SD) does not set a fixed cross polar potential. The polar convection is calculated using the *Heelis* model (Heelis et al., 1982) and the geomagnetic activity is therefore parametrized by the Kp index. As proxy for EUV absorption, WACCM-X also utilizes the F10.7 index. The longitudinal resolution is  $2.5^\circ$  and values are given in 3 hr intervals. Since the model is evaluated on hydrostatic pressure levels, the altitude range extends from 992.5 hPa near the ground up to approximately  $4 \cdot 10^{-10}$  hPa. The height resolution above approximately 50 km is  $1/4$  of the respective scale height. The corresponding geopotential altitudes are given for each time and position and extend roughly from the ground up to approximately 500 km. In the transition region, the geopotential height resolution varies between 1

and 5 km. The different parametrization of geomagnetic activity in the analyzed GAIA and WACCM-X runs are ideal to investigate its influence on neutral winds at different altitudes. However, since both models extend to the ground and are restrained to reanalysis of meteorological data (Stober et al., 2021), it is not feasible to separate the impacts of atmospheric forcing in these models.

### 3.3. Thermosphere Ionosphere Electrodynamic General Circulation Model

The Thermosphere Ionosphere Electrodynamic General Circulation Model (TIE-GCM) (Richmond et al., 1992) is a standalone ionosphere model and also part of the Coupled Magnetosphere-Ionosphere-Thermosphere Model (Qian et al., 2014). The data presented in this paper was generated from several runs performed with the TIE-GCM Model Version 2.0.

In contrast to the two models described above, TIE-GCM does not extend down to the ground, but applies a lower boundary condition at approximately 99 km altitude. The horizontal neutral winds and neutral temperatures at the boundary are specified by input files. These quantities include the monthly averaged amplitudes and phases of diurnal and semidiurnal tides which are by default given by the Global Scale Wave Model (GSWM) (Hagan & Forbes, 2002, 2003). For the present paper, the GSWM boundary data has been modified to give the tidal measurements from the Kiruna meteor radar for the investigated time. Performing separate runs with empirical tidal input and with zero tidal input allows to assess the impact of atmospheric dynamics and the forcing from below. Same as for WACCM-X, the *Heelis* model is applied to obtain the cross polar potentials and geomagnetic activity is parametrized according to the Heelis parametrization (Heelis et al., 1982). While per default solar irradiance is parametrized by the F10.7 index, we conduct an additional run with a fixed F10.7 index of 70 to identify the impact of EUV absorption. TIE-GCM gives output data on a  $2.5^\circ \times 2.5^\circ$  grid with a time resolution of 1 hr. Furthermore, TIE-GCM data is provided on logarithmic altitude coordinates (atmospheric ln pressure coordinate)  $\ln\left(\frac{p_0}{p}\right)$  for the pressure  $p$  at a certain altitude. The reference pressure  $p_0 = 5 \cdot 10^{-5}$  hPa corresponds roughly to approximately 225 km altitude and the atmospheric ln pressure coordinate ranges from  $-6.875$  to  $7.125$  in  $0.25$  increments. This corresponds to a resolution of  $1/4$  in scale height units. The geopotential altitude ranges from approximately 96 to 590 km with a resolution that steadily increases from approximately 2 to 18 km with increasing height.

## 4. Experiment Data

This section will give an overview on the results from analysis of experimental data obtained with the instruments presented in Section 2.

### 4.1. Neutral Wind

As described in Section 2.1, the four line of sight ion velocities measured were geometrically transformed to a geographic reference frame. From those, the steady state ion equation was applied to obtain neutral wind vectors. Figure 1 shows the calculated neutral winds in zonal and meridional directions for the measurement channel at 115 km altitude.

Error bars shown in Figure 1 are calculated from the ion velocity measurement uncertainties by propagation of uncertainty through the whole procedure described in Section 2.2. Uncertainties of the ion-neutral collision frequency, which can have a major impact (Williams & Virdi, 1989), are not shown. While the relative uncertainties at altitudes  $\geq 110$  km are reasonably small ( $\leq 40\%$ ), they tend to increase with decreasing altitudes ( $\leq 70\%$ ). The lower electron density results in smaller signal-to-noise ratios and consequently leads to increased statistical uncertainties in the derived incoherent scatter spectrum parameters. Neutral wind velocities calculated from EISCAT measurements at low altitudes should therefore be treated carefully when looking at absolute values. The determination of tidal oscillation amplitudes is still possible with reasonable accuracy due to the robustness of the ASF technique (see Section 2.4). The strong outliers at single timepoints (around day 19) and data gaps (around day 21) visible in Figure 1 are most likely caused by problems with the radar system and can also be handled by the ASF method.

The diurnal and semidiurnal amplitudes are determined separately for each altitude level. Figure 2 shows the amplitudes of tidal oscillations measured by the Kiruna meteor radar ( $80 \text{ km} \leq h \leq 104 \text{ km}$ ) and the EISCAT UHF in Tromsø ( $96 \text{ km} \leq h \leq 142 \text{ km}$ ). To see possible correlations, indices for geomagnetic activity and solar

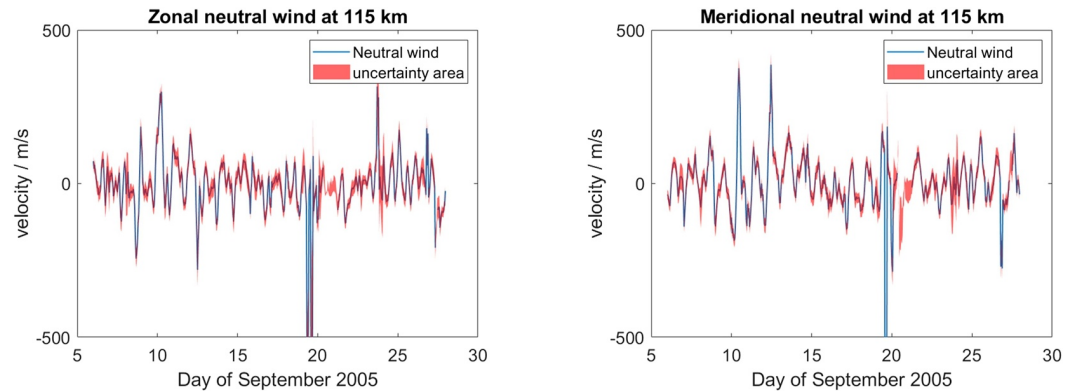


**Figure 1.** Neutral winds at 115 km altitude in zonal (left) and meridional (right) direction measured with the EISCAT radar. The uncertainty has been determined from the measurement uncertainty by means of Gaussian error propagation.

irradiance during the time of the measurement campaign are also shown in Figure 2. The geomagnetic activity is quantified by the Kp index since it is often used to parametrize polar plasma convection. The F10.7 index is used to quantify solar activity and EUV absorption.

Figure 2 shows the merged amplitudes of both systems and includes the transition altitude between both instruments at about 100 km. Additionally, the graphic indicates the presence of a data gap around September 21st for the EISCAT observations, whereas the meteor radar wind time series remains uninterrupted during the entire period. To compare the measurements in the overlap region, the wind velocities caused by tidal oscillations are calculated from the fitted amplitudes and phases. The tidal winds averaged across the coverage overlap of both instruments show moderate correlation ( $R = 0.54$ ). It should be noted that the overlap is at the edge of cover-

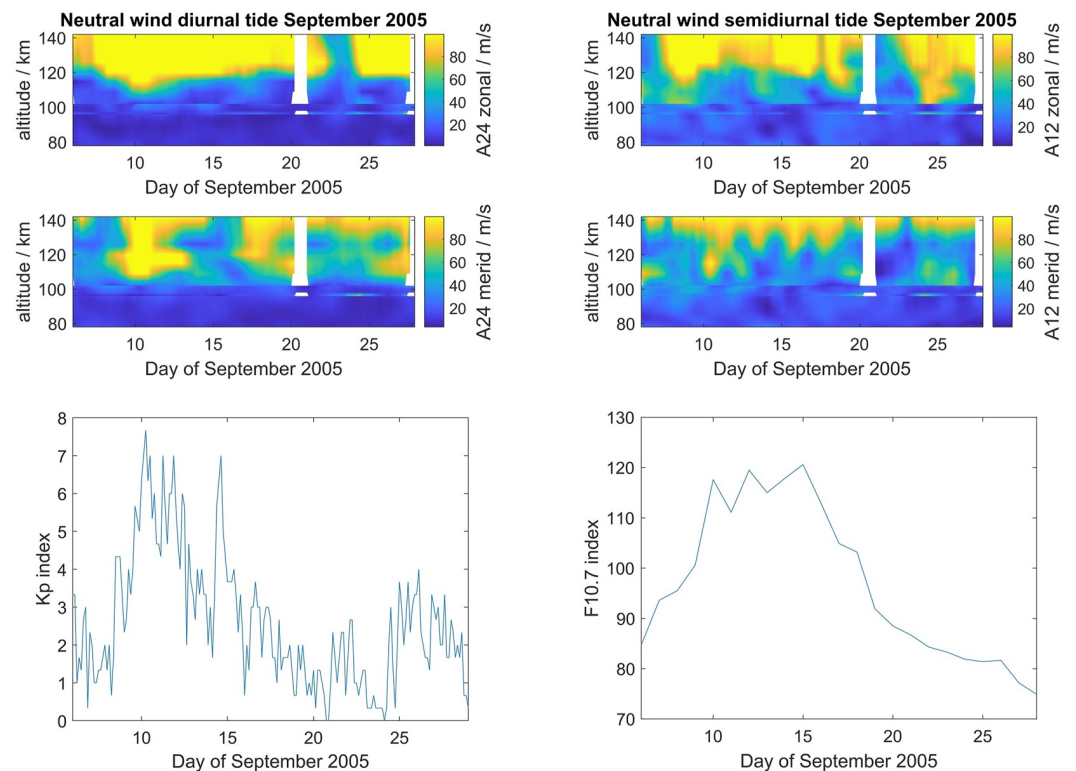


**Figure 2.** Top: the amplitudes of diurnal (left) and semidiurnal (right) oscillations in zonal (top) and meridional (bottom) direction during September 2005. Data from EISCAT and meteor radar are merged together. Bottom: the geomagnetic activity (Kp index, left) and the solar irradiance (F10.7 index, right) during the measurement time.

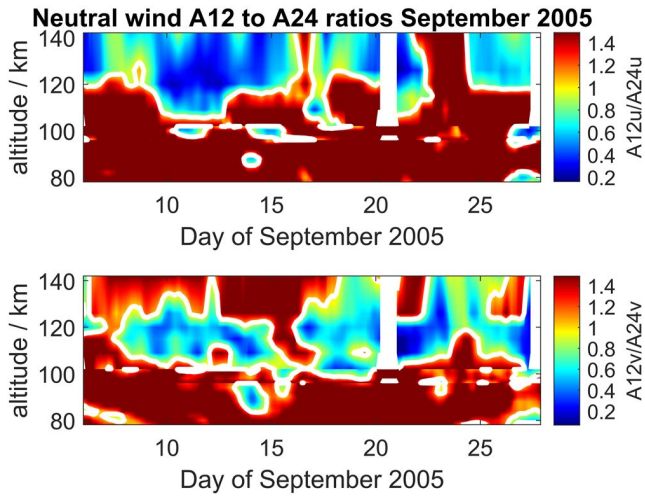


**Figure 3.** Ratio of semidiurnal to diurnal amplitudes in zonal (top) and meridional (bottom) neutral winds. The meridional component shows a two-band structure of dominant semidiurnal oscillations.

age of both systems where the respective uncertainties are increased. Therefore deviations of ISR and meteor radar measurements have to be expected. Considering these mitigating circumstances, the EISCAT neutral winds calculated with the procedure from Section 2.2 are validated.

While the amplitudes of both tidal modes generally increase with altitude, it can be seen that there are differences regarding altitudinal structure and time variability.

The next step is the determination of the dominant tidal mode at each time and altitude. Therefore, the amplitude ratio of semidiurnal to diurnal oscillations is calculated and shown in Figure 3.

The ratio of zonal amplitudes  $A_{12u}/A_{24u}$  in the upper plot of Figure 3 corresponds very much to what is expected from the classical tidal picture (Lindzen, 1979). Semidiurnal variations are predominant up to altitudes of approximately 110–120 km. Above that, diurnal oscillations have larger amplitudes most of the time. Meridional tidal amplitudes, on the other hand, show a distinctly different altitudinal structure. While the transition from predominant semidiurnal to diurnal tide also takes place at and around 110 km altitude, there is an upper band of strong semidiurnal oscillations especially during the first half of September. This apparent weakening of the upper 12 hr

band around equinox is an important feature since atmospherically forced semidiurnal tides have been shown to undergo such an autumn transition (Pedatella et al., 2021). Whether this upper band is generated in situ or forced by some atmospheric tidal mode that propagates unusually far up remains to be investigated in more detail.

#### 4.2. Phase Progression Analysis

As described, the ASF technique also allows to extract the phase of tidal oscillations which can be used to distinguish propagating and evanescent tidal modes. The time of maximum should be steadily shifted with altitude for an upward-propagating oscillation, showing as a swift change of phase. An evanescent tidal mode would result in a constant phase with altitude. A rapid transition from steadily shifted to constant phase would therefore suggest a transition of forcing mechanism. However, the phase of a propagating mode also asymptotes toward a constant value at higher altitudes which makes the distinction nontrivial. Figure 4 shows the phase of diurnal and semidiurnal oscillations obtained from ASF analysis of the combined EISCAT and meteor radar data set. Altitude profiles of the semidiurnal tide phases at an example time are shown as well.

The phases of diurnal and semidiurnal oscillations in Figure 4 show a complex mixing of tidal modes, since migrating and nonmigrating modes cannot be distinguished from local measurements. However, while there is a lot of dynamics in the tidal phases throughout the month, the classically expected structure can be seen when looking at the median over the entire measurement time. The median altitude profiles of semidiurnal phases in the zonal and meridional wind are shown in the bottom left corner of Figure 4. The phases show a steady shift in the time of maximum up to altitudes of approximately 110–120 km. Above that, the phase progression seems to stop or even reverse. This transition can be seen more clearly at specifically chosen timepoints, one of which is shown in the bottom right corner of Figure 4. The transition to a nearly constant phase seems to happen rapidly, especially in the meridional winds, indicating a transition from propagating to in situ tidal modes. However, due to the aforementioned asymptoting of the phases of propagating tidal modes, in situ generation of the high altitude semidiurnal oscillations cannot be conclusively confirmed from the altitude-phase plot alone.

#### 4.3. High Altitude ion Velocities

E-region neutral winds are inferred from the ion velocity observations of EISCAT. The ion velocities at approximately 300 km altitude allow to estimate the convection electric field required in Equation 1. If 12 hr oscillations of the neutral wind are forced by plasma convection at high altitudes, ion velocities at 300 km altitude should also exhibit significant semidiurnal amplitudes. Diurnal and semidiurnal amplitudes are determined by the same ASF applied on the neutral wind data and shown in Figure 5.

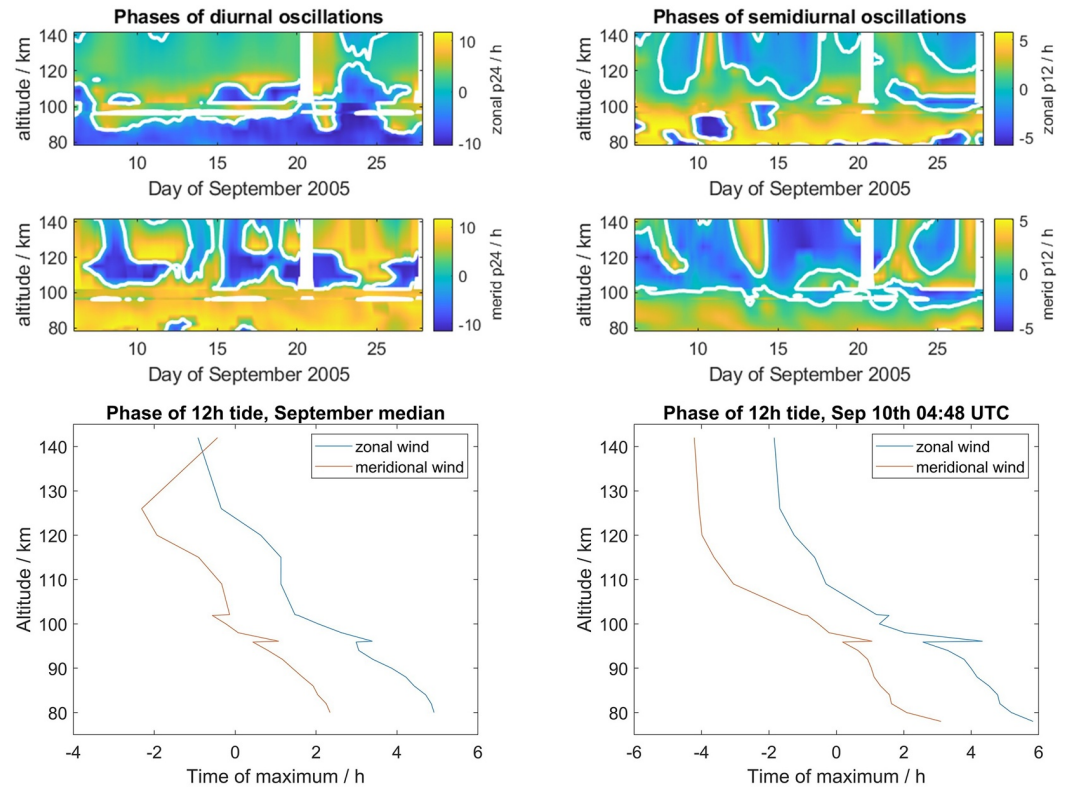


**Figure 4.** Top: phases of diurnal and semidiurnal oscillations obtained from a combined EISCAT and meteor radar neutral wind data set. Bottom: altitude profiles of 12 hr tide phases as median over the whole measurement time (left) and at an exemplary time (right).

The ion velocity oscillation amplitudes in Figure 5 show a general trend similar to the geomagnetic activity index plotted in Figure 2. The polar plasma convection is expected to be perceived as a diurnal oscillation of ion velocity by a local observer. Consequently, diurnal amplitudes are clearly larger than semidiurnal amplitudes. However, there are significant 12 hr oscillation amplitudes sometimes even exceeding 50% of the 24 hr amplitudes. A possible explanation for a perceived semidiurnal periodicity of the polar plasma convection might be an irregular shaped convection pattern.

The semidiurnal component of the polar plasma convection provides one possible interpretation for the neutral wind tidal oscillations shown in Figure 3. However, this cannot be definitely determined from the available

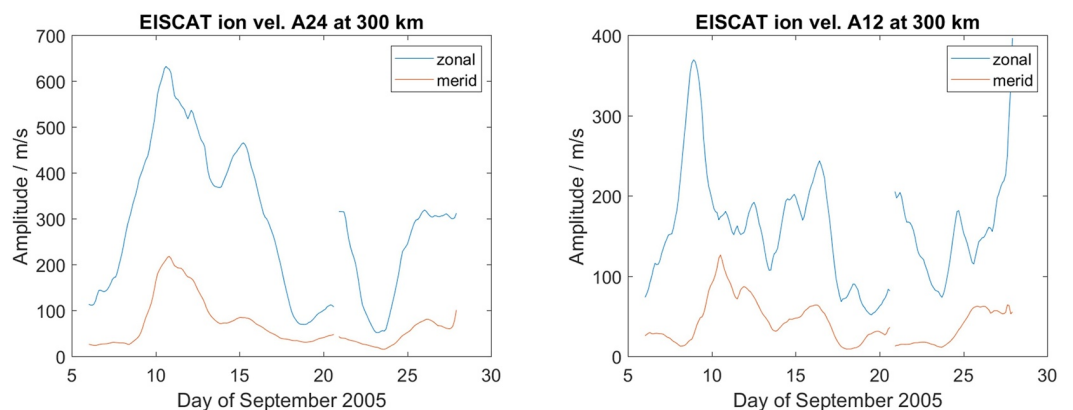


**Figure 5.** Diurnal (left) and semidiurnal (right) amplitudes in the ion velocities from the F-region altitude channel measured with EISCAT.

measurement data. Global ionosphere models can give additional insight in longitudinal wavenumbers of the observed tidal modes. Also, a possible variation of oscillation amplitude with latitude could be determined from model data. Such a variation would be expected in case the forcing mechanism is a high-latitude effect like polar plasma convection.

## 5. Model Data

This section will give an overview on the results from analysis of global simulation data with the models presented in Section 3.

### 5.1. Neutral Wind

GCMs provide neutral wind velocities on a global longitude and latitude grid. The model data is analyzed for the period from day 200–320 (19 July to 16 November) of the year 2005. The plots in this section are restricted to the days of the EISCAT measurement campaign to allow a direct comparison of the dynamics over these days. However, since the main interest of this work is to investigate the altitudinal structure of tidal oscillations, an altitude range from 80 to 300 km will be shown. The neutral wind velocities are analyzed at two latitudes, one of them corresponding to the measurement position in Tromsø, the other one for comparison at mid-latitudes (44°N). The GCM longitudinal resolution is 2.5° in all models.

As described in Section 1, the model data is not only fitted for the time period of neutral wind oscillations but also for zonal wave numbers  $0 \leq k \leq 3$  by the ASF. The amplitudes of each tidal mode were evaluated at 20°E longitude to ensure that a comparison with the observations is meaningful. As expected, the clearly dominating tidal modes for both diurnal and semidiurnal oscillations are the sun-synchronous migrating modes DW1 and SW2. Therefore, we only present the obtained amplitudes for these modes. To investigate the impact of forcing from below, TIE-GCM runs with different lower boundaries are compared. A third TIE-GCM run with constant low solar input is conducted to show the impact of EUV absorption.

#### 5.1.1. Impact of Geomagnetic Activity (GAIA and WACCM-X(SD))

As described in Section 3, the analyzed GAIA run applies a constant cross polar potential, corresponding to a low geomagnetic activity. The impact of geomagnetic activity will be determined by comparison to the WACCM-X(SD) run, for which plasma convection was parametrized with the Kp index. Additionally, we compare tidal amplitudes for both models at high and mid-latitudes to show the impact of high-latitude effects. Figure 6 shows the amplitudes of DW1 and SW2 oscillations obtained from GAIA and WACCM-X(SD) data evaluated at the Tromsø geographical position. To ensure comparability between data from model runs with different forcing or evaluated at different latitudes, the color scale is kept the same for all view graphs.

Semidiurnal amplitudes of zonal and meridional wind component show a pronounced maximum at or slightly above approximately 100 km altitude in both models. According to classical tidal theory, this is associated with upward-propagating atmospheric tides. The amplitude of vertically propagating tides is supposed to show an exponential growth up to the altitude at which molecular dissipation damps it, presumably somewhere between 100 and 130 km (Truskowski et al., 2014). At higher altitudes, the amplitude depends on the region and strength of in situ forcing mechanisms. At higher altitudes  $\geq 130$  km, there are distinct differences between the two models and also between zonal and meridional wind component. GAIA shows an upper band of strong semidiurnal amplitudes but only in the meridional and not in the zonal component. This asymmetry between zonal and meridional component agrees well with what has been detected in the EISCAT data (see Figure 3). The WACCM-X(SD) run also shows more than one region of strong 12 hr oscillations, though the altitude structure of this regions is more complicated than in the GAIA run. Also, the asymmetry between zonal and meridional component is not as pronounced as in GAIA. This might both be caused by the parametrization of geomagnetic activity and consequently different size, shape, and intensity of the plasma convection pattern. This can also be seen in the diurnal oscillation amplitudes where both models show large amplitudes in the meridional component at high altitudes. However, WACCM-X(SD) gives larger amplitudes and there are major differences between the models with regard to the zonal component.

It can be seen that both models give a complex structuring of SW2 oscillations, especially the existence of large amplitudes at high altitudes. Though there are distinct differences between both models, these might be caused

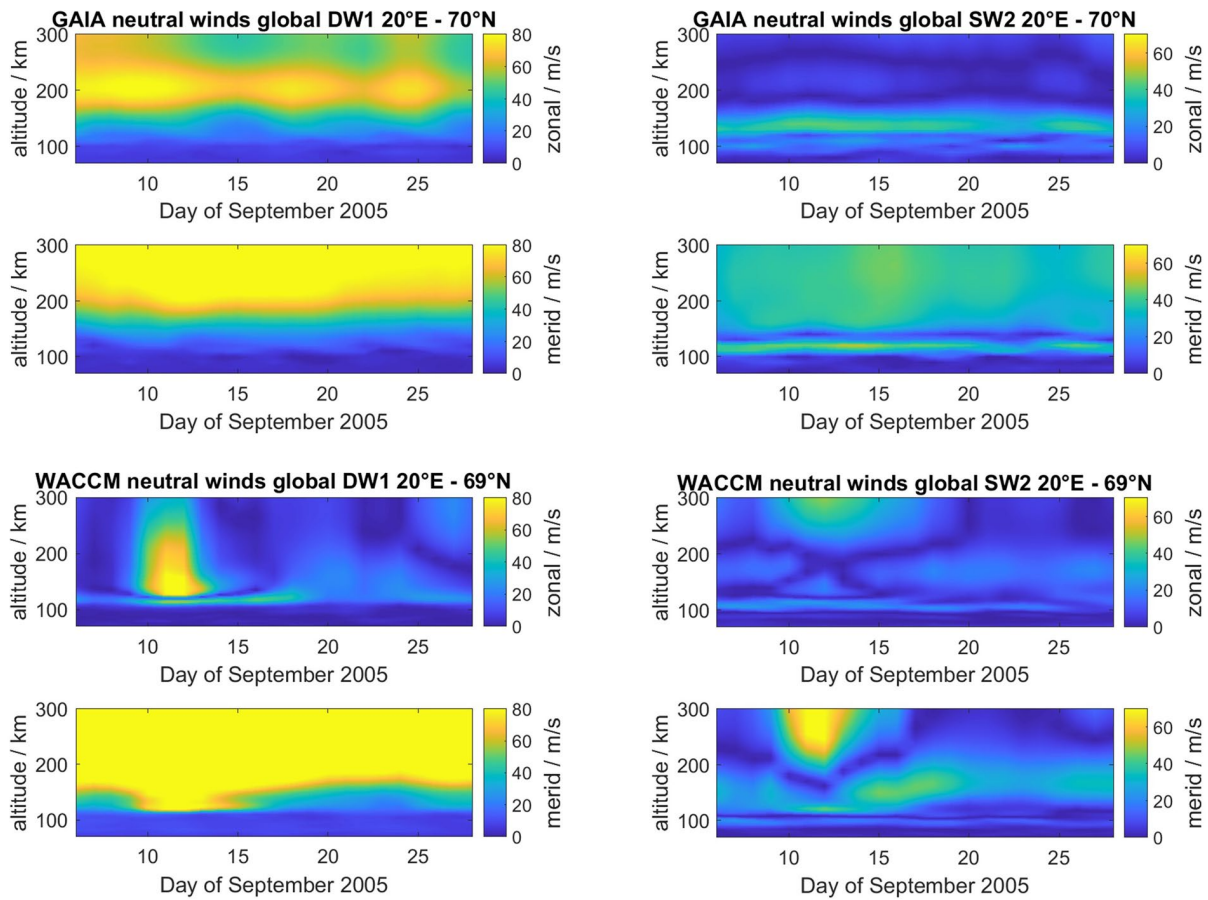


**Figure 6.** Comparison of GAIA (top) and WACCM-X(SD) (bottom) amplitudes of the DW1 (left) and SW2 (right) tidal modes at high-latitudes (70°N).

by the different parametrization of geomagnetic activity. A forcing of both DW1 and SW2 oscillations by polar plasma convection seems to provide a possible explanation of the observed results. However, other in situ forcing mechanisms need to be considered as well as the possibility that atmospheric tides interact with the in situ forced modes.

Polar plasma convection only impacts the high-latitude region and therefore any convection forced oscillations would not be present at mid- or low-latitudes. Evaluating model tidal amplitudes at mid-latitudes therefore allows to narrow down the possible forcing mechanisms. Figure 7 shows the amplitudes of the same tidal oscillation modes as Figure 6 but at 44°N latitude.

The diurnal amplitudes in zonal and meridional neutral winds are decreased in both models at all altitudes. There clearly is a strong high-latitude forcing mechanism of tidal oscillations at high altitudes. However, GAIA and WACCM-X(SD) show significantly different structures of diurnal oscillations.

The SW2 oscillation maximum at approximately 110 km associated with upward-propagating tides is also visible at mid-latitudes, providing confidence to our previous interpretation. The SW2 amplitudes at high altitudes, on the other hand, are significantly reduced. This suggests that there is a strong forcing mechanism of high altitude SW2 oscillations at high-latitudes. However, it also shows that there is likely not only one single forcing mechanism. The complex structuring of tidal oscillations at high altitudes is therefore presumably caused by the varying forcing strength and interference of several mechanisms. However, the main interest of this paper is to determine the mechanism causing the large amplitudes of high altitude SW2 oscillations at high-latitudes. While the strong 12 hr oscillations of EISCAT ion velocities at high altitudes as well as the asymmetry of zonal and meridional wind component seem to indicate polar plasma convection as one possible mechanism, the impact of propagating atmospheric and EUV-forced tides might be just as large.

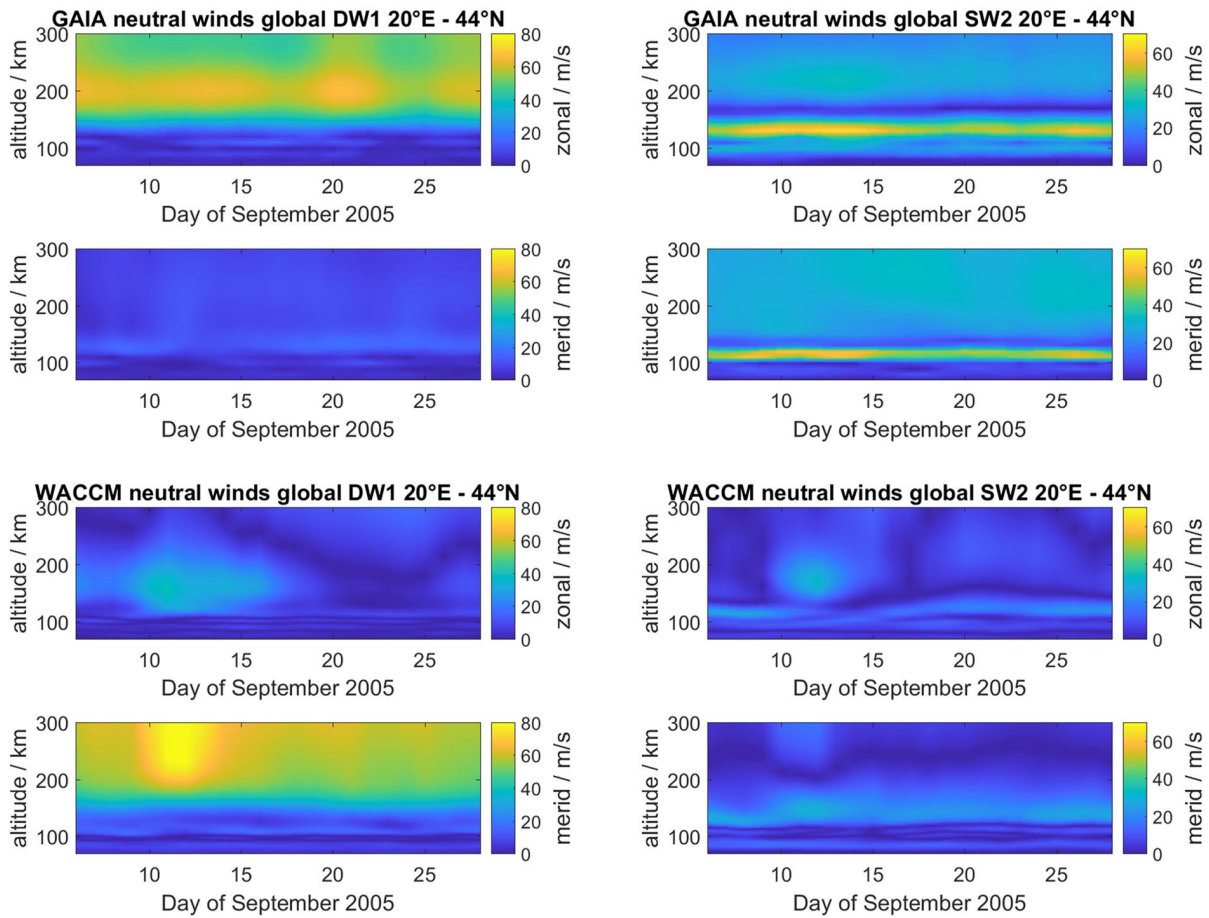


**Figure 7.** Comparison of GAIA (top) and WACCM-X(SD) (bottom) amplitudes of the DW1 (left) and SW2 (right) tidal modes at mid-latitudes (44°N).

### 5.1.2. Impact of Atmospheric Forcing (TIE-GCM)

Comprehensive models such as GAIA and WACCM-X involve complex processes, which have to be parametrized posing challenges to conduct and investigate more isolated processes. TIE-GCM offers the possibility to investigate the ionosphere and thermosphere by applying a well-defined lower boundary condition describing the middle atmospheric forcing. Figure 8 shows the results of two different model runs, one performed using an empirical input for tidal oscillations at 99 km and one with tidal amplitudes set to zero at the boundary. The dominance of sun-synchronous tidal modes is found in TIE-GCM as well and the dynamics of DW1 oscillations is similar to what has been found in the WACCM-X(SD) data. Therefore, further investigations are restricted to SW2 oscillations for the TIE-GCM model runs. As in the previous section, tidal amplitudes are evaluated at high- and mid-latitude.

At high-latitudes, the TIE-GCM run with empirical tidal forcing exhibits a similar SW2 amplitude structure as the ones shown in Figure 6 from GAIA and WACCM-X(SD). This run indicates a two band structure accompanied by a transition of the upper band around the autumn equinox. From the radar phase measurements in Figure 4 we assumed that the lower band is forced by upward-propagating tide, which is confirmed by the TIE-GCM run with zero tidal input at the boundary. In this run, shown on the right side of Figure 8, the lower band mostly vanishes, whereas the upper band appears to be not affected. This seems to exclude lower atmospheric forcing as origin of the upper SW2 band structure. At mid-latitudes, we obtain a similar picture as already found in Figure 7, showing a notably reduced SW2 amplitude at high altitudes and a nearly unaffected amplitude at lower altitudes. Most interestingly here, the high altitude SW2 oscillations seem to be partly forced by the propagating tides from the middle atmosphere since they are significantly reduced in the run with zero tidal forcing at the lower boundary. So while there clearly is strong in situ forcing of SW2 oscillations, upward-propagating atmospheric tides cannot

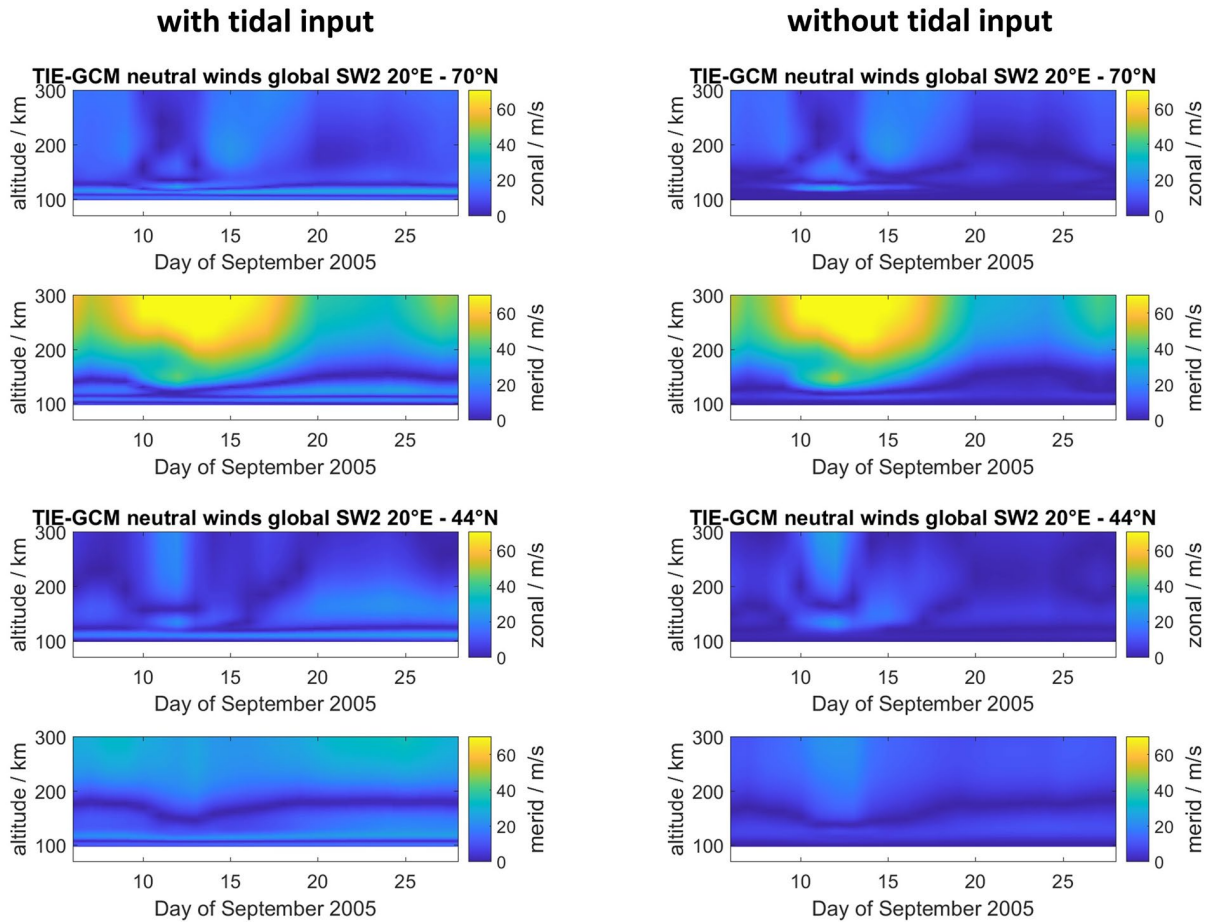


**Figure 8.** Amplitudes of SW2 tidal oscillation from the TIE-GCM model at high- (up) and mid-latitudes (bottom). Presented are two separate runs with imposed (left) and zero (right) atmospheric tidal input.

be completely neglected. Especially the interference of in situ and propagating modes is likely a reason for the complex structure of tidal oscillations. As for the in situ forcing mechanism, it should be noted that tidal oscillations forced by EUV absorption above the lower boundary are still present in TIE-GCM. The impact of EUV absorption is studied with an additional TIE-GCM run.

### 5.1.3. Impact of EUV Absorption

A TIE-GCM run with fixed daily  $F_{10.7} = 70$  and 81-day-averaged  $F_{10.7a} = 70$  as EUV-proxy has been conducted. In comparison with the actual  $F_{10.7}$  values in Figure 2 it can be seen that this corresponds to low EUV irradiance. As tidal input at the boundary, the same settings as for the run shown on the left side of Figure 8 have been applied. Figure 9 shows the SW2 oscillation amplitudes obtained from this new run, as before evaluated at high- and mid-latitudes.

It can be seen in Figure 9 that with a fixed, low EUV irradiance, the high altitude oscillation amplitudes are significantly reduced. Especially between the 10th and 15th of September, where the actual  $F_{10.7}$  index maximized (see Figure 2), there is a visible reduction of tidal amplitudes at  $\geq 180$  km altitude, both at high- and mid-latitudes. As expected from theory (Straus et al., 1975), the tidal amplitudes from EUV forcing seem to be larger at high-latitudes. It has to be considered that even for low  $F_{10.7}$  values there still is a gradient in EUV absorption between day and night side. Therefore tidal oscillations forced by EUV absorption are still present with reduced amplitude. The extension of the upper SW2 band to altitudes  $\lesssim 180$  km seems to remain the same for low EUV absorption. Also, there still is considerable dynamics of the high altitude oscillations. This makes a second in situ forcing mechanism, like polar plasma convection, a more likely explanation than the reduced and constant amplitudes due to EUV absorption gradients.

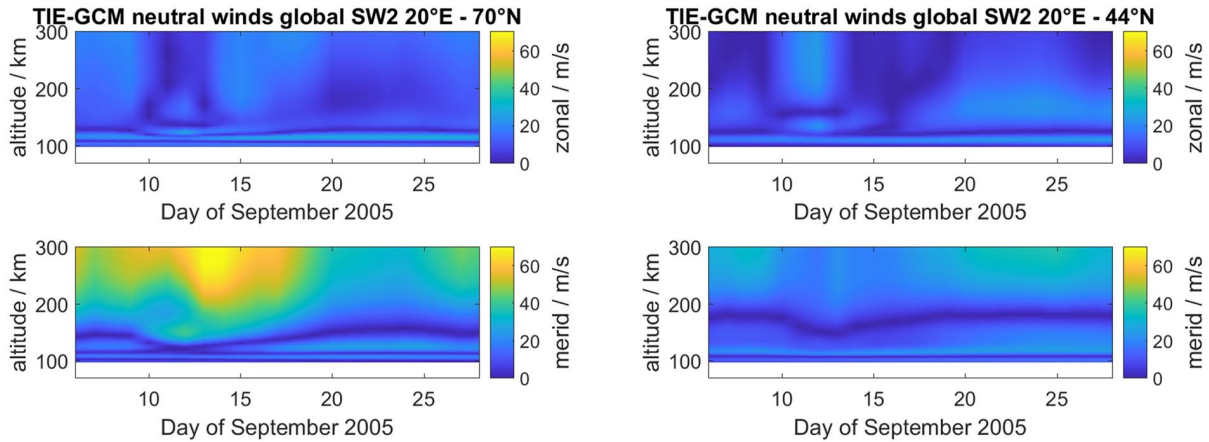


Figure 9. SW2 oscillations from a separate TIE-GCM run with fixed F10.7 and F10.7a values. Amplitudes are shown at high- (left) and mid-latitudes (right).

### 5.2. Phase Progression Analysis

As discussed in Section 4.2, propagating and evanescent tidal modes can be distinguished, to some extent, by means of phase progression analysis. Semidiurnal oscillations observed in EISCAT data below 120 km have been identified to correspond to upward-propagating atmospheric tides (Nozawa et al., 2010) (see also Section 4.2). To extend the altitude coverage into the F-layer at mid- and polar-latitudes, the phases of tidal oscillations in global models have been analyzed. Figure 10 shows the time of maximum of the SW2 tidal mode in the meridional winds extracted from GAIA and WACCM-X(SD) at 70°N latitude. To emphasize the autumn transition seen in the oscillation amplitudes, the whole range of model data from day 200 to day 320 is shown here. We also show the vertical phase profile of 12 hr oscillations as given by GSWM for September, where only upward-propagating and no in situ forced tides are included.

GAIA and WACCM-X(SD) show a steady phase progression at low altitudes and nearly constant phase at higher altitudes. Other than that, the SW2 phase is distinctly different in both models. However, the different forcings like gravity wave parametrization, reanalysis and cross polar potential can in principle all cause differences in phases between the two models. A nearly constant phase at high altitudes could be found for a propagating mode

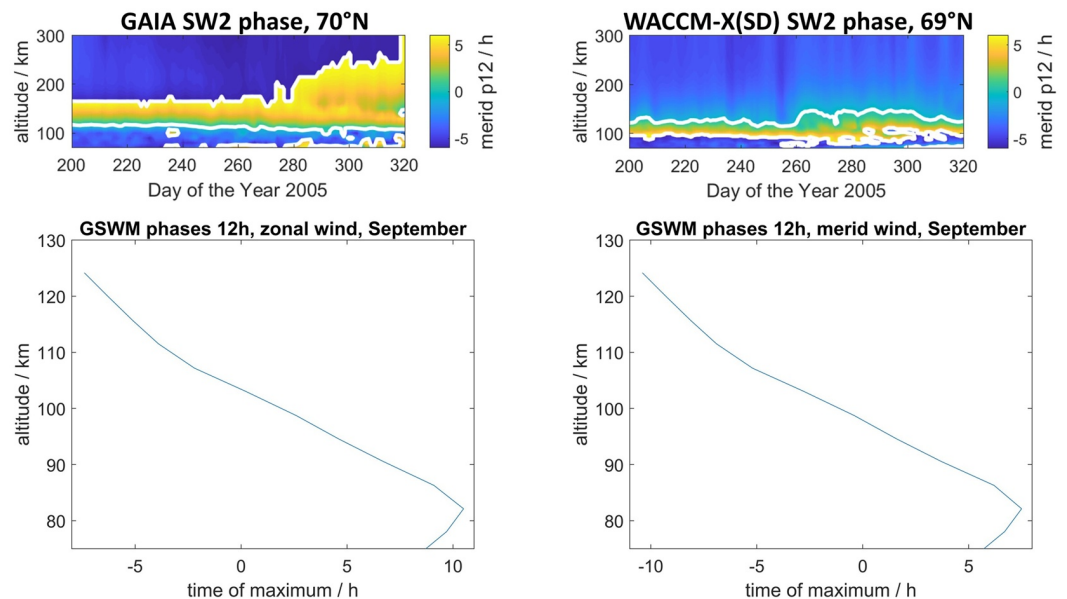
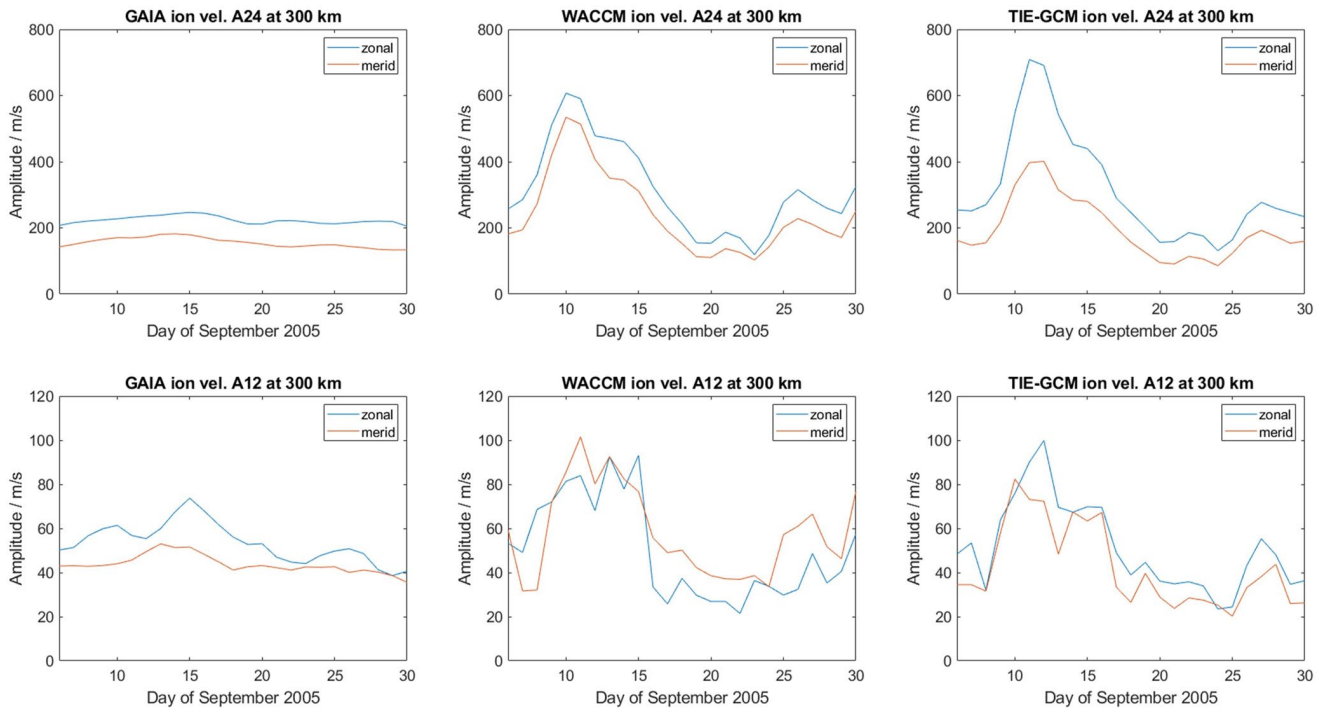


Figure 10. Top: Phases of the SW2 tidal mode in GAIA (left) and WACCM-X(SD) (right) at high-latitudes. Bottom: Phases of the 12 hr tide in zonal (left) and meridional (right) winds from GSWM at 69°N in September.



**Figure 11.** Diurnal (top) and semidiurnal (bottom) high altitude ion velocity amplitudes from GAIA, WACCM-X(SD), and TIE-GCM (left to right).

that asymptotes to constant phase as well as an evanescent tidal mode. This can be partly studied with the GSWM, since it does not include any in situ forcing. Consequently the GSWM phases show a steady phase progression similar to what is found at  $\lesssim 120$  km in measurements (see Figure 4). A slight deceleration of the phase progression can be seen at the highest GSWM altitudes (approximately 124 km) but no rapid transition as it has been found in Figure 4. This indicates that the phase transition found in measurements and models is caused by in situ forcing. However, it should be noted that GSWM phase gradients have been found to deviate notably from measurements at high-latitudes (Manson et al., 2002) and should therefore be considered with caution.

While the constant phase at high altitude is not a definite proof, it fits the previous conclusion that the lower SW2 band is caused by upward-propagating atmospheric tides and the upper SW2 band is in situ forced. Whether propagating and evanescent tidal modes are completely separated by altitude or overlap and interfere cannot be determined definitely. However, the sudden transition around equinox (DOY 265) that is visible in the phases, especially from GAIA data at high-latitudes, could be caused by interference of several tidal modes. Since it is known that atmospheric SW2 tides undergo a transition at that time of year (Pedatella et al., 2021), the interference of atmospheric and in situ tidal oscillations might be responsible for the observed autumn transition at high altitudes. Different in situ forced tidal modes cannot be separated from looking at the phases and the interaction of tidal modes can only be presumed. However, phase progression analysis is a helpful technique to quantify the respective influence of geomagnetic and atmospheric forces and to identify the altitude where the dominant processes change.

### 5.3. High Altitude ion Velocities

To see whether the polar plasma convection in the models also shows a relevant 12 hr oscillation component (as did the EISCAT measurements, see Section 4.3), the oscillation amplitudes of ion velocities at approximately 300 km altitude are calculated. Considering that GAIA uses a constant cross-polar potential, it is expected that plasma convection ion velocities should indicate increased discrepancies compared to the ISR observations. WACCM-X(SD) and TIE-GCM include the Kp index to parametrize geomagnetic activity and the general trend of ion velocity oscillations should therefore resemble the measurements in Figure 5. Figure 11 shows diurnal and semidiurnal oscillation amplitudes of the ion velocity at 300 km altitude from GAIA, WACCM-X(SD), and TIE-GCM.

It can be seen that the diurnal oscillation amplitudes are dominant and show a similar trend in TIE-GCM and WACCM-X(SD) which also resembles the trend found in the measurements. Semidiurnal oscillations also have significant amplitudes and tentatively also correlate with geomagnetic activity. It can be concluded that semidiurnal oscillations at high altitudes are forced by the same plasma convection as diurnal oscillations. GAIA ion velocity amplitudes are similar to WACCM-X(SD) and TIE-GCM amplitudes at low activity times and show little variability. The ion velocity oscillations of WACCM-X(SD) and TIE-GCM are highly similar in amplitudes and dynamics.

## 6. Summary

Oscillation amplitudes in ISR and meteor radar neutral wind measurements showed a distinctly different behavior in zonal and meridional direction. While the ratio of 12–24 hr oscillation amplitudes in zonal neutral winds fits well into the classical expectations, meridional neutral wind show a more complex structure. Meridional wind measurements showed a region of strong semidiurnal oscillations at  $\gtrsim 130$  km additionally to the expected large 12 hr amplitudes at  $\lesssim 110$  km. To determine the origin of these high altitude semidiurnal oscillations, runs from three ionosphere GCMs have been analyzed.

All three models also showed a multi-band structure with strong 12 hr oscillations at high altitudes in the meridional neutral wind component. The asymmetry between zonal and meridional component was also found in all model runs. There were distinct differences between the models regarding dynamics and structure of the high altitude semidiurnal oscillations, presumably caused by different parametrizations of atmospheric, geomagnetic and solar inputs. However, interpretation of the obtained results is possible to some extent.

Comparison at different latitudes showed that the high altitude SW2 amplitudes are forced by a high-latitude effect. Tidal phases obtained from measurement and model data suggested these oscillations to be in situ forced rather than propagating upward from the middle atmosphere. Separate TIE-GCM runs with and without atmospheric tidal input to the ionosphere confirmed this by showing that while the lower SW2 band depends on the atmospheric input, the upper SW2 band remained unaffected by it. An additional TIE-GCM run with fixed low solar irradiance showed that EUV absorption clearly contributes to forcing of 12 hr oscillations at high altitudes.

However, even for constant low EUV absorption, there are high altitude SW2 oscillations which show considerable variability. Also, notably strong 12 hr oscillation amplitudes have been found in the ion velocities at approximately 300 km altitude in both measurements and models. This indicates a strong impact of polar plasma convection on semidiurnal tidal oscillations in the high-latitude thermosphere. In situ forcing of tidal oscillations in the high-latitude ionosphere at high altitudes seems to be the most likely interpretation for the obtained model and measurement results. It seems that both EUV absorption and ion convection contribute significantly to the tidal oscillation amplitudes. Whether one mechanism is dominant could not be finally determined.

## 7. Conclusions

It has been shown that it is possible to perform combined observations of neutral wind velocities with meteor radars and incoherent scatter radars. Such simultaneous observations are of major importance when studying the coupling of atmospheric phenomena into the ionosphere. Another methodological improvement in this paper is the first use of the ASF technique on EISCAT measurements. This technique permits to resolve the day-to-day variability of unevenly sampled time series and an improved handling of the measurement uncertainties which are highly relevant in the incoherent scatter process. This allowed to investigate a larger altitude range which revealed a previously not reported two band structure of strong semidiurnal oscillations in meridional neutral winds. Tidal oscillations at higher altitudes are presumably in situ forced. Both polar plasma convection and EUV absorption are shown to be strong forcing mechanism at high-latitudes. However, propagating atmospheric tides might play an important role as well under specific conditions. The interference of several tidal modes from different origins might then result in the observed complex vertical structuring of tidal oscillations.

Future work should target a more detailed investigation of different in situ forcing mechanisms. The latitudinal propagation of in situ forced tidal modes could give insight on the forcing mechanism. Ideally, the tidal modes forced by plasma convection and EUV absorption can be separated and their interaction studied. This would require more long-time ISR measurement campaigns as they might become possible with the upcoming EISCAT

3D system. As for modeling, plasma convection models need to be investigated and compared with respect to the size and shape of the convection pattern.

### Data Availability Statement

The model and measurement data used in this paper as well as the input files for the conducted TIE-GCM runs can be found under <https://doi.org/10.5281/zenodo.6817130> (Günzkofer et al., 2022a). The data analysis and plotting software in the version used for this publication (Version 1) can be found under <https://doi.org/10.5281/zenodo.7072141> (Günzkofer et al., 2022b). All files are available under the Creative Commons Attribution 4.0 International license. In case of further questions about the data or the analysis software please contact the corresponding author.

### Acknowledgments

The authors would like to acknowledge the following data sources: EISCAT is an international association supported by research organizations in China (CRIRP), Finland (SA), Japan (NIPR and ISEE), Norway (NFR), Sweden (VR), and the United Kingdom (UKRI). For this study, a data set from the Ground-to-topside model of Atmosphere and Ionosphere for Aeronomy (GAIA) project carried out by the National Institute of Information and Communications Technology (NICT), Kyushu University, and Seikei University was used. The WACCM-X model has been developed at NCAR (see <https://www2.hao.ucar.edu/modeling/wacm-x>). The TIEGCM and related Thermosphere-Ionosphere models have been developed by the “Atmosphere Ionosphere Magnetosphere” (AIM) Section of the High Altitude Observatory (HAO) at NCAR (see <https://www.hao.ucar.edu/modeling/tgcm/>). The TIEGCM data was generated on the “Kratos” High-Performance Data Analysis Cluster (HPDA). The GSWM data has been obtained from the HAO UCAR website <https://www2.hao.ucar.edu/gswm-global-scale-wave-model>. H. Liu acknowledges support from JSPS KAKENHI grants 18H01270, 17KK0095, 20H00197, and JRPCs-LEAD with DFG (JPJSJPR 20181602). G. Stober is a member of the Oeschger Center for Climate Change Research. Open Access funding enabled and organized by Projekt DEAL.

### References

- Andrews, D. G., Holton, J. R., & Leovy, C. B. (1987). *Middle atmosphere dynamics* (Vol. 40). Academic Press.
- Barracough, D. R. (1988). IAGA division I working group 1: International geomagnetic reference field revision 1987. *Geophysical Journal International*, 93(1), 187–189. <https://doi.org/10.1111/j.1365-246X.1988.tb01397.x>
- Baumgarten, K., & Stober, G. (2019). On the evaluation of the phase relation between temperature and wind tides based on ground-based measurements and reanalysis data in the middle atmosphere. *Annales Geophysicae*, 37(4), 581–602. <https://doi.org/10.5194/angeo-37-581-2019> Retrieved from <https://angeo.copernicus.org/articles/37/581/2019/>
- Brekke, A., Doupinik, J. R., & Banks, P. M. (1973). A preliminary study of the neutral wind in the auroral E region. *Journal of Geophysical Research*, 78(34), 8235–8250. <https://doi.org/10.1029/JA078i034p08235>
- Chapman, S. (1956). The electrical conductivity of the ionosphere: A review. *Il Nuovo Cimento - B*, 4(S4), 1385–1412. <https://doi.org/10.1007/BF02746310>
- Collis, P. N. (1995). EISCAT data base for ionospheric modelling: F-region and topside ionosphere. *Advances in Space Research*, 16(1), 37–46. [https://doi.org/10.1016/0273-1177\(95\)00096-W](https://doi.org/10.1016/0273-1177(95)00096-W)
- Folkestad, K., Hagfors, T., & Westerlund, S. (1983). EISCAT: An updated description of technical characteristics and operational capabilities. *Radio Science*, 18(6), 867–879. <https://doi.org/10.1029/RS018i006p00867>
- Gasperini, F., Liu, H., & McInerney, J. (2020). Preliminary evidence of Madden-Julian oscillation effects on ultrafast tropical waves in the thermosphere. *Journal of Geophysical Research*, 125(5), e27649. <https://doi.org/10.1029/2019JA027649>
- Gelaro, R., McCarty, W., Suárez, M. J., Todling, R., Molod, A., Takacs, L., et al. (2017). The modern-era retrospective analysis for research and applications, version 2 (MERRA-2). *Journal of Climate*, 30(14), 5419–5454. <https://doi.org/10.1175/JCLI-D-16-0758.1>
- Grassmann, V. (1993). An incoherent scatter experiment for the measurement of particle collisions. *Journal of Atmospheric and Terrestrial Physics*, 55(4–5), 573–576. [https://doi.org/10.1016/0021-9169\(93\)90006-K](https://doi.org/10.1016/0021-9169(93)90006-K)
- Günzkofer, F., Pokhotelov, D., Stober, G., Liu, H., Liu, H., Mitchell, N., et al. (2022a). [Dataset] Determining the origin of tidal oscillations in the ionospheric transition region with EISCAT radar and global simulation data. Zenodo. <https://doi.org/10.5281/zenodo.6817130>
- Günzkofer, F., Pokhotelov, D., Stober, G., Liu, H., Liu, H., Mitchell, N., et al. (2022b). [Software] Determining the origin of tidal oscillations in the ionospheric transition region with EISCAT radar and global simulation data. Zenodo. <https://doi.org/10.5281/zenodo.7072141>
- Hagan, M. E., & Forbes, J. M. (2002). Migrating and nonmigrating diurnal tides in the middle and upper atmosphere excited by tropospheric latent heat release. *Journal of Geophysical Research: Atmospheres*, 107(D24), 4754. <https://doi.org/10.1029/2001JD001236>
- Hagan, M. E., & Forbes, J. M. (2003). Migrating and nonmigrating semidiurnal tides in the upper atmosphere excited by tropospheric latent heat release. *Journal of Geophysical Research: Space Physics*, 108(A2), 1062. <https://doi.org/10.1029/2002JA009466>
- Hedin, A. E. (1991). Extension of the MSIS thermosphere model into the middle and lower atmosphere. *Journal of Geophysical Research*, 96(A2), 1159–1172. <https://doi.org/10.1029/90JA02125>
- Heelis, R. A., Lowell, J. K., & Spiro, R. W. (1982). A model of the high-latitude ionospheric convection pattern. *Journal of Geophysical Research*, 87(A8), 6339–6345. <https://doi.org/10.1029/JA087iA08p06339>
- Hocking, W. K., Fuller, B., & Vandeppeer, B. (2001). Real-time determination of meteor-related parameters utilizing modern digital technology. *Journal of Atmospheric and Solar-Terrestrial Physics*, 63(2–3), 155–169. [https://doi.org/10.1016/S1364-6826\(00\)00138-3](https://doi.org/10.1016/S1364-6826(00)00138-3)
- Hurrell, J. W., Holland, M. M., Gent, P. R., Ghan, S., Kay, J. E., Kushner, P. J., et al. (2013). The community earth system model: A framework for collaborative research. *Bulletin of the American Meteorological Society*, 94(9), 1339–1360. <https://doi.org/10.1175/BAMS-D-12-00121.1>
- Jin, H., Miyoshi, Y., Pancheva, D., Mukhtarov, P., Fujiwara, H., & Shinagawa, H. (2012). Response of migrating tides to the stratospheric sudden warming in 2009 and their effects on the ionosphere studied by a whole atmosphere-ionosphere model GAIA with COSMIC and TIMED/SABER observations. *Journal of Geophysical Research: Space Physics*, 117(A10), A10323. <https://doi.org/10.1029/2012JA017650>
- Kelly, M. C. (2009). The Earth’s ionosphere: Plasma physics and electrodynamics (2nd ed.).
- Kobayashi, S., Ota, Y., Harada, Y., Ebata, A., Moriya, M., Onoda, H., et al. (2015). The JRA-55 reanalysis: General specifications and basic characteristics. *Journal of the Meteorological Society of Japan*, 93(1), 5–48. <https://doi.org/10.2151/jmsj.2015-001>
- Lee, W., Kim, Y. H., Lee, C., & Wu, Q. (2018). First comparison of mesospheric winds measured with a Fabry-Perot interferometer and meteor radar at the King Sejong Station (62.2°S, 58.8°W). *Journal of Astronomy and Space Sciences*, 35, 235–242. <https://doi.org/10.5140/JASS.2018.35.4.235>
- Lindzen, R. S. (1979). Atmospheric tides. *Annual Review of Earth and Planetary Sciences*, 7, 199–225. <https://doi.org/10.1146/annurev.ea.07.050179.001215>
- Liu, H., Sun, Y.-Y., Miyoshi, Y., & Jin, H. (2017). ENSO effects on MLT diurnal tides: A 21 year reanalysis data-driven GAIA model simulation. *Journal of Geophysical Research: Space Physics*, 122(5), 5539–5549. <https://doi.org/10.1002/2017JA024011>
- Liu, H.-L., Bardeen, C. G., Foster, B. T., Lauritzen, P., Liu, J., Lu, G., et al. (2018). Development and validation of the whole atmosphere community climate model with thermosphere and ionosphere extension (WACCM-X 2.0). *Journal of Advances in Modeling Earth Systems*, 10(2), 381–402. <https://doi.org/10.1002/2017MS001232>

- Manson, A. H., Meek, C., Hagan, M., Koshyk, J., Franke, S., Fritts, D., et al. (2002). Seasonal variations of the semi-diurnal and diurnal tides in the MLT: Multi-year MF radar observations from 2Å 70Å°N, modelled tides (GSWM, CMAM). *Annales Geophysicae*, 20(5), 661–677. <https://doi.org/10.5194/angeo-20-661-2002>
- Nicolls, M. J., Bahcivan, H., Hægström, I., & Rietveld, M. (2014). Direct measurement of lower thermospheric neutral density using multifrequency incoherent scattering. *Geophysical Research Letters*, 41(23), 8147–8154. <https://doi.org/10.1002/2014GL062204>
- Nozawa, S., & Brekke, A. (1999). Studies of the auroral E region neutral wind through a solar cycle: Quiet days. *Journal of Geophysical Research*, 104(A1), 45–66. <https://doi.org/10.1029/1998JA900013>
- Nozawa, S., Ogawa, Y., Oyama, S., Fujiwara, H., Tsuda, T., Brekke, A., et al. (2010). Tidal waves in the polar lower thermosphere observed using the EISCAT long run data set obtained in September 2005. *Journal of Geophysical Research: Space Physics*, 115(A8), A08312. <https://doi.org/10.1029/2009JA015237>
- Nygrén, T., Aikio, A. T., Kuula, R., & Voiculescu, M. (2011). Electric fields and neutral winds from monostatic incoherent scatter measurements by means of stochastic inversion. *Journal of Geophysical Research: Space Physics*, 116(A5), A05305. <https://doi.org/10.1029/2010JA016347>
- Oberheide, J., Forbes, J. M., Zhang, X., & Bruinsma, S. L. (2011). Climatology of upward propagating diurnal and semidiurnal tides in the thermosphere. *Journal of Geophysical Research: Space Physics*, 116(A11), A11306. <https://doi.org/10.1029/2011JA016784>
- Onogi, K., Tsutsui, J., Koide, H., Sakamoto, M., Kobayashi, S., Hatsushika, H., et al. (2007). The JRA-25 reanalysis. *Journal of the Meteorological Society of Japan*, 85(3), 369–432. <https://doi.org/10.2151/jmsj.85.369>
- Pedatella, N. M., Liu, H. L., Conte, J. F., Chau, J. L., Hall, C., Jacobi, C., et al. (2021). Migrating semidiurnal tide during the September equinox transition in the Northern Hemisphere. *Journal of Geophysical Research: Atmospheres*, 126(3), e33822. <https://doi.org/10.1029/2020JD033822>
- Picone, J. M., Hedin, A. E., Drob, D. P., & Aikin, A. C. (2002). NRLMSISE-00 empirical model of the atmosphere: Statistical comparisons and scientific issues. *Journal of Geophysical Research: Space Physics*, 107(A12), 1468. <https://doi.org/10.1029/2002JA009430>
- Pokhotelov, D., Becker, E., Stober, G., & Chau, J. L. (2018). Seasonal variability of atmospheric tides in the mesosphere and lower thermosphere: Meteor radar data and simulations. *Annales Geophysicae*, 36(3), 825–830. <https://doi.org/10.5194/angeo-36-825-2018>
- Qian, L., Burns, A. G., Emery, B. A., Foster, B., Lu, G., Maute, A., et al. (2014). The near tie-gcm: A community model of the coupled thermosphere/ionosphere system. In *Modeling the ionosphere-thermosphere system*. In *Geophysical monograph series* (Vol. 201, pp. 73–83). American Geophysical Union. <https://doi.org/10.1002/9781118704417.ch7>
- Richmond, A. D., Ridley, E. C., & Roble, R. G. (1992). A thermosphere/ionosphere general circulation model with coupled electrodynamics. *Geophysical Research Letters*, 19(6), 601–604. <https://doi.org/10.1029/92GL00401>
- Rienecker, M. M., Suarez, M. J., Gelaro, R., Todling, R., Bacmeister, J., Liu, E., et al. (2011). MERRA: NASA's modern-era retrospective analysis for research and applications. *Journal of Climate*, 24(14), 3624–3648. <https://doi.org/10.1175/JCLI-D-11-00015.1>
- Rino, C. L., Brekke, A., & Baron, M. J. (1977). High-resolution auroral zone E region neutral wind and current measurements by incoherent scatter radar. *Journal of Geophysical Research*, 82(16), 2295–2304. <https://doi.org/10.1029/JA082i016p02295>
- Schunk, R., & Nagy, A. (2009). *Ionospheres: Physics, plasma physics, and chemistry* (2nd ed.). Cambridge University Press. <https://doi.org/10.1017/CBO9780511635342>
- Schunk, R., & Walker, J. C. G. (1973). Theoretical ion densities in the lower ionosphere. *Planetary and Space Science*, 21(11), 1875–1896. [https://doi.org/10.1016/0032-0633\(73\)90118-9](https://doi.org/10.1016/0032-0633(73)90118-9)
- Smith, A. K. (2012). Global dynamics of the MLT. *Surveys in Geophysics*, 33(6), 1177–1230. <https://doi.org/10.1007/s10712-012-9196-9>
- Stober, G., Baumgarten, K., McCormack, J. P., Brown, P., & Czarniecki, J. (2020). Comparative study between ground-based observations and NAVGEM-HA analysis data in the mesosphere and lower thermosphere region. *Atmospheric Chemistry and Physics*, 20(20), 11979–12010. <https://doi.org/10.5194/acp-20-11979-2020>
- Stober, G., Kuchar, A., Pokhotelov, D., Liu, H., Liu, H.-L., Schmidt, H., et al. (2021). Interhemispheric differences of mesosphere-lower thermosphere winds and tides investigated from three whole-atmosphere models and meteor radar observations. *Atmospheric Chemistry and Physics*, 21(18), 13855–13902. <https://doi.org/10.5194/acp-21-13855-2021>
- Stober, G., Matthias, V., Jacobi, C., Wilhelm, S., Höffner, J., & Chau, J. L. (2017). Exceptionally strong summer-like zonal wind reversal in the upper mesosphere during winter 2015/16. *Annales Geophysicae*, 35(3), 711–720. <https://doi.org/10.5194/angeo-35-711-2017>
- Straus, J. M., Creekmore, S. P., Harris, R. M., Ching, B. K., & Chiu, Y. T. (1975). A global model for thermospheric dynamics - II. Wind, density, and temperature fields generated by EUV heating. *Journal of Atmospheric and Terrestrial Physics*, 37, 1245–1253. [https://doi.org/10.1016/0021-9169\(75\)90033-1](https://doi.org/10.1016/0021-9169(75)90033-1)
- Truskowski, A. O., Forbes, J. M., Zhang, X., & Palo, S. E. (2014). New perspectives on thermosphere tides: 1. Lower thermosphere spectra and seasonal-latitude structures. *Earth Planets and Space*, 66, 136. <https://doi.org/10.1186/s40623-014-0136-4>
- Williams, P. J. S., & Virdi, T. S. (1989). EISCAT observations of tidal modes in the lower thermosphere. *Journal of Atmospheric and Terrestrial Physics*, 51(7), 569–577. [https://doi.org/10.1016/0021-9169\(89\)90055-X](https://doi.org/10.1016/0021-9169(89)90055-X)
- Wu, Q., Jee, G., Lee, C., Kim, J.-H., Kim, Y. H., Ward, W., & Varney, R. H. (2017). First simultaneous multistation observations of the polar cap thermospheric winds. *Journal of Geophysical Research: Space Physics*, 122(1), 907–915. <https://doi.org/10.1002/2016JA023560>

---

# Inferring neutral winds in the ionospheric transition region from atmospheric-gravity-wave traveling-ionospheric-disturbance (AGW-TID) observations with the EISCAT VHF radar and the Nordic Meteor Radar Cluster

## Bibliographic information

Günzkofer F., Pokhotelov D., Stober G., Mann I., Vadas S. L., Becker E., Tjulin A., Kozlovsky A., Tsutsumi M., Gulbrandsen N., Nozawa S., Lester M., Belova E., Kero J., Mitchell N. J., and Borries C. Inferring neutral winds in the ionospheric transition region from AGW-TID observations with the EISCAT VHF radar and the Nordic Meteor Radar Cluster. *Annales Geophysicae*, **41**, 409-428, 2023.

DOI: <https://doi.org/10.5194/angeo-41-409-2023>

©2023. The Authors.

## Author's contribution

For this publication, I analyzed the EISCAT measurements with the Grand Unified Incoherent Scatter Design and Analysis Package (GUISDAP) to obtain the electron density. The EISCAT campaigns were planned and requested by myself, D. Pokhotelov, G. Stober, I. Mann, and A. Tjulin. The meteor radar measurements were provided by A. Kozlovsky, M. Tsutsumi, N. Gulbrandsen, S. Nozawa, M. Lester, E. Belova, J. Kero, and N. J. Mitchell. I implemented the Fourier filter techniques to filter wave signals from both EISCAT and meteor radar measurements as well as the algorithm that determines the wave phase lines and parameters. The application of Fourier filters was suggested by S. L. Vadas who, together with E. Becker, also contributed to the interpretation of the results. I implemented the non-linear least square fit of the dispersion relation to infer neutral wind profiles. My work was supervised by D. Pokhotelov, G. Stober, and C. Borries. As the first author, I wrote large parts of the manuscript, but all authors were involved in revising the text.



# Inferring neutral winds in the ionospheric transition region from atmospheric-gravity-wave traveling-ionospheric-disturbance (AGW-TID) observations with the EISCAT VHF radar and the Nordic Meteor Radar Cluster

Florian Günzkofer<sup>1</sup>, Dimitry Pokhotelov<sup>2</sup>, Gunter Stober<sup>3</sup>, Ingrid Mann<sup>4</sup>, Sharon L. Vadas<sup>5</sup>, Erich Becker<sup>5</sup>, Anders Tjulin<sup>6</sup>, Alexander Kozlovsky<sup>7</sup>, Masaki Tsutsumi<sup>8,9</sup>, Njal Gulbrandsen<sup>10</sup>, Satonori Nozawa<sup>11</sup>, Mark Lester<sup>12</sup>, Evgenia Belova<sup>13</sup>, Johan Kero<sup>13</sup>, Nicholas J. Mitchell<sup>14,15</sup>, and Claudia Borries<sup>1</sup>

<sup>1</sup>Institute for Solar-Terrestrial Physics, German Aerospace Center (DLR), Neustrelitz, Germany

<sup>2</sup>Institute of Physics, University of Greifswald, Greifswald, Germany

<sup>3</sup>Institute of Applied Physics and Oeschger Center for Climate Change Research, Microwave Physics, University of Bern, Bern, Switzerland

<sup>4</sup>Institute of Physics and Technology, UiT The Arctic University of Norway, Tromsø, Norway

<sup>5</sup>North West Research Associates (NWRA), Boulder, Colorado, USA

<sup>6</sup>EISCAT Scientific Association, Kiruna, Sweden

<sup>7</sup>Sodankylä Geophysical Observatory, University of Oulu, Oulu, Finland

<sup>8</sup>National Institute of Polar Research, Tachikawa, Japan

<sup>9</sup>The Graduate University for Advanced Studies (SOKENDAI), Tokyo, Japan

<sup>10</sup>Tromsø Geophysical Observatory, UiT The Arctic University of Norway, Tromsø, Norway

<sup>11</sup>Institute for Space-Earth Environmental Research, Nagoya University, Nagoya, Japan

<sup>12</sup>Department of Physics & Astronomy, University of Leicester, Leicester, UK

<sup>13</sup>Swedish Institute of Space Physics (IRF), Kiruna, Sweden

<sup>14</sup>British Antarctic Survey, Cambridge, UK

<sup>15</sup>Department of Electronic & Electrical Engineering, University of Bath, Bath, UK

**Correspondence:** Florian Günzkofer (florian.guenzkofer@dlr.de)

Received: 6 April 2023 – Discussion started: 14 April 2023

Revised: 21 August 2023 – Accepted: 13 September 2023 – Published: 18 October 2023

**Abstract.** Atmospheric gravity waves and traveling ionospheric disturbances can be observed in the neutral atmosphere and the ionosphere at a wide range of spatial and temporal scales. Especially at medium scales, these oscillations are often not resolved in general circulation models and are parameterized. We show that ionospheric disturbances forced by upward-propagating atmospheric gravity waves can be simultaneously observed with the EISCAT very high frequency incoherent scatter radar and the Nordic Meteor Radar Cluster. From combined multi-static measurements, both vertical and horizontal wave parameters can be determined by applying a specially developed Fourier filter analysis method. This method is demonstrated using the ex-

ample of a strongly pronounced wave mode that occurred during the EISCAT experiment on 7 July 2020. Leveraging the developed technique, we show that the wave characteristics of traveling ionospheric disturbances are notably impacted by the fall transition of the mesosphere and lower thermosphere. We also demonstrate the application of using the determined wave parameters to infer the thermospheric neutral wind velocities. Applying the dissipative anelastic gravity wave dispersion relation, we obtain vertical wind profiles in the lower thermosphere.

## 1 Introduction

Waves balanced by gravity and buoyancy forces are often referred to as gravity waves and originate in various fluids (Andrews, 2010). In the Earth's atmosphere, atmospheric gravity waves (AGWs) can be observed at a wide range of altitudes from the troposphere well into the thermosphere. In the ionosphere, which is coupled to the neutral atmosphere by ion-neutral collisions, AGWs can be observed as medium-scale traveling ionospheric disturbances (MS-TIDs) (Nicolls et al., 2014). Typical MS-TID wave periods are approximately 15–80 min (Kirchengast et al., 1996; Hocke and Schlegel, 1996). In this region, the wave is subject to electromagnetic effects (Kelly, 2009) in addition to the buoyancy and gravity forces and viscous damping (Pitteway and Hines, 1963; Vadas, 2007). The wavelengths and periods of AGW-TIDs depend on the generation mechanism and the state of the background atmosphere. These disturbances can be forced either by ionospheric processes (Brekke, 1979) or by upward-propagating gravity waves generated in the lower or middle atmosphere (Bauer, 1958; Hung et al., 1978; Vadas and Crowley, 2010; Smith, 2012; Nishioka et al., 2013; Azeem et al., 2015, 2017; Frissell et al., 2016; Xu et al., 2019; Becker et al., 2022a) or in the thermosphere via multi-step vertical coupling (Vadas and Becker, 2019; Becker et al., 2022a; Vadas et al., 2023a, b). Since ion-neutral collisions create TIDs from AGWs if a component of the AGWs velocity vector lies along the Earth's magnetic field line (e.g., Nicolls et al., 2014), we refer to these waves as AGW-TIDs independent of their generation region or mechanism in this study.

The wave picture in the thermosphere and ionosphere can be highly complicated, with several wave modes present. AGW-TIDs forced in the lower atmosphere are capable of propagating to these altitudes only under certain atmospheric conditions. This wave filtering (Lindzen, 1981; Smith, 1996) has a major impact on the mesosphere and lower thermosphere (MLT) region (Holton, 1992; Smith, 2012; Becker, 2012). Consequently, a large number of studies have investigated this impact (see, e.g., Hoffmann et al., 2010, 2011; Ern et al., 2011; Smith et al., 2017; Sarkhel et al., 2022, and references therein). Strong changes in AGW-TID activity in the MLT are caused by the seasonal variation of mesospheric mean winds (Stober et al., 2021d), especially during the spring and fall equinox transitions. The latter in particular has been shown to impact tidal waves in the mesosphere (Stober et al., 2020; Pedatella et al., 2021) and possibly well up in the thermosphere (Günzkofer et al., 2022). Investigating the impact of the MLT fall transition, the change in the MLT wind system around the autumn equinox (Stober et al., 2021d), on AGW-TIDs is one of the central topics of this paper.

The impact of background winds on AGW-TIDs can be seen from the wave dispersion relations, derived for zero viscosity (Hines, 1960), for small viscosity in a steady-state so-

lution (Pitteway and Hines, 1963), and for full viscosity for wave packets in an anelastic formulation (Vadas and Fritts, 2005). These dispersion relations show that horizontal and vertical wave characteristics are strongly dependent on the neutral atmosphere parameters and dynamics. Considering that the AGW-TID parameters can be derived from MLT observations, thermospheric neutral winds along the AGW propagation direction can be deduced by making use of the abovementioned dispersion relations (Vadas and Nicolls, 2009). Since neutral wind velocities are difficult to measure at altitudes  $\gtrsim 100$  km (Mitchell and Beldon, 2009), this would provide valuable information on thermosphere dynamics. Measurements of the various coupling processes in the MLT region are generally very difficult to obtain. A summary of measurement techniques at these altitudes can be found in Palmroth et al. (2021).

Simultaneous measurements with sufficient vertical resolution and horizontal coverage to determine gravity wave parameters, in particular the required spatial coverage to derive the horizontal wave numbers, are often not available. One possibility to perform such three-dimensional measurements is the use of phased array radars. This has been demonstrated for both incoherent scatter radars (ISRs) (e.g., Nicolls and Heinselman, 2007; Vadas and Nicolls, 2008, 2009) and coherent scatter radars (Rapp et al., 2011; Stober et al., 2013, 2018). Under certain assumptions, similar measurements are also possible using a classical ISR with multi-beam or beam-swinging capabilities (Nicolls et al., 2014). Other studies applied simultaneous measurements of a single-beam ISR and a global navigation satellite system (GNSS) receiver network to extract vertical or horizontal wavelength (van de Kamp et al., 2014). Applying high-resolution GNSS measurements of the total electron content (TEC) to detect and study MS-TIDs is a well-established method (Saito et al., 1998; Tsugawa et al., 2007; Onishi et al., 2009). However, since TEC is the height-integrated electron density, multiple wave modes might be mixed, which makes vertical and horizontal measurements of single wave modes more challenging and prone to observational biases. A more recent approach is the detection of TIDs in observations of strong natural radio sources with the Low-Frequency Array (LOFAR) radio telescope (Fallows et al., 2020; Boyde et al., 2022). Ionospheric irregularities can be observed at multiple altitude levels with a large horizontal coverage which allows for observing the horizontal scale and propagation direction of multiple TIDs.

In this work, a new strategy is presented utilizing measurements from the EISCAT ISR and the Nordic Meteor Radar Cluster (Stober et al., 2021c, 2022). Thereby, upward-propagating gravity waves can be observed simultaneously with the horizontally resolved wind fields obtained from the meteor radar measurements and ISR measurements that have a high vertical resolution. Since the Nordic Meteor Radar Cluster allows for altitude-resolved measurements, it is possible to obtain vertical and horizontal wavelength, wave period, and propagation direction of an individual wave mode.

Horizontal wavelengths can be assumed to be constant for a horizontally constant background wind field (Lighthill, 1978; Vadas and Nicolls, 2008). This is usually the case above the turbopause and has been confirmed in measurements (Nicolls and Heinselman, 2007). The further structure of the paper is as follows.

Section 2 will give an overview of the instruments utilized and the specifics of the analyzed measurements. The process of separating different wave modes and determining the wave parameters is presented in Sect. 3. The method we use to infer neutral winds via the gravity wave dispersion relations will be demonstrated there as well. Section 4 will present AGW-TID measurements conducted during the EISCAT campaign of autumn 2022, both before and after the MLT fall transition. This illustrates the impact of atmospheric transitions on ionospheric dynamics. In Sect. 5, the advantages and disadvantages of combined EISCAT and Nordic Meteor Radar Cluster AGW-TID measurements compared to previous approaches are discussed. The results are compared to these previous studies in Sect. 5 as well and possibilities for future work are discussed. Our conclusions are given in Sect. 6.

## 2 Instruments

### 2.1 EISCAT incoherent scatter radar

A general overview of the different EISCAT radars and experiments can be found in Tjulin (2021). We summarize the information on apparatuses and modes applied to this work.

The EISCAT Scientific Association operates a very high frequency (VHF) ISR with a frequency of 224 MHz near Tromsø, Norway (69.6° N, 19.2° E) (Folkestad et al., 1983). The VHF transmitter is operated at a maximum power of about 1.5 MW, and the co-located receiver antenna consists of four rectangular (30 m × 40 m) dishes.

All measurements were conducted in the *manda zenith common program 6 (CP6)* mode with the transmitter and co-located receiver pointed at 90° elevation. This mode allows for measurements up to ~ 200 km altitude with a high vertical resolution ranging from several hundred meters in the lower thermosphere to about 10 km at the highest altitudes. The plasma parameters have been obtained with version 9.2 of the Grand Unified Incoherent Scatter Design and Analysis Package (GUISDAP) (Lehtinen and Huuskonen, 1996). The time resolution of the obtained plasma parameters is determined by the post-experiment integration time of the ISR raw data, which has been set to 60 s. Data from two EISCAT measurement campaigns are utilized for this study.

#### Summer 2020

The first campaign was conducted on 3 consecutive days in July 2020 (7th to 9th). The EISCAT VHF radar was operated from 00:00–12:00 UTC on each of these days. One advan-

tage of this campaign is the continued low geomagnetic activity during the 3 measurement days of the observation campaign with  $K_p < 2$  on all 3 measurement days. The reduced ionospheric variability due to external forcing provides more favorable conditions for the detection of AGW-TIDs originating in the lower atmosphere. TID detection is done manually with a coherent wave structure being present for at least two wave periods and exhibiting downward phase progression. The relative electron density variations should be approximately  $\delta N_e/N_e \sim 0.01–0.05$  (Vadas and Nicolls, 2009; Nicolls et al., 2014). On 7 July 2020, a pronounced TID signature was found. This TID was used as a reference to implement and optimize the applied analysis method to isolate and separate different wave modes and to determine the wave parameters.

#### Autumn 2022

The second campaign was conducted during Autumn 2022 in two separate measurement intervals on 1 September and 13 October. This ensures that measurements are available before and after the MLT fall transition which is expected to take place over several days around the autumn equinox (Stober et al., 2021d). On both days, the EISCAT VHF radar was operated from 08:00–13:00 UTC using the same experiment mode as during the summer campaign. This period was chosen to minimize the impact of geomagnetic substorms which hamper the detection of TIDs. However, both measurement days did indicate the presence of TIDs. The highest geomagnetic activity during these two measurements occurred on 1 September around 09:00 UTC with  $K_p = 2.333$ .

### 2.2 Nordic Meteor Radar Cluster

Meteor radars have proven to be valuable and reliable instruments to measure neutral winds in the MLT region. These winds contain valuable information about atmospheric waves such as gravity waves, tides, and planetary waves at the MLT (e.g., Fritts et al., 2010; de Wit et al., 2016, 2017; McCormack et al., 2017; Pokhotelov et al., 2018; Stober et al., 2021b, d). The wind velocity is determined by measuring the Doppler shift of the coherent radar scattering from the thermalized plasma generated by meteoroids entering the Earth's atmosphere and forming an ambipolar diffusing plasma trail (Herlofson, 1951; Greenhow, 1952; McKinley, 1961; Poulter and Baggaley, 1977; Jones and Jones, 1990; Hocking et al., 2001; Stober et al., 2021a). For this work, we analyze measurements from the high-resolution 3DVAR+DIV retrieval, which is a part of ASGARD (Agile Software for Gravity wave Regional Dynamics) of the Nordic Meteor Radar Cluster (Stober et al., 2021c, 2022). This cluster consists of four meteor radars located in Tromsø (Norway; 69.6° N, 19.2° E), Alta (Norway; 70.0° N, 23.3° E), Kiruna (Sweden; 67.9° N, 21.1° E), and Sodankylä (Finland; 67.4° N, 26.6° E). The retrieved 3D wind fields cover the Nordic countries from ~ 66–

72° N latitude and  $\sim 12.5\text{--}31.5^\circ$  E longitude. The horizontal grid resolution is 30 km, and wind measurements are available from  $\sim 80\text{--}100$  km altitude at 2 km vertical resolution and 10 min time steps. This higher temporal resolution is possible due to the multi-static measurements that result in a much higher meteor trail detection rate within the overlapping observation volume compared to a monostatic meteor radar. For the visualization of horizontally resolved measurements and the correct geographic mapping with minimal projection errors, we leverage the *m\_map* software package (Pawlowicz, 2020).

### 3 Methods

The analysis of AGW-TIDs requires the processing of the ISR and meteor radar measurements. The applied techniques to extract and separate different wave modes from the radar data are described in this section using the data collected on 7 July 2020. We then leverage this methodology and apply the same procedures to observations carried out during several campaigns.

#### 3.1 EISCAT

Previous studies suggested that the magnetic-field-aligned ion velocity is the most promising ISR parameter to detect TIDs (Williams, 1989; Vlasov et al., 2011). However, since the investigated measurements are not conducted in a field-aligned geometry, our analysis focuses on the electron density to avoid any impacts of ionospheric electric fields (Williams, 1989). Figure 1 shows the electron density  $N_e$  measured on 7 July 2020 with the EISCAT VHF radar. A sliding window filter with a 60 s step size and a window length of 60 min is applied on each altitude level separately to subtract all larger-scale perturbations and to disclose the underlying GW signatures. The filtered absolute electron density variations  $\delta N_e$  are shown in Fig. 1 as well.

The electron density shows variations of several orders of magnitude across the observed altitude and time range. The sliding window filter removes the background mean and large-scale variations in time and altitude. The remaining residual fluctuations reveal several medium-scale structures in electron density. Further on, we focus on the pronounced wave structure visible from 08:00–12:00 UTC at altitudes  $\sim 110\text{--}170$  km indicated by a red box.

Figure 2 (top left) shows  $\delta N_e$  at the time–altitude range specified above. The electron density variations exhibit a strong wave pattern with downward phase progression. Such downward phase progression is expected and has been reported for upward-propagating AGW-TIDs (e.g., Hines, 1960; Williams, 1989; Kirchengast, 1997; Nicolls and Heinselman, 2007; Vlasov et al., 2011). After 10:00 UTC, the wave structures show signs of an interference pattern below 130 km altitude. This indicates the presence of addi-

tional, presumably downward-propagating, wave modes. We apply 2D Fourier filters to separate multiple present wave modes. This approach has been successfully demonstrated on model data (e.g., Vadas and Becker, 2018; Vadas and Becker, 2019). The electron density variations are interpolated on a  $72\text{ s} \times 5\text{ km}$  grid and a 2D fast Fourier transform (FFT)  $dN_e(t, h) \rightarrow \widehat{dN_e}(f, k_z)$  is performed. The resulting Fourier spectrum is shown in Fig. 2 (top right) with wave frequency  $f$  as abscissa and with vertical wave number  $k_z$  as ordinate. In such a 2D Fourier spectrum, the amplitudes of wave structures with downward phase progression are found for  $|f \cdot k_z| > 0$ . Consequently, two strong maxima corresponding to the observed upward-propagating wave structure can be identified in the first and third quadrants of the spectrum. As described in Eq. (1), a 2D step function is applied to suppress waves with upward phase progression from the Fourier spectrum.

$$\widehat{dN_e}'(f, k_z) = \sigma(f, k_z) \cdot \widehat{dN_e}(f, k_z);$$

$$\sigma(f, k_z) = \begin{cases} 0 & f \cdot k_z \leq 0, \\ 1 & f \cdot k_z > 0. \end{cases} \quad (1)$$

The filtered 2D Fourier spectrum  $\widehat{dN_e}'(f, k_z)$  is transformed to the filtered electron variations  $dN_e'(t, h)$  by means of a 2D inverse FFT. Figure 2 (bottom left) shows  $dN_e'(t, h)$  from only upward-propagating wave modes. This filtered wave field exhibits no more signs of wave interference. However, as we use a bandpass filter, there is a possibility that several upward-propagating wave modes are still present. The Fourier spectrum in Fig. 2 (top right) shows two smaller maxima at slightly higher frequencies ( $\sim 1$  mHz) than the dominant maxima. Additionally, the dominating maxima are limited to wave numbers  $k_z \lesssim 0.3\text{ km}^{-1}$ . In the second step, another filter function is applied to limit the Fourier spectrum to waves with period  $\tau \gtrsim 21$  min and vertical wavelength  $\lambda_z \gtrsim 21$  km. The inverse FFT of this spectrum gives the electron density variations presumably caused by a single AGW-TID wave mode which is shown in Fig. 2 (bottom right). The same method can be applied to obtain any of the other present wave modes. However, to demonstrate the following procedures, we will focus on this largest-amplitude wave.

After the wave mode of interest has been isolated, the goal is to determine vertical profiles of the wave period  $\tau$  and the vertical wavelength  $\lambda_z$ . The first step is to fit the filtered electron density variations at each altitude level separately as a wave function given by

$$dN_e = A \cdot \cos\left(\frac{2\pi}{\tau}t + \delta\right). \quad (2)$$

Equation (2) provides the fit function with the wave parameters amplitude  $A$ , period  $\tau$ , and phase shift  $\delta$ . The optimum parameters are determined by a least-square fit which yields the vertical profiles  $A(z)$ ,  $\tau(z)$ , and  $\delta(z)$ . Furthermore, we

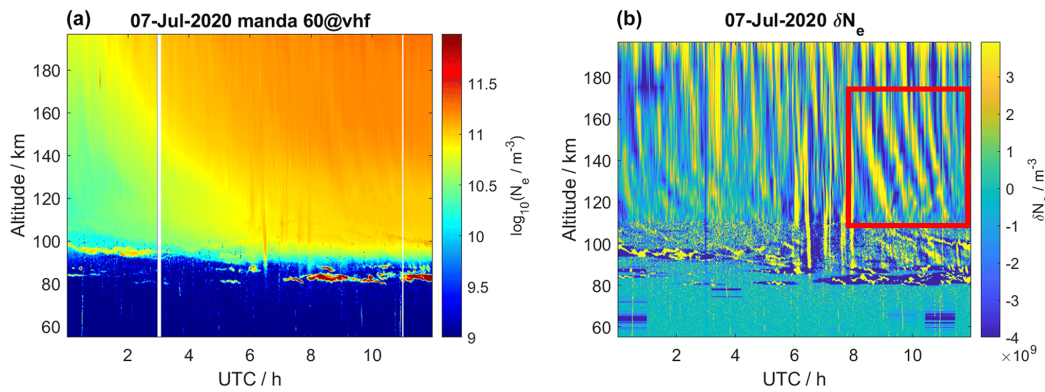


**Figure 1.** (a) Electron density measured with the EISCAT VHF radar on 7 July 2020. (b) Electron density variation calculated with a sliding window filter. The red box marks a strongly pronounced wave structure.

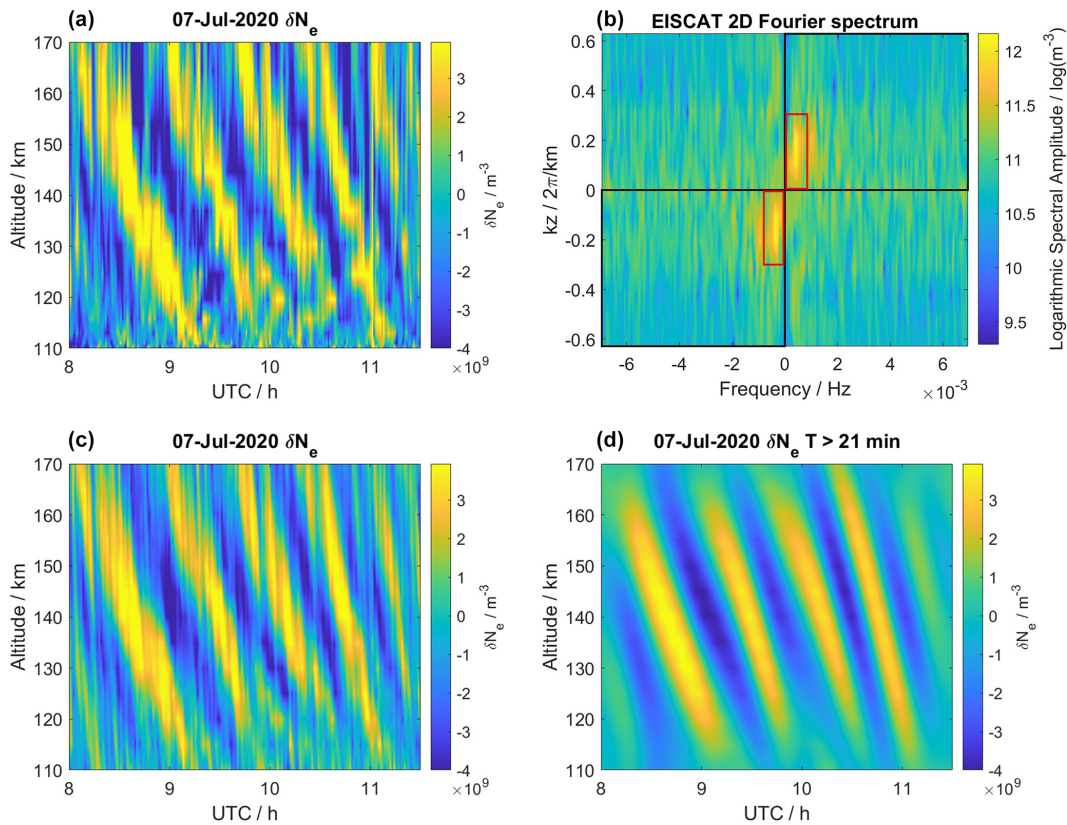


**Figure 2.** (a, b) Electron density variation  $\delta N_e$  (a) and associated 2D Fourier spectrum (b). (c, d)  $\delta N_e$  filtered for upward-propagating wave signals (c, filter edges shown as a black rectangle in the Fourier spectrum) and with additionally restricted wave parameters  $\tau \gtrsim 21$  min and  $\lambda_z \gtrsim 21$  km (d, filter edges shown as a red rectangle in the Fourier spectrum).

determine the times of the maxima from the wave period and phase shift profiles;

$$t_{\max}(z) = -\frac{\delta(z) \cdot \tau(z)}{2\pi} + t_0 + n \cdot \tau(z), \quad (3)$$

where  $n$  is a positive integer and  $t_0 = 08:00$  UTC. Connecting the times of maxima gives the vertical phase lines. Along

these phase lines, the vertical wave number  $k_z = 2\pi/\lambda_z$  can be determined by

$$k_z(z) = \frac{2\pi}{\tau} \frac{dt_{\max}(z)}{dz}. \quad (4)$$

Figure 3 (left) shows the fitted  $\delta N_e$  pattern, in which four phase lines are labeled by solid red and dashed black

lines. The vertical wavelength  $\lambda_z$  along the red phase line and the vertical profile of the wave period  $\tau$  are shown in Fig. 3 (right). A similar procedure was applied by Vadas and Nicolls (2009). It should be noted that  $\lambda_z < 0$  corresponds to downward phase progression; therefore, we show the absolute value  $|\lambda_z|$ .

The obtained profile of the vertical wavelength shows a steady increase from  $\sim 20$  to  $\sim 70$  km across the range of measurement altitudes. This agrees very well with previous results from both observations and models (e.g., Oliver et al., 1997; Vadas, 2007; Nicolls et al., 2014). The observed wave period  $\tau = 43.1 \pm 1.6$  min is nearly constant with altitude. The wave period is considerably larger than the buoyancy period of the neutral atmosphere, which increases approximately from 3–9 min across the transition region, but significantly smaller than the Coriolis period. For such medium-frequency waves (Fritts and Alexander, 2003; Sect. 2.1.2), the horizontal wavelength  $\lambda_H$  is much larger than the vertical wavelength  $\lambda_z$ , which, as will be shown later in this section, is also the case here. As described in Vadas and Becker (2018), the observed wave frequency is constant with altitude as long as the buoyancy frequency and the background horizontal wind do not change with time, which can be assumed for timescales of a few hours. Both the value of the measured wave period and the constant vertical profile agree with previous findings (e.g., Nicolls et al., 2014).

Though the Fourier filter has to be adjusted manually to account for the specific wave activity during a certain measurement time, the described procedure is an effective method to obtain vertical wave parameters from EISCAT measurements.

### 3.2 Meteor radar

Horizontal wave parameters are derived from measurements with the Nordic Meteor Radar Cluster. Figure 4 (left) shows the total horizontal wind velocity over the Nordic countries at 96 km altitude that was observed on 7 July 2020 at 10:00 UTC. These horizontally resolved 3D winds are analyzed to extract gravity waves, which are then linked to the TID measured with EISCAT. A time–altitude cross-section of wind measurements at 69° N, 22° E is shown in Fig. 4 (right).

In the first step, we identify potential gravity waves in the time–altitude domain for each grid cell in the Nordic domain. This is done by filtering the neutral wind measurements for a frequency band around the above-measured TID wave period of  $\tau \approx 43$  min. Waves on this timescale should be resolved in the 10 min resolution meteor radar measurements, and their oscillation period should be roughly constant with altitude. The analysis of time–altitude dynamics of meteor radar measurements is equivalent to the EISCAT analysis in the previous section. The main steps are illustrated in Fig. 5 for the selected grid cell at 69° N, 22° E.

Due to strong, large-scale changes in the background wind velocity with time and altitude, typical for northern hemispheric summer conditions at such high latitudes, a sliding window filter is applied with 60 min window length and 10 min time steps. The absolute velocity variations  $\delta u$  (top left) show signs of wave activity above 85 km at  $\sim 09:00$ – $11:00$  UTC. By applying a Fourier filter that allows only upward-propagating waves with periods of  $28 \text{ min} \lesssim \tau \lesssim 56 \text{ min}$ , we extract the underlying gravity wave mode at the cost of a slightly decreased amplitude (top right). Fitting the wave pattern (bottom left) and determining the wave parameters (bottom right), as described in Sect. 3.1, shows that the parameters of the detected wave mode fit well to those found in the EISCAT data at higher altitudes. The wave period  $\tau = 44.1 \pm 4.0$  min is nearly constant with altitude and is within the uncertainties of the wave period measured with EISCAT. The vertical wavelength strongly varies with altitude, exhibiting a minimum at approximately the altitude where the mesospheric summer wind reversal boundary occurs according to existing climatologies involving also some radars of the Nordic Meteor Radar Cluster (Stober et al., 2021d). At  $\sim 100$  km altitude, both total value ( $\lambda_z \approx 20$  km) and general trend fit well with the lowest altitudes of the profile shown in Fig. 3. This suggests that the detected wave mode is equivalent to the one seen in the EISCAT observations.

The analysis is repeated for each grid point of the Nordic Meteor Radar Cluster to obtain a horizontal field of filtered wind velocities. The horizontal wind field is Fourier filtered at each altitude level to emphasize the dominant horizontal wave numbers  $k_x$  and  $k_y$ . This reveals a northeastward-propagating wave mode that is strong enough to be detected at altitudes  $\geq 92$  km. The result of the horizontal wave analysis is shown in Fig. 6.

The horizontal wave parameters of interest are the horizontal wavelength  $\lambda_H$  and the propagation direction. Similar to the procedure for the vertical wave fitting, a horizontal wave function is defined in Eq. (5).

$$dU = A \cdot \sin\left(\frac{2\pi}{\lambda_H} \cdot (\cos\alpha \cdot x + \sin\alpha \cdot y) + \delta\right) \quad (5)$$

The wave propagation direction is defined as an angle  $\alpha$  that rotates counterclockwise from the geographical east direction. The least-square fit includes a phase shift  $\delta$  and a horizontally constant amplitude  $A$ . Figure 6 (top left) shows that the amplitude is indeed not horizontally constant; therefore, the fit is conducted on a reduced horizontal area from  $\sim 67.8$ – $71.1^\circ$  N latitude and  $18.4$ – $27^\circ$  E longitude. The fit shown in Fig. 6 (top right) yields a horizontal wavelength  $\lambda_H = 230$  km and a propagation direction of  $\alpha = 36.9^\circ$ . For altitudes  $\geq 92$  km, these parameters are approximately constant with altitude, which is in agreement with previous measurements and assumptions (Lighthill, 1978; Nicolls and Heinselman, 2007; Vadas and Nicolls, 2008). The obtained values for  $\lambda_H$  and  $\alpha$  are therefore assumed constant for all

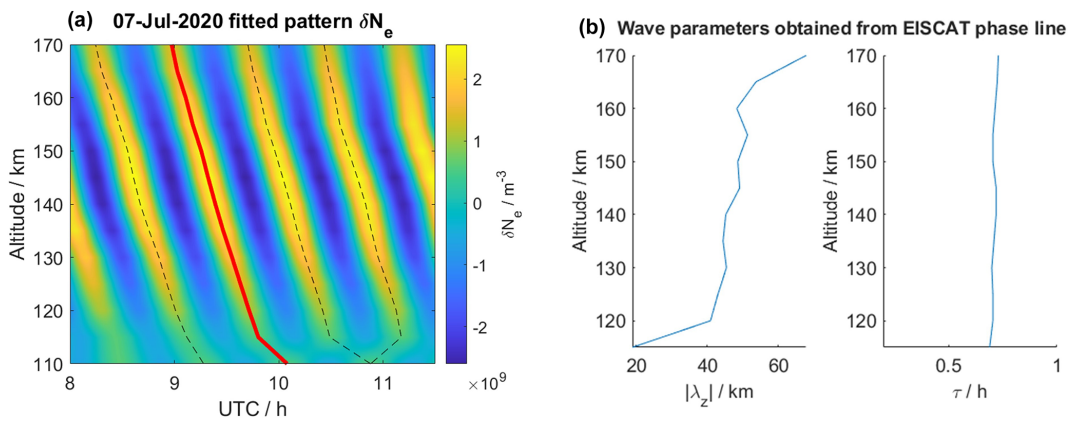


**Figure 3.** (a) Fitted wave pattern with phase lines (dashed). (b) Profiles of absolute vertical wavelength and wave period for the red phase line.

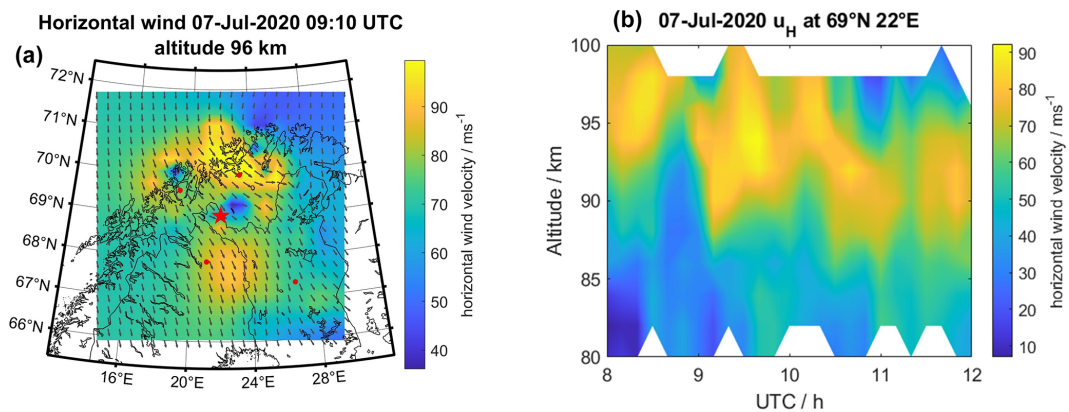


**Figure 4.** (a) Total horizontal wind velocity  $u_H$  measured by the Nordic Meteor Radar Cluster at 96 km altitude on 7 July 2020 at 10:00 UTC with grey arrows indicating the wind direction. The positions of the four meteor radars are marked as red dots. The position of the vertical cross-section in the right panel is indicated by a red star. (b) Time–altitude cross-section of  $u_H$  at  $69^\circ\text{N}$ ,  $22^\circ\text{E}$ .

altitudes. Furthermore, Fig. 6 (bottom) outlines the performance of the 3DVAR+DIV retrieval to infer the vertical and horizontal structure of such gravity waves. Although the sampling is given by randomly occurring meteors in space and time, the algorithm preserves the wave structure for the domain with a sufficient measurement response (measurement response not shown in this work; see for an example Stober et al., 2022).

### 3.3 Dispersion relation fit

The possibility of using AGW-TID observations and gravity wave dispersion relations (Hines, 1960; Vadas and Fritts, 2005) to infer neutral atmosphere parameters has been demonstrated in previous work (see, e.g., Nicolls and Heinselman, 2007; Vadas and Nicolls, 2008, 2009; van de Kamp et al., 2014). In particular, obtaining the vertical wave number  $k_z$  from ISR measurements has been established in these studies. However, the simultaneous measurement of the vertical and horizontal wavelengths of the same wave mode has

been difficult due to a lack of the observational capabilities of previous research instruments. Combining ISR measurements with the Nordic Meteor Radar Cluster provides a unique research capability to measure the thermospheric neutral wind covering the required spatial and temporal scales to enable such studies. The gravity wave dispersion relation gives the wave vector  $\mathbf{k}^2 = k_H^2 + k_z^2$  as

$$k^2 = \frac{N^2 k_H^2}{2\pi/\tau - |\mathbf{k}_H| \cdot U_{\parallel}} \cdot \gamma - \frac{1}{4H^2}, \tag{6}$$

with the Brunt–Väisälä (buoyancy) frequency  $N = \sqrt{-g/\rho(z) \cdot \partial\rho(z)/\partial z}$ , the atmospheric mass density profile  $\rho(z)$ , the observed wave period  $\tau$ , a viscosity term  $\gamma$ , and the atmospheric scale height  $H$ .  $U_{\parallel}$  is the neutral wind speed projected along the direction of the horizontal wave vector  $\mathbf{k}_H$ . It is defined as  $U_{\parallel} = (\mathbf{k}_H \cdot \mathbf{U}_H) / |\mathbf{k}_H|$ . The viscosity term of the anelastic dissipative dispersion relation

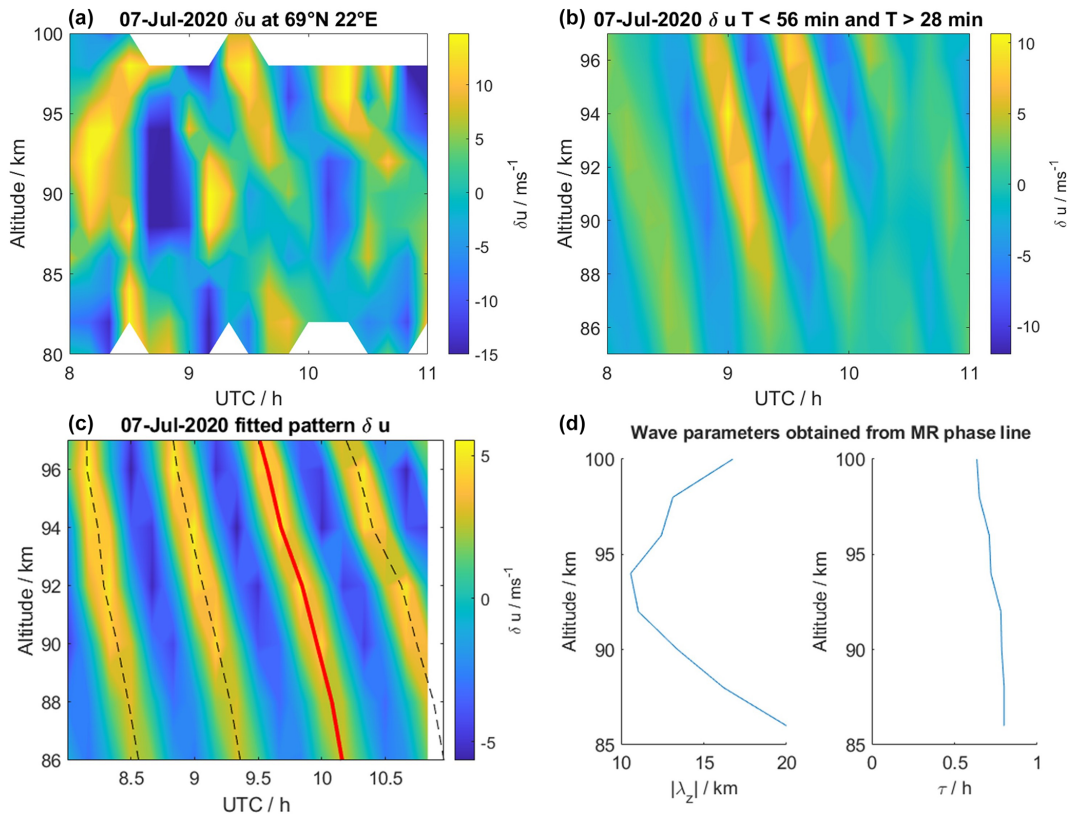


**Figure 5.** (a, b) Absolute variation of horizontal velocity  $\delta u$  in a time–altitude cross-section of the meteor radar measurements at 69° N, 22° E (a). Fourier filtering shows strong wave activity at 28 min  $\lesssim \tau \lesssim$  56 min (b). (c, d) The wave fitting (c) and phase line/wave parameter determination (d) methods are adapted from Sect. 3.1 and show that the wave parameters of the largest-amplitude wave agree well with the previously detected TID.

is, according to Vadas and Fritts (2005), given by

$$\gamma = \left\{ \left[ 1 + \frac{v^2}{4\omega_I^2} \left( k^2 - \frac{1}{4H^2} \right)^2 \left( \frac{1 - Pr^{-1}}{1 + 0.5\delta(1 + Pr^{-1})} \right)^2 \right] \cdot \left[ 1 + \delta(1 + Pr^{-1}) + \delta^2 Pr^{-1} \right] \right\}^{-1}, \quad (7)$$

with  $\delta = vk_z/H\omega_I$ , kinematic viscosity  $v$ , and the Prandtl number  $Pr = 0.7$ . In this study, the Prandtl number is assumed to be constant (Vadas and Fritts, 2005; Nicolls and Heinselman, 2007). In the zero-viscosity approximation ( $\gamma = 1$ ), Eq. (6) becomes the dispersion relation derived by Hines (1960). The neutral background atmosphere is taken from NRLMSISE-00 (Picone et al., 2002), and the kinematic viscosity is calculated from the Sutherland model (Sutherland, 1893). The vertical profiles of  $\lambda_z$  and  $\tau$  shown in Figs. 3 (right) and 5 (bottom right) are assumed to be associated with GWs, having altitude-independent values of  $\lambda_H = 230 \text{ km}$  and  $\alpha = 36.9^\circ$ . Equation (6) is solved for the optimum wind velocity  $U_{||}$ , applying a nonlinear least-square fit using a Levenberg–Marquardt algorithm (Marquardt, 1963). Figure 7 shows vertical profiles of the wind velocity along the propagation direction of the detected gravity wave. We

compare our results from both the viscous and non-viscous dispersion relation, measurements from the Nordic Meteor Radar Cluster projected to the AGW-TID propagation direction, and the empirical Horizontal Wind Model (HWM14; Drob et al., 2015) in Fig. 7.

It can be seen that the fitted wind velocities obtained from the viscous and non-viscous dispersion relations agree very well up to approximately 140 km altitude. Above that, the fit of the non-viscous dispersion relation no longer converges. This is mainly caused by the exponential increase of the kinematic viscosity that results in a breakdown of the zero-viscosity approximation. At altitudes  $\lesssim 100 \text{ km}$ , the fitted profiles are well within the range of the projected meteor radar measurements and associated uncertainties. The error bars in Fig. 7 show the upper and lower quartiles of all meteor radar wind velocity measurements during the interval 09:00–11:00 UTC. The comparison between the winds measured by the meteor radars and those derived from the wave parameters exhibits a reasonable agreement considering both statistical uncertainties (shaded blue area and error bars). This provides some confidence and validation of the applied approach to ensure that the neutral winds are reliable within the frame of the involved assumptions. The fitted wind ve-

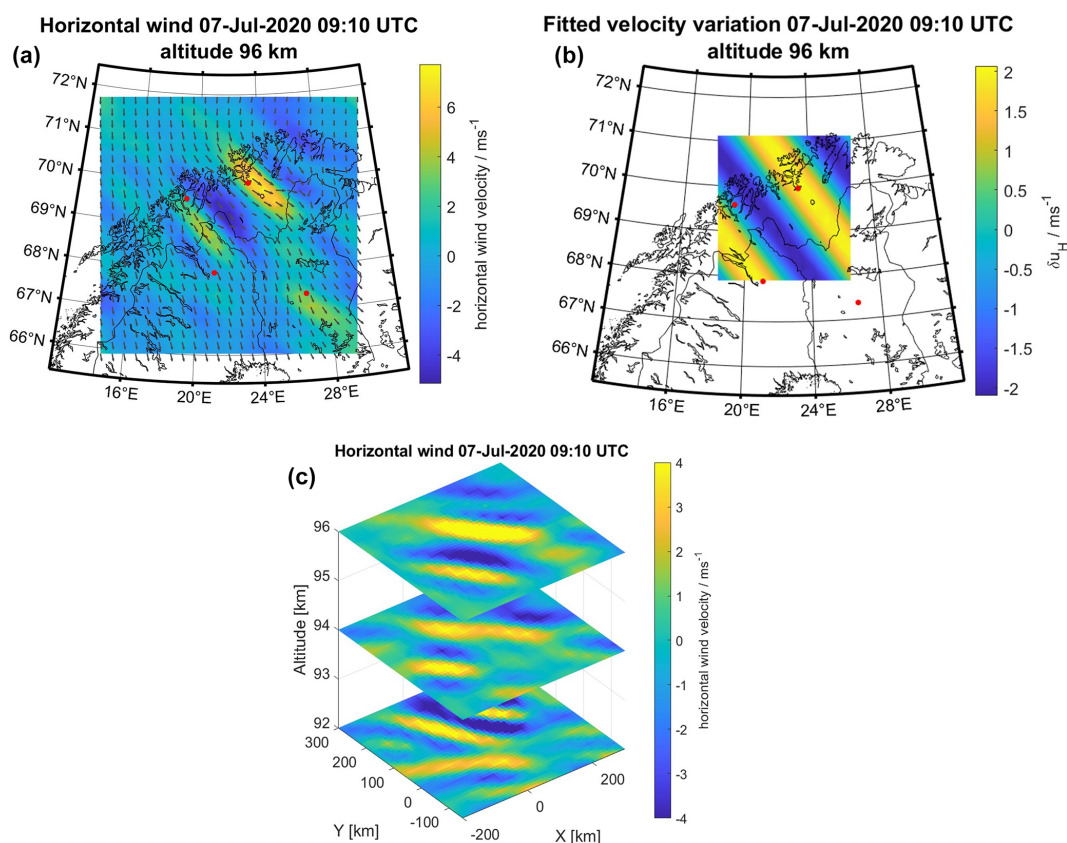


**Figure 6.** (a, b) Northeastward-propagating wave mode found in the filtered wind field ( $28 \text{ min} \leq \tau \leq 56 \text{ min}$ ) at 96 km altitude (a) and fitted wave pattern (b). The grey arrows in the left panel show the total wind field identical to the one shown in Fig. 4. (c) The wave mode can be detected at multiple altitude layers.

locity profiles follow the general trend of the profile given by HWM14, though the exact velocities are significantly different. Since HWM14 is an empirical model aiming to capture only the statistical climatology average wind velocity, such discrepancies are expected. To emphasize the sensitivity of the velocity fit procedure, the variations of the result for  $\lambda_z \pm 5 \text{ km}$  are shown as the shaded area in Fig. 7. It can be seen that, especially at altitudes below 110 km, variations within a few kilometers of the vertical wavelength can have a quite significant impact on the inferred wind velocity. This indicates that a more accurate determination of the wave parameters is required.

#### 4 AGW-TID parameters during the fall transition

Neutral wind observations at the altitude region from 90–150 km are important to investigate the E-region dynamo and vertical coupling as well as dynamical coupling processes between the ionized and neutral atmosphere (Baumjohann and Treumann, 1996). The above-described method to derive neutral winds at E-region altitudes leveraging AGW-dispersion relations and multi-instrument observations opens

the opportunity to study these processes under various conditions throughout the year. In the following, we apply this method to an AGW-TID event that occurred during the MLT fall transition. The fall transition is connected to the autumn equinox and has been shown to have a major impact on atmospheric tides in the MLT region (Stober et al., 2021d; Pedatella et al., 2021; Günzkofer et al., 2022). Other studies suggest that there is also an impact on the gravity wave forcing from below (Placke et al., 2015) which, consequently, will alter the observed wave parameters in the ionosphere. Figure 8 shows two electron density measurements collected with the EISCAT VHF radar on 1 September and 13 October 2022. The data are processed as described in Sect. 3. Both measurements exhibit signatures of TID activity indicating oscillation periods longer than  $\tau > 21 \text{ min}$ , as visualized in Fig. 8 (right panels).

As expected, the electron density is reduced for the October measurement compared to September, due to the generally lower elevation angle of the sun. Furthermore, the filtered data show gravity wave modes at around 10:00–12:00 UTC with wave periods shorter than 1 h. We also want to point out that the measurements on 1 September indicate the presence of a second wave mode with a notably larger

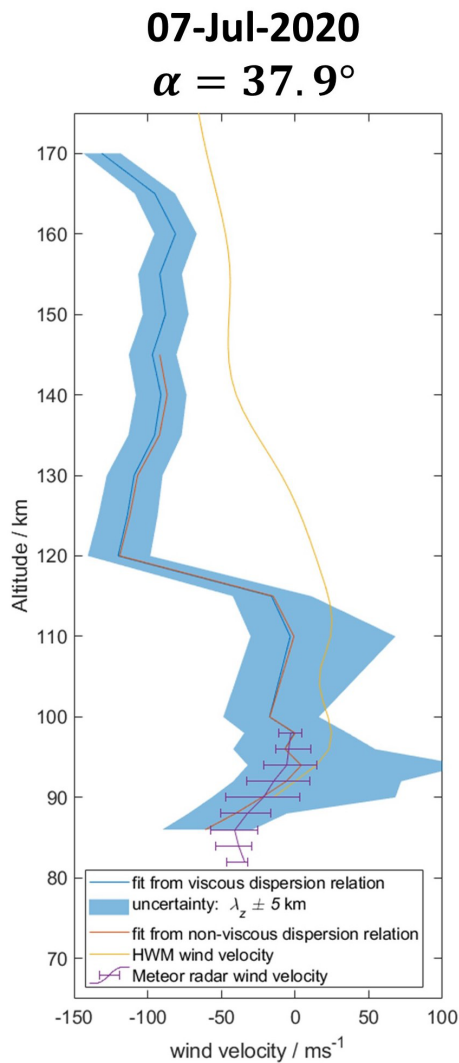


**Figure 7.** Comparison of wind velocities from dispersion relation fit, meteor radar measurements projected to the wave propagation direction, and HWM14. The shaded area shows the sensitivity of the fit for variations within  $\lambda_z \pm 5$  km.

period around 08:00–10:00 UTC. Applying our analysis procedure as described in Sect. 3, the identified wave modes are separated, and the gravity wave parameters are determined. Figure 9 shows the filtered (top) and fitted (middle) wave modes as well as the determined wave parameters (bottom).

Both TIDs observed on 1 September show a similar profile of the vertical wavelength, indicating a gentle increase up to the maximum at  $\sim 140$  km altitude with  $\lambda_z \approx 40$  km. Above that, the vertical wavelength decreases rapidly. However, the analysis of the longer period TID, detected between 08:00–10:00 UTC, exhibits an increased uncertainty above 155 km altitude. Both TIDs show a nearly constant wave period in the altitude range from 110–170 km. The long period TID in Fig. 8 has a mean wave period of  $\tau = 69.2 \pm 1.4$  min and for the other TID, we obtained a period of  $\tau = 26.9 \pm 0.4$  min.

The TID observed on 13 October shows a steady decrease in vertical wavelength from 120–170 km. The sharp increase in wavelength below 120 km is caused by an inaccurate fit of the pattern, as indicated by the increased fit uncertainty, and is therefore not physical. The vertical wavelengths resemble similar values between  $\sim 20$ –40 km in comparison to the TIDs that were found in our first measurements. The mean wave period is  $\tau = 33.5 \pm 2.0$  min and shows a slight tendency for a small increase in the period with increasing altitude. This is also reflected in the increased uncertainty.

It should be noted that the two TIDs at 10:00–12:00 UTC, though occurring at the same time of the day, exhibit notably different wave periods and vertical wavelength profiles. This might be the first indication of the impact of the MLT fall transition on the parameters of AGW-TIDs. The next step is to identify the observed TIDs in measurements of the Nordic Meteor Radar Cluster. As shown in Sect. 3, the meteor radar data are going to add horizontal information about the gravity waves and also provide information about the changes in the mean background winds during the fall transition. Since there was no signature in the meteor radar data of an AGW corresponding to the larger-scale TID observed on 1 September, the following analysis would be restricted to the two TIDs occurring around 10:00–12:00 UTC. A time–altitude cross-section of the filtered waves and the parameter analysis is shown in Fig. 10.

The horizontal winds from both measurements were filtered for  $21 \text{ min} < \tau < 42 \text{ min}$ . Most notably, below about 92 km, both AGWs are observed at similar wave periods slightly longer than 30 min, which is closer to the TID wave period found for the October event. While the AGW observed during October shows a constant wave period throughout the entire altitude range, the September AGW shows a transition to shorter wave periods at about 92–96 km altitude. The wave period above this transition is  $< 30$  min and close to the period of the September TID. A summary of the wave periods from the ISR and meteor radar AGW-TIDs is given in Table 1.

More important are the altitude-dependent changes of the vertical wavelength for both campaign periods during the fall transition. In September, the AGW exhibits a strong peak in vertical wavelength at 92 km altitude, whereas the October AGW event shows a nearly constant vertical wavelength at all observed altitudes in the meteor-radar-derived winds. At about 92 km our fitting method seems to suffer from rather large uncertainties due to a weaker amplitude of the filtered signal. This leads to an apparent downward propagation of some wave fronts in Fig. 10 (top, middle) which causes the determined phase lines to jump in between wave fronts. Apparently, at this altitude, other processes disturb the vertical propagation of the AGW. It should be considered that, during the fall transition at the beginning of September, the classical circulation pattern changes from the typical summer situation with the mesospheric zonal wind reversal with a strong vertical shear to a weaker mean background wind around Oc-

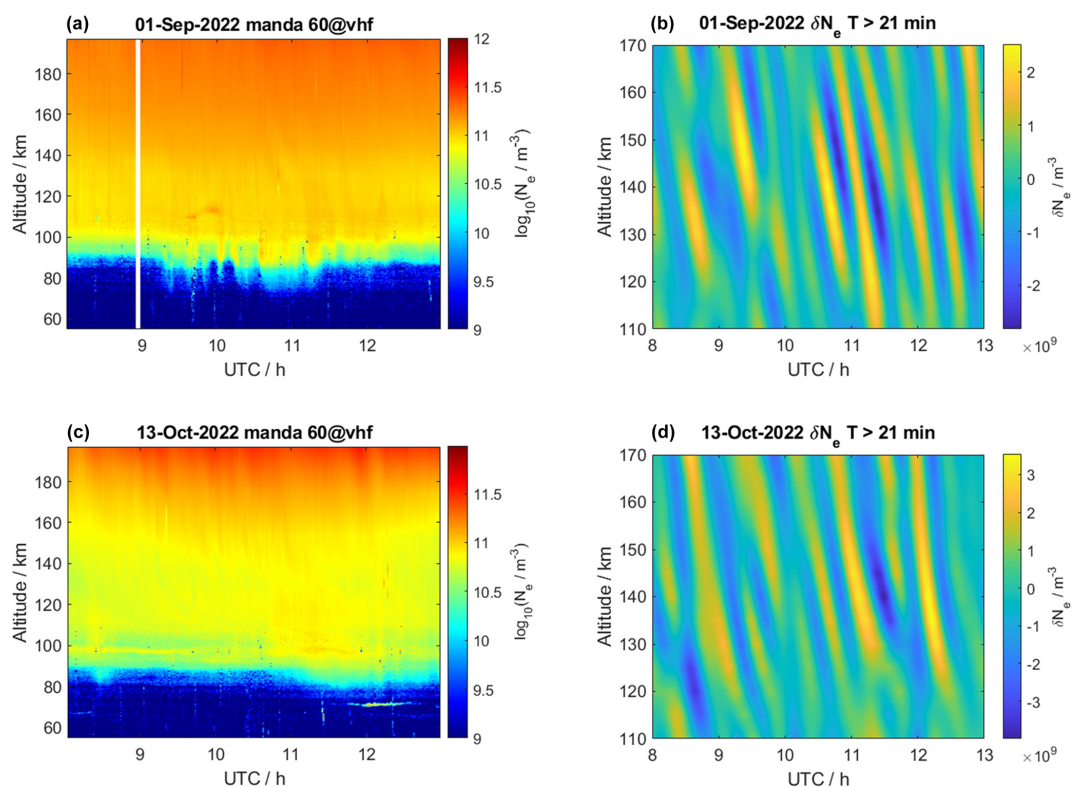


**Figure 8.** Electron densities measured with the EISCAT VHF radar (a, c) and TIDs filtered for  $\tau > 21$  min (b, d). Shown are the measurements before (1 September, a, b) and after (13 October, c, d) the fall transition.

**Table 1.** Summary of determined wave periods for the three detected TIDs/AGWs.

Date	1 September 2022	1 September 2022	13 October 2022
Time	08:00–10:00 UTC	10:00–12:00 UTC	10:00–12:00 UTC
$\tau$ [min] from EISCAT (110–170 km)	$69.2 \pm 1.4$	$26.9 \pm 0.4$	$33.5 \pm 2.0$
$\tau$ [min] from meteor radar (86–98 km)	–	$32.9 \pm 7.1$	$32.9 \pm 0.7$

tober before the winter circulation establishes (Stober et al., 2021d). Such vertical wind shears alter the vertical propagation conditions and, thus, can lead to changes in the observed gravity wave parameters for an observer in an Earth-fixed coordinate frame. Another possible cause for such a strong vertical shear at the MLT is related to atmospheric tides. In particular, the semidiurnal tide exhibits a sudden increase in amplitude during September and shows rather short vertical wavelengths posing favorable conditions to cause strong vertical shears in the flow. Furthermore, the semidiurnal tidal enhancement lasts only a few weeks around the beginning of September and disappears towards October, which further underlines the different dynamical situations of the large-scale flow between the 2 campaign days during the fall transition. Figure 11 shows the tidal amplitude and phase of the semidiurnal tide over Tromsø from the end of summer (August) until the end of the fall transition in October. The red vertical lines label the campaign days. It is evident that for the

event on 1 September, the semidiurnal tide showed a rather short vertical wavelength of about 40–60 km, providing favorable conditions to generate a strong vertical wind shear considering also the enhanced amplitude during this period. Hence, the year 2022 is representative of the typical climatological behavior for the fall transition and the evolution of the semidiurnal tidal amplitude and phase (Stober et al., 2021d).

As described in Sect. 3, the wave period filtering is repeated for all grid points of the Nordic Meteor Radar Cluster, and the horizontal wind field is Fourier filtered around the dominant horizontal wave numbers. Both AGWs can be observed in a horizontal cross-section which is visualized in Fig. 12 (September) and Fig. 13 (October).

Most notably, the two AGWs have different horizontal propagation directions. The September AGW propagates in a southwestward direction at an angle  $\alpha = 227.7^\circ$  rotated counterclockwise from the geographical east. The October AGW travels in a northwestward direction at an angle  $\alpha =$

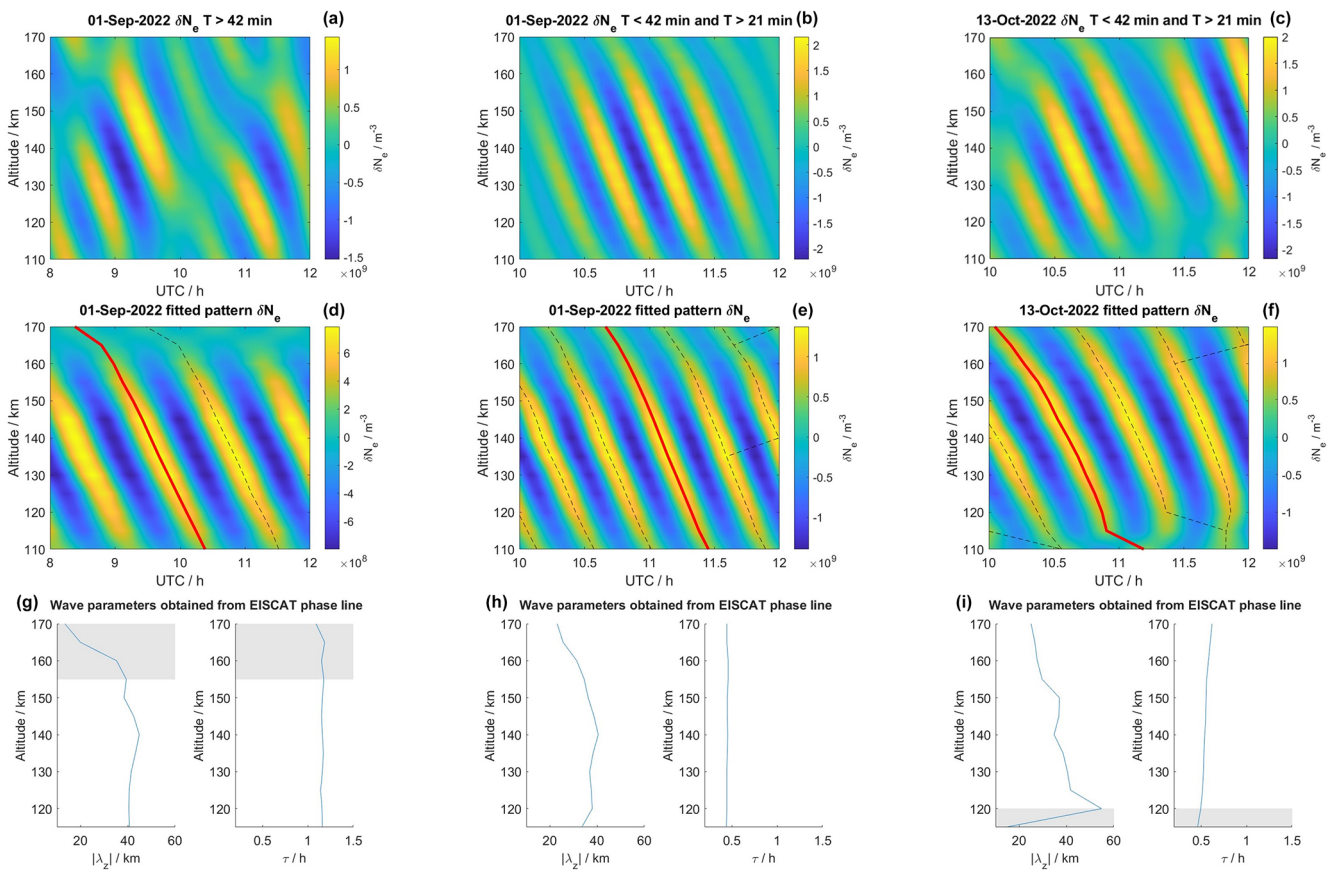


**Figure 9.** (a–c) EISCAT VHF electron density variations filtered to isolate each of the three identified wave modes. (d–f) Fits of the wave modes and the obtained phase lines. (g–i) Wave parameters determined for the red phase lines. The shaded areas indicate altitudes with a range normalized root-mean-square error NRMSE  $> 0.25$ .

$137.7^\circ$ . It can also be seen that their respective maximum amplitudes occur at different positions, though both AGWs are visible around the geographic coordinates of Tromsø. This increases the likelihood that these GWs correspond to the TIDs detected with the EISCAT VHF radar. The horizontal wavelengths are notably different as well, with  $\lambda_H = 150$  km for the September AGW event and with  $\lambda_H = 250$  km for the October AGW event. Both AGWs can be observed at multiple altitude levels at or above 94 km altitude, and their horizontal wavelengths remain roughly constant at these altitudes.

All wave parameters ( $\lambda_z$ ,  $\lambda_H$ ,  $\tau$ , and  $\alpha$ ) are determined for the two AGW-TIDs that were found in the measurements at 10:00–12:00 UTC. Leveraging the results of the wave analysis, we infer the vertical profile of background neutral wind velocities. The profiles for 1 September and 13 October are shown in Fig. 14. However, due to the very good agreement at the MLT and lower E-region between the viscous and non-viscous results obtained before, we limited the analysis to the viscous dispersion relation here. Similarly, to the previous analysis, the fit is compared to the HWM14 model and

the meteor radar measurements for the time interval where the AGW-TID was observed.

At the altitudes of the meteor radar measurements, both fitted profiles show a similar trend as the measurements, although there are sometimes substantial differences in the absolute values, especially on 1 September around 90–94 km. The largest deviations are found for the altitudes of the vertical transition due to the strong vertical shear and corresponding changes in the wind direction and magnitude at approximately  $\sim 94$  km that can be seen in Fig. 10. This leads to the conclusion that strong vertical shears imposed by the mean background winds or tides impact the accuracy and precision of the parameter determination and result in larger uncertainties in the neutral winds derived from the wave parameters. At the altitudes of the EISCAT measurements, the fitted velocity profiles show a similar general trend compared to the HWM14 profiles but sometimes indicate substantial magnitude differences. However, as mentioned in Sect. 3, this is attributed to the climatology nature of the HWM14 velocities, which cannot reflect specific synoptic situations due to a particular wave field or energetic forcing. The resemblance

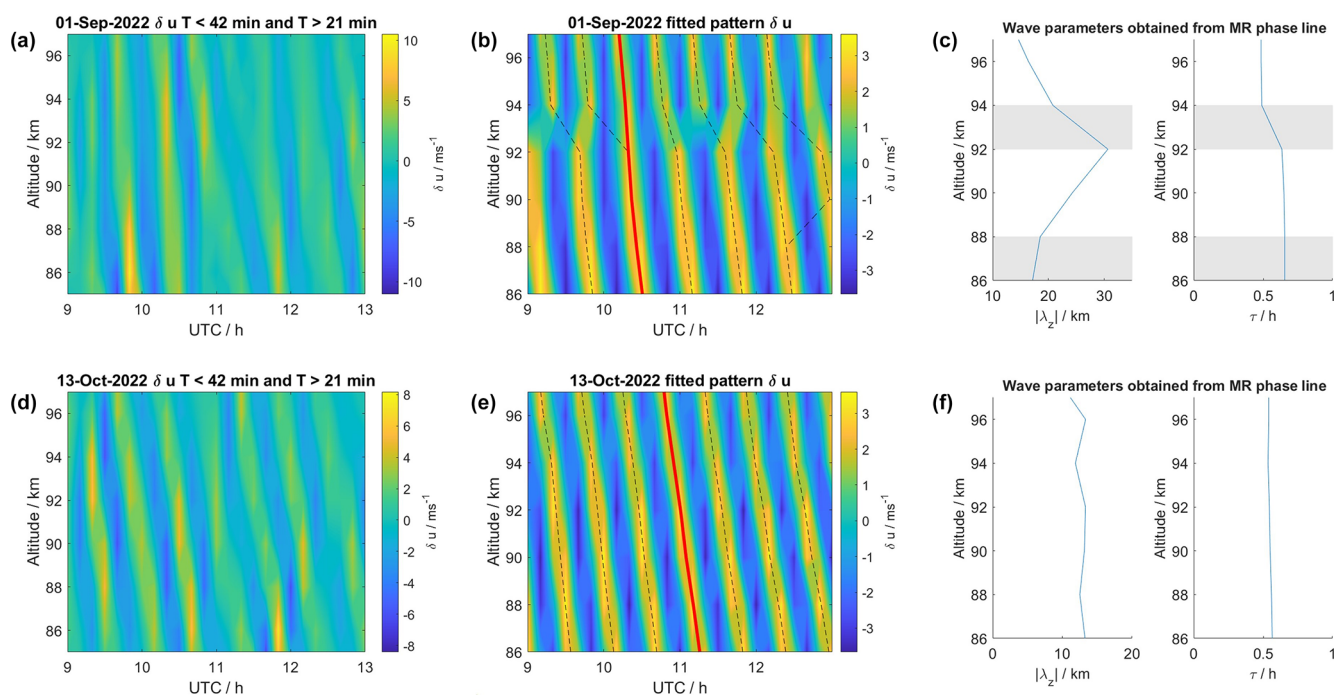


**Figure 10.** (a, d) Time–altitude cross-section of filtered horizontal wind variations measured with the Nordic Meteor Radar Cluster at 69° N, 22° E on 1 September (a) and 13 October (d) 2022 at 09:00–13:00 UTC. (b, e) Fitted gravity wave oscillations and obtained phase lines. (c, f) Wave parameters determined for the red phase lines. Shaded areas indicate NRMSE > 0.35.

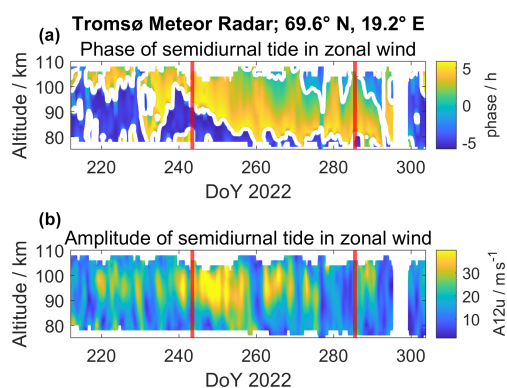


**Figure 11.** (a) Phase of semidiurnal zonal wind tide measured with the Tromsø meteor radar from August till October 2022. The vertical red lines mark the 2 measurement days of EISCAT. (b) The amplitude of the semidiurnal zonal wind tide shows a maximum in early-to-mid September.

of the fitted profiles with both measured and modeled profiles is a promising first result for this method.

### 5 Discussion

Combining observations with the EISCAT radar and the Nordic Meteor Radar Cluster provides a new capability to study AGW-TIDs. The presented approach avoids sev-

eral problems arising from previous techniques using either multi-beam ISR measurements or a combination of classical ISR and GNSS networks. Measurements with a phased array ISR would in addition permit the determination of both vertical and horizontal properties of a single wave mode. However, the horizontal resolution of such measurements is limited. Consequently, horizontal wavelength and propagation direction can only be roughly determined (Nicolls and Heinselman, 2007; Vadas and Nicolls, 2008). This should also limit the capability of inferring background neutral winds significantly. On the other hand, GNSS networks allow us to measure MS-TIDs with high spatial and temporal resolutions (Saito et al., 1998; Tsugawa et al., 2007). The disadvantage of this technique is that 2D TEC maps do not allow for the separation of different wave modes, which makes a combination with ISR measurements difficult (van de Kamp et al., 2014). The measurements of TIDs with the LOFAR radio telescope might provide additional information about AGW-TID wave parameters and propagation. The radio scattering due to ionospheric irregularities can be evaluated for several scattering altitudes, which allows for distinguishing different TID wave modes (Fallows et al., 2020). However, the vertical resolution of these measurements is presumably not sufficient to allow for determining vertical wavelengths. Even the measurement of horizontal wavelengths has proven difficult so far (Boyd et al., 2022). Nevertheless, TID measurements from radio scattering due to ionospheric irregularities might

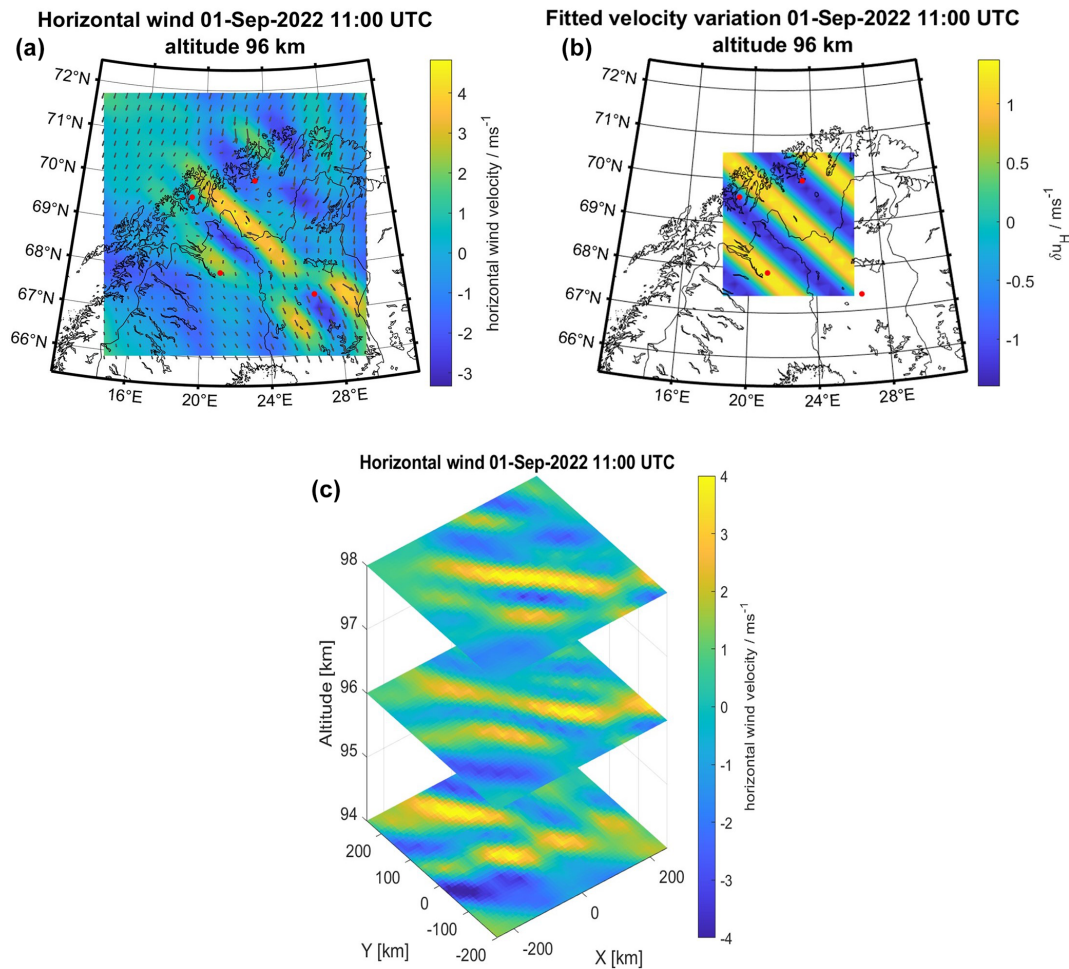


**Figure 12.** Horizontal cross-section of wind variations for 1 September, 11:00 UTC. Shown are the filtered wind variations (a), the wave fit (b), and a slice plot of three altitude levels (c).

provide an additional possibility to determine and validate AGW-TID wave parameters.

The AGW-TID wave parameters determined in this paper are all within the parameter range ( $\lambda_z \sim 10\text{--}100\text{ km}$ ,  $\lambda_H \sim 100\text{--}300\text{ km}$ ,  $\tau \sim 20\text{--}100\text{ min}$ ) found in several previous studies (see, e.g., Oliver et al., 1997; Kotake et al., 2007; Nicolls and Heinselman, 2007; Vadas, 2007; van de Kamp et al., 2014; Nicolls et al., 2014). It has been shown that daytime MS-TIDs are mostly connected to an upward-propagating AGW from lower atmospheric layers, whereas nighttime MS-TIDs can be generated by electrodynamic processes in the ionosphere, e.g., Joule heating or the Perkins instability (Tsugawa et al., 2007). These AGW-TIDs generated in situ are unlikely to propagate down to the altitudes covered by the Nordic Meteor Radar Cluster. Therefore, the simultaneous detection of daytime AGW-TIDs with the EISCAT radar and the Nordic Meteor Radar Cluster in this study underlines many of the results obtained in previous studies.

Future work should target the investigation of wave parameter changes caused by other atmospheric events besides the MLT fall transition. Events of special interest might be sudden stratospheric warmings, the “hiccup” of the autumn transition, and the spring transition, which all show distinct similarities and differences (Matthias et al., 2015, 2021). Determining wave parameters from simultaneous measurements with additional instruments would help to further refine the demonstrated method and possibly expand the range of investigated altitudes. These could include the well-established MS-TID measurements with GNSS networks as discussed above. Since both the Nordic Meteor Radar Cluster and GNSS networks allow for the determination of the propagation direction, single wave modes might be observed simultaneously and thereby linked to EISCAT measurements. Statistical studies of daytime and nighttime MS-TIDs suggested that the preferred propagation direction of these waves depends on the generation mechanism (Kotake et al., 2007; Tsugawa et al., 2007). These studies were conducted on measurements in the North American region, which makes a

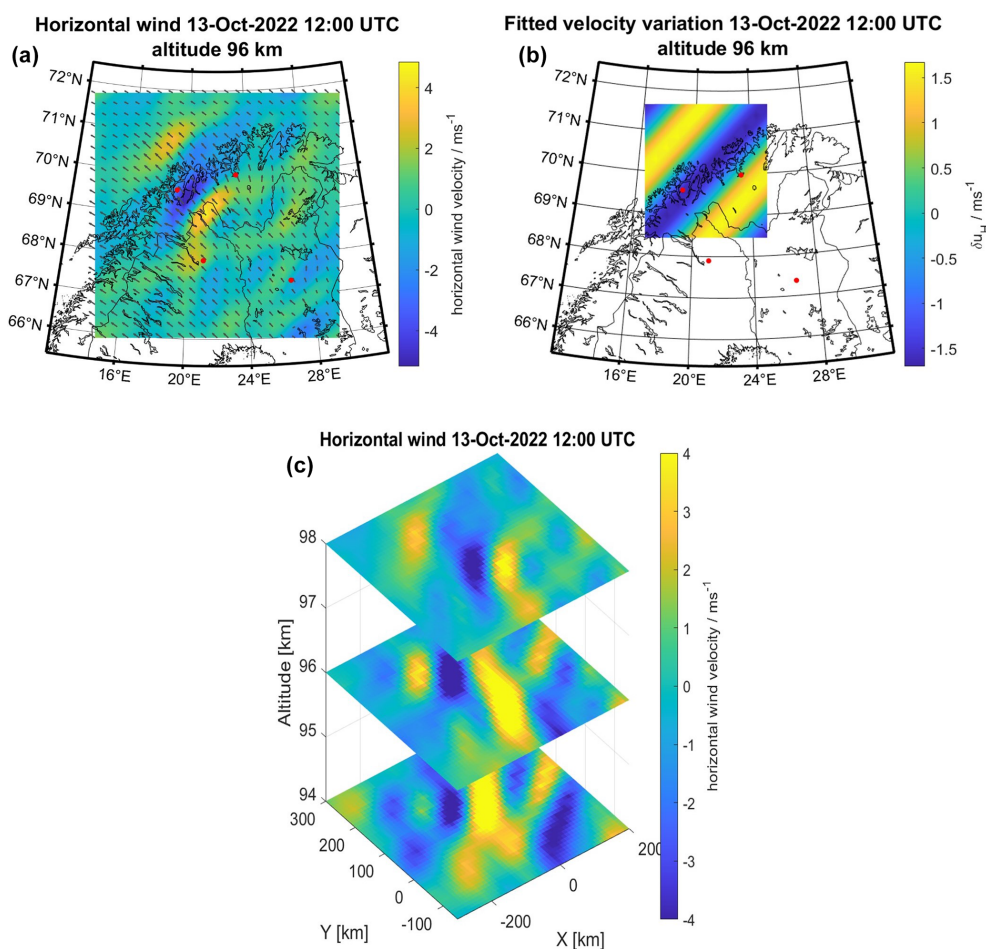


**Figure 13.** Horizontal cross-section of wind variations for 13 October, 12:00 UTC. Shown are the filtered wind variations (a), the wave fit (b), and a slice plot of three altitude levels (c).

comparison to our measurements in Fennoscandia difficult. Based on the work of van de Kamp et al. (2014), such studies could be conducted in this region combined with EISCAT and Nordic Meteor Radar Cluster measurements. The application of OH airglow spectrometers has been previously demonstrated (Wüst et al., 2018; Sarkhel et al., 2022) and could be applied as well. There are several planned satellite missions targeting the detection of AGWs in the MLT region that might provide valuable additional information (e.g., Gumbel et al., 2020; Sarris et al., 2023). Comparison to a gravity wave resolving atmosphere model like the High Altitude Mechanistic General Circulation Model (HIAMCM) (Becker and Vadas, 2020) would give valuable insight into the origin and generation of observed waves. This includes the potential role of secondary and tertiary gravity waves generated in the mesosphere and thermosphere (Vadas and Becker, 2018; Vadas and Becker, 2019) and the polar night jet (Becker et al., 2022a, b; Vadas et al., 2023a). Validation of the inferred velocity profiles above 100 km altitude is difficult with the presently available instruments. However,

the EISCAT\_3D system (McCrea et al., 2015; Stamm et al., 2021) could enable altitude-resolved multi-static ISR measurements from which neutral winds could be inferred. This would allow for verification of the inferred neutral wind profiles and the applied method in general. It could then be applied at other measurement sites where AGW-TIDs can be detected but where neutral winds cannot be measured directly.

## 6 Conclusions

It has been shown that vertical and horizontal wave parameters of AGW-TIDs can be determined from simultaneous measurements with the EISCAT VHF radar and the Nordic Meteor Radar Cluster. Such observations allow for studying the vertical coupling processes and propagation of AGW-TIDs. EISCAT and meteor radar measurements can be combined since they are only separated by about 10–20 km in altitude. High-time-resolution multi-static meteor radar measurements at 10 min steps allow us to estimate the wave

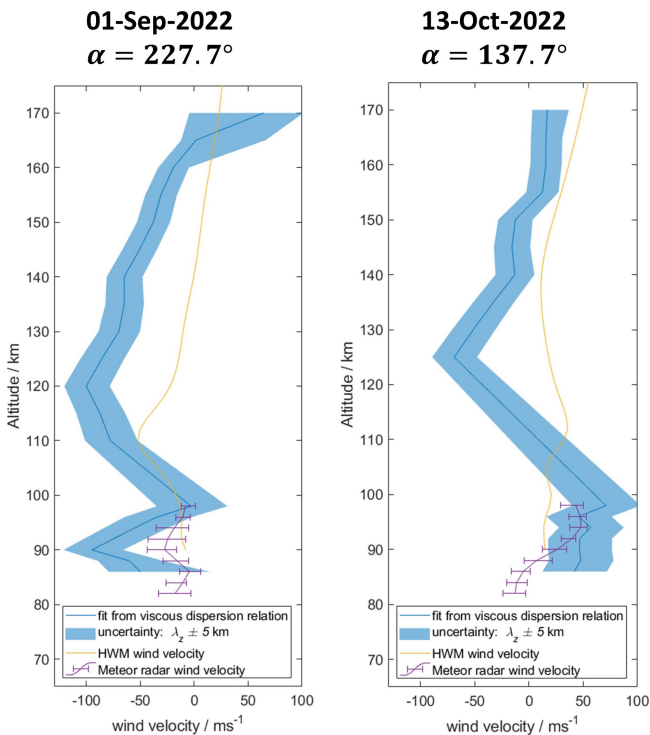


**Figure 14.** Wind velocity profiles along the propagation direction of the AGW-TIDs detected for each of the measurement days. The propagation direction is given as angle  $\alpha$  rotated counterclockwise from the geographic east. The shaded area shows the fit sensitivity for variations  $\lambda_z \pm 5$  km.

period and therefore specifically filter out wave modes detected in EISCAT measurements. The developed techniques to filter wave modes and determine wave parameters can be adapted to other EISCAT and meteor radar campaigns. We demonstrated the application of this method on two measurement campaigns conducted in early September and mid-October 2022, before and after the MLT fall transition. In both measurements, an AGW-TID occurring around 10:00–12:00 UTC with a wave period of roughly 30 min was detected. We showed that both waves exhibited a similar parameter range below  $\sim 90$  km. The September AGW-TID underwent notable changes in vertical wave parameters that were detected in the ionosphere. This shows that the fall transition impacts the ionospheric variability due to the amplification of semidiurnal tides in early September and the tidal minimum in October. Our study also shows that it is possible to apply the determined wave parameters to infer neutral wind velocity profiles in the thermosphere. While the absolute values of the inferred, measured, and modeled wind velocities did not always agree, the general trend of the profiles showed remarkable agreement considering the typical statistical errors. This indicates that this method provides a possibility for reliable neutral wind estimates in the thermosphere, given more refinement and validation. A more ex-

tensive data collection from the multi-instrument AGW-TID measurements discussed above, including ISR, meteor radar, GNSS, ground- and satellite-based airglow imagers as well as explicit wave simulations is going to improve the database to study the vertical coupling and permit further refinement of the applied procedures. Extending these studies to other events, e.g., sudden stratospheric warmings, will help us to understand the impact of atmospheric variability on the ionosphere. As already mentioned, the upcoming EISCAT\_3D system will allow us to verify the inferred neutral wind profiles so that the presented method might become a generally applicable tool for neutral wind measurements in the lower ionosphere.

**Data availability.** The data are available under the Creative Commons Attribution 4.0 International license at <https://doi.org/10.5281/zenodo.7752777> (Günzkofer et al., 2023). Please contact Alexander Kozlovsky ([alexander.kozlovsky@oulu.fi](mailto:alexander.kozlovsky@oulu.fi)) for the Nordic Meteor Radar Cluster 3DVAR+DIV retrievals.

**Author contributions.** FG performed the data analysis and wrote large parts of the paper. DP, GS, and IM suggested the idea for the multi-static EISCAT experiment and were the principal investigators (PIs) of the July 2020 EISCAT campaign. AT provided the analysis of ion velocity vectors and helped to plan the EISCAT experiments. SLV suggested the application of Fourier filters, and SLV and ErB provided feedback on the AGW-TID analysis. AK, MT, NG, SN, ML, EvB, JK, and NLM are PIs of the Nordic Meteor Radar Cluster. All the authors provided feedback and were involved in revising the manuscript. The supervision of FG by CB is supported by the University of Bern.

**Competing interests.** At least one of the (co-)authors is a member of the editorial board of *Annales Geophysicae*. The peer-review process was guided by an independent editor, and the authors also have no other competing interests to declare.

**Disclaimer.** Publisher's note: Copernicus Publications remains neutral with regard to jurisdictional claims made in the text, published maps, institutional affiliations, or any other geographical representation in this paper. While Copernicus Publications makes every effort to include appropriate place names, the final responsibility lies with the authors.

**Special issue statement.** This article is part of the special issue "Special issue on the joint 20th International EISCAT Symposium and 15th International Workshop on Layered Phenomena in the Mesopause Region". It is a result of the Joint 20th International EISCAT Symposium 2022 and 15th International Workshop on Layered Phenomena in the Mesopause Region, Eskilstuna, Sweden, 15–19 August 2022.

**Acknowledgements.** EISCAT is an international association supported by research organizations in China (CRIRP), Finland (SA), Japan (NIPR), Norway (NFR), Sweden (VR), and the United Kingdom (UKRI). This work uses pyglow, a Python package that wraps several upper-atmosphere climatological models. The pyglow package is open source and available at <https://github.com/timduly4/pyglow/> (last access: 16 October 2023). Dmitry Pokhotelov acknowledges discussions with Richard Fallows on the LOFAR scintillation work. The Esrange meteor radar operation, maintenance, and data collection were provided by the Esrange Space Center of the Swedish Space Corporation. The Nordic Meteor Radar Cluster data analysis and calculations were performed on UBELIX (<http://www.id.unibe.ch/hpc>, last access: 20 February 2023), the high-performance computing (HPC) cluster at the University of Bern. Gunter Stober is a member of the Oeschger Center for Climate Change Research (OCCR).

**Financial support.** This research has been supported by the STFC (grant no. ST/S000429/1) and the Japan Society for the Promotion of Science (JSPS, Grants-in-Aid for Scientific Research, grant no. 17H02968). This research has been supported by the Schweizerischer Nationalfonds zur Förderung der Wissenschaftlichen Forschung (grant no. 200021-200517/1). Ingrid Mann is supported by the Research Council of Norway (grant no. NFR 275503). Sharon L. Vadas was supported by NSF grant AGS-1832988.

**Review statement.** This paper was edited by Noora Partamies and reviewed by Stephan C. Buchert and Maxime Grandin.

## References

- Andrews, D. G.: An introduction to atmospheric physics, Cambridge University Press, ISBN 978-0-511-72966-9, 2010.
- Azeem, I., Yue, J., Hoffmann, L., Miller, S. D., Straka, W. C., and Crowley, G.: Multisensor profiling of a concentric gravity wave event propagating from the troposphere to the ionosphere, *Geophys. Res. Lett.*, 42, 7874–7880, <https://doi.org/10.1002/2015GL065903>, 2015.
- Azeem, I., Vadas, S. L., Crowley, G., and Makela, J. J.: Traveling ionospheric disturbances over the United States induced by gravity waves from the 2011 Tohoku tsunami and comparison with gravity wave dissipative theory, *J. Geophys. Res.-Space*, 122, 3430–3447, <https://doi.org/10.1002/2016JA023659>, 2017.
- Bauer, S. J.: An Apparent Ionospheric Response to the Passage of Hurricanes, *J. Geophys. Res.*, 63, 265–269, <https://doi.org/10.1029/JZ063i001p00265>, 1958.
- Baumjohann, W. and Treumann, R. A.: Basic space plasma physics, Imperial College Press, <https://doi.org/10.1142/p015>, 1996.
- Becker, E.: Dynamical Control of the Middle Atmosphere, *Space Sci. Rev.*, 168, 283–314, <https://doi.org/10.1007/s11214-011-9841-5>, 2012.
- Becker, E. and Vadas, S. L.: Explicit Global Simulation of Gravity Waves in the Thermosphere, *J. Geophys. Res.-Space*, 125, e28034, <https://doi.org/10.1029/2020JA028034>, 2020.
- Becker, E., Goncharenko, L., Harvey, V. L., and Vadas, S. L.: Multi-Step Vertical Coupling During the January 2017 Sudden Stratospheric Warming, *J. Geophys. Res.-Space*, 127, e2022JA030866, <https://doi.org/10.1029/2022JA030866>, 2022a.
- Becker, E., Vadas, S. L., Bossert, K., Harvey, V. L., Zülicke, C., and Hoffmann, L.: A High-Resolution Whole-Atmosphere Model With Resolved Gravity Waves and Specified Large-Scale Dynamics in the Troposphere and Stratosphere, *J. Geophys. Res.-Atmos.*, 127, e2021JD035018, <https://doi.org/10.1029/2021JD035018>, 2022b.
- Boyde, B., Wood, A., Dorrian, G., Fallows, R. A., Themens, D., Mielich, J., Elvidge, S., Mevius, M., Zucca, P., Dabrowski, B., Krankowski, A., Vocks, C., and Bisi, M.: Lensing from small-scale travelling ionospheric disturbances observed using LOFAR, *J. Space Weather Spac.*, 12, 34, <https://doi.org/10.1051/swsc/2022030>, 2022.
- Brekke, A.: On the relative importance of Joule heating and the Lorentz force in generating atmospheric gravity waves and infrasound waves in the auroral electrojets, *J. Atmos. Terr. Phys.*, 41, 475–479, [https://doi.org/10.1016/0021-9169\(79\)90072-2](https://doi.org/10.1016/0021-9169(79)90072-2), 1979.
- de Wit, R. J., Janches, D., Fritts, D. C., and Hibbins, R. E.: QBO modulation of the mesopause gravity wave momentum flux over Tierra del Fuego, *Geophys. Res. Lett.*, 43, 4049–4055, <https://doi.org/10.1002/2016GL068599>, 2016.
- de Wit, R. J., Janches, D., Fritts, D. C., Stockwell, R. G., and Coy, L.: Unexpected climatological behavior of MLT gravity wave momentum flux in the lee of the Southern Andes hot spot, *Geophys. Res. Lett.*, 44, 1182–1191, <https://doi.org/10.1002/2016GL072311>, 2017.
- Drob, D. P., Emmert, J. T., Meriwether, J. W., Makela, J. J., Doornbos, E., Conde, M., Hernandez, G., Noto, J., Zawdie, K. A., McDonald, S. E., Huba, J. D., and Klenzing, J. H.: An update to the Horizontal Wind Model (HWM): The quiet time thermosphere, *Earth Space Sci.*, 2, 301–319, <https://doi.org/10.1002/2014EA000089>, 2015.
- Ern, M., Preusse, P., Gille, J. C., Hepplewhite, C. L., Mlynyczak, M. G., Russell III, J. M., and Riese, M.: Implications for atmospheric dynamics derived from global observations of gravity wave momentum flux in stratosphere and mesosphere, *J. Geophys. Res.-Atmos.*, 116, D19107, <https://doi.org/10.1029/2011JD015821>, 2011.
- Fallows, R. A., Forte, B., Astin, I., Allbrook, T., Arnold, A., Wood, A., Dorrian, G., Mevius, M., Rothkaehl, H., Matyjasiak, B., Krankowski, A., Anderson, J. M., Asgekar, A., Avruch, I. M., Bentum, M., Bisi, M. M., Butcher, H. R., Ciardi, B., Dabrowski, B., Damstra, S., de Gasperin, F., Duscha, S., Eislöffel, J., Franzen, T. M. O., Garrett, M. A., Griefmeier, J.-M., Gunst, A. W., Hoefl, M., Hörandel, J. R., Iacobelli, M., Intema, H. T., Koopmans, L. V. E., Maat, P., Mann, G., Nelles, A., Paas, H., Pandey, V. N., Reich, W., Rowlinson, A., Rüter, M., Schwarz, D. J., Serylak, M., Shulevski, A., Smirnov, O. M., Soida, M., Steinmetz, M., Thoudam, S., Toribio, M. C., van Ardenne, A., van Bommel, I. M., van der Wiel, M. H. D., van Haarlem, M. P., Vermeulen, R. C., Vocks, C., Wijers, R. A. M. J., Wucknitz, O., Zarka, P., and Zucca, P.: A LOFAR observation of ionospheric scintillation from two simultaneous travelling ionospheric disturbances, *J. Space Weather Spac.*, 10, 10, <https://doi.org/10.1051/swsc/2020010>, 2020.
- Folkestad, K., Hagfors, T., and Westerlund, S.: EISCAT: An updated description of technical characteristics

- and operational capabilities, *Radio Sci.*, 18, 867–879, <https://doi.org/10.1029/RS018i006p00867>, 1983.
- Frissell, N. A., Baker, J. B. H., Ruohoniemi, J. M., Greenwald, R. A., Gerrard, A. J., Miller, E. S., and West, M. L.: Sources and characteristics of medium-scale traveling ionospheric disturbances observed by high-frequency radars in the North American sector, *J. Geophys. Res.-Space*, 121, 3722–3739, <https://doi.org/10.1002/2015JA022168>, 2016.
- Fritts, D. C. and Alexander, M. J.: Gravity wave dynamics and effects in the middle atmosphere, *Rev. Geophysics*, 41, 1003, <https://doi.org/10.1029/2001RG000106>, 2003.
- Fritts, D. C., Janches, D., and Hocking, W. K.: Southern Argentina Agile Meteor Radar: Initial assessment of gravity wave momentum fluxes, *J. Geophys. Res.-Atmos.*, 115, D19123, <https://doi.org/10.1029/2010JD013891>, 2010.
- Greenhow, J. S.: Characteristics of Radio Echoes from Meteor Trails: III The Behaviour of the Electron Trails after Formation, *P. Phys. Soc. Lond. B*, 65, 169, <https://doi.org/10.1088/0370-1301/65/3/301>, 1952.
- Gumbel, J., Megner, L., Christensen, O. M., Ivchenko, N., Murtagh, D. P., Chang, S., Dillner, J., Ekebrand, T., Giono, G., Hammar, A., Hedin, J., Karlsson, B., Krus, M., Li, A., McCallion, S., Olenčenko, G., Pak, S., Park, W., Rouse, J., Stegman, J., and Witt, G.: The MATS satellite mission – gravity wave studies by Mesospheric Airglow/Aerosol Tomography and Spectroscopy, *Atmos. Chem. Phys.*, 20, 431–455, <https://doi.org/10.5194/acp-20-431-2020>, 2020.
- Günzkofer, F., Pokhotelov, D., Stober, G., Liu, H., Liu, H.-L., Mitchell, N. J., Tjulin, A., and Borries, C.: Determining the Origin of Tidal Oscillations in the Ionospheric Transition Region With EISCAT Radar and Global Simulation Data, *J. Geophys. Res.-Space*, 127, e2022JA030861, <https://doi.org/10.1029/2022JA030861>, 2022.
- Günzkofer, F., Pokhotelov, D., Stober, G., Mann, I., Vadas, S. L., Becker, E., Tjulin, A., Kozlovsky, A., Tsutsumi, M., Gulbrandsen, N., Nozawa, S., Lester, M., Belova, E., Kero, J., Mitchell, N., Tjulin, A., and Borries, C.: Inferring neutral winds in the ionospheric transition region from AGW-TID observations with the EISCAT VHF radar and the Nordic Meteor Radar Cluster, Zenodo [data set], <https://doi.org/10.5281/zenodo.7752777>, 2023.
- Herlofson, N.: Plasma resonance in ionospheric irregularities, *Ark. Fys.*, 3, 247–297, 1951.
- Hines, C. O.: Internal atmospheric gravity waves at ionospheric heights, *Can. J. Phys.*, 38, 1441, <https://doi.org/10.1139/p60-150>, 1960.
- Hocke, K. and Schlegel, K.: A review of atmospheric gravity waves and travelling ionospheric disturbances: 1982–1995, *Ann. Geophys.*, 14, 917–940, <https://doi.org/10.1007/s00585-996-0917-6>, 1996.
- Hocking, W. K., Fuller, B., and Vandeppeer, B.: Real-time determination of meteor-related parameters utilizing modern digital technology, *J. Atmos. Sol.-Terr. Phys.*, 63, 155–169, [https://doi.org/10.1016/S1364-6826\(00\)00138-3](https://doi.org/10.1016/S1364-6826(00)00138-3), 2001.
- Hoffmann, P., Becker, E., Singer, W., and Placke, M.: Seasonal variation of mesospheric waves at northern middle and high latitudes, *J. Atmos. Sol.-Terr. Phys.*, 72, 1068–1079, <https://doi.org/10.1016/j.jastp.2010.07.002>, 2010.
- Hoffmann, P., Rapp, M., Singer, W., and Keuer, D.: Trends of mesospheric gravity waves at northern middle latitudes during summer, *J. Geophys. Res.-Atmos.*, 116, D00P08, <https://doi.org/10.1029/2011JD015717>, 2011.
- Holton, J. R.: An introduction to dynamic meteorology, edited by: Dmowska, R., Holton, J. R., and Rossby, H. T., Elsevier Academic Press, ISBN 0-12-354015-1, 1992.
- Hung, R. J., Phan, T., and Smith, R. E.: Observation of gravity waves during the extreme tornado outbreak of 3 April 1974, *J. Atmos. Terr. Phys.*, 40, 831–843, [https://doi.org/10.1016/0021-9169\(78\)90033-8](https://doi.org/10.1016/0021-9169(78)90033-8), 1978.
- Jones, J. and Jones, W.: Oblique-scatter of radio waves from meteor trains: long wavelength approximation, *Planet. Space Sci.*, 38, 925–932, [https://doi.org/10.1016/0032-0633\(90\)90059-Y](https://doi.org/10.1016/0032-0633(90)90059-Y), 1990.
- Kelly, M. C.: The Earth's Ionosphere: Plasma Physics and Electrodynamics, 2nd Edn., Elsevier Academic Press, ISBN 978-0-12-088425-4, 2009.
- Kirchengast, G.: Characteristics of high-latitude TIDs from different causative mechanisms deduced by theoretical modeling, *J. Geophys. Res.-Space*, 102, 4597–4612, <https://doi.org/10.1029/96JA03294>, 1997.
- Kirchengast, G., Hocke, K., and Schlegel, K.: The gravity wave – TID relationship: insight via theoretical model – EISCAT data comparison, *J. Atmos. Terr. Phys.*, 58, 233–243, [https://doi.org/10.1016/0021-9169\(95\)00032-1](https://doi.org/10.1016/0021-9169(95)00032-1), 1996.
- Kotake, N., Otsuka, Y., Ogawa, T., Tsugawa, T., and Saito, A.: Statistical study of medium-scale traveling ionospheric disturbances observed with the GPS networks in Southern California, *Earth Planet. Space*, 59, 95–102, <https://doi.org/10.1186/BF03352681>, 2007.
- Lehtinen, M. S. and Huuskonen, A.: General incoherent scatter analysis and GUISDAP, *J. Atmos. Terr. Phys.*, 58, 435–452, [https://doi.org/10.1016/0021-9169\(95\)00047-X](https://doi.org/10.1016/0021-9169(95)00047-X), 1996.
- Lighthill, J.: Waves in fluids, Cambridge University Press, ISBN 0521216893, 1978.
- Lindzen, R. S.: Turbulence and stress owing to gravity wave and tidal breakdown, *J. Geophys. Res.-Oceans*, 86, 9707–9714, <https://doi.org/10.1029/JC086iC10p09707>, 1981.
- Marquardt, D. W.: An algorithm for least-squares estimation of nonlinear parameters, *J. Soc. Ind. Appl. Math.*, 11, 431–441, 1963.
- Matthias, V., Shepherd, T. G., Hoffmann, P., and Rapp, M.: The Hiccup: a dynamical coupling process during the autumn transition in the Northern Hemisphere – similarities and differences to sudden stratospheric warmings, *Ann. Geophys.*, 33, 199–206, <https://doi.org/10.5194/angeo-33-199-2015>, 2015.
- Matthias, V., Stober, G., Kozlovsky, A., Lester, M., Belova, E., and Kero, J.: Vertical Structure of the Arctic Spring Transition in the Middle Atmosphere, *J. Geophys. Res.-Atmos.*, 126, e2020JD034353, <https://doi.org/10.1029/2020JD034353>, 2021.
- McCormack, J., Hoppel, K., Kuhl, D., de Wit, R., Stober, G., Espy, P., Baker, N., Brown, P., Fritts, D., Jacobi, C., Janches, D., Mitchell, N., Ruston, B., Swadley, S., Viner, K., Whitcomb, T., and Hibbins, R.: Comparison of mesospheric winds from a high-altitude meteorological analysis system and meteor radar observations during the boreal winters of 2009–2010 and 2012–2013, *J. Atmos. Sol.-Terr. Phys.*, 154, 132–166, <https://doi.org/10.1016/j.jastp.2016.12.007>, 2017.
- McCrea, I., Aikio, A., Alfonsi, L., Belova, E., Buchert, S., Clilverd, M., Engler, N., Gustavsson, B., Heinselman, C., Kero, J., Kosch, M., Lamy, H., Leyser, T., Ogawa, Y., Oksavik, K., Pellinen-Wannberg, A., Pitout, F., Rapp, M., Stanis-

- lawska, I., and Vierinen, J.: The science case for the EISCAT\_3D radar, *Progress in Earth and Planetary Science*, 2, 21, <https://doi.org/10.1186/s40645-015-0051-8>, 2015.
- McKinley, D. W. R.: *Meteor science and engineering*, McGraw-Hill, LCCN 60053127, 1961.
- Mitchell, N. J. and Beldon, C. L.: Gravity waves in the mesopause region observed by meteor radar: 1. A simple measurement technique, *J. Atmos. Sol.-Terr. Phys.*, 71, 866–874, <https://doi.org/10.1016/j.jastp.2009.03.011>, 2009.
- Nicolls, M. J. and Heinselman, C. J.: Three-dimensional measurements of traveling ionospheric disturbances with the Poker Flat Incoherent Scatter Radar, *Geophys. Res. Lett.*, 34, L21104, <https://doi.org/10.1029/2007GL031506>, 2007.
- Nicolls, M. J., Vadas, S. L., Aponte, N., and Sulzer, M. P.: Horizontal parameters of daytime thermospheric gravity waves and E region neutral winds over Puerto Rico, *J. Geophys. Res.-Space*, 119, 575–600, <https://doi.org/10.1002/2013JA018988>, 2014.
- Nishioka, M., Tsugawa, T., Kubota, M., and Ishii, M.: Concentric waves and short-period oscillations observed in the ionosphere after the 2013 Moore EF5 tornado, *Geophys. Res. Lett.*, 40, 5581–5586, <https://doi.org/10.1002/2013GL057963>, 2013.
- Oliver, W. L., Otsuka, Y., Sato, M., Takami, T., and Fukao, S.: A climatology of F region gravity wave propagation over the middle and upper atmosphere radar, *J. Geophys. Res.-Space*, 102, 14499–14512, <https://doi.org/10.1029/97JA00491>, 1997.
- Onishi, T., Tsugawa, T., Otsuka, Y., Berthelier, J.-J., and Lebreton, J.-P.: First simultaneous observations of daytime MSTIDs over North America using GPS-TEC and DEMETER satellite data, *Geophys. Res. Lett.*, 36, L11808, <https://doi.org/10.1029/2009GL038156>, 2009.
- Palmroth, M., Grandin, M., Sarris, T., Doornbos, E., Tourgaidis, S., Aikio, A., Buchert, S., Clilverd, M. A., Dandouras, I., Heelis, R., Hoffmann, A., Ivchenko, N., Kervalishvili, G., Knudsen, D. J., Kotova, A., Liu, H.-L., Malaspina, D. M., March, G., Marchaudon, A., Marghitsu, O., Matsuo, T., Miloch, W. J., Moretto-Jørgensen, T., Mpaloukidis, D., Olsen, N., Papadakis, K., Pfaff, R., Pirnaris, P., Siemes, C., Stolle, C., Suni, J., van den IJssel, J., Verronen, P. T., Visser, P., and Yamauchi, M.: Lower-thermosphere-ionosphere (LTI) quantities: current status of measuring techniques and models, *Ann. Geophys.*, 39, 189–237, <https://doi.org/10.5194/angeo-39-189-2021>, 2021.
- Pawlowicz, R.: *M\_Map: A mapping package for MATLAB*, version 1.4m, MATLAB [software], <https://www.eoas.ubc.ca/~rich/map.html> (last access: 16 October 2023), 2020.
- Pedatella, N. M., Liu, H. L., Conte, J. F., Chau, J. L., Hall, C., Jacobi, C., Mitchell, N., and Tsutsumi, M.: Migrating Semidiurnal Tide During the September Equinox Transition in the Northern Hemisphere, *J. Geophys. Res.-Atmos.*, 126, e33822, <https://doi.org/10.1029/2020JD033822>, 2021.
- Picone, J. M., Hedin, A. E., Drob, D. P., and Aikin, A. C.: NRLMSISE-00 empirical model of the atmosphere: Statistical comparisons and scientific issues, *J. Geophys. Res.-Space*, 107, SIA 15-1–SIA 15-16, <https://doi.org/10.1029/2002JA009430>, 2002.
- Pitteway, M. L. V. and Hines, C. O.: The viscous damping of atmospheric gravity waves, *Can. J. Phys.*, 41, 1935, <https://doi.org/10.1139/p63-194>, 1963.
- Placke, M., Hoffmann, P., Latteck, R., and Rapp, M.: Gravity wave momentum fluxes from MF and meteor radar measurements in the polar MLT region, *J. Geophys. Res.-Space*, 120, 736–750, <https://doi.org/10.1002/2014JA020460>, 2015.
- Pokhotelov, D., Becker, E., Stober, G., and Chau, J. L.: Seasonal variability of atmospheric tides in the mesosphere and lower thermosphere: meteor radar data and simulations, *Ann. Geophys.*, 36, 825–830, <https://doi.org/10.5194/angeo-36-825-2018>, 2018.
- Poulter, E. and Baggaley, W.: Radiowave scattering from meteoric ionization, *J. Atmos. Terr. Phys.*, 39, 757–768, [https://doi.org/10.1016/0021-9169\(77\)90137-4](https://doi.org/10.1016/0021-9169(77)90137-4), 1977.
- Rapp, M., Latteck, R., Stober, G., Hoffmann, P., Singer, W., and Zeche, M.: First three-dimensional observations of polar mesosphere winter echoes: Resolving space-time ambiguity, *J. Geophys. Res.-Space*, 116, A11307, <https://doi.org/10.1029/2011JA016858>, 2011.
- Saito, A., Fukao, S., and Miyazaki, S.: High resolution mapping of TEC perturbations with the GSI GPS Network over Japan, *Geophys. Res. Lett.*, 25, 3079–3082, <https://doi.org/10.1029/98GL52361>, 1998.
- Sarkhel, S., Stober, G., Chau, J. L., Smith, S. M., Jacobi, C., Mondal, S., Mlynczak, M. G., and Russell III, J. M.: A case study of a ducted gravity wave event over northern Germany using simultaneous airglow imaging and wind-field observations, *Ann. Geophys.*, 40, 179–190, <https://doi.org/10.5194/angeo-40-179-2022>, 2022.
- Sarris, T., Palmroth, M., Aikio, A., Buchert, S. C., Clemmons, J., Clilverd, M., Dandouras, I., Doornbos, E., Goodwin, L. V., Grandin, M., Heelis, R., Ivchenko, N., Moretto-Jørgensen, T., Kervalishvili, G., Knudsen, D., Liu, H.-L., Lu, G., Malaspina, D. M., Marghitsu, O., Maute, A., Miloch, W. J., Olsen, N., Pfaff, R., Stolle, C., Talaat, E., Thayer, J., Tourgaidis, S., Verronen, P. T., and Yamauchi, M.: Plasma-neutral interactions in the lower thermosphere-ionosphere: The need for in situ measurements to address focused questions, *Frontiers in Astronomy and Space Sciences*, 9, 1063190, <https://doi.org/10.3389/fspas.2022.1063190>, 2023.
- Smith, A. K.: Longitudinal Variations in Mesospheric Winds: Evidence for Gravity Wave Filtering by Planetary Waves, *J. Atmos. Sci.*, 53, 1156–1173, [https://doi.org/10.1175/1520-0469\(1996\)053<1156:LVMWE>2.0.CO;2](https://doi.org/10.1175/1520-0469(1996)053<1156:LVMWE>2.0.CO;2), 1996.
- Smith, A. K.: Global Dynamics of the MLT, *Surv. Geophys.*, 33, 1177–1230, <https://doi.org/10.1007/s10712-012-9196-9>, 2012.
- Smith, S. M., Stober, G., Jacobi, C., Chau, J. L., Gerding, M., Mlynczak, M. G., Russell, J. M., Baumgardner, J. L., Mendillo, M., Lazzarin, M., and Umbriaco, G.: Characterization of a Double Mesospheric Bore Over Europe, *J. Geophys. Res.-Space*, 122, 9738–9750, <https://doi.org/10.1002/2017JA024225>, 2017.
- Stamm, J., Vierinen, J., Urco, J. M., Gustavsson, B., and Chau, J. L.: Radar imaging with EISCAT 3D, *Ann. Geophys.*, 39, 119–134, <https://doi.org/10.5194/angeo-39-119-2021>, 2021.
- Stober, G., Sommer, S., Rapp, M., and Latteck, R.: Investigation of gravity waves using horizontally resolved radial velocity measurements, *Atmos. Meas. Tech.*, 6, 2893–2905, <https://doi.org/10.5194/amt-6-2893-2013>, 2013.
- Stober, G., Sommer, S., Schult, C., Latteck, R., and Chau, J. L.: Observation of Kelvin–Helmholtz instabilities and gravity waves in the summer mesopause above Andenes in Northern Norway, *Atmos. Chem. Phys.*, 18, 6721–6732, <https://doi.org/10.5194/acp-18-6721-2018>, 2018.

- Stober, G., Baumgarten, K., McCormack, J. P., Brown, P., and Czarnecki, J.: Comparative study between ground-based observations and NAVGEM-HA analysis data in the mesosphere and lower thermosphere region, *Atmos. Chem. Phys.*, 20, 11979–12010, <https://doi.org/10.5194/acp-20-11979-2020>, 2020.
- Stober, G., Brown, P., Campbell-Brown, M., and Weryk, R. J.: Triple-frequency meteor radar full wave scattering – Measurements and comparison to theory, *Astron. Astrophys.*, 654, A108, <https://doi.org/10.1051/0004-6361/202141470>, 2021a.
- Stober, G., Janches, D., Matthias, V., Fritts, D., Marino, J., Moffat-Griffin, T., Baumgarten, K., Lee, W., Murphy, D., Kim, Y. H., Mitchell, N., and Palo, S.: Seasonal evolution of winds, atmospheric tides, and Reynolds stress components in the Southern Hemisphere mesosphere–lower thermosphere in 2019, *Ann. Geophys.*, 39, 1–29, <https://doi.org/10.5194/angeo-39-1-2021>, 2021b.
- Stober, G., Kozlovsky, A., Liu, A., Qiao, Z., Tsutsumi, M., Hall, C., Nozawa, S., Lester, M., Belova, E., Kero, J., Espy, P. J., Hibbins, R. E., and Mitchell, N.: Atmospheric tomography using the Nordic Meteor Radar Cluster and Chilean Observation Network De Meteor Radars: network details and 3D-Var retrieval, *Atmos. Meas. Tech.*, 14, 6509–6532, <https://doi.org/10.5194/amt-14-6509-2021>, 2021c.
- Stober, G., Kuchar, A., Pokhotelov, D., Liu, H., Liu, H.-L., Schmidt, H., Jacobi, C., Baumgarten, K., Brown, P., Janches, D., Murphy, D., Kozlovsky, A., Lester, M., Belova, E., Kero, J., and Mitchell, N.: Interhemispheric differences of mesosphere–lower thermosphere winds and tides investigated from three whole-atmosphere models and meteor radar observations, *Atmos. Chem. Phys.*, 21, 13855–13902, <https://doi.org/10.5194/acp-21-13855-2021>, 2021d.
- Stober, G., Liu, A., Kozlovsky, A., Qiao, Z., Kuchar, A., Jacobi, C., Meek, C., Janches, D., Liu, G., Tsutsumi, M., Gulbrandsen, N., Nozawa, S., Lester, M., Belova, E., Kero, J., and Mitchell, N.: Meteor radar vertical wind observation biases and mathematical debiasing strategies including the 3DVAR+DIV algorithm, *Atmos. Meas. Tech.*, 15, 5769–5792, <https://doi.org/10.5194/amt-15-5769-2022>, 2022.
- Sutherland, W.: LII. The viscosity of gases and molecular force, *The London, Edinburgh, and Dublin Philosophical Magazine and Journal of Science*, 36, 507–531, <https://doi.org/10.1080/14786449308620508>, 1893.
- Tjulin, A.: EISCAT experiments, Tech. rep., EISCAT Scientific Association, [https://eiscat.se/wp-content/uploads/2021/03/Experiments\\_v20210302.pdf](https://eiscat.se/wp-content/uploads/2021/03/Experiments_v20210302.pdf) (last access: 16 October 2023), 2021.
- Tsugawa, T., Otsuka, Y., Coster, A. J., and Saito, A.: Medium-scale traveling ionospheric disturbances detected with dense and wide TEC maps over North America, *Geophys. Res. Lett.*, 34, L22101, <https://doi.org/10.1029/2007GL031663>, 2007.
- Vadas, S. L.: Horizontal and vertical propagation and dissipation of gravity waves in the thermosphere from lower atmospheric and thermospheric sources, *J. Geophys. Res.-Space*, 112, A06305, <https://doi.org/10.1029/2006JA011845>, 2007.
- Vadas, S. L. and Becker, E.: Numerical modeling of the excitation, propagation, and dissipation of primary and secondary gravity waves during wintertime at McMurdo Station in the Antarctic, *J. Geophys. Res.-Atmos.*, 123, 9326–9369, <https://doi.org/10.1029/2017JD027970>, 2018.
- Vadas, S. L. and Becker, E.: Numerical Modeling of the Generation of Tertiary Gravity Waves in the Mesosphere and Thermosphere During Strong Mountain Wave Events Over the Southern Andes, *J. Geophys. Res.-Space*, 124, 7687–7718, <https://doi.org/10.1029/2019JA026694>, 2019.
- Vadas, S. L. and Crowley, G.: Sources of the traveling ionospheric disturbances observed by the ionospheric TIDBIT sounder near Wallops Island on 30 October 2007, *J. Geophys. Res.-Space*, 115, A07324, <https://doi.org/10.1029/2009JA015053>, 2010.
- Vadas, S. L. and Fritts, D. C.: Thermospheric responses to gravity waves: Influences of increasing viscosity and thermal diffusivity, *J. Geophys. Res.-Atmos.*, 110, D15103, <https://doi.org/10.1029/2004JD005574>, 2005.
- Vadas, S. L. and Nicolls, M. J.: Using PFISR measurements and gravity wave dissipative theory to determine the neutral, background thermospheric winds, *Geophys. Res. Lett.*, 35, L02105, <https://doi.org/10.1029/2007GL031522>, 2008.
- Vadas, S. L. and Nicolls, M. J.: Temporal evolution of neutral, thermospheric winds and plasma response using PFISR measurements of gravity waves, *J. Atmos. Sol.-Terr. Phys.*, 71, 744–770, <https://doi.org/10.1016/j.jastp.2009.01.011>, 2009.
- Vadas, S. L., Becker, E., Figueiredo, C., Bossert, K., Harding, B. J., and Gasque, L. C.: Primary and Secondary Gravity Waves and Large-Scale Wind Changes Generated by the Tonga Volcanic Eruption on 15 January 2022: Modeling and Comparison With ICON-MIGHTI Winds, *J. Geophys. Res.-Space*, 128, e2022JA031138, <https://doi.org/10.1029/2022JA031138>, 2023a.
- Vadas, S. L., Figueiredo, C., Becker, E., Huba, J., Themens, D. R., Hindley, N. P., Mrak, S., Galkin, I., and Bossert, K.: Traveling ionospheric disturbances induced by the secondary gravity waves from the Tonga eruption on 15 January 2022: Modeling with MESORAC/HIAMCM/SAMI3 and comparison with GPS/TEC and ionosonde data, *J. Geophys. Res.-Space*, 128, e2023JA031408, <https://doi.org/10.1029/2023JA031408>, 2023b.
- van de Kamp, M., Pokhotelov, D., and Kauristie, K.: TID characterised using joint effort of incoherent scatter radar and GPS, *Ann. Geophys.*, 32, 1511–1532, <https://doi.org/10.5194/angeo-32-1511-2014>, 2014.
- Vlasov, A., Kauristie, K., van de Kamp, M., Luntama, J.-P., and Pogoreltsev, A.: A study of Traveling Ionospheric Disturbances and Atmospheric Gravity Waves using EISCAT Svalbard Radar IPY-data, *Ann. Geophys.*, 29, 2101–2116, <https://doi.org/10.5194/angeo-29-2101-2011>, 2011.
- Williams, P. J. S.: Observations of atmospheric gravity waves with incoherent scatter radar, *Adv. Space Res.*, 9, 65–72, [https://doi.org/10.1016/0273-1177\(89\)90342-6](https://doi.org/10.1016/0273-1177(89)90342-6), 1989.
- Wüst, S., Offenwanger, T., Schmidt, C., Bittner, M., Jacobi, C., Stober, G., Yee, J.-H., Mlynczak, M. G., and Russell III, J. M.: Derivation of gravity wave intrinsic parameters and vertical wavelength using a single scanning OH(3-1) airglow spectrometer, *Atmos. Meas. Tech.*, 11, 2937–2947, <https://doi.org/10.5194/amt-11-2937-2018>, 2018.
- Xu, S., Yue, J., Xue, X., Vadas, S. L., Miller, S. D., Azeem, I., Straka, W., Hoffmann, L., and Zhang, S.: Dynamical Coupling Between Hurricane Matthew and the Middle to Upper Atmosphere via Gravity Waves, *J. Geophys. Res.-Space*, 124, 3589–3608, <https://doi.org/10.1029/2018JA026453>, 2019.



---

# Evaluation of the Empirical Joule Heating Rate Scaling Factor in TIE-GCM With EISCAT Measurements

## Bibliographic information

**Günzkofer F.**, Liu, H., Stober G., Pokhotelov D., and Borries C. Evaluation of the Empirical Joule Heating Rate Scaling Factor in TIE-GCM With EISCAT Measurements. *Earth and Space Science*, **11**, e2023EA003447, 2024.

DOI: <https://doi.org/10.1029/2023EA003447>

©2024. The Authors.

## Related Publications

Nykiel G., Ferreira A., **Günzkofer F.**, Iochem P., Tasnim S., and Sato H. Large-Scale Traveling Ionospheric Disturbances over the European sector during the geomagnetic storm on March 23-24, 2023: Energy Deposition in the Source Regions and the Propagation Characteristics. *Journal of Geophysical Research: Space Physics*, **129**, e2023JA032145, 2024.

## Author's contribution

This publication was elaborated and written during my stay as a SCOSTEP visiting scholar at Kyushu University, Japan. The paper was conceptualized in close cooperation with my local host, H. Liu who also supervised my work. For this work, I downloaded, pre-processed, and analyzed over 2000 hours of EISCAT measurements. This required me to implement a stochastic inversion method to obtain 3D ion velocity vectors from EISCAT beam-swing measurements. I performed two TIE-GCM runs, one with *Heelis* and one with *Weimer* polar plasma convection, for each measurement campaign included in the analysis. I calculated local and height-integrated Joule heating rates applying both measurement and model plasma parameters. The required model Joule heating scaling factor was determined by a non-linear least-square fit and it was investigated how the scaling changes with various parameters. For this, I implemented the required fitting and statistical binning methods. G. Stober and C. Borries contributed to the supervision of this work and D. Pokhotelov suggested the thematic frame of the publication. As the first author, I wrote large parts of the manuscript, but all authors were involved in revising the text.

# Earth and Space Science

## RESEARCH ARTICLE

10.1029/2023EA003447

## Evaluation of the Empirical Scaling Factor of Joule Heating Rates in TIE-GCM With EISCAT Measurements

Florian Günzkofer<sup>1</sup>, Huixin Liu<sup>2</sup>, Gunter Stober<sup>3</sup>, Dimitry Pokhotelov<sup>4</sup>, and Claudia Borries<sup>1</sup>

### Key Points:

- The constant Joule heating scaling factor in TIE-GCM is inadequate to compensate for the underestimation under various geomagnetic conditions
- Joule heating rates calculated from 2,220 hr of EISCAT measurements are compared to TIE-GCM runs driven with the *Heelis* and *Weimer* convection models
- The required scaling factor varies significantly with the *Kp* index, the Kan-Lee merging electric field, and the magnetic local time

### Correspondence to:

F. Günzkofer and H. Liu,  
florian.guenzkofer@dlr.de;  
liu.huixin.295@m.kyushu-u.ac.jp

### Citation:

Günzkofer, F., Liu, H., Stober, G., Pokhotelov, D., & Borries, C. (2024). Evaluation of the empirical scaling factor of Joule heating rates in TIE-GCM with EISCAT measurements. *Earth and Space Science*, 11, e2023EA003447. <https://doi.org/10.1029/2023EA003447>

Received 23 NOV 2023  
Accepted 9 MAR 2024

### Author Contributions:

**Conceptualization:** Florian Günzkofer, Huixin Liu  
**Formal analysis:** Florian Günzkofer  
**Investigation:** Florian Günzkofer  
**Methodology:** Florian Günzkofer  
**Software:** Florian Günzkofer  
**Supervision:** Huixin Liu, Gunter Stober, Claudia Borries  
**Validation:** Florian Günzkofer  
**Writing – original draft:** Florian Günzkofer, Huixin Liu  
**Writing – review & editing:** Huixin Liu, Gunter Stober, Dimitry Pokhotelov, Claudia Borries

© 2024 The Authors. Earth and Space Science published by Wiley Periodicals LLC on behalf of American Geophysical Union.

This is an open access article under the terms of the [Creative Commons Attribution-NonCommercial-NoDerivs License](https://creativecommons.org/licenses/by-nc-nd/4.0/), which permits use and distribution in any medium, provided the original work is properly cited, the use is non-commercial and no modifications or adaptations are made.

<sup>1</sup>Institute for Solar-Terrestrial Physics, German Aerospace Center (DLR), Neustrelitz, Germany, <sup>2</sup>Department of Earth and Planetary Sciences, Kyushu University, Fukuoka, Japan, <sup>3</sup>Institute of Applied Physics & Oeschger Center for Climate Change Research, Microwave Physics, University of Bern, Bern, Switzerland, <sup>4</sup>Institute of Physics, University of Greifswald, Greifswald, Germany

**Abstract** Joule heating is one of the main energy inputs into the thermosphere-ionosphere system. Precise modeling of this process is essential for any space weather application. Existing thermosphere-ionosphere models tend to underestimate the actual Joule heating rate quite significantly. The Thermosphere-Ionosphere-Electrodynamics General-Circulation-Model applies an empirical scaling factor of 1.5 for compensation. We calculate vertical profiles of Joule heating rates from approximately 2,220 hr of measurements with the EISCAT incoherent scatter radar and the corresponding model runs. We investigate model runs with the plasma convection driven by both the *Heelis* and the *Weimer* model. The required scaling of the Joule heating profiles is determined with respect to the *Kp* index, the Kan-Lee merging electric field  $E_{KL}$ , and the magnetic local time. Though the default scaling factor of 1.5 appears to be adequate on average, we find that the required scaling varies strongly with all three parameters ranging from 0.46 to ~20 at geomagnetically disturbed and quiet times, respectively. Furthermore, the required scaling is significantly different in runs driven by the *Heelis* and *Weimer* model. Adjusting the scaling factor with respect to the *Kp* index,  $E_{KL}$ , the magnetic local time, and the choice of convection model would reduce the difference between Joule heating rates calculated from measurement and model plasma parameters.

**Plain Language Summary** The vast majority of the energy input to the Earth system originates from the sun. This includes the absorption of various types of radiation, for example, ultraviolet radiation in the ozone layer or visible light and infrared radiation at the surface. In the upper atmosphere above about 80 km altitude, the absorption of extreme ultraviolet radiation and soft X-rays plays a major role. However, other processes also contribute significantly to the heating of this region, for example, the energy dissipation in the form of electric currents flowing along electric fields, also known as Joule heating. Joule heating is highly variable and can be drastically enhanced especially during solar storms, which can have potentially disastrous effects on satellites. Accurate modeling, and therefore also prediction, of Joule heating is not possible at the moment since thermosphere-ionosphere models have to scale the Joule heating empirically to fit the actual values. We investigate how the required scaling changes under different geophysical conditions.

## 1. Introduction

Heating in the upper atmosphere is caused by several different mechanisms and their respective impacts vary strongly with geomagnetic activity and location. Ionospheric modeling and space weather prediction require understanding and accurately describing these processes such as energetic particle precipitation or absorption of extreme ultraviolet and soft X-ray radiation. At high latitudes, especially during geomagnetic active periods, the *Joule heating* due to the dissipation of ionospheric currents is of major importance for the ionosphere-thermosphere system. The local Joule heating rate is defined as

$$q_J = \mathbf{j} \cdot (\mathbf{E} + \mathbf{u} \times \mathbf{B}) \quad (1)$$

with the current density  $\mathbf{j}$ , the electric field  $\mathbf{E}$ , the neutral wind  $\mathbf{u}$ , and the magnetic field  $\mathbf{B}$ .

At high latitudes, ionospheric currents are associated with the polar plasma convection, which results from the interaction of the Earth's magnetic field and the interplanetary magnetic field (IMF) carried by the solar wind (e.g., Baumjohann & Treumann, 1996; Kelley, 2009; Schunk & Nagy, 2009). The convection pattern gives rise to an electric field  $\mathbf{E}_\perp$  perpendicular to the nearly vertical magnetic field lines. In this situation, two types of currents

can be distinguished: Pedersen currents  $\mathbf{j}_P(\parallel \mathbf{E}_\perp)$  parallel to the electric field and Hall currents  $\mathbf{j}_H(\parallel \mathbf{E}_\perp \times \mathbf{B})$  perpendicular to both the electric field and the magnetic field lines. From Equation 1, it can be seen that only Pedersen currents contribute to the Joule heating rate. Introducing the Pedersen conductivity  $\sigma_P$ , the Pedersen current can be written as  $\mathbf{j}_P = \sigma_P(\mathbf{E}_\perp + \mathbf{u} \times \mathbf{B})$ . Including the neutral dynamo effect due to the neutral wind  $\mathbf{u}(z)$ , the altitude-dependent Joule heating rate is

$$q_J(z) = \sigma_P(z)(\mathbf{E}_\perp + \mathbf{u}(z) \times \mathbf{B}(z))^2 \quad [\text{Wm}^{-3}]. \quad (2)$$

Integration of Equation 2 gives the height-integrated Joule heating rate

$$Q_J = \int_{z_1}^{z_2} \sigma_P(z)(\mathbf{E}_\perp + \mathbf{u}(z) \times \mathbf{B}(z))^2 dz \quad [\text{Wm}^{-2}]. \quad (3)$$

Assuming empirical neutral atmosphere densities and winds, the height-integrated Joule heating rate  $Q_J$  can be determined from satellite observations (e.g., Foster et al., 1983; Palmroth et al., 2005; Rich et al., 1991). To determine the vertical profile of the local Joule heating rate  $q_J$ , incoherent scatter radar (ISR) measurements can be applied (e.g., Kavanagh et al., 2022; Thayer, 1998, 2000; Vickrey et al., 1982). Global thermosphere-ionosphere (T-I) models provide vertical profiles of  $q_J$  at all geographic locations and are therefore a valuable addition to local ISR measurements (e.g., Deng & Ridley, 2007; Deng et al., 2009; Huang et al., 2012; Maute, 2017; Weimer, 2005). However, it has been noted that T-I models tend to underestimate the actual Joule heating rate quite significantly (Codrescu et al., 1995; Deng & Ridley, 2007). The Thermosphere-Ionosphere-Electrodynamics Global-Circulation-Model (TIE-GCM) (Richmond et al., 1992) therefore multiplies the Joule heating rate by a constant empirical factor of  $f = 1.5$  (Codrescu et al., 1995; Emery et al., 1999). This study aims to investigate the required scaling factor under various conditions and whether a constant  $f = 1.5$  is actually appropriate. For this purpose, we will compare TIE-GCM Joule heating rates ( $q_J^M$  and  $Q_J^M$ ) with Joule heating rates that are calculated from TIE-GCM neutral parameters and EISCAT ISR plasma parameters measurements, that is, electric field and electron density, ( $q_J^E$  and  $Q_J^E$ ).

An important point to consider is the representation of the polar plasma convection in T-I models. Since the plasma convection depends on the interaction of the IMF with the Earth's magnetic field, a physical convection model would require coupled modeling of the solar wind, the magnetosphere, and the ionosphere. However, ionosphere-thermosphere models generally apply empirical convection models. Two of the most commonly applied convection models are the *Heelis* model (Heelis et al., 1982) and the *Weimer* model (Weimer, 2005). The *Heelis* model applies the  $K_p$  index as an input parameter which quantifies the geomagnetic activity from global magnetometer measurements. The *Weimer* model fits the electrostatic potential for given solar wind/IMF parameters using a set of spherical harmonics (Weimer, 2005). We use the Kan-Lee merging electric field  $E_{KL}$  (Kan & Lee, 1979) to combine the solar wind and IMF parameters applied by the *Weimer* convection model. It has been found that  $E_{KL}$  correlates well with the polar cap potential (Weimer, 1995). The Kan-Lee merging electric field is defined as

$$E_{KL} = v_{sw} B_T \sin^2\left(\frac{\theta}{2}\right) \quad (4)$$

with the solar wind velocity  $v_{sw}$ ,  $B_T = (B_y^2 + B_z^2)^{0.5}$ , and  $\theta = \arctan(B_y/B_z)$ , with the interplanetary magnetic field components  $B_y$  and  $B_z$  in the GSM coordinate system (Laundal & Richmond, 2017). Since the TIE-GCM can be driven by both the *Heelis* and the *Weimer* convection models, we will compare the performance of both models within TIE-GCM to obtain Joule heating rates for different forcing conditions. It has been shown that the Joule heating rate strongly depends on the magnetic local time (MagLT) (Baloukidis et al., 2023; Foster et al., 1983) and therefore we will also investigate how the required  $f$  factor varies with MagLT.

Section 2 will introduce the EISCAT ISR instrument and the TIE-GCM. The applied measurement mode as well as the geophysical conditions during the measurements will be described. In Section 3, we will show how local and height-integrated Joule heating rates are calculated from both measurements and model results. This includes an introduction to the *stochastic inversion* method that is applied to obtain 3D ion velocity and electric field

**Table 1**  
*Distribution of Measurement Time With the Kp Index and E<sub>KL</sub>*

Kp	Measurement time (hr)	E <sub>KL</sub> (mVm <sup>-1</sup> )	Measurement time (hr)
0	186.6	0–0.1	484.2
0.333	311	0.1–0.2	328.2
0.667	263.5	0.2–0.35	410.8
1	195.7	0.35–0.5	360.9
1.333	160.3	0.5–0.7	245.1
1.667	182.5	0.7–0.9	130.9
2	156.1	0.9–1.15	120.7
2.333–2.667	206.7	1.15–1.6	81.5
3–3.333	168	>1.6	60.5
3.667–4	125		
4.333–5	139		
5.333–6	62.1		
>6	35.6		
Σ	2,192.1	Σ	2,222.8

vectors from ISR measurements. The comparison of Joule heating rates calculated completely from model results  $q_J^M$  and constrained with EISCAT measurements  $q_J^E$  is shown in Section 4. The evaluation of the empirical Joule heating scaling factor is presented in Section 4 as well and Section 5 discusses the obtained results. Section 6 will conclude the paper and give an outlook on possible future investigations.

## 2. Measurements and Models

### 2.1. EISCAT UHF Incoherent Scatter Radar

The EISCAT Ultra High Frequency (UHF) ISR at Tromsø, Norway (69.6°N, 19.2°E) (Folkestad et al., 1983) has a peak transmission power of about 1.5–2 MW. The radar transmission frequency is 930 MHz and the employed dish has a diameter of 32 m. This results in a beam width of about 0.7° corresponding to an antenna directive gain of approximately 48.1 dBi.

To obtain 3D electric field vectors, the EISCAT ISR can either be operated in combination with two remote receivers (tristatic) or in a beam-swing mode (monostatic) (Kavanagh et al., 2022). For this study, we will analyze approximately 2,220 hr of EISCAT measurements in the beam-swing mode, also known as *Common Program* (CP) 2. In this mode, the radar dish is rotated through four measurement positions with a total cycle time of 6 min, and the beam-aligned ion velocity is measured in each position. The time resolution of ~0.1 hr results in approximately 22,200 measurement points. The EISCAT CP 2 and other experiment modes are described in Tjulin (2021).

Following Nygrén et al. (2011), we perform a *stochastic inversion* to obtain the F-region 3D ion velocity vector. The ionospheric electric field can be calculated from the ion velocities. The method and its application in this study are described in more detail in Section 3. Other parameters available from the ISR measurements are the electron density  $N_e$ , and the ion/electron temperatures  $T_i$  and  $T_e$ . In the E-region, these parameters are binned in 13 altitude gates with a vertical resolution of 5 km at 95–125 and 10 km at 135–185 km altitude.

As mentioned before, we will investigate Joule heating rates for different geophysical conditions ( $K_p$  index and  $E_{KL}$ ) and magnetic local times. Table 1 gives the distribution of measurement time with the  $K_p$  index and  $E_{KL}$ .

**Table 2**  
*Distribution of Measurement Time in Hours With Respect to the Kp Index and MagLT*

Kp/MagLT	03–09	09–15	15–21	21–03	Σ
0–2	312	380.7	406.7	356.3	1,455.7
2–4	128.3	136.7	137.4	97.3	499.7
4–9	51.3	45.2	66.5	73.7	236.7
Σ	491.6	562.6	610.6	527.3	2,192.1

**Table 3**

*Distribution of Measurement Time in Hours With Respect to  $E_{KL}$  and MagLT*

$E_{KL}$ (mV m <sup>-1</sup> )/MagLT	03–09	09–15	15–21	21–03	$\Sigma$
0–0.2	164	213.5	215	219.9	<b>812.4</b>
0.2–0.5	183.5	225.4	181.1	181.7	<b>771.7</b>
>0.5	149	135.8	218.5	135.4	<b>638.7</b>
$\Sigma$	<b>496.5</b>	<b>574.7</b>	<b>614.6</b>	<b>537</b>	<b>2,222.8</b>

Investigating the bins given in Table 1 is only possible if the values are taken throughout the entire day and MagLT variations are neglected. Tables 2 and 3 give the bin resolution and measurement time per bin if variations with the  $K_p$  index/ $E_{KL}$  and MagLT are investigated simultaneously.

A seasonal dependence of the Joule heating rate and the required scaling factor has been shown before (Emery et al., 1999; Foster et al., 1983). Figure 1 shows the distribution of the EISCAT measurements by day of year. It can be seen that most EISCAT CP2 measurements took place in January or around the September equinox. The distribution shown in Figure 1 does not allow to investigate the seasonal dependence of the Joule heating rates and the required scaling. For the results shown in this paper, all measurements have been considered independent of the day of year.

## 2.2. TIE-GCM

The Thermosphere-Ionosphere-Electrodynamics General-Circulation-Model (TIE-GCM) (Richmond et al., 1992) is a global model of the coupled ionosphere-thermosphere system. The lower boundary is at about 96 km altitude where atmospheric tides are specified by the Global Scale Wave Model (GSWM) (Hagan & Forbes, 2002, 2003). The TIE-GCM output is given on a  $2.5^\circ \times 2.5^\circ$  longitude-latitude grid. The vertical resolution is 1/4 in scale height units equivalent to a resolution of  $\sim 2$ –18 km. The time resolution of the TIE-GCM is set to 30 s and the model output is given in 1 hr intervals. The solar activity is parameterized with the F10.7 solar flux which is measured daily. The range of F10.7 varies from  $\sim 70$ –170 sfu (solar flux units). The database includes 2 days (09 and 13 September 2005) with exceptionally high solar flux conditions of F10.7  $\sim 700$  sfu and F10.7  $\sim 300$  sfu. The data presented in this paper was generated from several runs performed with the TIE-GCM Version 2.0.

As mentioned in Section 1, the polar plasma potential, and hence the electric field, is given by an empirical convection model. Both the *Heelis* model (Heelis et al., 1982) and the *Weimer* model (Weimer, 2005) can be applied for that purpose. We performed two TIE-GCM runs for each EISCAT measurement, driven with either of the two convection models. It should be mentioned explicitly that the model runs were performed using realistic F10.7 and  $K_p$  index and time-advanced solar wind/IMF parameters. The model data is binned into the same E-region altitude gates as the EISCAT plasma parameters. Since the model output intervals are larger than the

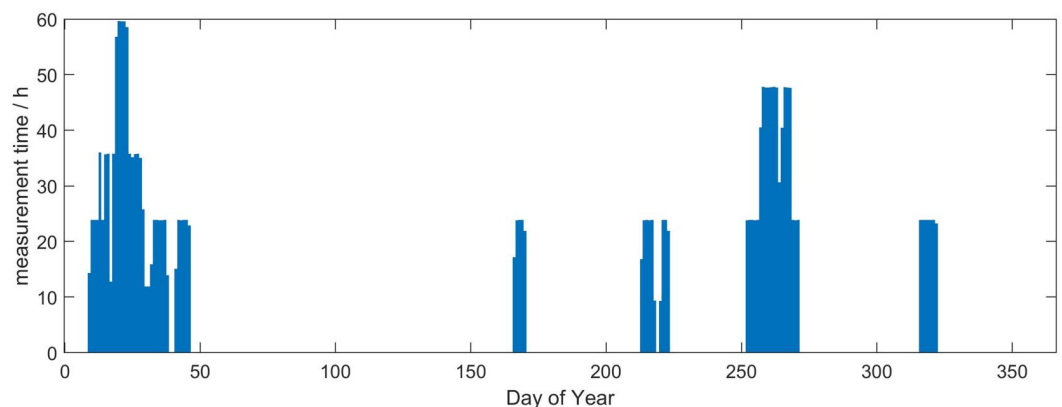


**Figure 1.** Seasonal distribution EISCAT measurement time included in the database.

measurement time resolution, we apply a nearest-neighbor interpolation on the model data. The same interpolation is performed on the  $Kp$  index and  $E_{KL}$  data. This allows to bin the Joule heating rates  $q_J^M$  and  $q_J^E$  according to Tables 1–3. Since there is a one-to-one correspondence of the  $Kp$  index and the solar wind/IMF parameters, it is valid to bin *Heelis*-driven runs with  $E_{KL}$  and *Weimer*-driven runs with the  $Kp$  index.

### 3. Method

The application of *stochastic inversion* to infer 3D ion velocity vectors from EISCAT beam-swing measurements is described in detail by Nygrén et al. (2011). We will summarize the implementation of the method for this paper and refer to Nygrén et al. (2011) for further information. The *stochastic inversion* method allows solving the linear problem

$$\mathbf{M} = \mathbf{A}\mathbf{x} + \epsilon \quad (5)$$

where the vector of unknown variables  $\mathbf{x}$  is determined from the measurement vector  $\mathbf{M}$  under consideration of the measurement uncertainties  $\epsilon$ . This requires an adequate formulation of the theory matrix  $\mathbf{A}$ .

In the F-region ionosphere, the east- and northward ion velocities  $v_E^F$  and  $v_N^F$  can be assumed constant with altitude while the vertical ion velocity  $v_z^F$  changes with height (Nygrén et al., 2011). Therefore, the unknown vector  $\mathbf{x}$  for each 6 min beam-swing cycle consists of one  $v_E^F$  value, one  $v_N^F$  values, and  $n_G$   $v_z^{FG}$  values where  $n_G$  is the number of pre-defined F-region altitude gates. We define  $n_G = 14$  altitude gates ranging from 230 to 515 km altitude with a resolution of 15 km (230–260 km), 20 km (280–360 km), and 25 km (390–515 km). Ideally, one measurement cycle consists of four pointing directions and therefore the total number of beam-aligned ion velocity measurements for each beam-swing cycle is  $4 \cdot n_G$ . Though F region electron densities are large enough to allow for ISR measurements at most times, it has to be considered that the fit of the incoherent scatter spectrum does not converge for one or more beams during some cycles. Beam-swing cycles with less than four converging ISR measurements are disregarded for the analysis in this paper. For each measurement position, the azimuth angle  $\alpha$  and the elevation angle  $\beta$  are known and the measurements can be expressed by the standard radial wind equation

$$M_i^G = \sin\alpha_i \cos\beta_i v_E^F + \cos\alpha_i \cos\beta_i v_N^F + \sin\beta_i v_z^{FG} \quad (6)$$

for  $i = [1, 4]$ . The transformation coefficients in Equation 6 give the  $i$ th line of the theory matrix  $\mathbf{A}_G$  for a single altitude gate. Repeating this for each altitude gate gives the complete theory matrix  $\mathbf{A}$  (see Nygrén et al., 2011, Equation 21).

Since the F-region ionosphere can be assumed to be collisionless, the perpendicular electric field can be approximated by the electric drift formula

$$\mathbf{E}_\perp = -\mathbf{v}^F \times \mathbf{B}. \quad (7)$$

As for the magnetic field  $B$ , the International Geomagnetic Reference Field (IGRF) (Alken et al., 2021; Barraclough, 1988) is employed.  $\mathbf{E}_\perp$  is calculated at 300 km altitude and linearly scaled with the increasing magnetic field strength at lower altitudes, that is, the ratio of E-region to F-region magnetic field strength  $B^E/B^F \approx 1.1$  (Nozawa et al., 2010).  $\mathbf{E}_\perp$  can then be applied to calculate the local Joule heating rate in the E-region given by Equation 2. Numerical integration of the 13 E-region altitude gates gives the height-integrated Joule heating rate  $Q_J$ . Although the TIE-GCM gives the local Joule heating rate as an output variable, we calculate  $q_J^M$  from Equation 2 assuming the F-region  $\mathbf{v}^F$  at 300 km altitude. This way, we ensure that any differences between  $q_J^M$  and  $q_J^E$  are due to the application of EISCAT plasma parameters and not due to any potential differences in the calculation method.

The Pedersen conductivity in Equation 2 is given as (Baumjohann & Treumann, 1996)

$$\sigma_P = \left( \frac{\nu_{en}}{\nu_{en}^2 + \Omega_e^2} + \frac{m_e}{m_i} \frac{\nu_{in}}{\nu_{in}^2 + \Omega_i^2} \right) \frac{N_e e^2}{m_e}. \quad (8)$$

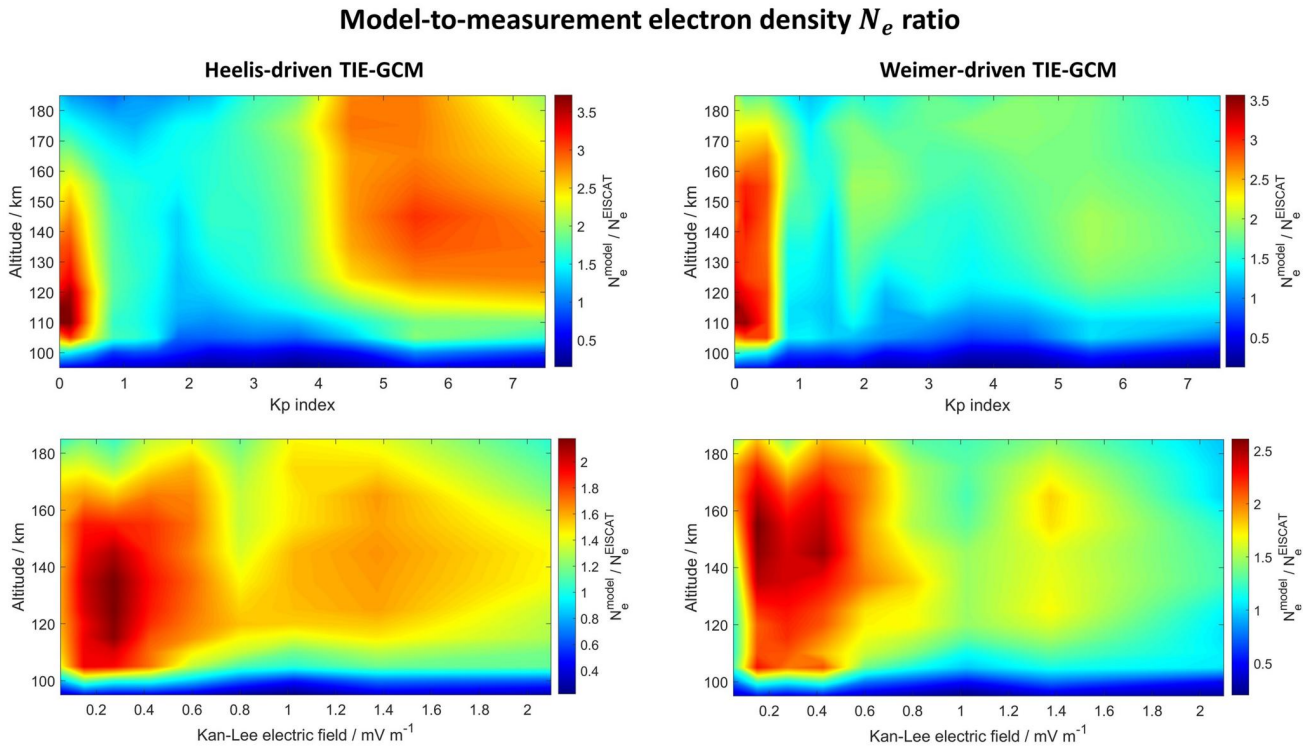


**Figure 2.** Ratio of electron densities  $N_e$  as given by TIE-GCM, driven with either *Heelis* or *Weimer* convection, to EISCAT measurements. The electron densities have been binned with respect to the  $Kp$  index and  $E_{KL}$ .

The ion/electron-neutral collision frequencies  $\nu_{in}$  and  $\nu_{en}$ , ion/electron gyro-frequencies  $\Omega_i$  and  $\Omega_e$  and the mean ion mass  $m_i$  are taken from TIE-GCM runs for the calculation of both  $q_J^M$  and  $q_J^E$ . The electron density  $N_e$  is taken from EISCAT measurements when calculating  $q_J^E$  and from the TIE-GCM output when calculating  $q_J^M$ . Whether the calculation of  $q_J^E$  should be done with model or measurement  $N_e$ , is up to discussion. Taking the model  $N_e$  would ensure that the differences of  $q_J^E$  and  $q_J^M$  are entirely caused by the plasma convection and therefore allow to evaluate the two convection models in comparison to ISR measurements. On the other hand, if the EISCAT ISR measured electron density is applied,  $q_J^E$  is closer to the actual Joule heating rate which is of interest when the empirical Joule heating scaling factor is adjusted. Therefore, the EISCAT measured  $N_e$  is applied for the calculation of  $q_J^E$  throughout the paper. Figure 2 gives the ratios of model-to-measurement electron density for both *Heelis*- and *Weimer*-driven runs binned with respect to the  $Kp$  index and  $E_{KL}$ . It can be seen from Equations 2 and 8 that this factor linearly propagates to the Joule heating rates.

The vertical profile of the neutral wind  $\mathbf{u}(z)$  in Equations 2 and 3 is always taken from TIE-GCM. Especially for periods of low geomagnetic activity, the neutral wind contribution to the Joule heating rate can not be neglected (Baloukidis et al., 2023; Vickrey et al., 1982).

#### 4. Results

After calculating  $q_J^M$  and  $q_J^E$  for each time-point, the profiles are binned with respect to the  $Kp$  index,  $E_{KL}$ , and MagLT. For each bin, a median profile  $q_J^E(z)$  and two median profiles  $q_J^M(z)$ , one for *Heelis*- and one for *Weimer*-driven model runs, are calculated. The optimum empirical scaling factor  $f$  is determined by a non-linear least-square fit of  $q_J^E(z) - f \cdot q_J^M(z) = 0$ . This is demonstrated in Figure 3 for 230 hr of data during September 2005 with  $Kp > 2$  conditions.

The model profiles in Figure 3a are linearly scaled to fit  $q_J^E$  which results in the profiles shown in Figure 3b. From the non-linear least-square fit, it is found that the optimum scaling factors for the model runs with *Heelis* and

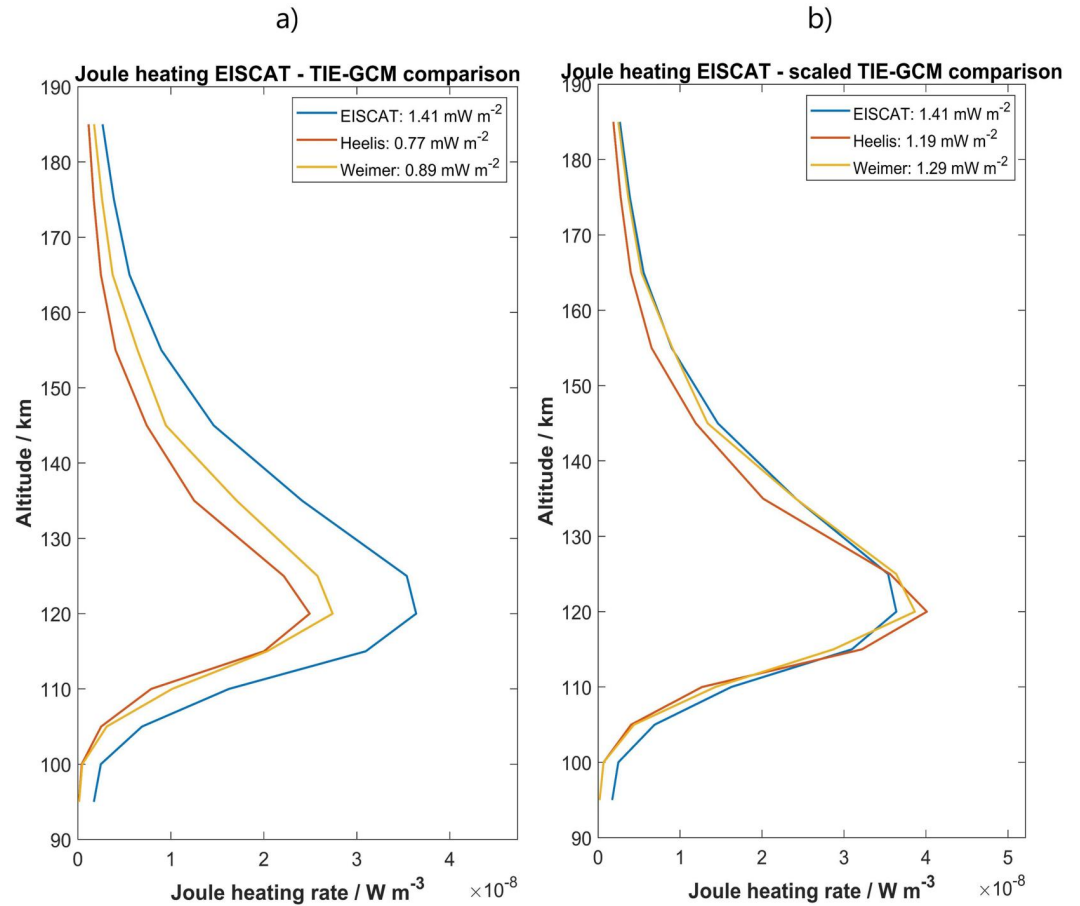


**Figure 3.** (a) Joule heating profiles  $q_J^E$  calculated with EISCAT plasma parameters and  $q_J^M$  calculated from TIE-GCM simulations with both *Heelis* and *Weimer* plasma convection for  $Kp > 2$ . (b) The two model profiles are scaled with the optimum scaling factors  $f_H = 1.60$  and  $f_W = 1.41$  to fit  $q_J^E$ .

*Weimer* plasma convection are  $f_H = 1.60$  and  $f_W = 1.41$ . These are very close to the default value  $f = 1.5$  in the TIE-GCM.

For further analysis, an extended database of approximately 2,220 hr of EISCAT measurements and TIE-GCM simulations is applied. The data is binned according to the  $Kp$  index and  $E_{KL}$  ranges given in Table 1. We investigate the optimum profile scaling factor  $f$  and the mean-squared difference of the vertical Joule heating rate profiles. The mean-squared difference is calculated as  $MSD = 1/n_z \cdot \sum_{i=1}^{n_z} (q_{J,i}^E - q_{J,i}^M)^2$  where  $n_z = 13$  is the number of altitude gates, and  $q_{J,i}^E$  and  $q_{J,i}^M$  are the discretized Joule heating rate profiles. We also investigate the absolute and relative difference between the height-integrated Joule heating rates  $Q_J^M$  and  $Q_J^E$ . Figure 4 shows the variation of these quantities with the  $Kp$  index.

For the TIE-GCM runs driven with the *Heelis* convection model, it can be seen in Figure 4a that the model would require a significantly larger scaling factor to fit the EISCAT-constrained Joule heating rates at  $Kp < 4$  conditions. In Figures 4b–4d, the results are shown for the application of the default  $f = 1.5$  and the optimized  $f$  from Figure 4a. An adjustment of the scaling factor reduces the  $MSD$  in Figure 4b by two orders of magnitude. Due to the generally lower Joule heating rates at  $Kp < 4$ , the absolute difference  $\Delta Q_{abs} = Q_J^E - Q_J^M$  in Figure 4c is very low. Nevertheless, it can be seen that the height-integrated Joule heating rate gets slightly closer to  $Q_J^E$  by adjusting the scaling factor for *Heelis*-driven runs at  $Kp < 4$ . The relative difference  $\Delta Q_{rel} = (Q_J^E - Q_J^M)/Q_J^E$  in Figure 4d would be notably reduced. For  $Kp > 4$ , the default scaling factor  $f = 1.5$  seems to be appropriate or even too large for *Heelis*-driven TIE-GCM runs. The  $MSD$  of

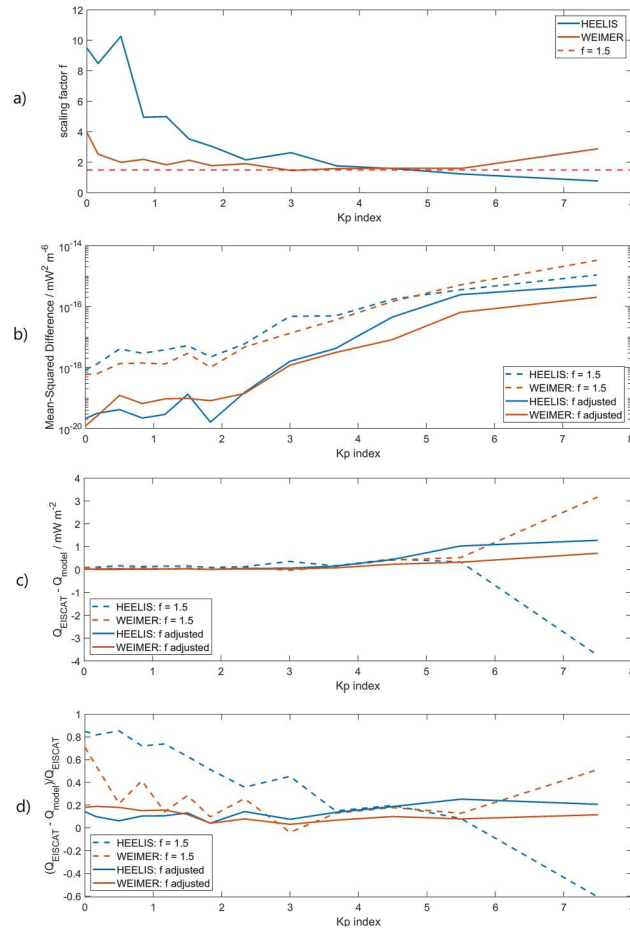


**Figure 4.** (a) Scaling factor  $f$ , (b) the mean-squared difference of  $Q_J^M$  and  $Q_J^E$ , (c) the absolute and (d) the relative difference of the height-integrated Joule heating rates  $Q_J^M$  and  $Q_J^E$ . The dotted lines in (b)–(d) give the results for  $f = 1.5$  and the solid lines in case the scaling factors from (a) are applied to calculate the model Joule heating rate.

the Joule heating rate profiles is significantly larger at  $Kp > 4$  than at lower geomagnetic activity and could be decreased by adjusting the scaling factor. However,  $\Delta Q_{abs}$  and  $\Delta Q_{rel}$  are actually increased for the adjusted scaling factor at  $Kp \sim 5$ . At  $Kp > 5$ , on the other hand,  $Q_J^M$  is far too high for the default  $f = 1.5$  and adjusting the scaling factor would bring it significantly closer to  $Q_J^E$ .

The TIE-GCM runs driven with the *Weimer* convection model require a scaling factor  $f > 1.5$  at  $Kp < 4$  conditions. The *MSD* of  $q_J^M$  and  $q_J^E$  would be significantly reduced by adjusting the scaling factor. The relative difference would generally be reduced at  $Kp < 4$  by adjusting the scaling factor while  $\Delta Q_{abs}$  does not change notably. At  $Kp > 5$ , *Weimer*-driven model runs clearly underestimate the Joule heating rate. An adjustment of the scaling factor would significantly reduce the profile *MSD* as well as  $\Delta Q_{abs}$  and  $\Delta Q_{rel}$ .

In summary, the TIE-GCM results show very different behavior for *Heelis*- and *Weimer*-driven polar plasma convection. For the default scaling factor  $f = 1.5$ , the *Heelis*-driven model runs underestimate the Joule heating rate at  $Kp < 4$  and overestimate it at  $Kp > 5$ . For *Weimer*-driven model runs, the default  $f = 1.5$  seems to work considerably well at  $Kp < 4$ . While the *MSD* of the Joule heating rate profiles could be slightly decreased by adjusting the scaling factor, the height-integrated Joule heating rate would remain approximately the same. At  $Kp > 4$ , however, the Joule heating rates are clearly underestimated for the  $f = 1.5$  case and an adjustment of the scaling factor would reduce the gap between the model Joule heating rates and those constrained by EISCAT measurements.

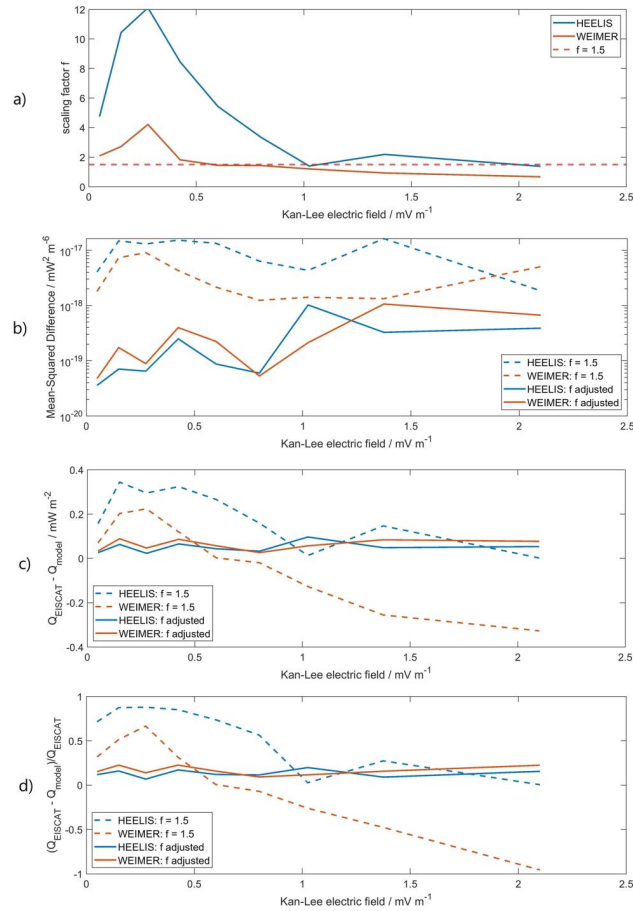


**Figure 5.** (a) Scaling factor  $f$ , (b) the mean-squared difference of  $q_J^M$  and  $q_J^E$ , (c) the absolute and (d) the relative difference of the height-integrated Joule heating rates  $Q_J^M$  and  $Q_J^E$ . The dotted lines in (b)–(d) give the results for  $f = 1.5$  and the solid lines in case the scaling factors from (a) are applied to calculate the model Joule heating rate.

As mentioned in Section 1, the *Weimer* convection model determines the polar plasma potential from solar wind and IMF parameters. Therefore, the analysis above is repeated for the Kan-Lee merging electric field  $E_{KL}$  bins listed in Table 1. The results are shown in Figure 5.

The required scaling factor in Figure 5a shows that *Heelis*-driven TIE-GCM runs generally underestimate the Joule heating rate for most  $E_{KL}$  values. An adjustment of the scaling factor would reduce the *MSD* of the vertical Joule heating rate profiles by at least one order of magnitude for all  $E_{KL}$  values as shown in Figure 5b. This can also be seen in Figure 5c, where  $\Delta Q_{abs}$  would be decreased by adjusting the scaling factor at all conditions with the exception of  $E_{KL} \sim 1 \text{ mV m}^{-1}$  and  $E_{KL} \gtrsim 2 \text{ mV m}^{-1}$ . The same result is found for the relative difference in Figure 5d.

For the *Weimer*-driven model runs, it is found in Figure 5a that by applying a constant  $f = 1.5$ , the Joule heating rate is underestimated for  $E_{KL} \lesssim 0.5 \text{ mV m}^{-1}$  and overestimated for  $E_{KL} \gtrsim 1 \text{ mV m}^{-1}$ . Figures 5c and 5d show that an adjustment of the scaling factor would reduce  $\Delta Q_{abs}$  and  $\Delta Q_{rel}$  for these  $E_{KL}$  ranges. Especially at  $E_{KL} \gtrsim 1 \text{ mV m}^{-1}$ , the *Weimer*-driven model Joule heating rates would be significantly closer to the measurement-constrained results if the scaling factor is adjusted.

It has been reported previously that the Joule heating rate varies strongly with the magnetic local time (Baloukidis et al., 2023; Foster et al., 1983). We will therefore investigate the Joule heating rates separately for four MagLT bins covering the dawn sector (03–09 MagLT), the noon sector (09–15 MagLT), the dusk sector (15–21 MagLT), and the midnight sector (21–03 MagLT). To obtain enough measurement time in each investigated bin, the *Kp* index and  $E_{KL}$  bins are enlarged as stated in Tables 2 and 3. In total, we obtain vertical Joule heating rate profiles

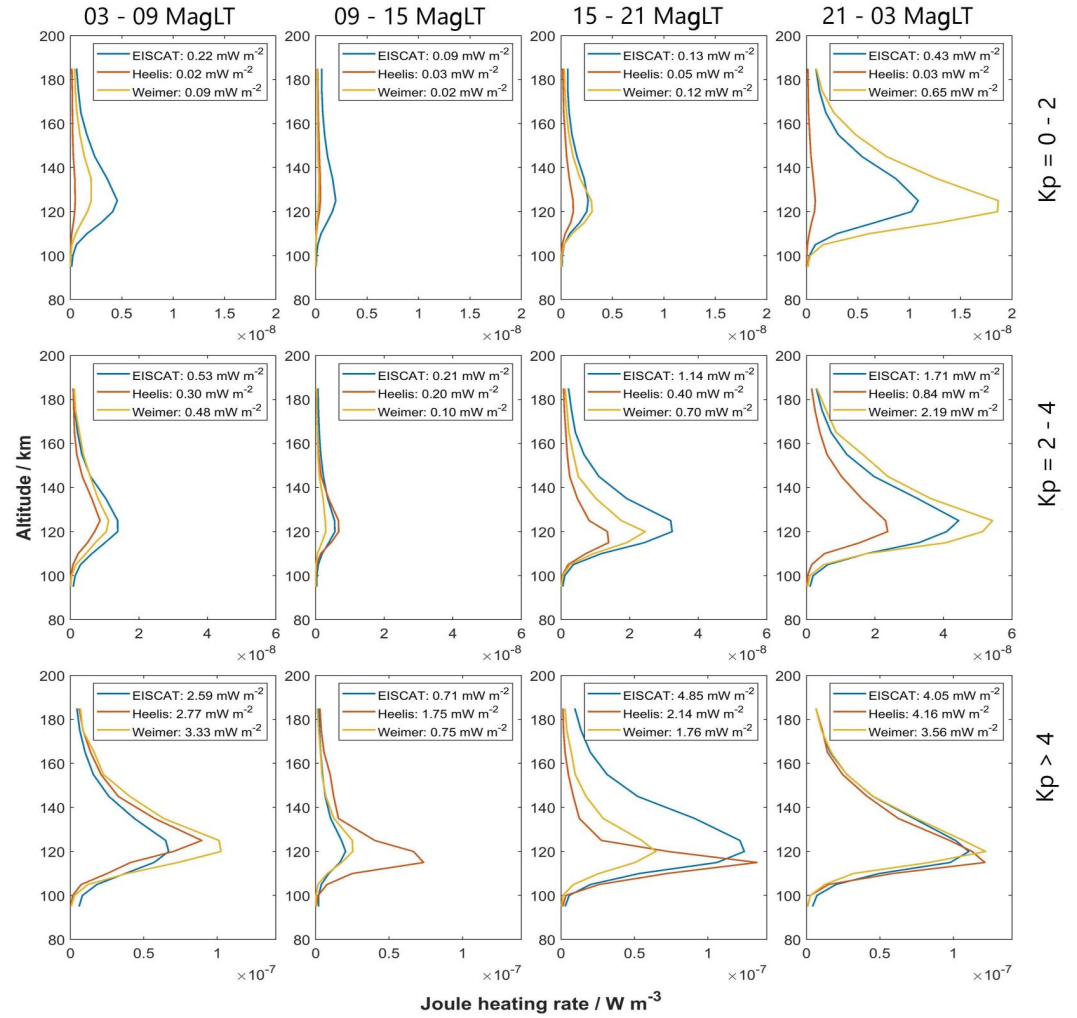


**Figure 6.** Median vertical profiles of the Joule heating rate  $q_J^M$  and  $q_J^E$  for 12 bins of varying  $K_p$  index and magnetic local time. The default  $f = 1.5$  has been applied to the model Joule heating rate profiles. The respective height-integrated Joule heating rates are given in the legends.

and the associated height-integrated Joule heating rates for 12 bins. Figure 6 shows the  $q_J$  profiles binned with respect to the  $K_p$  index and MagLT.

As expected, the Joule heating rate increases with the  $K_p$  index which can be seen from the maxima of the vertical profiles and the height-integrated Joule heating rates given in Figure 6. This is found for both  $q_J^M$  and  $q_J^E$ .  $q_J^E$  is generally lowest in the noon MagLT sector and largest in the midnight MagLT sector. The important exception is for  $K_p > 4$ , where the largest  $q_J^E$  is actually found in the dusk MagLT sector. For the model runs, both driven by *Heelis* and *Weimer* convection, it is found that the Joule heating rate is lowest in the noon sector and largest in the midnight sector for all  $K_p$  ranges. The model profiles shown in Figure 6 have been scaled with the default factor  $f = 1.5$ . The *Heelis*-driven model Joule heating rates are generally lower than those constrained by EISCAT measurements for  $K_p < 4$ . This agrees with Figure 4 where it has been shown that *Heelis*-driven runs require a larger than default scaling factor at  $K_p < 4$ . At  $K_p > 4$ , however,  $q_J^M$  approximately fits the EISCAT-constrained  $q_J^E$  or even exceeds it for the noon sector, where  $q_J^E$  is overall lowest.

At  $K_p < 4$ , the default-scaled *Weimer*-driven TIE-GCM runs show Joule heating rates lower than  $q_J^E$  at all magnetic local times except for the midnight MagLT sector. For  $K_p > 4$ , however, the  $q_J^M$  profiles from *Weimer*-driven runs

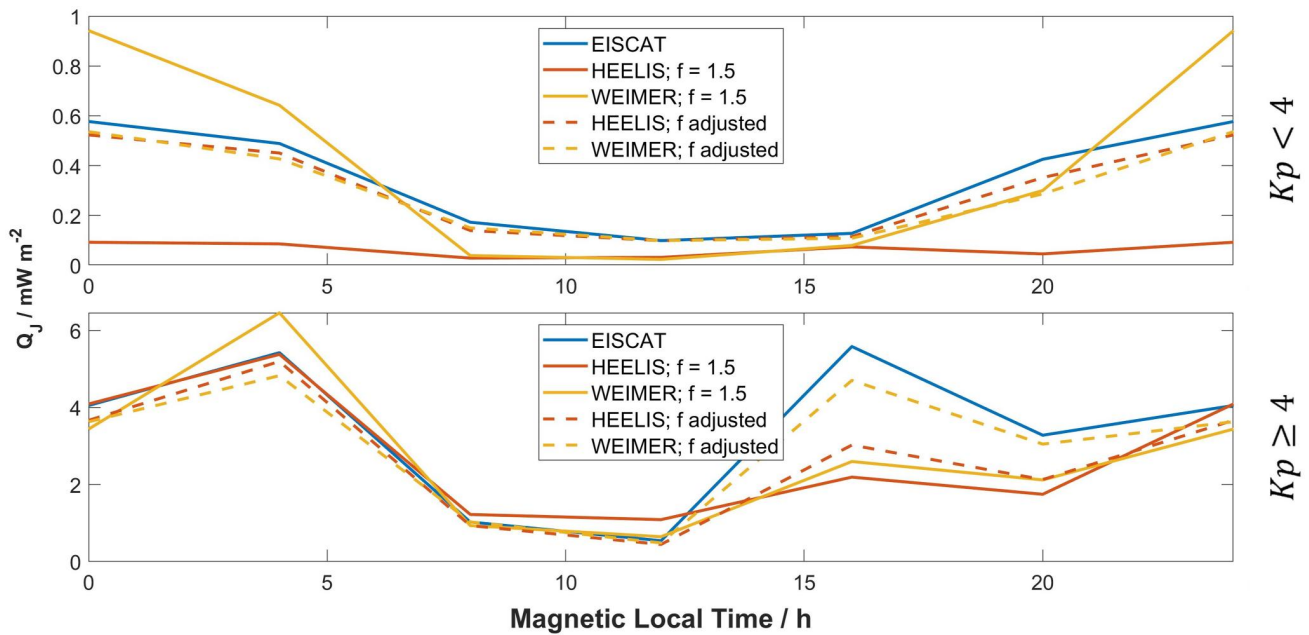


**Figure 7.** Variation of the height-integrated Joule heating rates  $Q_J^M$  and  $Q_J^E$  with magnetic local time for  $Kp < 4$  (top) and  $Kp \geq 4$  (bottom). The model results are shown as dashed lines for the default  $f = 1.5$  and solid lines for an adjusted scaling factor.

fit the  $q_j^E$  profiles very well, except for the dusk MagLT sector. Here, the Joule heating is clearly underestimated by the model runs.

In summary, it can be seen from Figure 6 that the magnetic local time very much impacts the vertical Joule heating profiles  $q_j^M$  and  $q_j^E$  and the required scaling. This can also be seen from the variation of the height-integrated Joule heating rates  $Q_J^M$  and  $Q_J^E$  with magnetic local time shown in Figure 7. Two cases of geomagnetic activity,  $Kp < 4$  and  $Kp \geq 4$ , are distinguished.

As noticed before, Figure 7 shows that Joule heating rates are largest during nighttime for  $Kp < 4$ . While the *Heelis*-driven runs give a very low height-integrated Joule heating rate at all MagLTs,  $Q_J^M$  from *Weimer*-driven runs is lower than  $Q_J^E$  during daytime and larger during nighttime. Adjusting the scaling factor would reduce the difference between EISCAT-constrained and model height-integrated Joule heating rates at all magnetic local times.

At  $Kp > 4$ , the  $Q_J^E$  maximum is around 16 MagLT, and the largest  $Q_J^M$  are found around 4 MagLT. It can be seen in Figure 6 that all model runs give distinctly larger Joule heating rates than the EISCAT-constrained calculations for  $Kp > 4$ , 3–9 MagLT. It should be noted that at  $Kp > 4$ , the *Heelis*-driven runs scaled with  $f = 1.5$  reproduce  $Q_J^E$  extremely well at about 0–6 MagLT, while the *Weimer*-driven runs give  $Q_J^M$  very close to  $Q_J^E$  at around 6–12 MagLT. Therefore, the required scaling factor does not only change with the  $Kp$  index and convection model but also with magnetic local time. Similar to Figure 4a, the required scaling factors for the dawn, noon, dusk, and midnight MagLT sectors are shown in Figure 8.

The large scaling factor required for *Heelis*-driven runs at low  $Kp$  values seen in Figure 4 is mostly caused by the dawn and midnight sectors (see Figures 8a and 8d). During the noon and dusk sector in Figures 8b and 8c, the *Heelis*-driven runs underestimate the Joule heating for low  $Kp$  values less strongly. At high  $Kp$  values, the differences between  $Q_J^M$  and  $Q_J^E$  seems to be well accounted for by the default  $f = 1.5$  except for the noon sector where  $f$  should be reduced.

The *Weimer*-driven TIE-GCM runs seem to underestimate the Joule heating rate at low  $Kp$  values during the dawn and noon sectors. During the dusk and midnight sectors,  $f = 1.5$  seems to be appropriate in order to reproduce  $Q_J^E$ . In Figure 4, it has been noted that *Weimer*-driven model runs tend to underestimate the Joule heating rate more

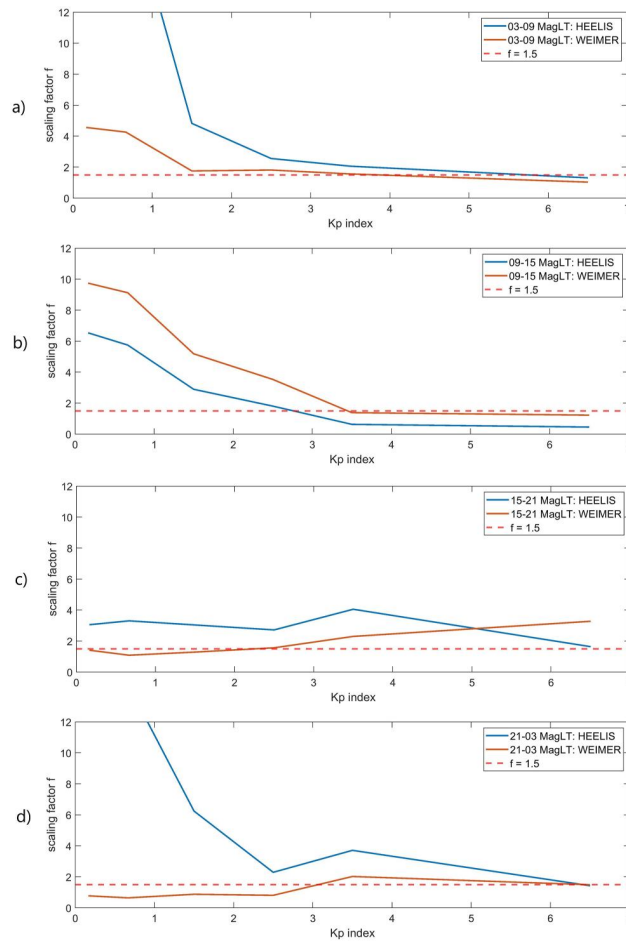


**Figure 8.**  $Kp$  index dependence of the required Joule heating scaling factor  $f$  for the different magnetic local time sectors (a) 03–09, (b) 09–15, (c) 15–21, and (d) 21–03.

than covered by  $f = 1.5$  for  $Kp > 4$ . As can be seen in Figure 8c, this is actually only the case for the dusk MagLT sector where EISCAT-constrained Joule heating rates were largest. During all other MagLT sectors,  $f = 1.5$  appears to be very close to the required scaling factor at  $Kp > 4$ .

In summary, the required scaling factor changes significantly not only with the  $Kp$  index but also with the magnetic local time. Adjusting the scaling factor  $f$  with respect to MagLT might therefore result in a notably better agreement of Joule heating rates calculated from measurement and model results. The  $E_{KL}$  dependence for different MagLT sectors is investigated with the bins listed in Table 3. The Joule heating profiles for the respective bins are shown in Figure 9, the model run profiles have again been scaled with  $f = 1.5$ .

It can be seen that the Joule heating rate generally but not strictly increases with  $E_{KL}$ . The strongest Joule heating is found for the midnight MagLT sector and the weakest Joule heating for the noon MagLT sector at all  $E_{KL}$  conditions. The MagLT dependence of the Joule heating rate therefore agrees well with Figure 6.

The *Heelis*-driven TIE-GCM runs give too low Joule heating rates in all 12 bins, indicating that in these runs  $E_{KL}$  and the Joule heating rate are not well correlated. This can be explained by the fact that *Heelis*-driven runs do not apply any solar wind information as input. However, the *Weimer*-driven runs show a behavior very similar to what has been found in Figure 6. At  $E_{KL} > 0.5 \text{ mV m}^{-1}$  and in the MagLT midnight sector, *Weimer*-driven TIE-GCM runs give Joule heating profiles that fit  $q_j^E$  very well or even exceed them. At all other conditions, the model runs tend to underestimate the Joule heating. Figure 10 displays the variation of the height-integrated Joule heating rate with MagLT, distinguished for the two cases  $E_{KL} < 0.5 \text{ mV m}^{-1}$  and  $E_{KL} \geq 0.5 \text{ mV m}^{-1}$ .

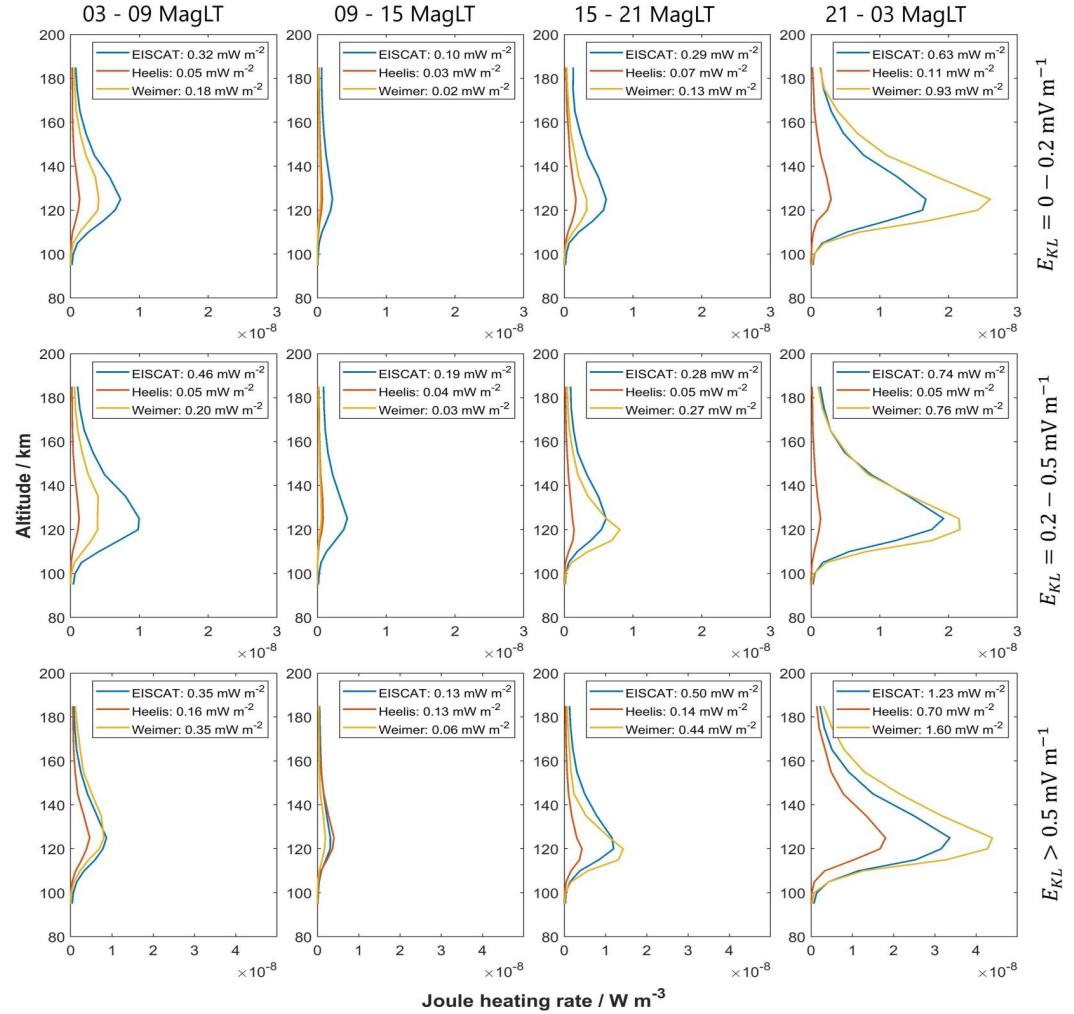


**Figure 9.** Median vertical profiles of the Joule heating rates  $q_j^M$  and  $q_j^E$  for 12 bins of varying  $E_{KL}$  and magnetic local time. The default  $f = 1.5$  has been applied to the model Joule heating rate profiles. The respective height-integrated Joule heating rates are given in the legends.

For  $E_{KL} < 0.5 \text{ mV m}^{-1}$ , the results are nearly equivalent to the  $Kp < 4$  case shown in Figure 7.  $Q_j$  is generally largest at MagLT midnight and *Heelis*-driven runs give extremely low Joule heating rates at all magnetic local time sectors. The *Weimer*-driven runs overestimate the heating rate at nighttime and underestimate it at daytime. Adjusting the scaling factor would significantly decrease the difference between  $Q_j^M$  and  $Q_j^E$  for all magnetic local times.

For  $E_{KL} \geq 0.5 \text{ mV m}^{-1}$ , the results are quite similar to the low geophysical activity conditions. The height-integrated Joule heating rate is largest during the midnight MagLT sector. The *Heelis*-driven TIE-GCM runs reproduce  $Q_j^E$  well at about 8–16 MagLT but strongly underestimate the Joule heating for all other times. The *Weimer*-driven runs also reproduce  $Q_j^E$  very well at about 8–16 MagLT and slightly overestimate it at most other magnetic local times. An adjustment of the scaling factor would improve the height-integrated Joule heating rate in both *Heelis*- and *Weimer*-driven runs at all magnetic local times compared to the EISCAT-constrained Joule heating rates.

For the four MagLT sectors investigated in Figure 9, the required scaling factors at different  $E_{KL}$  conditions are shown in Figure 11.

The distinctly larger Joule heating scaling required for *Heelis*-driven model runs at low  $E_{KL}$  values is mostly rooted in the dawn and midnight MagLT sectors shown in Figures 11a and 11d. This is similar to what has been

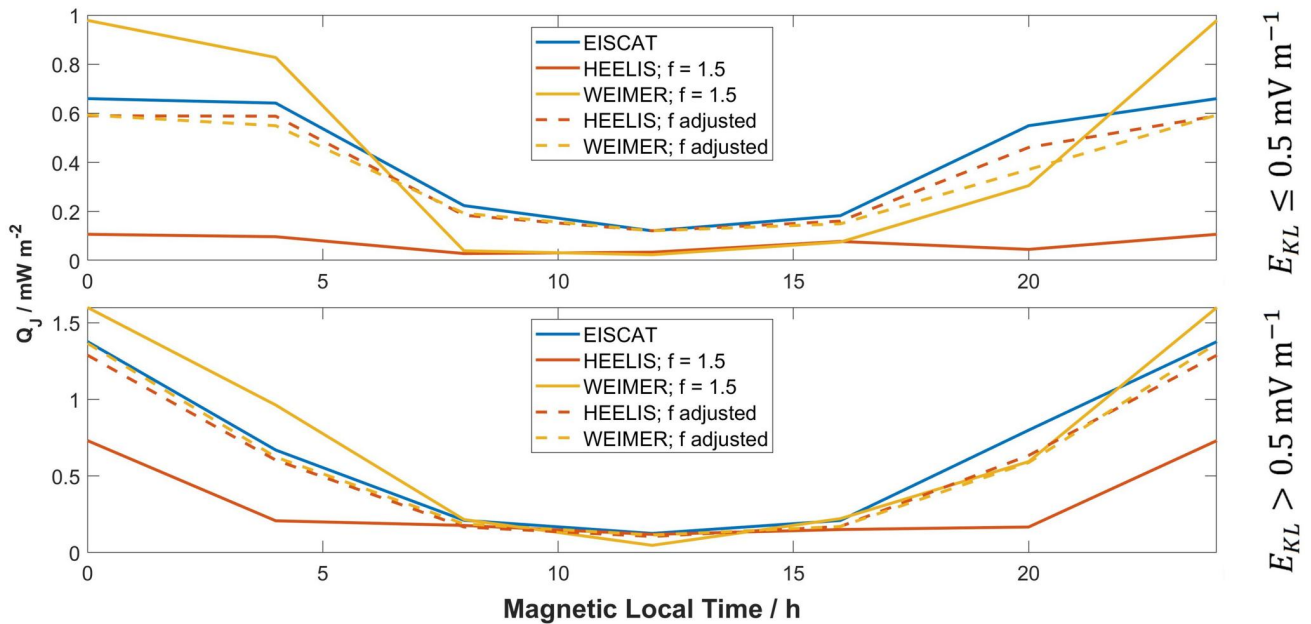


**Figure 10.** Variation of the height-integrated Joule heating rates  $Q_J^M$  and  $Q_J^E$  with magnetic local time for  $E_{KL} < 0.5 \text{ mV m}^{-1}$  (top) and  $E_{KL} \geq 0.5 \text{ mV m}^{-1}$  (bottom). The model results are shown as dashed lines for the default  $f = 1.5$  and solid lines for an adjusted scaling factor.

found in Figure 8. However, as has been noted in Figure 9, the default  $f = 1.5$  is too low for *Heelis*-driven runs under most  $E_{KL}$  and MagLT conditions. The exception is for  $E_{KL} \gtrsim 0.8 \text{ mV m}^{-1}$  during the MagLT noon sector in Figure 11 where a scaling factor slightly lower than  $f = 1.5$  would lead to the best fit. This is equivalent to what has been found for  $Kp > 3$  in Figure 8.

For the *Weimer*-driven runs, the required scaling factor is very close to the default  $f = 1.5$  for the majority of  $E_{KL}$  conditions and magnetic local times. The clearest deviation is found for  $E_{KL} \lesssim 0.6 \text{ mV m}^{-1}$  during the noon MagLT sector though the required scaling factor is larger than 1.5 for all  $E_{KL}$  conditions in that sector. This agrees very well with Figures 7 and 8b, and 10 which all showed that the Joule heating rate is underestimated around MagLT noon time in *Weimer*-driven TIE-GCM runs.

The optimum scaling factors  $f_H$  and  $f_W$  for *Heelis*- and *Weimer*-driven TIE-GCM runs for 13  $Kp$  bins and 9  $E_{KL}$  bins are shown in Table 4. Tables 5 and 6 give the optimum scaling factors  $f_H$  and  $f_W$  for the four investigated MagLT sectors in three bins of  $Kp$  index and  $E_{KL}$  respectively.

## 5. Discussion

Codrescu et al. (1995) showed that a scaling of the Joule heating in global circulation models is necessary to account for the contribution of processes on time-scales not resolved in the models. The factor  $f = 1.5$  has been implemented in the TIE-GCM as the default factor and, as shown in this study, seems to be appropriate as average factor for all convection models, magnetic local times and geophysical conditions. The general trend that the largest  $q_J$  occurs around midnight and the lowest  $q_J$  is observed around noon magnetic local time agrees well with previous studies (e.g., Baloukidis et al., 2023; Rodger et al., 2001). The exception is that when applying EISCAT plasma parameters at  $Kp > 4$ , the strongest Joule heating is found in the dusk MagLT sector. Foster et al. (1983) reported a maximum of Joule heating rates in the MagLT dusk sector for  $3 \leq Kp \leq 6$  during summer. However, since our data includes comparably few measurements during summer, the dusk maximum of Joule heating found in this paper might not be related to the findings by Foster et al. (1983). Baloukidis et al. (2023) showed that this trend is also found in TIE-GCM runs driven by the *Weimer* convection model. However, the variation of Joule heating with magnetic local time is not exactly reproduced by the model which introduces increased heating rates for MagLT noon time and lower heating rates during the rest of the day (Baloukidis et al., 2023). Similarly, they showed an increase of the Joule heating rate with increasing  $Kp$  index, though the trend is not equally strong in Joule heating rates calculated from measurements and model results. The findings of Baloukidis et al. (2023)

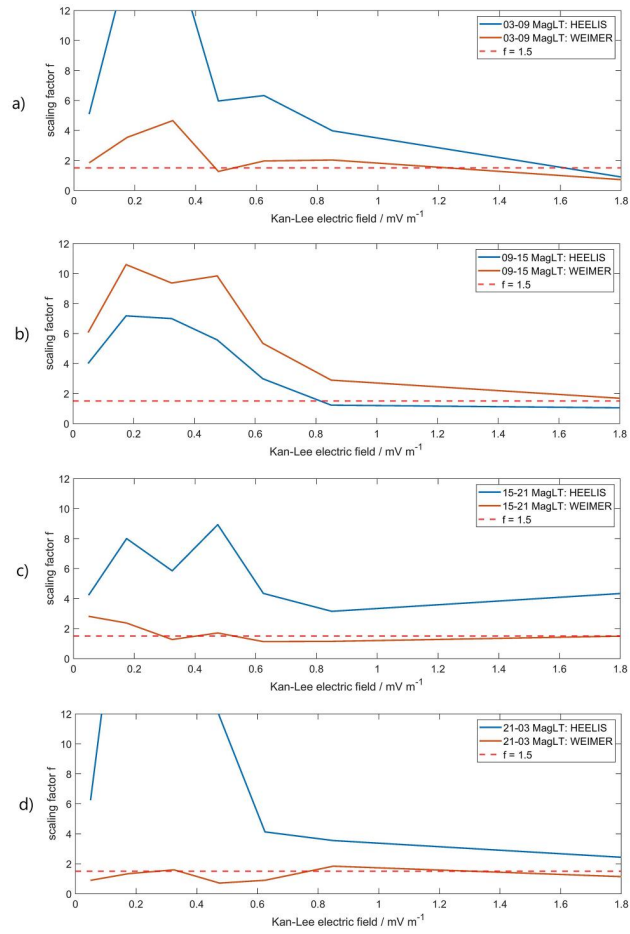


**Figure 11.**  $E_{KL}$  dependence of the required Joule heating scaling factor  $f$  for the different magnetic local time sectors (a) 03–09, (b) 09–15, (c) 15–21, and (d) 21–03.

**Table 4**

Adjusted Scaling Factors  $f_H$  and  $f_W$  for Heelis- and Weimer-Driven Model Runs With Respect to  $K_p$  Index and  $E_{KL}$

$K_p$	$f_H$	$f_W$	$E_{KL}$ ( $\text{mV m}^{-1}$ )	$f_H$	$f_W$
0	9.50	3.97	0–0.1	4.76	2.09
0.333	8.49	2.53	0.1–0.2	10.44	2.72
0.667	10.26	2.00	0.2–0.35	12.11	4.21
1	4.96	2.19	0.35–0.5	8.44	1.82
1.333	5.00	1.84	0.5–0.7	5.44	1.45
1.667	3.53	2.14	0.7–0.9	3.35	1.44
2	3.05	1.78	0.9–1.15	1.40	1.21
2.333–2.667	2.16	1.91	1.15–1.6	2.19	0.93
3–3.333	2.63	1.46	>1.6	1.38	0.67
3.667–4	1.77	1.59			
4.333–5	1.59	1.61			
5.333–6	1.24	1.60			
>6	0.77	2.89			

**Table 5**  
Adjusted Scaling Factor  $f_H$  and  $f_W$  for Heelis- and Weimer-Driven Model Runs With Respect to the Kp Index and MagLT

Kp/MagLT	03–09	09–15	15–21	21–03
<b>0–2</b>	$f_H = 13.32$	$f_H = 5.59$	$f_H = 3.45$	$f_H = 18.91$
	$f_W = 3.16$	$f_W = 8.31$	$f_W = 1.40$	$f_W = 0.87$
<b>2–4</b>	$f_H = 2.68$	$f_H = 1.32$	$f_H = 3.57$	$f_H = 2.89$
	$f_W = 1.88$	$f_W = 2.90$	$f_W = 2.20$	$f_W = 1.24$
<b>4–9</b>	$f_H = 1.31$	$f_H = 0.46$	$f_H = 1.64$	$f_H = 1.43$
	$f_W = 1.04$	$f_W = 1.23$	$f_W = 3.28$	$f_W = 1.49$

could be mostly confirmed in this paper and extended by also considering *Heelis*-driven TIE-GCM runs as well as variations with the Kan-Lee merging electric field  $E_{KL}$ .

Past studies have shown that it is advantageous to adjust the scaling factor with regard to certain parameters, for example, in Emery et al. (1999)  $f = 1.5$  was applied in the winter and  $f = 2.5$  in the summer hemisphere. Foster et al. (1983) showed a strong seasonal dependence of the height-integrated Joule heating rate. It is likely that this variation, similar to the variation with geophysical activity and MagLT, is not exactly reproduced by the models. However, as shown in Figure 1, the measurements investigated in this paper are not equally spread across the year and, thus, a detailed analysis of the scaling parameter for all seasons with similar statistics is not yet feasible from the available database.

It should be considered, that not only the models but also the measurements do not resolve all processes contributing to the spatial and temporal variations of Joule heating. Codrescu et al. (1995) noted that there is a considerable variability of the electric field on time-scales  $\lesssim 5$  min that leads to an underestimation of Joule heating rates. The measurement resolution of 6 min applied in this paper, therefore, does not include the contribution of fast-dynamic processes either. Brekke and Kamide (1996) showed that frictional heating terms related to the inertia of the ions lead to a heating contribution of oscillating electric fields. Fast-changing electric fields on a time-scale  $\sim 1$  s could increase the maximum of the Joule heating rate profile by about 10% (Brekke & Kamide, 1996). However, these time-scales are currently far below the resolution of both ISR measurements and T-I models. But it can be assumed that the required scaling of model Joule heating rates has to be further adjusted once measurements are able to resolve shorter time-scales.

One major assumption for the present study was the application of TIE-GCM neutral winds and ion-neutral collision frequencies for both measurement and model calculations. It is possible to calculate neutral winds from EISCAT CP2 measurements (Brekke et al., 1973; Günzkofer et al., 2022; Nozawa et al., 2010) but this, in turn, requires knowledge of the ion-neutral collision frequency. The ion-neutral collision frequency can be measured from dual-frequency EISCAT experiments (Grassmann, 1993; Günzkofer, Liu, et al., 2023; Günzkofer, Stober, et al., 2023; Nicolls et al., 2014) which is not possible in combination with beam-swing measurements. A direct measurement of the collision frequency, and subsequently the neutral wind, would lead to more accurate Joule heating rate estimations and allow for a better evaluation of the model results.

**Table 6**  
Adjusted Scaling Factor  $f_H$  and  $f_W$  for Heelis- and Weimer-Driven Model Runs With Respect to  $E_{KL}$  and MagLT

$E_{KL}$ (mV m <sup>-1</sup> )/MagLT	03–09	09–15	15–21	21–03
<b>0–0.2</b>	$f_H = 8.90$	$f_H = 4.49$	$f_H = 5.61$	$f_H = 9.27$
	$f_W = 2.52$	$f_W = 6.62$	$f_W = 2.86$	$f_W = 1.00$
<b>0.2–0.5</b>	$f_H = 13.00$	$f_H = 7.62$	$f_H = 6.25$	$f_H = 21.15$
	$f_W = 3.42$	$f_W = 10.63$	$f_W = 1.18$	$f_W = 1.27$
<b>&gt;0.5</b>	$f_H = 3.04$	$f_H = 1.28$	$f_H = 4.47$	$f_H = 2.92$
	$f_W = 1.51$	$f_W = 2.61$	$f_W = 1.30$	$f_W = 1.14$

It should also be noted that the energy deposition by Joule heating strongly depends on the local position within the convection pattern (Foster et al., 1983). So in addition to the strength of the convection pattern, that is, the electric fields and the ion velocities, the size and shape of the convection pattern are of high importance. Both, the *Heelis* and the *Weimer* convection model, have been shown to struggle with giving the accurate size of the convection pattern (Pokhotelov et al., 2008). One possible improvement might be the application of the *assimilative mapping of ionospheric electrodynamics* method to obtain the high-latitude plasma convection (Cousins et al., 2013; Pokhotelov et al., 2021; Richmond & Kamide, 1988).

## 6. Conclusion

It has been shown that Joule heating rates calculated from EISCAT plasma and TIE-GCM neutral parameters vary similarly with respect to the  $K_p$  index, the Kan-Lee merging electric field  $E_{KL}$  and the magnetic local time as Joule heating rates calculated from only TIE-GCM parameters. However, the variations are not equally strong and, therefore, the empirical scaling of Joule heating rates in TIE-GCM runs should be adjusted with respect to these parameters. Significant differences between TIE-GCM runs driven with the *Heelis* and *Weimer* convection models have been found and the scaling factor should be adjusted with respect to this as well. The measurement-constrained Joule heating rate changes drastically with magnetic local time with the largest heating rates in the midnight sector (for  $K_p < 4$  and all  $E_{KL}$  values) and the dusk sector (for  $K_p > 4$ ). While the model runs generally show the same trend, it can be seen that the required scaling factor is distinctly different for the investigated MagLT sectors. In conclusion, it has been shown that the choice of polar plasma convection model, the magnetic local time, and the geophysical conditions, that is, the  $K_p$  index and the Kan-Lee merging electric field, impact the required scaling factor. The seasonal dependence of the required scaling factor cannot be determined with the current measurement data set. Applying the adjusted scaling factor  $f$  found in our study would bring the Joule heating rate estimation by the TIE-GCM closer to the Joule heating rates calculated from EISCAT plasma parameters.

For future investigations, extending the data set to sufficiently cover all seasons is crucial. The current gaps in the data set are due to the fact that only certain measurements with the EISCAT ISR, that is, *CP2* campaigns, can be applied to derive Joule heating rates. The upcoming EISCAT\_3D system (McCrea et al., 2015) will be a major advance as the phased-array concept allows for multi-beam measurements and therefore does not require the rotation of a large radar dish. The EISCAT\_3D radar will allow to create a large database suitable for the derivation of Joule heating rates within a short time of operation. Another advantage of phased-array multi-beam experiments is the possibility to perform pulse-to-pulse beam steering or software beam forming to collect data from many different beam directions without the need to mechanically steer the beam. Since all radar beams are available at nearly the same time, the time resolution of 3D ion velocity vectors will be the same as for the other ISR plasma parameters.

## Acknowledgments

EISCAT is an international association supported by research organizations in China (CRIRP), Finland (SA), Japan (NIPR and ISEE), Norway (NFR), Sweden (VR), and the United Kingdom (UKRI). The TIE-GCM and related Thermosphere-Ionosphere models have been developed by the “Atmosphere Ionosphere Magnetosphere” (AIM) Section of the High Altitude Observatory (HAO) at NCAR (see <http://www.hao.ucar.edu/modeling/tgcm>). The TIE-GCM data was generated on the “Kratos” High-Performance Data Analysis Cluster (HPDA) at the German Aerospace Center (DLR) Jena. Gunter Stober is a member of the Oeschger Center for Climate Change Research (OCCR). Huixin Liu acknowledges supports by JSPS Grants 17KK0095, 18H01270, 20H00197, 22K21345. This work is carried out at Kyushu University with the support of the SCOSTEP SVS program and the JSPS PBASE program. Open Access funding enabled and organized by Projekt DEAL.

## Data Availability Statement

The data are available under the Creative Commons Attribution 4.0 International license at <https://doi.org/10.5281/zenodo.10162944> (Günzkofer, Liu, et al., 2023).

## References

- Alken, P., Thébault, E., Beggan, C. D., Amit, H., Aubert, J., Baerenzung, J., et al. (2021). International geomagnetic reference field: The thirteenth generation. *Earth Planets and Space*, 73(1), 49. <https://doi.org/10.1186/s40623-020-01288-x>
- Baloukidis, D., Sarris, T., Tourgaidis, S., Pinaris, P., Aikio, A., Virtanen, I., et al. (2023). A comparative assessment of the distribution of Joule heating in altitude as estimated in TIE-GCM and EISCAT over one solar cycle. *Journal of Geophysical Research: Space Physics*, 128(12), e2023JA031526. <https://doi.org/10.1029/2023JA031526>
- Barraclough, D. R. (1988). IAGA division I working group 1: International geomagnetic reference field revision 1987. *Geophysical Journal International*, 93(1), 187–189. <https://doi.org/10.1111/j.1365-246X.1988.tb01397.x>
- Baumjohann, W., & Treumann, R. A. (1996). *Basic space plasma physics*. Imperial College Press. <https://doi.org/10.1142/p015>
- Brekke, A., Doupnik, J. R., & Banks, P. M. (1973). A preliminary study of the neutral wind in the auroral E region. *Journal of Geophysical Research*, 78(34), 8235–8250. <https://doi.org/10.1029/JA078i034p08235>
- Brekke, A., & Kamide, Y. (1996). On the relationship between Joule and frictional heating in the polar ionosphere. *Journal of Atmospheric and Terrestrial Physics*, 58(1), 139–143. [https://doi.org/10.1016/0021-9169\(95\)00025-9](https://doi.org/10.1016/0021-9169(95)00025-9)
- Codrescu, M. V., Fuller-Rowell, T. J., & Foster, J. C. (1995). On the importance of E-field variability for Joule heating in the high-latitude thermosphere. *Geophysical Research Letters*, 22(17), 2393–2396. <https://doi.org/10.1029/95GL01909>
- Cousins, E. D. P., Matsuo, T., & Richmond, A. D. (2013). SuperDARN assimilative mapping. *Journal of Geophysical Research: Space Physics*, 118(12), 7954–7962. <https://doi.org/10.1002/2013JA019321>

- Deng, Y., Maute, A., Richmond, A. D., & Roble, R. G. (2009). Impact of electric field variability on Joule heating and thermospheric temperature and density. *Geophysical Research Letters*, *36*(8), L08105. <https://doi.org/10.1029/2008GL036916>
- Deng, Y., & Ridley, A. J. (2007). Possible reasons for underestimating Joule heating in global models: E field variability, spatial resolution, and vertical velocity. *Journal of Geophysical Research*, *112*(A9), A09308. <https://doi.org/10.1029/2006JA012006>
- Emery, B. A., Lathuillere, C., Richards, P. G., Roble, R. G., Buonsanto, M. J., Knipp, D. J., et al. (1999). Time dependent thermospheric neutral response to the 2-11 November 1993 storm period. *Journal of Atmospheric and Solar-Terrestrial Physics*, *61*(3-4), 329-350. [https://doi.org/10.1016/S1364-6826\(98\)00137-0](https://doi.org/10.1016/S1364-6826(98)00137-0)
- Folkstæd, K., Hagfors, T., & Westerlund, S. (1983). EISCAT: An updated description of technical characteristics and operational capabilities. *Radio Science*, *18*(6), 867-879. <https://doi.org/10.1029/RS018i006p00867>
- Foster, J. C., St.-Maurice, J. P., & Abreu, V. J. (1983). Joule heating at high latitudes. *Journal of Geophysical Research*, *88*(A6), 4885-4897. <https://doi.org/10.1029/JA088iA06p04885>
- Grassmann, V. (1993). An incoherent scatter experiment for the measurement of particle collisions. *Journal of Atmospheric and Terrestrial Physics*, *55*(4-5), 573-576. [https://doi.org/10.1016/0021-9169\(93\)90006-K](https://doi.org/10.1016/0021-9169(93)90006-K)
- Günzkofer, F., Liu, H., Stober, G., Pokhotelov, D., & Borries, C. (2023). Evaluation of the empirical scaling factor of Joule heating rates in TIEGCM with EISCAT measurements [Dataset]. *Zenodo*. <https://doi.org/10.5281/zenodo.10162944>
- Günzkofer, F., Pokhotelov, D., Stober, G., Liu, H., Liu, H. L., Mitchell, N. J., et al. (2022). Determining the origin of tidal oscillations in the ionospheric transition region with EISCAT radar and global simulation data. *Journal of Geophysical Research: Space Physics*, *127*(10), e2022JA030861. <https://doi.org/10.1029/2022JA030861>
- Günzkofer, F., Stober, G., Pokhotelov, D., Miyoshi, Y., & Borries, C. (2023). Difference spectrum fitting of the ion-neutral collision frequency from dual-frequency EISCAT measurements. *Atmospheric Measurement Techniques*, *16*(23), 5897-5907. <https://doi.org/10.5194/amt-16-5897-2023>
- Hagan, M. E., & Forbes, J. M. (2002). Migrating and nonmigrating diurnal tides in the middle and upper atmosphere excited by tropospheric latent heat release. *Journal of Geophysical Research*, *107*(D24), 4754. <https://doi.org/10.1029/2001JD001236>
- Hagan, M. E., & Forbes, J. M. (2003). Migrating and nonmigrating semidiurnal tides in the upper atmosphere excited by tropospheric latent heat release. *Journal of Geophysical Research*, *108*(A2), 1062. <https://doi.org/10.1029/2002JA009466>
- Heelis, R. A., Lowell, J. K., & Spiro, R. W. (1982). A model of the high-latitude ionospheric convection pattern. *Journal of Geophysical Research*, *87*(A8), 6339-6345. <https://doi.org/10.1029/JA087iA08p06339>
- Huang, Y., Richmond, A. D., Deng, Y., & Roble, R. (2012). Height distribution of Joule heating and its influence on the thermosphere. *Journal of Geophysical Research*, *117*(A8), A08334. <https://doi.org/10.1029/2012JA017885>
- Kan, J. R., & Lee, L. C. (1979). Energy coupling function and solar wind-magnetosphere dynamo. *Geophysical Research Letters*, *6*(7), 577-580. <https://doi.org/10.1029/GL006i007p00577>
- Kavanagh, A. J., Ogawa, Y., & Woodfield, E. E. (2022). Two techniques for determining F-region ion velocities at meso-scales: Differences and impacts on Joule heating. *Journal of Geophysical Research: Space Physics*, *127*(6), e30062. <https://doi.org/10.1029/2021JA030062>
- Kelley, M. C. (2009). *The Earth's ionosphere: Plasma physics and electrodynamics* (2nd ed.). Elsevier Academic Press.
- Laundal, K. M., & Richmond, A. D. (2017). Magnetic coordinate systems. *Space Science Reviews*, *206*(1-4), 27-59. <https://doi.org/10.1007/s11214-016-0275-y>
- Maute, A. (2017). Thermosphere-ionosphere-electrodynamics general circulation model for the ionospheric connection explorer: TIEGCM-ICON. *Space Science Reviews*, *212*(1-2), 523-551. <https://doi.org/10.1007/s11214-017-0330-3>
- McCrea, I., Aikio, A., Alfonsi, L., Belova, E., Buchert, S., Clilverd, M., et al. (2015). The science case for the EISCAT\_3D radar. *Progress in Earth and Planetary Science*, *2*(1), 21. <https://doi.org/10.1186/s40645-015-0051-8>
- Nicolls, M. J., Bahcivan, H., Häggström, I., & Rietveld, M. (2014). Direct measurement of lower thermospheric neutral density using multi-frequency incoherent scattering. *Geophysical Research Letters*, *41*(23), 8147-8154. <https://doi.org/10.1002/2014GL062204>
- Nozawa, S., Ogawa, Y., Oyama, S., Fujiwara, H., Tsuda, T., Brekke, A., et al. (2010). Tidal waves in the polar lower thermosphere observed using the EISCAT long run data set obtained in September 2005. *Journal of Geophysical Research*, *115*(A8), A08312. <https://doi.org/10.1029/2009JA015237>
- Nygrén, T., Aikio, A. T., Kuula, R., & Voiculescu, M. (2011). Electric fields and neutral winds from monostatic incoherent scatter measurements by means of stochastic inversion. *Journal of Geophysical Research*, *116*(A5), A05305. <https://doi.org/10.1029/2010JA016347>
- Palmroth, M., Janhunen, P., Pulkkinen, T. I., Aksnes, A., Lu, G., Østgaard, N., et al. (2005). Assessment of ionospheric Joule heating by GUMICS-4 MHD simulation, AMIE, and satellite-based statistics: Towards a synthesis. *Annales Geophysicae*, *23*(6), 2051-2068. <https://doi.org/10.5194/angeo-23-2051-2005>
- Pokhotelov, D., Fernandez-Gomez, I., & Borries, C. (2021). Polar tongue of ionisation during geomagnetic superstorm. *Annales Geophysicae*, *39*(5), 833-847. <https://doi.org/10.5194/angeo-39-833-2021>
- Pokhotelov, D., Mitchell, C. N., Spencer, P. S. J., Hairston, M. R., & Heelis, R. A. (2008). Ionospheric storm time dynamics as seen by GPS tomography and in situ spacecraft observations. *Journal of Geophysical Research*, *113*(A3), A00A16. <https://doi.org/10.1029/2008JA013109>
- Rich, F. J., Gussenhoven, M. S., Hardy, D. A., & Høleman, E. (1991). Average height-integrated Joule heating rates and magnetic deflection vectors due to field-aligned currents during sunspot minimum. *Journal of Atmospheric and Terrestrial Physics*, *53*(3-4), 293-308. [https://doi.org/10.1016/0021-9169\(91\)90113-L](https://doi.org/10.1016/0021-9169(91)90113-L)
- Richmond, A. D., & Kamide, Y. (1988). Mapping electrodynamic features of the high-latitude ionosphere from localized observations. *Technique*, *93*(A6), 5741-5759. <https://doi.org/10.1029/JA093iA06p05741>
- Richmond, A. D., Ridley, E. C., & Roble, R. G. (1992). A thermosphere/ionosphere general circulation model with coupled electrodynamics. *Geophysical Research Letters*, *19*(6), 601-604. <https://doi.org/10.1029/92GL00401>
- Rodger, A. S., Wells, G. D., Moffett, R. J., & Bailey, G. J. (2001). The variability of Joule heating, and its effects on the ionosphere and thermosphere. *Annales Geophysicae*, *19*(7), 773-781. <https://doi.org/10.5194/angeo-19-773-2001>
- Schunk, R., & Nagy, A. (2009). *Ionospheres: Physics, plasma physics, and chemistry*. Cambridge Academic Press. <https://doi.org/10.1017/CBO9780511635342>
- Thayer, J. P. (1998). Height-resolved Joule heating rates in the high-latitude E region and the influence of neutral winds. *Journal of Geophysical Research*, *103*(A1), 471-487. <https://doi.org/10.1029/97JA02536>
- Thayer, J. P. (2000). High-latitude currents and their energy exchange with the ionosphere-thermosphere system. *Journal of Geophysical Research*, *105*(A10), 23015-23024. <https://doi.org/10.1029/1999JA000409>
- Tjulín, A. (2021). *Eiscat experiments* (Technical Report). EISCAT Scientific Association. Retrieved from [https://eiscat.se/wp-content/uploads/2021/03/Experiments\\_v20210302.pdf](https://eiscat.se/wp-content/uploads/2021/03/Experiments_v20210302.pdf)

- Vickrey, J. F., Vondrak, R. R., & Matthews, S. J. (1982). Energy deposition by precipitating particles and Joule dissipation in the auroral ionosphere. *Journal of Geophysical Research*, *87*(A7), 5184–5196. <https://doi.org/10.1029/JA087iA07p05184>
- Weimer, D. R. (1995). Models of high-latitude electric potentials derived with a least error fit of spherical harmonic coefficients. *Journal of Geophysical Research*, *100*(A10), 19595–19608. <https://doi.org/10.1029/95JA01755>
- Weimer, D. R. (2005). Improved ionospheric electrodynamic models and application to calculating Joule heating rates. *Journal of Geophysical Research*, *110*(A5), A05306. <https://doi.org/10.1029/2004JA010884>

---

# Difference spectrum fitting of the ion-neutral collision frequency from dual-frequency EISCAT measurements

## Bibliographic information

**Günzkofer F.**, Stober G., Pokhotelov D., Miyoshi Y., and Borries C. Difference spectrum fitting of the ion-neutral collision frequency from dual-frequency EISCAT measurements. *Atmospheric Measurement Techniques*, **16**, 5797-5807, 2023.

DOI: <https://doi.org/10.5194/amt-16-5897-2023>

©2023. The Authors.

## Related Publications

Stober G., Weryk R., Janches D., Dawkins E. C. M., **Günzkofer F.**, Hormaechea J. L., Pokhotelov D. Polarization dependency of transverse scattering and collisional coupling to the ambient atmosphere from meteor trails - theory and observations. *Planetary and Space Science*, **237**, 105768, 2023.

## Author's contribution

For this publication, I implemented the *difference spectrum* method to analyze incoherent scatter spectra from simultaneous measurements with the EISCAT UHF and VHF radars. This required some alterations to the standard EISCAT analysis software package GUIDAP to extract the spectra. I performed the scaling of VHF incoherent scatter spectra to the frequencies of the UHF spectrum. This scaling process included the determination of the  $\beta$  parameter to account for technical differences of the UHF and VHF ISRs. I applied a non-linear least-square fitting algorithm to determine the vertical profiles of ion-neutral collision frequency. To my knowledge, this paper is the first application of the *difference spectrum* method and the second paper presenting direct measurements of ion-neutral collision frequencies from dual-frequency EISCAT experiments. I implemented the equations to calculate neutral density profiles from the obtained collision frequencies. The GAIA model data that were applied for comparison to the obtained neutral density profiles were provided by Y. Miyoshi. My work was supervised by G. Stober, D. Pokhotelov, and C. Borries. As the first author, I wrote large parts of the manuscript, but all authors were involved in revising the text.



# Difference spectrum fitting of the ion–neutral collision frequency from dual-frequency EISCAT measurements

Florian Günzkofer<sup>1</sup>, Gunter Stober<sup>2,3</sup>, Dmitry Pokhotelov<sup>4</sup>, Yasunobu Miyoshi<sup>5</sup>, and Claudia Borries<sup>1</sup>

<sup>1</sup>Institute for Solar-Terrestrial Physics, German Aerospace Center (DLR), Neustrelitz, Germany

<sup>2</sup>Institute of Applied Physics, Microwave Physics, University of Bern, Bern, Switzerland

<sup>3</sup>Oeschger Center for Climate Change Research (OCCR), University of Bern, Bern, Switzerland

<sup>4</sup>Institute of Physics, University of Greifswald, Greifswald, Germany

<sup>5</sup>Department of Earth and Planetary Sciences, Kyushu University, Fukuoka, Japan

**Correspondence:** Florian Günzkofer (florian.guenzkofer@dlr.de)

Received: 3 July 2023 – Discussion started: 15 September 2023

Revised: 23 October 2023 – Accepted: 14 November 2023 – Published: 8 December 2023

**Abstract.** The plasma–neutral coupling in the mesosphere–lower thermosphere strongly depends on the ion–neutral collision frequency across that region. Most commonly, the collision frequency profile is calculated from the climatologies of atmospheric models. However, previous measurements indicated that the collision frequency can deviate notably from the climatological average. Direct measurement of the ion–neutral collision frequency with multifrequency incoherent scatter radar (ISR) measurements has been discussed before, though actual measurements have been rare. The previously applied multifrequency analysis method requires a special simultaneous fit of the two incoherent scatter spectra, which is not possible with standard ISR analysis software. The *difference spectrum* method allows us to infer ion–neutral collision frequency profiles from multifrequency ISR measurements based on standard incoherent scatter analysis software, such as the Grand Unified Incoherent Scatter Design and Analysis Package (GUISDAP) software. In this work, we present the first results by applying the difference spectrum method. Ion–neutral collision frequency profiles obtained from several multifrequency EISCAT ISR campaigns are presented. The profiles obtained with the difference spectrum method are compared to previous collision frequency measurements, both from multifrequency ISR and other measurements, as well as results from empirical and comprehensive atmosphere models. Ion–neutral collision frequency measurements can be applied to improve first-principle ionospheric models.

## 1 Introduction

The magnetospheric current system is closed in the ionospheric dynamo region at approximately 80–130 km altitude due to the maxima of transverse conductivities at these altitudes (Baumjohann and Treumann, 1996). These maxima occur due to the special relations between ion/electron–neutral collision frequencies ( $\nu_{in}$ ,  $\nu_{en}$ ) and ion/electron gyrofrequencies ( $\omega_i$ ,  $\omega_e$ ). In the dynamo region, electrons are coupled with the Earth’s magnetic field lines ( $\nu_{en} \ll \omega_e$ ), whereas ions are decoupled due to frequent collisions with neutral particles ( $\nu_{in} \gg \omega_i$ ) (Brekke et al., 1974). Due to the transition from a collisional to a collisionless plasma, the dynamo region is also often referred to as the ionospheric transition region, and we will use both terms synonymously.

Knowledge of the vertical collision frequency profiles is essential for understanding and predicting ionospheric conductivities and their impact on the atmosphere–ionosphere coupling, e.g., due to the Joule dissipation of Pedersen currents. The impact of ion–neutral collisions on the diffusion of meteor trails makes direct collision frequency measurements important for the analysis of meteor radar data as well (Stober et al., 2023). Neutral wind measurements with incoherent scatter radars (ISRs) also require a priori knowledge of the collision frequencies in the dynamo region (e.g., Brekke et al., 1973; Nozawa et al., 2010; Günzkofer et al., 2022).  $\nu_{in}$  and  $\nu_{en}$  can be calculated by leveraging simplified and idealized relations derived by Chapman (1956) for the ion–neutral collision frequency,

$$\nu_{in} = 2.6 \times 10^{-9} \cdot (n_n + n_i) \cdot A^{-0.5}, \quad (1)$$

and by Nicolet (1953) for the electron–neutral collision frequency,

$$\nu_{en} = 5.4 \times 10^{-10} \cdot n_n \cdot T_e^{0.5}. \quad (2)$$

In Eqs. (1) and (2),  $n_n$  and  $n_i$  are neutral and ion volume densities per cubic centimeter, respectively;  $A$  is the mean atomic mass number; and  $T_e$  is the electron temperature (Kelly, 2009). However, the neutral density  $n_n$  is often taken from empirical atmosphere models such as NRLMSISE-00 (Picone et al., 2002), which introduce a major source of uncertainty when estimating the collision frequencies from the above equations. The relations in Eqs. (1) and (2) are derived assuming ion–neutral and electron–neutral collisions as elastic rigid–sphere collisions (Nicolet, 1953; Chapman, 1956).

There are multiple approaches for direct or indirect measurements of collision frequencies in the ionosphere.

It was shown that it is possible to infer the ion–neutral collision frequency utilizing line-of-sight ion velocity  $v_i$  measurements from ISRs (Nygren et al., 1987). Such an indirect measurement method, however, requires specific conditions and assumptions and is therefore only applicable above  $\sim 106$  km altitude and for electric fields  $E \gtrsim 20$  mV m<sup>−1</sup> (for a more detailed discussion of this method, see Oyama et al., 2012, and references therein). The ion–neutral collision frequency can also be directly inferred from ISR measurements due to its impact on the incoherent scatter spectrum (e.g., Dougherty and Farley, 1963; Farley, 1966; Grassmann, 1993a). However, the shape of the incoherent scatter spectrum is ambiguous towards changes in the collision frequency and changes in ion and electron temperatures  $T_i$  and  $T_e$ . The ambiguity can be overcome by assuming  $T_e = T_i$ ; however, this assumption has to be considered carefully. A summary and discussion of multiple studies that followed this approach with the EISCAT ISR can be found in Nygrén (1996). In these studies, it was generally assumed that at high latitudes  $T_e = T_i$  is valid for low-geomagnetic-activity conditions and below  $\sim 110$  km altitude.

The ion–neutral collision frequency can also be inferred from two incoherent scatter spectra obtained with simultaneous measurements of two ISRs, with well-separated transmitter frequencies. This is possible at the EISCAT site in Tromsø, Norway, where two ISRs with transmitter frequencies of 929 and 224 MHz are operated. Many methods to analyze EISCAT dual-frequency measurements to obtain ion–neutral collision frequencies have been suggested (Grassmann, 1993b). However, actual dual-frequency measurements have been scarce, and only one study performed an analysis to derive collision frequencies (Nicolls et al., 2014). It should be noted that the EISCAT ISR systems are the only ones capable of performing dual-frequency measurements. In their study, Nicolls et al. (2014) followed an approach

suggested by Grassmann (1993b) that requires the simultaneous fitting of both measured spectra to obtain the optimum parameters from the combined fit. This method requires a customized ISR spectrum fitting algorithm and, therefore, cannot be applied within the standard EISCAT analysis software, Grand Unified Incoherent Scatter Design and Analysis Package (GUISDAP). An alternative method suggested by Grassmann (1993b) is the so-called difference spectrum fitting, which combines the spectra after the standard ISR analysis.

In this work, the applicability of the difference spectrum fitting for the measurement of ion–neutral collision frequencies using the two EISCAT ISR systems (UHF and VHF) is demonstrated. We compare the obtained profiles to the results from Nicolls et al. (2014) as well as to other collision frequency measurement methods. The vertical profile of neutral particle density can be inferred from the measured ion–neutral collision frequency, either by applying Eq. (1) or any other collision frequency relation, though most require certain assumptions on the atmospheric composition across the ionospheric dynamo region. The neutral density profiles can be partially validated by meteor radar measurements in the mesosphere–lower thermosphere (MLT) region (Stober et al., 2012; Stober et al., 2014; Dawkins et al., 2023) or by leveraging occultation measurements from satellites of X-ray sources such as the Crab Nebula (Katsuda et al., 2023). Since measurements of atmospheric densities in the ionospheric dynamo region are very rare, dual-frequency ISR measurements allow us to obtain the valuable information required for the validation of atmosphere models. The results of our analysis will be compared to several atmosphere models.

## 2 Instruments and models

### 2.1 EISCAT UHF and VHF radar

The EISCAT Scientific Association operates an ultrahigh-frequency (UHF) and a very-high-frequency (VHF) ISR with frequencies of 929 and 224 MHz, respectively, near Tromsø, Norway (69.6° N, 19.2° E) (Folkestad et al., 1983). The UHF transmitter operates with a power of about 1.5–2 MW. The dish used for transmitting and receiving is 32 m in diameter. The VHF transmitter has a peak power of about 1.5 MW, and the co-located VHF receiver antenna consists of four rectangular (30 m × 40 m) dishes. To perform the dual-frequency analysis, both systems have to be operated at the same time in the same radar mode. A summary of all EISCAT experimental modes can be found in Tjulin (2021). In this work, multiple EISCAT campaigns are analyzed.

#### 2.1.1 August 2013 and September 2021 campaigns

Nicolls et al. (2014) planned and analyzed the EISCAT campaign on 29 August 2013 from 07:00–11:00 UTC. The measurements were conducted with both ISRs operating in the

*beata* radar mode, pointing to the geographical north with an elevation of  $45^\circ$ . This experiment mode allows measurements from about 80 to 500 km altitude, with a vertical resolution of 5–10 km in the transition region.

On 27 September 2021 from 08:00–12:00 UTC, a dual-frequency EISCAT campaign was conducted leveraging the same radar mode and geometry.

### 2.1.2 October 2022 campaign

On 13 October 2022 from 08:00–13:00 UTC, a dual-frequency EISCAT campaign was conducted in the *mandazimuth* experiment mode, also known as the EISCAT Common Programme (CP) 6. As the name suggests, the radar was pointed to the local zenith at  $90^\circ$  elevation. This mode allows measurements between about 70 and 200 km, with a vertical resolution of about 0.4–10 km in the transition region.

## 2.2 NRLMSIS

Since measurements of ion–neutral collision frequencies are rarely available, climatological profiles from empirical atmosphere models often have to be assumed. One application of such profiles is the derivation of neutral winds from ISR ion velocity measurements (e.g., Nozawa et al., 2010; Günzkofer et al., 2022). The mass spectrometer and incoherent scatter radar (MSIS) model (Hedin, 1991) is available in many different versions and is one of the most commonly used empirical atmosphere models. In this paper, we will use empirical atmosphere models both for comparison to measurement data and to obtain profiles of neutral atmosphere parameters that are not available from measurements. Two MSIS versions are applied, NRLMSISE-00 (Picone et al., 2002) and NRLMSIS 2.0 (Emmert et al., 2021).

## 2.3 GAIA

The Ground-to-topside model of Atmosphere and Ionosphere for Aeronomy (GAIA) is a global circulation model giving neutral dynamics for all altitudes from the ground up to  $\sim 600$  km (Jin et al., 2012). The GAIA output was compared and verified with experimental data from numerous different apparatuses for time spans up to several decades. A comparison to meteor radar wind climatologies at the MLT can be found in Stober et al. (2021). GAIA simulations are nudged up to  $\sim 30$  km altitude to the Japanese Reanalysis data (JRA-25/55; Kobayashi et al., 2015). In this study, we use data from GAIA on a grid with a resolution of  $1^\circ$  in latitude and  $2.5^\circ$  in longitude. The GAIA output is available with a vertical resolution of  $1/5$  of the scale height.

## 3 Difference spectrum fitting of the ion–neutral collision frequency

In this section, we describe the difference spectrum fitting method equivalent to Grassmann (1993b), though we changed the notation of some variables. Furthermore, results from multiple EISCAT campaigns are presented. As mentioned in Sect. 1, the main advantage of this method over other approaches described in Grassmann (1993b) is that it can be applied on top of already existing ISR analysis. It, therefore, does not require detailed knowledge of the ISR spectrum fitting process. For all EISCAT data presented in this paper, the fitting of ISR spectra is done with Version 9.2 of GUIDAP (Lehtinen and Huuskonen, 1996). As a priori guesses for the spectra fits, GUIDAP utilizes the climatology models MSIS and IRI. For a weak signal-to-noise ratio, the fitting returns the a priori climatology parameter profiles. However, for a sufficiently good signal quality, the choice of a priori climatology has no impact on the fitted parameters.

In the following, we will distinguish between measured spectra  $S(\omega_x + \delta\omega)$  and theoretical spectra  $s(\omega_x + \delta\omega, N_e, T_i, T_e, v_{in}, v_i)$  with the transmitter frequency  $\omega_x$ . During the fitting process, the measured incoherent scatter spectra  $S(\omega_{VHF} + \delta\omega)$  and  $S(\omega_{UHF} + \delta\omega)$  are saved. The measured VHF spectrum can be scaled to UHF frequencies, knowing the ratio  $\xi = \omega_{UHF}/\omega_{VHF} \approx 4.15$  for the EISCAT systems. According to Grassmann (1993b), the scaled VHF spectrum  $\tilde{S}(\omega_{UHF} + \delta\omega)$  is equivalent to a UHF incoherent scatter spectrum for the scaled parameters  $\xi^2 \cdot N_e$  and  $\xi \cdot v_{in}$ , meaning,

$$\begin{aligned} & \xi^2 \cdot S(\omega_{VHF} + \delta\omega) \\ &= \tilde{S}(\omega_{UHF} + \delta\omega) \\ &= s\left(\omega_{UHF} + \delta\omega, \xi^2 \cdot N_e, T_i, T_e, \xi \cdot v_{in}, v_i\right). \end{aligned} \quad (3)$$

The UHF spectrum and scaled VHF spectrum can be combined into a single difference spectrum,

$$D(\omega_{UHF} + \delta\omega) = S(\omega_{UHF} + \delta\omega) - \beta \cdot \tilde{S}(\omega_{UHF} + \delta\omega), \quad (4)$$

where the additional parameter  $\beta$  is included to account for technical differences between the UHF and VHF radars. As described in Grassmann (1993b),  $\beta$  is determined at sufficiently high altitudes, where  $v_{in} = 0$  and therefore  $D(\omega_{UHF} + \delta\omega) = 0$  can be assumed. It can be seen from Eq. (4) that the two radar frequencies have to be distinctly different. If  $\xi$  is close to 1, the difference spectrum would be in the range of the measurement uncertainties, and no information could be inferred from it.

Figure 1 compares the measured UHF spectrum (top left) with the VHF spectrum after scaling (top right). It can be seen that the spectral intensity maximizes at approximately 200–300 km altitude.  $\beta$  is therefore determined at about 260 km, where the plasma can be assumed as collisionless. Figure 1 (middle) shows the UHF and VHF spectra at three

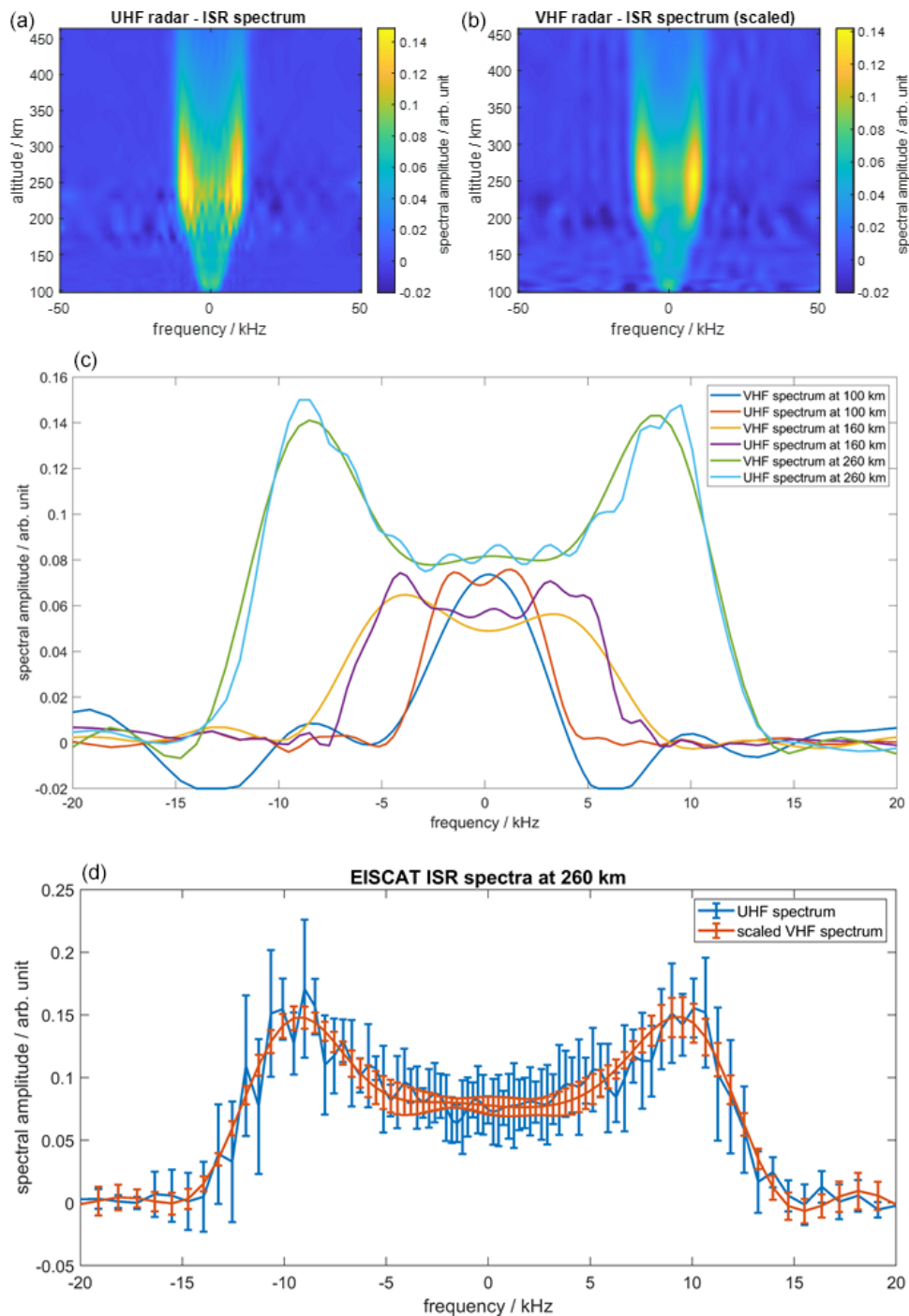


**Figure 1.** EISCAT UHF (a) and scaled VHF (b) spectra measured on 27 September 2021. (c) Comparison of spectra at 260, 160, and 100 km altitudes. It can be seen how the incoherent scatter spectrum changes shape with increasing collision frequency. (d) The UHF and scaled VHF at 260 km altitude with statistical uncertainties over a range of 10 min.

selected altitudes: 260 km, where  $\beta$  is determined, and at two altitudes in the upper and lower transition regions at 160 and 100 km, respectively. At 260 km, both spectra exhibit the typical ISR double-peak shape. As described by Grassmann (1993b), the double-peak shape disappears with increasing

$v_{in}$ , first for the VHF spectrum and at lower altitudes for the UHF spectrum as well. In Fig. 1 (bottom), the UHF and scaled VHF spectra at 260 km altitude are shown for a 10 min interval, with the statistical uncertainty throughout that period. Whether the uncertainties are caused by a variation of

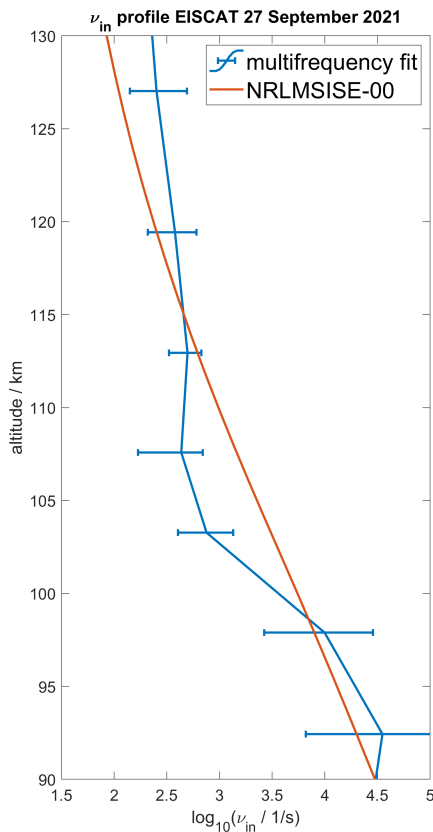


**Figure 2.** Median vertical profile of  $\nu_{in}$  on 27 September 2021 from 08:00–12:00 UTC. One profile fit is performed every 60 s, and the error bars mark the statistical interquartile range. For comparison, a climatological median profile is calculated from the NRLMSISE-00 model.

the ionospheric plasma parameters within this interval or are the result of uncertainties of the incoherent scatter measurements cannot be conclusively determined. The measured difference spectrum is calculated according to Eq. (4) and fitted to the theoretical difference spectrum function,

$$\begin{aligned}
 & d(\omega + \delta\omega, N_e, T_i, T_e, \nu_{in}, \nu_i) \\
 &= s(\omega_{UHF} + \delta\omega, N_e, T_i, T_e, \nu_{in}, \nu_i) \\
 &- \beta \cdot s(\omega_{UHF} + \delta\omega, \xi^2 \cdot N_e, T_i, T_e, \xi \cdot \nu_{in}, \nu_i). \quad (5)
 \end{aligned}$$

It can be seen from Eq. (3) that the scaled VHF spectrum corresponds to a UHF spectrum with scaled collision frequency  $\xi \cdot \nu_{in}$ . The parameters  $T_i$  and  $T_e$  are not affected by the frequency scaling. Therefore, the difference spectrum in Eq. (5) allows us to infer  $\nu_{in}$ ,  $T_i$ , and  $T_e$  without ambiguity or any further assumptions. Figure 2 shows the vertical profile of the ion–neutral collision frequency at 90–150 km altitude for 27 September 2021 from 08:00–12:00 UTC.

The fitted ion–collision frequency profile shows reasonable values across the whole ionospheric transition region. The error bars shown in Fig. 2 mark the upper and lower

quartile of the geophysical variation during the 4 h of measurement. The uncertainties of the ISR spectra are not obtained during the GUIDAP fitting process. However, it can be assumed that for a large enough signal-to-noise ratio the geophysical variation exceeds the effects of the ISR spectrum uncertainty. Below  $\sim 120$  km, the fitted profile oscillates around the climatological mean calculated with Eq. (1) from the NRLMSISE-00 neutral density. At altitudes above 120 km, the fitting method shows a general tendency to larger collision frequencies in comparison with the NRLMSISE-00 model.

As mentioned earlier, there is only one previous multifrequency ISR experiment. The EISCAT campaign from 27 September 2021 was run in the same radar mode as the experiment on 29 August 2013. This allows us to directly apply the developed difference spectrum fitting method to these measurements and compare them to the results shown in Nicolls et al. (2014). However, the fitted profiles for this campaign show a strong dependence on which altitude  $h_\beta$  is used to determine the  $\beta$  parameter. The fitted  $\nu_{in}$  profiles for three different altitudes  $h_\beta$  are shown in Fig. 3 for 20 August 2013 from 07:00–11:00 UTC.

The  $h_\beta = 260$  km profile deviates strongly from the climatological NRLMSIS profile and shows a nearly constant collision frequency at  $\sim 110$ – $150$  km altitude. This is unexpected and has to be discussed carefully. The two profiles for  $h_\beta = 200$  km and  $h_\beta = 150$  km show more resemblance to the climatological average, though the propagated uncertainties are larger compared to the first profile. The  $h_\beta = 150$  km profile is also very similar to the profile shown in Nicolls et al. (2014). The vertical profiles of the  $\beta$  parameter versus the altitude where it is determined are shown in Fig. 4 for the two campaigns on 29 August 2013 and 27 September 2021.

Since the  $\beta$  parameter does not exhibit a general trend over the timescale of a single measurement campaign, Fig. 4 shows the median  $\beta$  profile for each of the two campaigns. It can be seen that the  $\beta$  parameter has changed in the time between the two campaigns. The variation with altitude is more pronounced for the August 2013 campaign, with an altitude change rate of  $1.22 \times 10^{-4} \text{ km}^{-1}$ . For the September 2021 campaign, the gradient of the  $\beta$  profile is  $4.78 \times 10^{-5} \text{ km}^{-1}$ . This might explain the distinct changes in the August 2013  $\nu_{in}$  profile shown in Fig. 3. However, what causes these changes in  $\beta$  with altitude remains to be discussed.

The third dual-frequency EISCAT campaign was conducted on 13 October 2022. For this campaign, a different radar mode was applied, which enables a better vertical resolution in the MLT region in exchange for a reduced absolute vertical coverage. Figure 5 shows the  $\nu_{in}$  profile obtained from simultaneous *manda zenith* measurements, with the EISCAT UHF and VHF radars at 80–100 km altitude. A climatology profile from the NRLMSISE-00 model is shown as well as the a priori collision frequency profile applied during the difference spectrum fit. The a priori profile is obtained from the  $\nu_{in}$  values given by the single-frequency GUIDAP

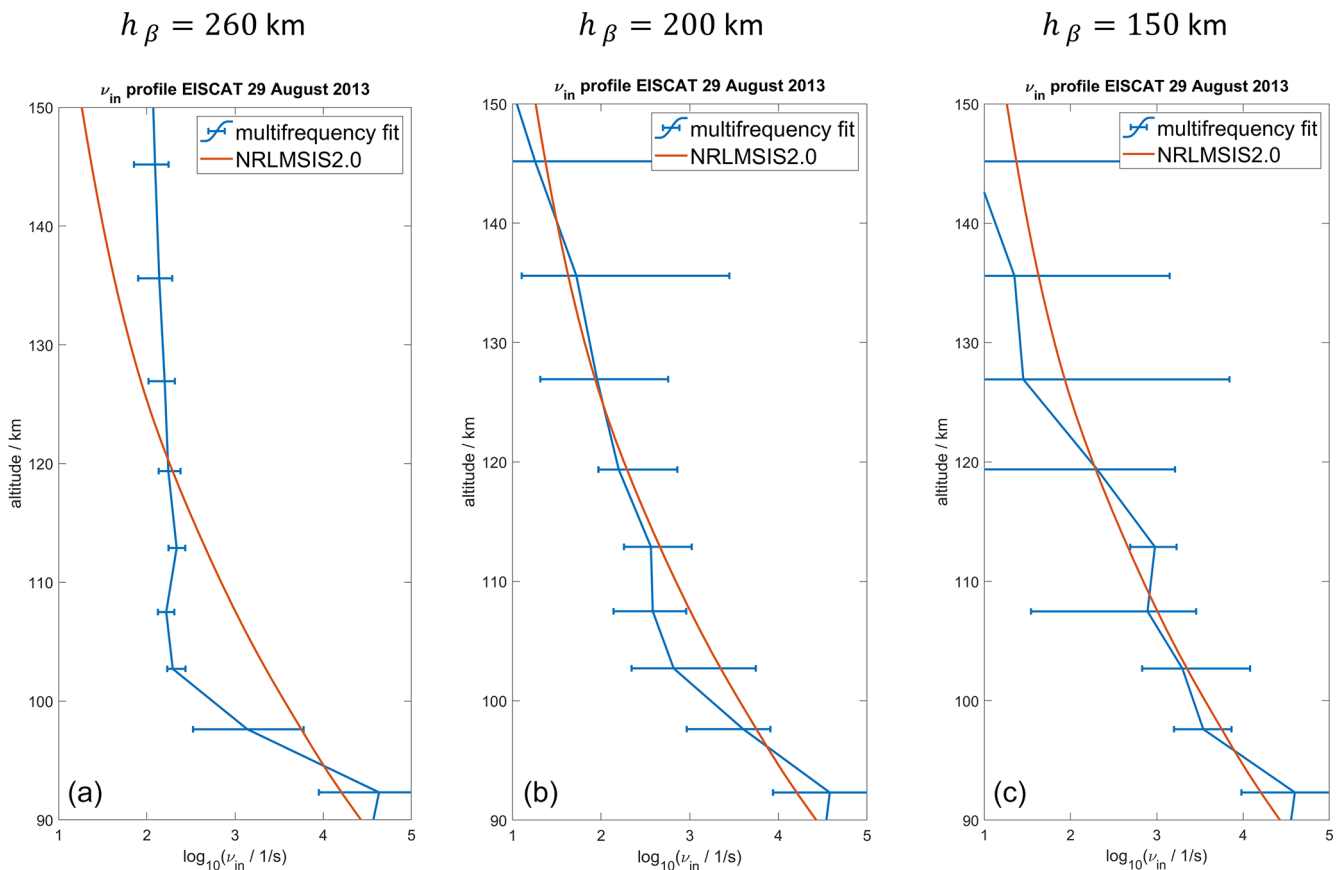


**Figure 3.**  $\nu_{\text{in}}$  profiles for three different  $h_{\beta}$ . The  $\beta$  parameter was determined at 260 km altitude in panel (a), 200 km in panel (b), and 150 km in panel (c).

analysis of the UHF measurements. The single-frequency result is close to a climatological profile with slightly lower values than the NRLMSISE-00 profile.

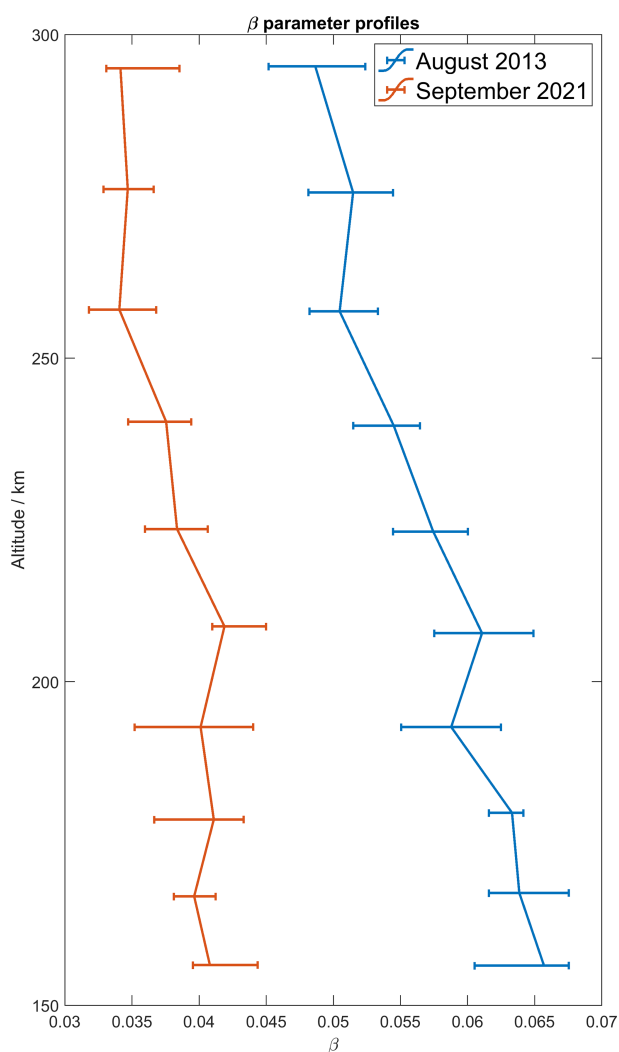
It can be seen in Fig. 5 that the dual-frequency fit has almost no measurement response at altitudes  $\lesssim 85$  km, where the fitted profile is identical to the a priori profile. Thus, at those altitudes, there is not enough signal-to-noise ratio left to drive the profile away from the a priori profile.

#### 4 Neutral density measurements and comparison to atmospheric models

Equation (1) describes how the ion–neutral collision frequency can be calculated from the neutral particle density  $n_n$  and the mean ion mass  $A$ , assuming the mean ion mass equals the mean neutral atom/molecule mass. Equation (1) assumes ion–neutral collisions as rigid-sphere collisions (Chapman, 1956) and allows us to calculate the neutral particle densities from the measured ion–neutral collision frequency profiles. Instead of rigid-sphere collisions, the ion–neutral collision frequency can be calculated assuming Maxwell collisions (Dalgarno et al., 1958). When calculating the neutral

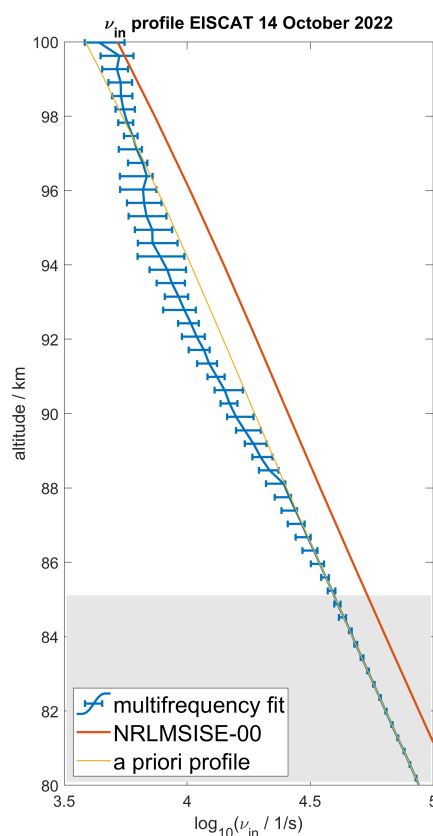
particle density with this method, it is necessary to know the relative abundance of each neutral particle species as well as the neutral particle polarizability, which can be found in, e.g., Schunk and Nagy (2009). Since this method evaluates the collisions for each ion and neutral species separately, resonant ion–neutral interactions between the same species have to be considered. The parameters for resonant collisions are available in Schunk and Nagy (2009) as well. Resonant collision parameters depend on the ion temperature  $T_i$ , which is available from the EISCAT measurements.

Figure 6 shows two neutral particle density profiles calculated with different collision models compared to two profiles directly taken from neutral atmosphere models. The neutral densities are calculated from the ion–neutral collision frequency profile obtained for the 29 August 2013 campaign with the  $\beta$  parameter determined at 150 km altitude. The uncertainties shown in Fig. 6 are predominantly caused by the uncertainties of the collision frequency profile in Fig. 3. The geophysical variation of the model’s neutral atmosphere background is comparably small, and, therefore, the uncertainties are the same for all measured profiles. The profile calculated from the rigid-sphere collision formula in Eq. (1) assumes the mean particle mass  $A$  as given by GAIA,



**Figure 4.** Profiles of the  $\beta$  parameter vs. the altitude where it has been determined for the EISCAT campaigns on 29 August 2013 and 27 September 2021.

which spans a range of  $\sim 26$ – $29$  amu across the transition region. Neutral density profiles calculated from Eq. (1) for the  $A$  profile from the NRLMSIS 2.0 model or a constant  $A = 30.5$  amu profile, which is a previously used assumption for the transition region (e.g., Nozawa et al., 2010), are nearly identical to the one shown in Fig. 6 and are therefore not shown either. The neutral densities calculated under the assumption of Maxwell collisions (Schunk and Nagy, 2009) are nearly equivalent to those calculated for rigid-sphere collisions. The Maxwell collision neutral density profile, too, is only shown for the GAIA model atmospheric composition, since profiles calculated for different compositions are nearly identical. It can be seen that the neutral density profiles calculated from ion–neutral collision measurements are sensitive to neither the choice of collision model nor the assumed atmospheric composition. Furthermore, we added two neu-



**Figure 5.** High-altitude resolution  $\nu_{in}$  profile from EISCAT *mandala* zenith measurements. The grey area marks the altitude where the dual-frequency fit did not converge.

tral density profiles from atmosphere models for comparison. The NRLMSIS 2.0 profile is the same one used to calculate the ion–neutral collision frequency profiles in Fig. 3. The neutral density profile obtained from GAIA shows a slightly different value but also without any vertical structure of the neutral density, other than the smooth climatology.

The variability of the measured neutral density profile  $n_{n,mes}$  can be seen from the relative variation  $(n_{n,mes} - n_{n,MSIS})/n_{n,MSIS} = \delta n_n/n_{n,MSIS}$ . For a better comparison with Nicolls et al. (2014), we calculate the relative variation of neutral mass density  $\delta\rho/\rho_{MSIS}$ . Since the atmospheric composition has to be assumed for the calculation of neutral particles already, this step does not require any additional assumptions.

Figure 7 shows the relative variation of measured neutral mass density compared to the NRLMSIS 2.0 model. It can be seen that the neutral mass density measurements oscillate around the MSIS climatology below 120 km altitude with a relative amplitude of  $\sim 0.5$ – $1$ . The obtained profile renders previously presented results (Fig. 5 in Nicolls et al., 2014). Deviations of the vertical profile from the climatological background were interpreted as tidal or lower-frequency oscillations.

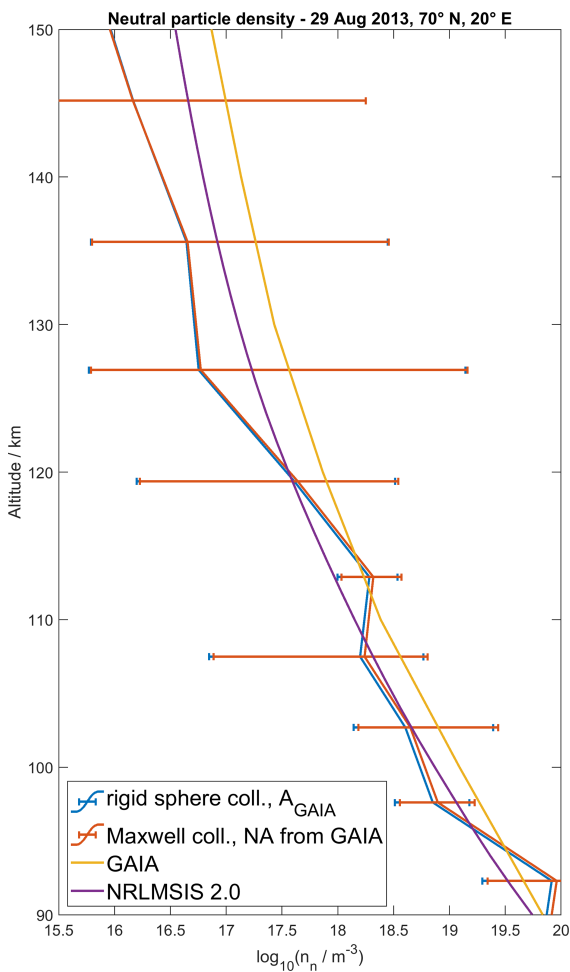


**Figure 6.** Neutral density profiles calculated from the measured ion–neutral collision frequencies for either rigid-sphere or Maxwell collisions. For both methods, the mean neutral mass and the abundances of the different neutral species (NA) have been taken from GAIA. For comparison, profiles from the NRLMSIS 2.0 and GAIA models are shown.

## 5 Discussion

Since there have been no previous experimental studies applying the difference spectrum method, the obtained results can only be compared to multifrequency measurements applying a different analysis method and both direct and indirect measurements of the ion–neutral collision frequency. The  $\nu_{in}$  profiles in Fig. 3 can be compared to the results by Nicolls et al. (2014), since they were obtained from the same measurements. The profile obtained for the  $\beta$  parameter determined at  $h_\beta = 150$  km altitude agrees well with the results obtained in Nicolls et al. (2014). As shown in Fig. 4, the  $\beta$  parameter is altitude dependent for the EISCAT campaign on 29 August 2013, though it is expected to be roughly constant for all altitudes where  $\nu_{in} \approx 0$  can be assumed (Grassmann, 1993b). The  $\beta$  profile for the EISCAT measurements from

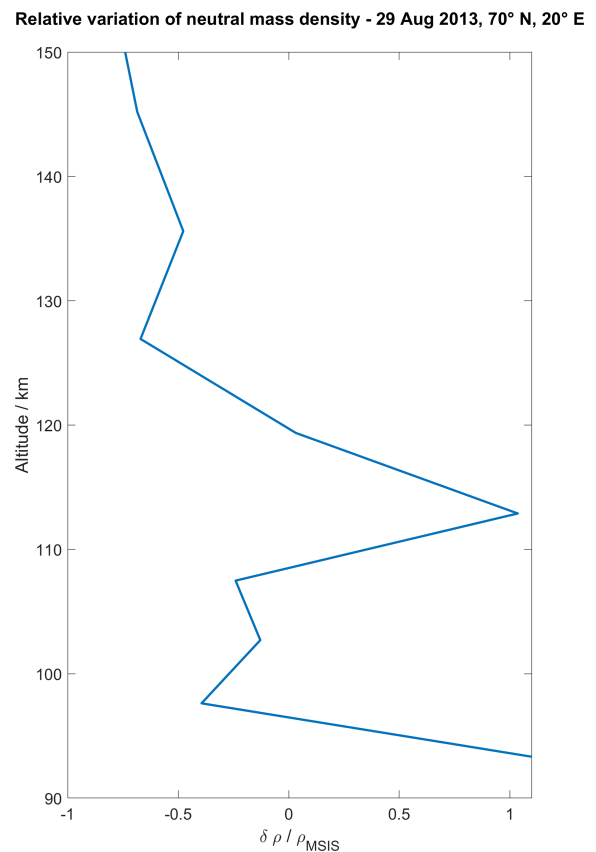


**Figure 7.** Variation of the neutral mass density calculated from the measured ion–neutral collision frequency profile relative to the NRLMSIS 2.0 mass density.

27 September 2021 shows a distinctly lower rate of change with altitude. Since there are more than 8 years between the two measurements, technical updates of the system might explain the different behavior of the parameter. Since the beam shapes of the UHF and the VHF system are not identical, the scatter volumes are close but also not identical. Therefore, already minor system updates or degradations of one of the systems can significantly impact the result of our dual-frequency analysis, which is performed under the assumption of identical scatter volumes. The decrease in  $\beta$  with altitude indicates that the amplitude of the UHF spectrum decreases more strongly with altitude than the amplitude of the VHF spectrum.

The  $\nu_{in}$  profile obtained for 27 September 2021, shown in Fig. 2, shows an increased collision frequency above 115 km altitude compared to the climatology. This agrees with previous findings (Fig. 2 in Nygrén, 1996), which show an increase in  $\nu_{in}$  compared to the MSIS-86 climatology above 110 km for a single campaign on 26 August 1985. Nygrén (1996) combined both the direct measurement of  $\nu_{in}$  from the ISR spectrum, assuming  $T_e = T_i$ , and the indirect measurement from vertical ion drifts. Oyama et al. (2012) also reported an increased collision frequency above about 120 km

during ionospheric heating events at E-region altitudes. They interpreted this as the result of an upward motion of denser neutral gas from lower altitudes. In Fig. 2, the minimum of  $\nu_{\text{in}}$  around 105 km altitude, in combination with the very slow decrease above, could be explained by thermospheric gas being transported upward from the altitude of the minimum.

Ion–neutral collision frequency measurements are of special interest for atmospheric physics, since they allow us to infer information about neutral gas densities in the MLT region. There are multiple methods to calculate collision frequencies from neutral particle densities, two of which are presented in Fig. 6 for the EISCAT measurements on 29 August 2013. One method assumes both ions and neutrals to be rigid spheres, while the other assumes Maxwell collision between the ions and the polarized neutrals. While the rigid-sphere collision model only requires assumptions on the mean neutral particle mass, the abundances of the different neutral particle sorts have to be assumed for the Maxwell collision model. Figure 6 shows that the choice of collision model has a far greater impact on the neutral density profile than the assumptions about mean neutral mass or particle abundances. Comparison to one empirical atmosphere model (NRLMSIS 2.0) and one physics-based model (GAIA) resulted in expectable agreement and disagreement. Both models display a smooth neutral density profile and do not capture small-scale dynamics but, on the other hand, indicate the expected vertical behavior. For validation of our measurements, a gravity-wave-resolving model, which includes incompressibility terms for small scales such as the High Altitude Mechanistic general Circulation Model (HIAMCM) (Becker and Vadas, 2020), would be required. In future studies, the inferred neutral density profiles could also be validated by comparison to meteor radar measurements. The neutral particle density can be obtained from meteor radar measurements, with the meteor peak flux altitude as a proxy (Stober et al., 2012). Figure 7 was designed following the example of Fig. 5 in Nicolls et al. (2014), and they agree reasonably well. The relative variation of the neutral mass density shows periodic oscillations, which were interpreted as the result of tides and lower-frequency oscillations by Nicolls et al. (2014).

Additionally, there are possible improvements to the general analysis of ISR measurements, applicable for all described collision frequency measurements, including the one presented in this paper. One possible improvement for all discussed analysis techniques could be the application of full profile analysis (Lehtinen et al., 1996). Instead of analyzing each altitude gate independently, as is done in this study and Nicolls et al. (2014), the total vertical profile of the plasma parameters could be fitted during full profile analysis. The assumption that the plasma parameters are constant within each altitude gate is, therefore, not required for full profile analysis (Lehtinen et al., 1996).

## 6 Conclusions

In this paper, we presented the first application of the difference spectrum method to analyze multifrequency ISR measurements to obtain direct measurements of the ion–neutral collision frequency. We showed that this method can be applied in combination with standard ISR analysis software (GUISDAP). Comparison to the only previous multifrequency ISR measurement, which applied special software to analyze two ISR measurements simultaneously, showed reasonable agreement. Therefore the difference spectrum method can be applied as an equivalent multifrequency ISR analysis method, generally applicable without the requirement of highly specialized ISR analysis software. This is the main advantage of the method presented here over other multifrequency methods. Multifrequency methods are generally advantageous for collision frequency measurements, since they do not require additional assumptions like  $T_e = T_i$  or strong electric fields.

We presented ion–neutral collision frequency profiles from three different EISCAT multifrequency campaigns. The measurements from 29 August 2013 were applied for comparison to the other multifrequency analysis method. Contrary to our expectation, the scaling parameter  $\beta$  was not constant at nearly collisionless altitudes, which could indicate a problem with one of the systems at the time. The second multifrequency campaign that we analyzed was conducted on 27 September 2021 in the same radar mode as the previous campaign. The vertical  $\beta$  parameter profile exhibited a significantly lower gradient in the F region for these measurements. At about 100–115 km altitude, the measurements showed a notably lower collision frequency than the climatology, while the collision frequency was larger than the climatology above 115 km. This might be the result of an upward motion of neutral gas due to ionospheric heating, e.g., caused by Joule dissipation. The third analyzed multifrequency campaign was conducted on 13 October 2022 and applied a different radar mode than the previous ones. The EISCAT *manda* radar mode allows measurements in the lower thermosphere with a very high altitude resolution, which might be helpful to study phenomena with a small-scale altitude structure.

In general, further improvement of the difference spectrum method, as well as multifrequency experiments, is required. Possible improvements would be the already mentioned application of full profile analysis of the ion–neutral collision frequency or the general improvement of ISR fitting by including the exact ion chemistry of the ionosphere. Validation of our collision frequency and neutral density measurements is difficult due to the general lack of observational methods in the ionospheric transition region. However, the *manda* measurements cover and resolve a good part of the meteor radar altitudes at about 80–110 km. Meteor radar neutral density measurements could be one possibility to verify multifrequency ISR experiments. As shown in Sect. 4, the

comparison to neutral atmosphere models is only somewhat meaningful, as long as the models do not include the incompressibility terms for small-scale variability, e.g., due to gravity waves. Considering the lack of atmospheric measurement methods in the ionospheric dynamo region, the method presented here is highly valuable because it provides information about this important region.

*Data availability.* The data are available under the Creative Commons Attribution 4.0 International license at <https://doi.org/10.5281/zenodo.8074787> (Günzkofer et al., 2023).

*Author contributions.* FG performed the data analysis and wrote large parts of the manuscript. DP suggested the idea to analyze multifrequency experiments. All authors provided feedback and were involved in revising the manuscript.

*Competing interests.* The contact author has declared that none of the authors has any competing interests.

*Disclaimer.* Publisher's note: Copernicus Publications remains neutral with regard to jurisdictional claims made in the text, published maps, institutional affiliations, or any other geographical representation in this paper. While Copernicus Publications makes every effort to include appropriate place names, the final responsibility lies with the authors.

*Acknowledgements.* EISCAT is an international association supported by research organizations in China (CRIRP), Finland (SA), Japan (NIPR and ISEE), Norway (NFR), Sweden (VR), and the United Kingdom (UKRI). The dataset used for this study is from the Ground-to-topside model of the Atmosphere and Ionosphere for Aeronomy (GAIA) project carried out by the National Institute of Information and Communications Technology (NICT), Kyushu University, and Seikei University. Gunter Stober is a member of the Oeschger Center for Climate Change Research (OCCR).

*Financial support.* The article processing charges for this open-access publication were covered by the German Aerospace Center (DLR).

*Review statement.* This paper was edited by Wen Yi and reviewed by three anonymous referees.

## References

- Baumjohann, W. and Treumann, R. A.: Basic space plasma physics, World Scientific, <https://doi.org/10.1142/p015>, 1996.
- Becker, E. and Vadas, S. L.: Explicit Global Simulation of Gravity Waves in the Thermosphere, *J. Geophys. Res.-Space*, 125, e28034, <https://doi.org/10.1029/2020JA028034>, 2020.
- Brekke, A., Doupnik, J. R., and Banks, P. M.: A preliminary study of the neutral wind in the auroral E region, *J. Geophys. Res.*, 78, 8235–8250, <https://doi.org/10.1029/JA078i034p08235>, 1973.
- Brekke, A., Doupnik, J. R., and Banks, P.: Incoherent scatter measurements of E region conductivities and currents in the auroral zone, *J. Geophys. Res.*, 79, 3773–3790, <https://doi.org/10.1029/JA079i025p03773>, 1974.
- Chapman, S.: The electrical conductivity of the ionosphere: A review, *Il Nuovo Cimento*, 4, 1385–1412, <https://doi.org/10.1007/BF02746310>, 1956.
- Dalgarno, A., McDowell, M. R. C., and Williams, A.: The Mobilities of Ions in Unlike Gases, *Philos. T. Roy. Soc. A*, 250, 411–425, <https://doi.org/10.1098/rsta.1958.0002>, 1958.
- Dawkins, E. C. M., Stober, G., Janches, D., Carrillo-Sánchez, J. D., Lieberman, R. S., Jacobi, C., Moffat-Griffin, T., Mitchell, N. J., Cobbett, N., Batista, P. P., Andrioli, V. F., Burity, R. A., Murphy, D. J., Kero, J., Gulbrandsen, N., Tsutsumi, M., Kozlovsky, A., Kim, J. H., Lee, C., and Lester, M.: Solar Cycle and Long-Term Trends in the Observed Peak of the Meteor Altitude Distributions by Meteor Radars, *Geophys. Res. Lett.*, 50, e2022GL101953, <https://doi.org/10.1029/2022GL101953>, 2023.
- Dougherty, J. P. and Farley, D. T., J.: A Theory of Incoherent Scattering of Radio Waves by a Plasma, 3 Scattering in a Partly Ionized Gas, *J. Geophys. Res.-Space*, 68, 5473, <https://doi.org/10.1029/JZ068i019p05473>, 1963.
- Emmert, J. T., Drob, D. P., Picone, J. M., Siskind, D. E., Jones, M., Mlynzcak, M. G., Bernath, P. F., Chu, X., Doornbos, E., Funke, B., Goncharenko, L. P., Hervig, M. E., Schwartz, M. J., Sheese, P. E., Vargas, F., Williams, B. P., and Yuan, T.: NRLM-SIS 2.0: A Whole Atmosphere Empirical Model of Temperature and Neutral Species Densities, *Astr. Soc. P.*, 8, e01321, <https://doi.org/10.1029/2020EA001321>, 2021.
- Farley, D. T.: A theory of incoherent scattering of radio waves by a plasma: 4. The effect of unequal ion and electron temperatures, *J. Geophys. Res.-Space*, 71, 4091–4098, <https://doi.org/10.1029/JZ071i017p04091>, 1966.
- Folkestad, K., Hagfors, T., and Westerlund, S.: EISCAT: An updated description of technical characteristics and operational capabilities, *Radio Sci.*, 18, 867–879, <https://doi.org/10.1029/RS018i006p00867>, 1983.
- Grassmann, V.: The effect of different collision operators on EISCAT's standard data analysis model, *J. Atmos. Terr. Phys.*, 55, 567–571, [https://doi.org/10.1016/0021-9169\(93\)90005-J](https://doi.org/10.1016/0021-9169(93)90005-J), 1993a.
- Grassmann, V.: An incoherent scatter experiment for the measurement of particle collisions, *J. Atmos. Terr. Phys.*, 55, 573–576, [https://doi.org/10.1016/0021-9169\(93\)90006-K](https://doi.org/10.1016/0021-9169(93)90006-K), 1993b.
- Günzkofer, F., Pokhotelov, D., Stober, G., Liu, H., Liu, H. L., Mitchell, N. J., Tjulin, A., and Borries, C.: Determining the Origin of Tidal Oscillations in the Ionospheric Transition Region With EISCAT Radar and Global Simulation Data, *J. Geophys. Res.-Space*, 127, e2022JA030861, <https://doi.org/10.1029/2022JA030861>, 2022.

- Günzkofer, F., Stober, G., Pokhotelov, D., Miyoshi, Y., and Borries, C.: [Dataset] Difference spectrum fitting of the ion-neutral collision frequency from dual-frequency EISCAT measurements, Zenodo [data set], <https://doi.org/10.5281/zenodo.8074787>, 2023.
- Hedin, A. E.: Extension of the MSIS thermosphere model into the middle and lower atmosphere, *J. Geophys. Res.-Space*, 96, 1159–1172, <https://doi.org/10.1029/90JA02125>, 1991.
- Jin, H., Miyoshi, Y., Pancheva, D., Mukhtarov, P., Fujiwara, H., and Shinagawa, H.: Response of migrating tides to the stratospheric sudden warming in 2009 and their effects on the ionosphere studied by a whole atmosphere-ionosphere model GAIA with COSMIC and TIMED/SABER observations, *J. Geophys. Res.-Space*, 117, A10323, <https://doi.org/10.1029/2012JA017650>, 2012.
- Katsuda, S., Enoto, T., Lommen, A. N., Mori, K., Motizuki, Y., Nakajima, M., Ruhl, N. C., Sato, K., Stober, G., Tashiro, M. S., Terada, Y., and Wood, K. S.: Long-Term Density Trend in the Mesosphere and Lower Thermosphere From Occultations of the Crab Nebula With X-Ray Astronomy Satellites, *J. Geophys. Res.-Space*, 128, e2022JA030797, <https://doi.org/10.1029/2022JA030797>, 2023.
- Kelly, M. C.: *The Earth's Ionosphere: Plasma Physics and Electrodynamics*, Second Edition, Elsevier Academic Press, ISBN 978-0-12-088425-4, 2009.
- Kobayashi, S., Ota, Y., Harada, Y., Ebita, A., Moriya, M., Onoda, H., Onogi, K., Kamahori, H., Kobayashi, C., Endo, H., Miyaoka, K., and Takahashi, K.: The JRA-55 Reanalysis: General Specifications and Basic Characteristics, *J. Meteorol. Soc. Jpn.*, 93, 5–48, <https://doi.org/10.2151/jmsj.2015-001>, 2015.
- Lehtinen, M. S. and Huuskonen, A.: General incoherent scatter analysis and GUIDAP, *J. Atmos. Terr. Phys.*, 58, 435–452, [https://doi.org/10.1016/0021-9169\(95\)00047-X](https://doi.org/10.1016/0021-9169(95)00047-X), 1996.
- Lehtinen, M. S., Huuskonen, A., and Pirttilä, J.: First experiences of full-profile analysis with GUIDAP, *Ann. Geophys.*, 14, 1487–1495, <https://doi.org/10.1007/s00585-996-1487-3>, 1996.
- Nicolet, M.: The collision frequency of electrons in the ionosphere, *J. Atmos. Terr. Phys.*, 3, 200–211, [https://doi.org/10.1016/0021-9169\(53\)90110-X](https://doi.org/10.1016/0021-9169(53)90110-X), 1953.
- Nicolls, M. J., Bahcivan, H., Häggström, I., and Rietveld, M.: Direct measurement of lower thermospheric neutral density using multifrequency incoherent scattering, *Geophys. Res. Lett.*, 41, 8147–8154, <https://doi.org/10.1002/2014GL062204>, 2014.
- Nozawa, S., Ogawa, Y., Oyama, S., Fujiwara, H., Tsuda, T., Brekke, A., Hall, C. M., Murayama, Y., Kawamura, S., Miyaoka, H., and Fujii, R.: Tidal waves in the polar lower thermosphere observed using the EISCAT long run data set obtained in September 2005, *J. Geophys. Res.-Space*, 115, A08312, <https://doi.org/10.1029/2009JA015237>, 2010.
- Nygrén, T.: Studies of the E-region ion-neutral collision frequency using the EISCAT incoherent scatter radar, *Adv. Space Res.*, 18, 79–82, [https://doi.org/10.1016/0273-1177\(95\)00843-4](https://doi.org/10.1016/0273-1177(95)00843-4), 1996.
- Nygrén, T., Jalonen, L., and Huuskonen, A.: A new method of measuring the ion-neutral collision frequency using incoherent scatter radar, *Planet. Space Sci.*, 35, 337–343, [https://doi.org/10.1016/0032-0633\(87\)90160-7](https://doi.org/10.1016/0032-0633(87)90160-7), 1987.
- Oyama, S., Kurihara, J., Watkins, B. J., Tsuda, T. T., and Takahashi, T.: Temporal variations of the ion-neutral collision frequency from EISCAT observations in the polar lower ionosphere during periods of geomagnetic disturbances, *J. Geophys. Res.-Space*, 117, A05308, <https://doi.org/10.1029/2011JA017159>, 2012.
- Picone, J. M., Hedin, A. E., Drob, D. P., and Aikin, A. C.: NRLMSISE-00 empirical model of the atmosphere: Statistical comparisons and scientific issues, *J. Geophys. Res.-Space*, 107, 1468, <https://doi.org/10.1029/2002JA009430>, 2002.
- Schunk, R. and Nagy, A.: *Ionospheres: Physics, Plasma Physics, and Chemistry*, edited by: Houghton, J. T., Rycroft, M. J., and Dessler, A. J., Cambridge University Press, <https://doi.org/10.1017/CBO9780511635342>, 2009.
- Stober, G., Jacobi, C., Matthias, V., Hoffmann, P., and Gerding, M.: Neutral air density variations during strong planetary wave activity in the mesopause region derived from meteor radar observations, *J. Atmos. Sol.-Terr. Phys.*, 74, 55–63, <https://doi.org/10.1016/j.jastp.2011.10.007>, 2012.
- Stober, G., Matthias, V., Brown, P., and Chau, J. L.: Neutral density variation from specular meteor echo observations spanning one solar cycle, *Geophys. Res. Lett.*, 41, 6919–6925, <https://doi.org/10.1002/2014GL061273>, 2014.
- Stober, G., Kuchar, A., Pokhotelov, D., Liu, H., Liu, H.-L., Schmidt, H., Jacobi, C., Baumgarten, K., Brown, P., Janches, D., Murphy, D., Kozlovsky, A., Lester, M., Belova, E., Kero, J., and Mitchell, N.: Interhemispheric differences of mesosphere–lower thermosphere winds and tides investigated from three whole-atmosphere models and meteor radar observations, *Atmos. Chem. Phys.*, 21, 13855–13902, <https://doi.org/10.5194/acp-21-13855-2021>, 2021.
- Stober, G., Weryk, R., Janches, D., Dawkins, E. C., Günzkofer, F., Hormaechea, J. L., and Pokhotelov, D.: Polarization dependency of transverse scattering and collisional coupling to the ambient atmosphere from meteor trails – theory and observations, *Planet. Space Sci.*, 237, 105768, <https://doi.org/10.1016/j.pssp.2023.105768>, 2023.
- Tjulín, A.: EISCAT experiments, Tech. rep., EISCAT Scientific Association, [https://eiscat.se/wp-content/uploads/2021/03/Experiments\\_v20210302.pdf](https://eiscat.se/wp-content/uploads/2021/03/Experiments_v20210302.pdf) (last access: 6 December 2023), 2021.

# Appendix B

## Climatology of $\nu_{in}/\omega_i \approx 0$ condition

The assumption of a collision-less ionosphere is applied several times in this thesis. It is required for the calculation of the electric field in Günzkofer et al. (2022, 2024) and the determination of the  $\beta$  parameter in Günzkofer et al. (2023b). Notably, "collision-less" does not mean that the ion-neutral frequency approaches zero, i.e.  $\nu_{in} \rightarrow 0$ . It rather means that  $\nu_{in}$  is considerably lower than the ion gyro-frequency  $\omega_i = qB/m_i$ , i.e.  $\omega_i \gg \nu_{in}$ , with the ion charge  $q$ , ion mass  $m_i$ , and magnetic field strength  $B$ . In the collision-less case, the Lorenz force term of the ion momentum equation dominates the friction force term. The ions are coupled to the magnetic field lines and a one-dimensional ion motion can be assumed so that the ion adiabatic coefficient is  $\gamma_i \approx 3$ .

As shown in Figure 1.4, the altitude where  $\nu_{in} = \omega_i$  is approximately at 120 km though the investigations in Günzkofer et al. (2023b) have shown that this altitude might very well be higher. Due to the exponential decrease of  $\nu_{in}$  with altitude, it is often assumed that  $\omega_i \gg \nu_{in}$  is immediately fulfilled above the ionospheric dynamo region. The climatology of the ratio  $\nu_{in}/\omega_i$  at high latitudes is shown in Figure B.1 for one whole year.

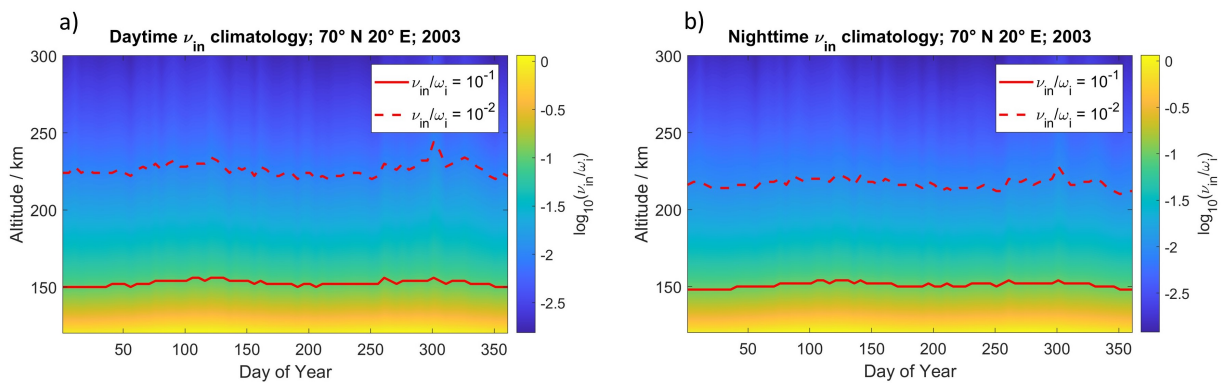


Figure B.1: Climatology ratio of ion-neutral collision to gyro-frequency  $\nu_{in}/\omega_i$  at high latitudes during the year 2003. There are differences between a) daytime and b) nighttime. The altitudes at which  $\nu_{in}/\omega_i = 10^{-1}$  and  $\nu_{in}/\omega_i = 10^{-2}$  are marked by red solid and dotted lines.

The climatology is shown for the year 2003 which was around the maximum of a strong solar cycle. The ratio  $\nu_{in}/\omega_i$  is expected to correlate with solar activity due to the expansion of the thermosphere under increased solar irradiation. Figure B.1 a) and b) show the climatologies for the day- and nighttime respectively. It can be seen that at approximately 150 km altitude, the assumption of a collision-less ionosphere causes uncertainties in the order of 10%. At about 225 km altitude, these uncertainties are already reduced to an order of 1%. The calculation of electric fields at 300 km altitude under the assumption of a collision-less ionosphere, as done in Günzkofer et al. (2022, 2024), is therefore well justified. The determination of the  $\beta$  parameter in Günzkofer et al. (2023b) is done at an altitude range of 150 – 250 km. While the upper altitudes of this range seem to be well justified, there are considerable uncertainties when determining the  $\beta$  parameter at 150 km altitude. These uncertainties of the collision-less condition need to be considered in that case.

# Bibliography

- Akbari, H., Bhatt, A., La Hoz, C., and Semeter, J. L.: Incoherent Scatter Plasma Lines: Observations and Applications, *Space science reviews*, 212, 249–294, <https://doi.org/10.1007/s11214-017-0355-7>, 2017.
- Alken, P., Thébaud, E., Beggan, C. D., Amit, H., Aubert, J., Baerenzung, J., Bondar, T. N., Brown, W. J., Califf, S., Chambodut, A., Chulliat, A., Cox, G. A., Finlay, C. C., Fournier, A., Gillet, N., Grayver, A., Hammer, M. D., Holschneider, M., Huder, L., Hulot, G., Jager, T., Kloss, C., Korte, M., Kuang, W., Kuvshinov, A., Langlais, B., Léger, J. M., Lesur, V., Livermore, P. W., Lowes, F. J., Macmillan, S., Magnes, W., Manda, M., Marsal, S., Matzka, J., Metman, M. C., Minami, T., Morschhauser, A., Mound, J. E., Nair, M., Nakano, S., Olsen, N., Pavón-Carrasco, F. J., Petrov, V. G., Ropp, G., Rother, M., Sabaka, T. J., Sanchez, S., Saturnino, D., Schnepf, N. R., Shen, X., Stolle, C., Tangborn, A., Tøffner-Clausen, L., Toh, H., Torta, J. M., Varner, J., Vervelidou, F., Vigneron, P., Wardinski, I., Wicht, J., Woods, A., Yang, Y., Zeren, Z., and Zhou, B.: International Geomagnetic Reference Field: the thirteenth generation, *Earth, Planets and Space*, 73, 49, <https://doi.org/10.1186/s40623-020-01288-x>, 2021.
- Andrews, D. G.: *An Introduction to Atmospheric Physics*, Cambridge University Press, 2000.
- Andrews, D. G., Holton, J. R., and Leovy, C. B.: *Middle atmosphere dynamics.*, Academic Press, Inc., 1987.
- Appleton, E. V.: The Existence of more than one Ionised Layer in the Upper Atmosphere, *Nature*, 120, 330, <https://doi.org/10.1038/120330a0>, 1927.
- Appleton, E. V. and Barnett, M. A. F.: On Some Direct Evidence for Downward Atmospheric Reflection of Electric Rays, *Proceedings of the Royal Society of London Series A*, 109, 621–641, <https://doi.org/10.1098/rspa.1925.0149>, 1925.
- Baloukidis, D., Sarris, T., Tourgaidis, S., Pirnaris, P., Aikio, A., Virtanen, I., Buchert, S., and Papadakis, K.: A Comparative Assessment of the Distribution of Joule Heating in Altitude as Estimated in TIE-GCM and EISCAT Over One Solar Cycle, *Journal of Geophysical Research (Space Physics)*, 128, e2023JA031526, <https://doi.org/10.1029/2023JA031526>, 2023.

- Barraclough, D. R.: IAGA Division I Working Group 1: International Geomagnetic Reference Field revision 1987., *Geophysical Journal International*, 93, 187–189, <https://doi.org/10.1111/j.1365-246X.1988.tb01397.x>, 1988.
- Bartels, J., Heck, N. H., and Johnston, H. F.: The three-hour-range index measuring geomagnetic activity, *Terrestrial Magnetism and Atmospheric Electricity*, 44, 411, <https://doi.org/10.1029/TE044i004p00411>, 1939.
- Bates, D. R. and Massey, H. S. W.: The Basic Reactions in the Upper Atmosphere. II. The Theory of Recombination in the Ionized Layers, *Proceedings of the Royal Society of London Series A*, 192, 1–16, <https://doi.org/10.1098/rspa.1947.0134>, 1947.
- Baumjohann, W. and Treumann, R. A.: Basic space plasma physics, Imperial College Press, <https://doi.org/10.1142/p015>, 1996.
- Becker, E. and Vadas, S. L.: Secondary Gravity Waves in the Winter Mesosphere: Results From a High-Resolution Global Circulation Model, *Journal of Geophysical Research (Atmospheres)*, 123, 2605–2627, <https://doi.org/10.1002/2017JD027460>, 2018.
- Bering, E. A. and Mozer, F. S.: A measurement of perpendicular current density in an aurora, *Journal of Geophysical Research*, 80, 3961, <https://doi.org/10.1029/JA080i028p03961>, 1975.
- Bilitza, D., Pezzopane, M., Truhlik, V., Altadill, D., Reinisch, B. W., and Pignalberi, A.: The International Reference Ionosphere Model: A Review and Description of an Ionospheric Benchmark, *Reviews of Geophysics*, 60, e2022RG000792, <https://doi.org/10.1029/2022RG000792>, 2022.
- Borries, C., Ferreira, A. A., Nykiel, G., and Borges, R. A.: A new index for statistical analyses and prediction of travelling ionospheric disturbances, *Journal of Atmospheric and Solar-Terrestrial Physics*, 247, 106069, <https://doi.org/10.1016/j.jastp.2023.106069>, 2023.
- Brekke, A.: On the relative importance of Joule heating and the Lorentz force in generating atmospheric gravity waves and infrasound waves in the auroral electrojets, *Journal of Atmospheric and Terrestrial Physics*, 41, 475–479, [https://doi.org/10.1016/0021-9169\(79\)90072-2](https://doi.org/10.1016/0021-9169(79)90072-2), 1979.
- Brekke, A. and Kamide, Y.: On the relationship between Joule and frictional heating in the polar ionosphere., *Journal of Atmospheric and Terrestrial Physics*, 58, 139–143, [https://doi.org/10.1016/0021-9169\(95\)00025-9](https://doi.org/10.1016/0021-9169(95)00025-9), 1996.
- Brekke, A., Doupnik, J. R., and Banks, P. M.: A preliminary study of the neutral wind in the auroral E region, *Journal of Geophysical Research*, 78, 8235–8250, <https://doi.org/10.1029/JA078i034p08235>, 1973.

- Chapman, S.: The electrical conductivity of the ionosphere: A review, *Il Nuovo Cimento*, 4, 1385–1412, <https://doi.org/10.1007/BF02746310>, 1956.
- Codrescu, M. V., Fuller-Rowell, T. J., and Foster, J. C.: On the importance of E-field variability for Joule heating in the high-latitude thermosphere, *Geophysical Research Letters*, 22, 2393–2396, <https://doi.org/10.1029/95GL01909>, 1995.
- Dang, T., Li, X., Luo, B., Li, R., Zhang, B., Pham, K., Ren, D., Chen, X., Lei, J., and Wang, Y.: Unveiling the Space Weather During the Starlink Satellites Destruction Event on 4 February 2022, *Space Weather*, 20, e2022SW003152, <https://doi.org/10.1029/2022SW003152>, 2022.
- Drob, D. P., Emmert, J. T., Meriwether, J. W., Makela, J. J., Doornbos, E., Conde, M., Hernandez, G., Noto, J., Zawdie, K. A., McDonald, S. E., Huba, J. D., and Klenzing, J. H.: An update to the Horizontal Wind Model (HWM): The quiet time thermosphere, *Earth and Space Science*, 2, 301–319, <https://doi.org/10.1002/2014EA000089>, 2015.
- Dungey, J. W.: Interplanetary Magnetic Field and the Auroral Zones, *Physical Review Letters*, 6, 47–48, <https://doi.org/10.1103/PhysRevLett.6.47>, 1961.
- Emery, B. a., Lathuillere, C., Richards, P. G., Roble, R. G., Buonsanto, M. J., Knipp, D. J., Wilkinson, P., Sipler, D. P., and Niecejewski, R.: Time dependent thermospheric neutral response to the 2-11 November 1993 storm period, *Journal of Atmospheric and Solar-Terrestrial Physics*, 61, 329–350, [https://doi.org/10.1016/S1364-6826\(98\)00137-0](https://doi.org/10.1016/S1364-6826(98)00137-0), 1999.
- Forbes, J. M., Palo, S. E., and Zhang, X.: Variability of the ionosphere, *Journal of Atmospheric and Solar-Terrestrial Physics*, 62, 685–693, [https://doi.org/10.1016/S1364-6826\(00\)00029-8](https://doi.org/10.1016/S1364-6826(00)00029-8), 2000.
- Fritts, D. C. and Alexander, M. J.: Gravity wave dynamics and effects in the middle atmosphere, *Reviews of Geophysics*, 41, 1003, <https://doi.org/10.1029/2001RG000106>, 2003.
- Gauss, C.: *Allgemeine Theorie des Erdmagnetismus*, Werke Bd, V, Göttingen, pp. 119–193, 1838.
- Glassmeier, K. H. and Tsurutani, B. T.: Carl Friedrich Gauss - General Theory of Terrestrial Magnetism - a revised translation of the German text, *History of Geo- and Space Sciences*, 5, 11–62, <https://doi.org/10.5194/hgss-5-11-2014>, 2014.
- Grassmann, V.: An incoherent scatter experiment for the measurement of particle collisions, *Journal of Atmospheric and Terrestrial Physics*, 55, 573–576, [https://doi.org/10.1016/0021-9169\(93\)90006-K](https://doi.org/10.1016/0021-9169(93)90006-K), 1993.

- Günzkofer, F., Pokhotelov, D., Stober, G., Liu, H., Liu, H. L., Mitchell, N. J., Tjulin, A., and Borries, C.: Determining the Origin of Tidal Oscillations in the Ionospheric Transition Region With EISCAT Radar and Global Simulation Data, *Journal of Geophysical Research (Space Physics)*, 127, e2022JA030861, <https://doi.org/10.1029/2022JA030861>, 2022.
- Günzkofer, F., Pokhotelov, D., Stober, G., Mann, I., Vadas, S. L., Becker, E., Tjulin, A., Kozlovsky, A., Tsutsumi, M., Gulbrandsen, N., Nozawa, S., Lester, M., Belova, E., Kero, J., Mitchell, N. J., and Borries, C.: Inferring neutral winds in the ionospheric transition region from atmospheric-gravity-wave traveling-ionospheric-disturbance (AGW-TID) observations with the EISCAT VHF radar and the Nordic Meteor Radar Cluster, *Annales Geophysicae*, 41, 409–428, <https://doi.org/10.5194/angeo-41-409-2023>, 2023a.
- Günzkofer, F., Stober, G., Pokhotelov, D., Miyoshi, Y., and Borries, C.: Difference spectrum fitting of the ion-neutral collision frequency from dual-frequency EISCAT measurements, *Atmospheric Measurement Techniques*, 16, 5897–5907, <https://doi.org/10.5194/amt-16-5897-2023>, 2023b.
- Günzkofer, F., Liu, H., Stober, G., Pokhotelov, D., and Borries, C.: Evaluation of the Empirical Scaling Factor of Joule Heating Rates in TIE-GCM With EISCAT Measurements, *Earth and Space Science*, 11, e2023EA003447, <https://doi.org/10.5194/amt-16-5897-2023>, 2024.
- Häusler, K. and Lühr, H.: Nonmigrating tidal signals in the upper thermospheric zonal wind at equatorial latitudes as observed by CHAMP, *Annales Geophysicae*, 27, 2643–2652, <https://doi.org/10.5194/angeo-27-2643-2009>, 2009.
- Hedin, A. E.: Extension of the MSIS thermosphere model into the middle and lower atmosphere, *Journal of Geophysical Research*, 96, 1159–1172, <https://doi.org/10.1029/90JA02125>, 1991.
- Heelis, R. A., Lowell, J. K., and Spiro, R. W.: A model of the high-latitude ionospheric convection pattern, *Journal of Geophysical Research*, 87, 6339–6345, <https://doi.org/10.1029/JA087iA08p06339>, 1982.
- Heinselman, C. J. and Nicolls, M. J.: A Bayesian approach to electric field and E-region neutral wind estimation with the Poker Flat Advanced Modular Incoherent Scatter Radar, *Radio Science*, 43, RS5013, <https://doi.org/10.1029/2007RS003805>, 2008.
- Hocke, K. and Schlegel, K.: A review of atmospheric gravity waves and travelling ionospheric disturbances: 1982-1995, *Annales Geophysicae*, 14, 917–940, <https://doi.org/10.1007/s00585-996-0917-6>, 1996.
- Hocking, W. K., Fuller, B., and Vandeppeer, B.: Real-time determination of meteor-related parameters utilizing modern digital technology, *Journal of Atmospheric and*

- Solar-Terrestrial Physics, 63, 155–169, [https://doi.org/10.1016/S1364-6826\(00\)00138-3](https://doi.org/10.1016/S1364-6826(00)00138-3), 2001.
- Hurrell, J. W., Holland, M. M., Gent, P. R., Ghan, S., Kay, J. E., Kushner, P. J., Lamarque, J. F., Large, W. G., Lawrence, D., Lindsay, K., Lipscomb, W. H., Long, M. C., Mahowald, N., Marsh, D. R., Neale, R. B., Rasch, P., Vavrus, S., Vertenstein, M., Bader, D., Collins, W. D., Hack, J. J., Kiehl, J., and Marshall, S.: The Community Earth System Model: A Framework for Collaborative Research, *Bulletin of the American Meteorological Society*, 94, 1339–1360, <https://doi.org/10.1175/BAMS-D-12-00121.1>, 2013.
- Immel, T. J., Sagawa, E., England, S. L., Henderson, S. B., Hagan, M. E., Mende, S. B., Frey, H. U., Swenson, C. M., and Paxton, L. J.: Control of equatorial ionospheric morphology by atmospheric tides, *Geophysical Research Letters*, 33, L15108, <https://doi.org/10.1029/2006GL026161>, 2006.
- Ishii, M., Berdermann, J., Forte, B., Hapgood, M., Bisi, M. M., and Romano, V.: Space weather impact on radio communication and navigation, *Advances in Space Research*, 2024.
- Jin, H., Miyoshi, Y., Fujiwara, H., and Shinagawa, H.: Electrodynamics of the formation of ionospheric wave number 4 longitudinal structure, *Journal of Geophysical Research (Space Physics)*, 113, A09307, <https://doi.org/10.1029/2008JA013301>, 2008.
- Jin, H., Miyoshi, Y., Pancheva, D., Mukhtarov, P., Fujiwara, H., and Shinagawa, H.: Response of migrating tides to the stratospheric sudden warming in 2009 and their effects on the ionosphere studied by a whole atmosphere-ionosphere model GAIA with COSMIC and TIMED/SABER observations, *Journal of Geophysical Research (Space Physics)*, 117, A10323, <https://doi.org/10.1029/2012JA017650>, 2012.
- Kavanagh, A. J., Ogawa, Y., and Woodfield, E. E.: Two Techniques for Determining F-Region Ion Velocities at Meso-Scales: Differences and Impacts on Joule Heating, *Journal of Geophysical Research (Space Physics)*, 127, e30062, <https://doi.org/10.1029/2021JA030062>, 2022.
- Kelley, M. C.: *The Earth's Ionosphere: Plasma Physics and Electrodynamics*, Second Edition, Elsevier Academic Press, 2009.
- Kofman, W. and Lathuillere, C.: EISCAT multipulse technique and its contribution to auroral ionosphere and thermosphere description, *Journal of Geophysical Research*, 90, 3520–3524, <https://doi.org/10.1029/JA090iA04p03520>, 1985.
- Landau, L.: On the vibrations of the electronic plasma, *Zhurnal eksperimentalnoi i teoreticheskoi fiziki*, 16, 574–586, 1946.
- Lehtinen, M. S. and Huuskonen, A.: General incoherent scatter analysis and GUIDAP, *Journal of Atmospheric and Terrestrial Physics*, 58, 435–452, [https://doi.org/10.1016/0021-9169\(95\)00047-X](https://doi.org/10.1016/0021-9169(95)00047-X), 1996.

- Lindzen, R. S.: Atmospheric Tides, *Annual Review of Earth and Planetary Sciences*, 7, 199, <https://doi.org/10.1146/annurev.ea.07.050179.001215>, 1979.
- Liu, H.-L., Bardeen, C. G., Foster, B. T., Lauritzen, P., Liu, J., Lu, G., Marsh, D. R., Maute, A., McInerney, J. M., Pedatella, N. M., Qian, L., Richmond, A. D., Roble, R. G., Solomon, S. C., Vitt, F. M., and Wang, W.: Development and Validation of the Whole Atmosphere Community Climate Model With Thermosphere and Ionosphere Extension (WACCM-X 2.0), *Journal of Advances in Modeling Earth Systems*, 10, 381–402, <https://doi.org/10.1002/2017MS001232>, 2018.
- Liu, H. L., Wang, W., Huba, J. D., Lauritzen, P. H., and Vitt, F.: Atmospheric and Ionospheric Responses to Hunga-Tonga Volcano Eruption Simulated by WACCM-X, *Geophysical Research Letters*, 50, e2023GL103682, <https://doi.org/10.1029/2023GL103682>, 2023.
- Lühr, H. and Manoj, C.: The complete spectrum of the equatorial electrojet related to solar tides: CHAMP observations, *Annales Geophysicae*, 31, 1315–1331, <https://doi.org/10.5194/angeo-31-1315-2013>, 2013.
- Marchant, E.: The Heaviside Layer, *Proceedings of the Institute of Radio Engineers*, 4, 511–520, <https://doi.org/10.1109/JRPROC.1916.217279>, 1916.
- Matzka, J., Stolle, C., Yamazaki, Y., Bronkalla, O., and Morschhauser, A.: The Geomagnetic Kp Index and Derived Indices of Geomagnetic Activity, *Space Weather*, 19, e2020SW002641, <https://doi.org/10.1029/2020SW002641>, 2021.
- McCrea, I., Aikio, A., Alfonsi, L., Belova, E., Buchert, S., Clilverd, M., Engler, N., Gustavsson, B., Heinselman, C., Kero, J., Kosch, M., Lamy, H., Leyser, T., Ogawa, Y., Oksavik, K., Pellinen-Wannberg, A., Pitout, F., Rapp, M., Stanislawski, I., and Vierinen, J.: The science case for the EISCAT\_3D radar, *Progress in Earth and Planetary Science*, 2, 21, <https://doi.org/10.1186/s40645-015-0051-8>, 2015.
- Nicolet, M.: The collision frequency of electrons in the ionosphere, *Journal of Atmospheric and Terrestrial Physics*, 3, 200–211, [https://doi.org/10.1016/0021-9169\(53\)90110-X](https://doi.org/10.1016/0021-9169(53)90110-X), 1953.
- Nicolls, M. J. and Heinselman, C. J.: Three-dimensional measurements of traveling ionospheric disturbances with the Poker Flat Incoherent Scatter Radar, *Geophysical Research Letters*, 34, L21104, <https://doi.org/10.1029/2007GL031506>, 2007.
- Nicolls, M. J., Varney, R. H., Vadas, S. L., Stamus, P. A., Heinselman, C. J., Cosgrove, R. B., and Kelley, M. C.: Influence of an inertia-gravity wave on mesospheric dynamics: A case study with the Poker Flat Incoherent Scatter Radar, *Journal of Geophysical Research (Atmospheres)*, 115, D00N02, <https://doi.org/10.1029/2010JD014042>, 2010.

- Nicolls, M. J., Vadas, S. L., Sulzer, M. P., and Aponte, N.: Horizontal and Vertical Wave Parameters of Thermospheric Gravity Waves, and Relationship to Neutral Winds, in: AGU Spring Meeting Abstracts, vol. 2013, pp. SA22A-06, 2013.
- Nicolls, M. J., Bahcivan, H., Häggström, I., and Rietveld, M.: Direct measurement of lower thermospheric neutral density using multifrequency incoherent scattering, *Geophysical Research Letters*, 41, 8147–8154, <https://doi.org/10.1002/2014GL062204>, 2014.
- Nozawa, S., Ogawa, Y., Oyama, S., Fujiwara, H., Tsuda, T., Brekke, A., Hall, C. M., Murayama, Y., Kawamura, S., Miyaoka, H., and Fujii, R.: Tidal waves in the polar lower thermosphere observed using the EISCAT long run data set obtained in September 2005, *Journal of Geophysical Research (Space Physics)*, 115, A08312, <https://doi.org/10.1029/2009JA015237>, 2010.
- Nygrén, T.: Studies of the E-region ion-neutral collision frequency using the EISCAT incoherent scatter radar, *Advances in Space Research*, 18, 79–82, [https://doi.org/10.1016/0273-1177\(95\)00843-4](https://doi.org/10.1016/0273-1177(95)00843-4), 1996.
- Nygrén, T., Jalonen, L., and Huuskonen, A.: A new method of measuring the ion-neutral collision frequency using incoherent scatter radar, *Planetary and Space Science*, 35, 337–343, [https://doi.org/10.1016/0032-0633\(87\)90160-7](https://doi.org/10.1016/0032-0633(87)90160-7), 1987.
- Nygrén, T., Aikio, A. T., Kuula, R., and Voiculescu, M.: Electric fields and neutral winds from monostatic incoherent scatter measurements by means of stochastic inversion, *Journal of Geophysical Research (Space Physics)*, 116, A05305, <https://doi.org/10.1029/2010JA016347>, 2011.
- Oberheide, J., Forbes, J. M., Zhang, X., and Bruinsma, S. L.: Climatology of upward propagating diurnal and semidiurnal tides in the thermosphere, *Journal of Geophysical Research (Space Physics)*, 116, A11306, <https://doi.org/10.1029/2011JA016784>, 2011.
- Oyama, S., Kurihara, J., Watkins, B. J., Tsuda, T. T., and Takahashi, T.: Temporal variations of the ion-neutral collision frequency from EISCAT observations in the polar lower ionosphere during periods of geomagnetic disturbances, *Journal of Geophysical Research (Space Physics)*, 117, A05308, <https://doi.org/10.1029/2011JA017159>, 2012.
- Palmroth, M., Grandin, M., Sarris, T., Doornbos, E., Tourgaidis, S., Aikio, A., Buchert, S., Clilverd, M. A., Dandouras, I., Heelis, R., Hoffmann, A., Ivchenko, N., Kervalishvili, G., Knudsen, D. J., Kotova, A., Liu, H.-L., Malaspina, D. M., March, G., Marchaudon, A., Marghita, O., Matsuo, T., Miloch, W. J., Moretto-Jørgensen, T., Mpaloukidis, D., Olsen, N., Papadakis, K., Pfaff, R., Pirnaris, P., Siemes, C., Stolle, C., Suni, J., van den IJssel, J., Verronen, P. T., Visser, P., and Yamauchi, M.: Lower-thermosphere-ionosphere (LTI) quantities: current status of measuring techniques and models, *Annales Geophysicae*, 39, 189–237, <https://doi.org/10.5194/angeo-39-189-2021>, 2021.

- Picone, J. M., Hedin, A. E., Drob, D. P., and Aikin, A. C.: NRLMSISE-00 empirical model of the atmosphere: Statistical comparisons and scientific issues, *Journal of Geophysical Research (Space Physics)*, 107, 1468, <https://doi.org/10.1029/2002JA009430>, 2002.
- Pokhotelov, D., Becker, E., Stober, G., and Chau, J. L.: Seasonal variability of atmospheric tides in the mesosphere and lower thermosphere: meteor radar data and simulations, *Annales Geophysicae*, 36, 825–830, <https://doi.org/10.5194/angeo-36-825-2018>, 2018.
- Pulkkinen, A., Bernabeu, E., Thomson, A., Viljanen, A., Pirjola, R., Boteler, D., Eichner, J., Cilliers, P. J., Welling, D., Savani, N. P., Weigel, R. S., Love, J. J., Balch, C., Ngwira, C. M., Crowley, G., Schultz, A., Kataoka, R., Anderson, B., Fugate, D., Simpson, J. J., and MacAlester, M.: Geomagnetically induced currents: Science, engineering, and applications readiness, *Space Weather*, 15, 828–856, <https://doi.org/10.1002/2016SW001501>, 2017.
- Rapp, M., Gumbel, J., and Lübken, F. J.: Absolute density measurements in the middle atmosphere, *Annales Geophysicae*, 19, 571–580, <https://doi.org/10.5194/angeo-19-571-2001>, 2001.
- Rawer, K., Bilitza, D., and Ramakrishnan, S.: Goals and status of the international reference ionosphere., *Reviews of Geophysics and Space Physics*, 16, 177–181, <https://doi.org/10.1029/RG016i002p00177>, 1978.
- Richmond, A. D., Ridley, E. C., and Roble, R. G.: A thermosphere/ionosphere general circulation model with coupled electrodynamics, *Geophysical Research Letters*, 19, 601–604, <https://doi.org/10.1029/92GL00401>, 1992.
- Rino, C. L., Brekke, A., and Baron, M. J.: High-resolution auroral zone E region neutral wind and current measurements by incoherent scatter radar, *Journal of Geophysical Research*, 82, 2295, <https://doi.org/10.1029/JA082i016p02295>, 1977.
- Rishbeth, H.: F-region links with the lower atmosphere?, *Journal of Atmospheric and Solar-Terrestrial Physics*, 68, 469–478, <https://doi.org/10.1016/j.jastp.2005.03.017>, 2006.
- Rishbeth, H. and Garriott, O. K.: *Introduction to ionospheric physics*, Academic Press, Inc., 1969.
- Sarris, T. E., Talaat, E. R., Palmroth, M., Dandouras, I., Armandillo, E., Kervalishvili, G., Buchert, S., Tourgaidis, S., Malaspina, D. M., Jaynes, A. N., Paschalidis, N., Sample, J., Halekas, J., Doornbos, E., Lappas, V., Moretto Jørgensen, T., Stolle, C., Clilverd, M., Wu, Q., Sandberg, I., Pirnaris, P., and Aikio, A.: Daedalus: a low-flying spacecraft for in situ exploration of the lower thermosphere-ionosphere, *Geoscientific Instrumentation, Methods and Data Systems*, 9, 153–191, <https://doi.org/10.5194/gi-9-153-2020>, 2020.
- Schunk, R. and Nagy, A.: *Ionospheres: Physics, Plasma Physics, and Chemistry*, Cambridge Academic Press, <https://doi.org/10.1017/CBO9780511635342>, 2009.

- Stober, G.: Remote sensing of Middle Atmospheric Dynamics at mid- and polar latitudes, [https://www.ub.unibe.ch/recherche/sondersammlungen/bernensia/dissertationen\\_der\\_universitaet\\_bern/index\\_ger.html](https://www.ub.unibe.ch/recherche/sondersammlungen/bernensia/dissertationen_der_universitaet_bern/index_ger.html), Habilitationsschrift, University of Bern, 2019.
- Stober, G., Kozlovsky, A., Liu, A., Qiao, Z., Tsutsumi, M., Hall, C., Nozawa, S., Lester, M., Belova, E., Kero, J., Espy, P. J., Hibbins, R. E., and Mitchell, N.: Atmospheric tomography using the Nordic Meteor Radar Cluster and Chilean Observation Network De Meteor Radars: network details and 3D-Var retrieval, *Atmospheric Measurement Techniques*, 14, 6509–6532, <https://doi.org/10.5194/amt-14-6509-2021>, 2021a.
- Stober, G., Kuchar, A., Pokhotelov, D., Liu, H., Liu, H.-L., Schmidt, H., Jacobi, C., Baumgarten, K., Brown, P., Janches, D., Murphy, D., Kozlovsky, A., Lester, M., Belova, E., Kero, J., and Mitchell, N.: Interhemispheric differences of mesosphere-lower thermosphere winds and tides investigated from three whole-atmosphere models and meteor radar observations, *Atmospheric Chemistry & Physics*, 21, 13 855–13 902, <https://doi.org/10.5194/acp-21-13855-2021>, 2021b.
- Stober, G., Liu, A., Kozlovsky, A., Qiao, Z., Kuchar, A., Jacobi, C., Meek, C., Janches, D., Liu, G., Tsutsumi, M., Gulbrandsen, N., Nozawa, S., Lester, M., Belova, E., Kero, J., and Mitchell, N.: Meteor radar vertical wind observation biases and mathematical debiasing strategies including the 3DVAR+DIV algorithm, *Atmospheric Measurement Techniques*, 15, 5769–5792, <https://doi.org/10.5194/amt-15-5769-2022>, 2022.
- Stober, G., Weryk, R., Janches, D., Dawkins, E. C. M., Günzkofer, F., Hormaechea, J. L., and Pokhotelov, D.: Polarization dependency of transverse scattering and collisional coupling to the ambient atmosphere from meteor trails - theory and observations, , 237, 105768, <https://doi.org/10.1016/j.jpss.2023.105768>, 2023.
- Straus, J. M., Creekmore, S. P., Harris, R. M., Ching, B. K., and Chiu, Y. T.: A global model for thermospheric dynamics - II. Wind, density, and temperature fields generated by EUV heating., *Journal of Atmospheric and Terrestrial Physics*, 37, 1245–1253, [https://doi.org/10.1016/0021-9169\(75\)90197-X](https://doi.org/10.1016/0021-9169(75)90197-X), 1975.
- Thayer, J. P.: High-latitude currents and their energy exchange with the ionosphere-thermosphere system, *Journal of Geophysical Research*, 105, 23 015–23 024, <https://doi.org/10.1029/1999JA000409>, 2000.
- Tjulín, A.: EISCAT Experiments, Tech. rep., URL [https://eiscat.se/wp-content/uploads/2022/02/Experiments\\_v20220203.pdf](https://eiscat.se/wp-content/uploads/2022/02/Experiments_v20220203.pdf), last accessed: April 11, 2024, 2022.
- Tsugawa, T., Otsuka, Y., Coster, A. J., and Saito, A.: Medium-scale traveling ionospheric disturbances detected with dense and wide TEC maps over North America, *Geophysical Research Letters*, 34, L22101, <https://doi.org/10.1029/2007GL031663>, 2007.

- Vadas, S. L. and Becker, E.: Numerical Modeling of the Excitation, Propagation, and Dissipation of Primary and Secondary Gravity Waves during Wintertime at McMurdo Station in the Antarctic, *Journal of Geophysical Research (Atmospheres)*, 123, 9326–9369, <https://doi.org/10.1029/2017JD027974>, 2018.
- Vadas, S. L. and Fritts, D. C.: Thermospheric responses to gravity waves: Influences of increasing viscosity and thermal diffusivity, *Journal of Geophysical Research (Atmospheres)*, 110, D15103, <https://doi.org/10.1029/2004JD005574>, 2005.
- Vadas, S. L., Zhao, J., Chu, X., and Becker, E.: The Excitation of Secondary Gravity Waves From Local Body Forces: Theory and Observation, *Journal of Geophysical Research (Atmospheres)*, 123, 9296–9325, <https://doi.org/10.1029/2017JD027970>, 2018.
- van de Kamp, M., Pokhotelov, D., and Kauristie, K.: TID characterised using joint effort of incoherent scatter radar and GPS, *Annales Geophysicae*, 32, 1511–1532, <https://doi.org/10.5194/angeo-32-1511-2014>, 2014.
- Vickrey, J. F., Vondrak, R. R., and Matthews, S. J.: Energy deposition by precipitating particles and Joule dissipation in the auroral ionosphere, *Journal of Geophysical Research*, 87, 5184–5196, <https://doi.org/10.1029/JA087iA07p05184>, 1982.
- Vlasov, A., Kauristie, K., van de Kamp, M., Luntama, J. P., and Pogoreltsev, A.: A study of Traveling Ionospheric Disturbances and Atmospheric Gravity Waves using EISCAT Svalbard Radar IPY-data, *Annales Geophysicae*, 29, 2101–2116, <https://doi.org/10.5194/angeo-29-2101-2011>, 2011.
- Weimer, D. R.: Improved ionospheric electrodynamic models and application to calculating Joule heating rates, *Journal of Geophysical Research (Space Physics)*, 110, A05306, <https://doi.org/10.1029/2004JA010884>, 2005.
- Williams, P. J. S. and Viridi, T. S.: EISCAT observations of tidal modes in the lower thermosphere, *Journal of Atmospheric and Terrestrial Physics*, 51, 569–577, [https://doi.org/10.1016/0021-9169\(89\)90055-X](https://doi.org/10.1016/0021-9169(89)90055-X), 1989.

# Danksagung

Zunächst möchte ich mich bei **Markus Rapp** für die Betreuung meiner Promotion bedanken. Danke, dass du dir stets Zeit genommen hast für unsere regelmäßigen Treffen und bei Fragen immer verfügbar warst. Danke auch für das stets ehrliche und direkte Feedback. Ein sehr großer Dank geht auch an meine beiden fachlichen Betreuer, **Gunter Stober** und **Dimitry Pokhotelov**. Ohne euer großes Engagement und natürlich auch eure fachliche Kompetenz wäre diese Doktorarbeit nicht möglich gewesen.

Ebenso geht ein großer Dank an **Claudia Borries**, in deren Abteilung des DLR Instituts für solar-terrestrische Physik ich meine Promotion erarbeiten durfte. Danke, dass du bei jeglichen Fragen stets zur Verfügung standst und dich mit großem Engagement um den Erfolg meiner Promotion bemüht hast.

Bei meinen zahlreichen Kollaborationspartnern/Co-Autoren möchte ich mich natürlich für die erfolgreiche und auch sehr angenehme Zusammenarbeit bedanken. Obwohl ich nicht alle persönlich nennen kann, möchte ich mich im Speziellen bei **Huixin Liu** bedanken, die mir einen dreimonatigen Aufenthalt an der Kyushu Universität in Japan ermöglichte.

Meinen Kollegen am DLR-SO Institut möchte ich für die sehr angenehme Arbeitsatmosphäre und für zahlreiche unterhaltsame Mittags- und Kaffeepausen danken. Leider kann ich auch hier nicht alle einzeln nennen, möchte allerdings einige Personen hervorheben und hoffe alle anderen wissen, dass sie nicht weniger gemeint sind. Danke an **Olaf Frauenberger**, der als mein DLR Mentor immer ein Auge auf den reibungslosen Ablauf meiner Promotion hatte. Danke an **Frank Heymann**, dass du dir stets für die IT Probleme aller Kollegen Zeit nimmst. Ebenso danke an **Arthur F**, **Arthur G**, **Gloria**, **Hanna**, **Helen**, **Katja**, **Pelin** und alle andere Doktoranden an unserem Institut. Mit euch war es sowohl bei der Arbeit als auch außerhalb immer sehr unterhaltsam. Danke an **Andrea**, **Antje** und **Bianca** für die tadellose Organisation von Dienstreisen, Weihnachtsfeiern und dem allgemeinen Büroalltag.

Zu guter Letzt geht ein riesengroßes Dankeschön an meine Familie. Danke an meine Eltern, dass ihr mich immer bei allem unterstützt habt, egal wo mein Weg mich hinführte. Danke an meine Schwester Kristina, dass ich Onkel der tollsten Nichte der Welt sein darf. Und natürlich vielen lieben Dank an meine Jessi, einfach dafür dass du da bist.